INVESTIGATING THE APPLICATIONS OF ELECTROPORATION THERAPY FOR TARGETED TREATMENT OF GLIOBLASTOMA MULTIFORME BASED ON MALIGNANT PROPERTIES OF CELLS

Jill W. Ivey

Dissertation submitted to the faculties of the
Virginia Polytechnic Institute and State University
in partial fulfillment of the requirements for the degree of

Doctor of Philosophy
in
Biomedical Engineering

Scott S. Verbridge
Rafael V. Davalos
John H. Rossmeisl
Yong Woo Lee
Zhi Sheng

July 27, 2017
Blacksburg, VA

Keywords: pulsed electric fields, tissue engineering, hydrogels, brain cancer therapy, glioma, cell morphology, bipolar pulses, high frequency

Investigating the Applications of Electroporation Therapy for Targeted Treatment of Glioblastoma Multiforme Based on Malignant Properties of Cells

Jill W. Ivey

ABSTRACT

Glioblastoma multiforme (GBM) is the most common and lethal primary brain cancer with an average survival time of 15 months. GBM is considered incurable with even the most aggressive multimodal therapies and is characterized by near universal recurrence. Irreversible electroporation (IRE) is a cellular ablation method currently being investigated as a therapy for a variety of cancers. Application of IRE involves insertion of electrodes into tissue to deliver pulsed electric fields (PEFs), which destabilize the cell membrane past the point of recovery, thereby inducing cell death. While this treatment modality has numerous advantages, the lack of selectivity for malignant cells limits its application in the brain where damage to healthy tissue is especially deleterious. In this dissertation we hypothesize that a form of IRE therapy, high-frequency IRE (H-FIRE), may be able to act as a selective targeted therapy for GBM due to its ability to create an electric field inside a cell to interact with altered inner organelles. Through a comprehensive investigation involving experimental testing combined with numerical modeling, we have attained results in strong support of this hypothesis. Using tissue engineered hydrogels as our platform for therapy testing, we demonstrate selective ablation of GBM cells. We develop mathematical models that predict the majority of the electric field produced by H-FIRE pulses reach the inside of the cell. We demonstrate that the increased nuclear to cytoplasm ratio (NCR) of malignant GBM cells compared to healthy brain—evidenced *in vivo* and in *in vitro* tissue mimics—is correlated with greater ablation volumes and thus lower electric field thresholds for cell death when treated with H-FIRE. We enhance the selectivity achieved with H-FIRE using a molecularly targeted drug that

induces an increase in NCR. We tune the treatment pulse parameters to increase selective malignant cell killing. Finally, we demonstrate the ability of H-FIRE to ablate therapy-resistant GBM cells which are a focus of many next-generation GBM therapies. We believe the evidence presented in this dissertation represents the beginning stages in the development of H-FIRE as a selective therapy to be used for treatment of human brain cancer.

Investigating the Applications of Electroporation Therapy for Targeted Treatment of Glioblastoma Multiforme Based on Malignant Properties of Cells

Jill W. Ivey

GENERAL AUDIENCE ABSTRACT

Glioblastoma multiforme (GBM) is the most common and lethal primary brain cancer with an average survival time of 15 months. GBM is considered incurable with even the most aggressive multimodal therapies and is characterized by near universal recurrence. Irreversible electroporation (IRE) is a therapy currently being developed for the treatment of a variety of cancers. Application of IRE involves the delivery of energy directly into the tumor tissue in the form of pulsed electric fields (PEFs). These PEFs destabilize the cell membrane past the point of recovery, thereby inducing cell death. Though this treatment modality has numerous advantages, the lack of selectivity for malignant cells limits its application in the brain where damage to healthy tissue is especially deleterious. In this dissertation we hypothesize that a form of IRE therapy, high-frequency IRE (H-FIRE), may be able to act as a selective targeted therapy for GBM due to its ability to create electric fields inside cells. Because cancer is characterized by alterations in inner organelles compared to healthy cells, electric fields inside the cell may be able to target these alterations resulting in selective malignant cell killing. Through a comprehensive investigation involving experimental testing combined with numerical modeling, we have attained results in strong support of this hypothesis. We have successfully demonstrated selective ablation of malignant GBM cells. We have shown that the increased nuclear to cytoplasm ratio (NCR) of malignant GBM cells compared to healthy brain—evidenced *in vivo* and in *in vitro* tissue mimics—is correlated with greater ablation volumes and thus lower electric field thresholds for cell death when treated with H-FIRE. We have enhanced the selectivity

achieved with H-FIRE using a molecularly targeted drug that induces an increase in NCR. We have tuned the treatment parameters to increase selective malignant cell killing. Finally, we have demonstrated the ability of H-FIRE to ablate therapy-resistant GBM cells which are a focus of many next-generation GBM therapies. We believe the evidence presented in this dissertation represents the beginning stages in the development of H-FIRE as a selective therapy to be used for treatment of human brain cancer.

To my mom, dad, and sister…

Acknowledgements

I have had the great advantage in life to have always been surrounded by people who are supportive and encouraging of me. I grew up in a household where the love of science and learning was instilled in me from a young age. My parents always taught me I could do anything I set my mind to and have kept encouraging me with that notion through all the tough spots on the journey that has brought me to where I am today. I would like to thank my parents for leading me through example, for always encouraging and supporting me, and for providing me with everything I have ever needed to succeed. I would like to thank my sister Kate for being my companion in life and for being the smarter sibling, forcing me to prove my worth. Endless thanks are due to my whole family for allowing me to grow up in an environment full of love, care, fun, happiness, and intellectual-stimulation. I dedicate this dissertation to you all.

Thanks also to my advisor, Dr. Verbridge, for giving me the opportunity to work in an amazing lab on a project I am passionate about. Thank you for all your guidance, your expertise, and your inspiration that have made me a better researcher, a more discerning scientist, and a better writer. I would also like to thank Dr. Davalos for his endless collaboration that has guided this project and introduced me to valuable new engineering tools. Thank you to the members of my committee for the collaboration that has made this project possible, for asking the tough questions that have made me a better researcher, and for guiding my journey through graduate school.

Thank you as well to the members of the Verbridge and Davalos labs for your support, your help brainstorming, and for sharing your knowledge and expertise. Thanks specifically to Megan Cox for keeping our entire lab running. Without you, my success would have never been possible.

Thanks to Eduardo Latouche for the endless hours of experiments, troubleshooting, brainstorming, and fun. You made this project and all its many obstacles enjoyable. Thanks finally to the friends that have made these past five years so fun. Thanks especially to Shannon Mumma for always supporting and encouraging me and pushing me to be the best version of myself both personally and academically. And thanks for giving Watson and I a home full of fun and motivation during the endless days of writing. Without the help and support of all these people and many more, I would not be where I am or who I am today.

Table of Contents

List of Figures

List of Tables

List of frequent abbreviations

AC – Alternating current

BSA – Bovine serum albumin

BBB – Blood brain barrier

DC – Direct current

DMEM – Dulbecco’s Modified Eagle Medium

eA1 – ephrinA1

ECM – Extracellular matrix

ECT – Electrochemotherapy

EGFR – Epidermal growth factor receptor

FEM – Finite element model

FBS – Fetal bovine serum

FGFR – Fibroblast growth factor receptor

GBM – Glioblastoma multiforme

GSC – Glioma stem cell

H-FIRE – High frequency irreversible electroporation

IRE – Irreversible electroporation

MDR – Multiple drug resistance

NCR – Nuclear to cytoplasm ratio

NGF – Nerve growth factor

NHA – Normal human astrocyte

nsPEF – Nanosecond pulsed electric field

nTMP – Nuclear transmembrane potential

PDMS – Polydimethylsiloxane

PEF – Pulsed electric field

PM – Plasma membrane

PS – Penicillin/streptomycin

RE – Reversible electroporation

TME – Tumor microenvironment

TMP – Transmembrane potential

TMZ - Temozolomide

Chapter 1 Overview

1.1 Motivation

Despite tremendous advances in our understanding of the biology of cancer at the genetic and molecular level, the prognosis for many cancers remains poor. Cancer is a ubiquitous disease in today's society, partly due to the aging population, with about 40% of people diagnosed with cancer in their lifetimes (1). Irreverent of our push to find new and more effective cancer cures, cancer incidence and death are expected to increase in the next two decades. By 2030, it is projected that worldwide cancer incidence with rise by 50% and worldwide cancer deaths will rise by 60% (1, 2). Such a wide-reaching problem with so few effective solutions, has drawn the attention of many researchers looking to tackle this problem in innovative ways.

Though the prognosis of some cancers has improved with new treatments, malignancies of the central nervous system remain the third leading cause of death in adolescents and adults aged 15-34 years, and are the leading cause of cancer death in children (3). Glioblastoma multiforme (GBM), the most common and deadly primary brain tumor, has a dismal prognosis that has remained relatively unchanged despite many attempts at new therapies. The failure of current treatments to greatly extend life expectancy is attributable to a few classes of therapy resistant cell that propel tumor recurrence, which is nearly universal with GBM. A GBM tumor proves fatal within about 14 months even with multimodal intervention (4). The most common approaches to the treatment of GBM involve surgery (5), radiation therapy (6), and/or chemotherapeutic regimens (7). Neither single therapies nor treatments used in combination are curative and they are often debilitating to the patient. Though emerging therapies have been developed and shown some

promise, such as carmustine wafers (8) or molecular therapies such as bevacizumab (9, 10), results are often contradictory and no treatment other than surgery, radiation, and temozolomide therapy has been widely accepted. There exists a real need for next-generation GBM therapies, for use alone or in combination with current therapies, which can target the resistant cell populations and prevent tumor recurrence.

This work was motivated by the desire to approach GBM treatment from a new perspective often overlooked in therapy development. Rather than focus on biological phenotypes typically considered as cancer targets yet problematic due to their variable expression, our research motivation is to find a different class of targets. While physical hallmarks of tumors are commonly used for diagnosis, they are rarely considered as therapeutic targets. Physical phenotypes are often well conserved across a given cancer and are known to impact disease progression (11), making them a valuable target to be investigated. The desire to explore targets left relatively unexplored for GBM treatment, the physical alterations of the GBM cell, in order to find a new therapy that may overcome current treatment barriers, is the motivation of this dissertation.

1.2 Project goals

The goal of this project was to develop, characterize, and test a selective therapy for the treatment of GBM. The focus of the selective therapy for this particular cancer was on the two types of therapy-resistant cells commonly found in the tumor that currently are considered responsible for tumor recurrence and contribute largely to the poor prognosis—invasive cells and glioma stem cells. The overall goal of the therapy, therefore, was to target a conserved malignant alteration in

a way that affected both quiescent glioma stem cells, and could safely kill malignant cells in an environment surrounded by healthy cells (Figure 1.1).

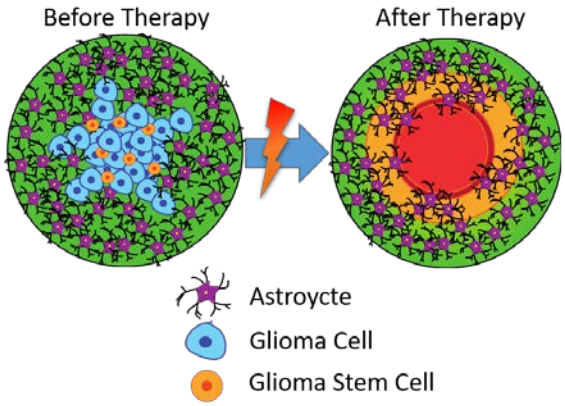

Figure 1.1 Concept illustration of project goals for targeted therapy. *The goal of the selective therapy to be developed is the ablation of glioma cells invading into healthy astrocytes past the tumor margin as well as therapy-resistant glioma stem cells*

Irreversible electroporation (IRE) is a clinically used cancer therapy involving the application of pulsed electric fields to a tissue for cell ablation. However, the lack of selectivity of IRE limits its efficacy for invasive cancers such as GBM, especially in an organ as sensitive as the brain. It was hypothesized at the onset of this project that pulse parameters involved in the application of IRE could be tuned in such a way that the field may interact with the inside of a cell. The altered cancerous inner organelles, such as the enlarged nucleus, could therefore be a possible target. This hypothesis motivated the subsequent studies. The goals for testing this hypothesis involved:

1- identifying a cancerous alteration to be targeted

2- demonstrating selective ablation of malignant bulk tumor cells

3- demonstrating selective ablation of glioma stem cells

4- enhancing the selectivity of the therapy for malignant cells to improve clinical application

1.3 Document organization

This document is organized into nine chapters. Chapter 2 presents a review of the current state of cancer and current treatment options with a focus on GBM. Chapter 3 presents a review of electroporation phenomenon and the leverage of electroporation for cancer therapy. Chapter 4 presents experimental and finite element modeling evidence for the selective ablation of malignant cells by H-FIRE based on enlarged nuclear to cytoplasm ratio (NCR). This chapter is an adaptation of the work published as:

J.W. Ivey, E.L. Latouche, M.B. Sano, J.H. Rossmeisl, R.V. Davalos, S.S. Verbridge, Targeted cellular ablation based on the morphology of malignant cells, *Scientific Reports*, 5, (2015).

Chapter 5 presents an investigation into the use of a molecular targeted therapy to induce a selective NCR increase in malignant cells which enhances H-FIRE selectivity. This chapter is an adaptation of work published as:

J.W. Ivey, E.L. Latouche, M.L. Richards, G.J. Lesser, W. Debinski, R.V. Davalos, S.S. Verbridge, Enhancing Irreversible Electroporation by Manipulating Cellular Biophysics with a Molecular Adjuvant, *Biophysical Journal*, 113, 472-480 (2017).

Chapter 6 looks closely at pulse parameters which can be tuned for enhanced malignant cell selectivity. Chapter 7 presents evidence demonstrating the ability of H-FIRE to ablate therapy-resistant glioma stem cells. Finally, Chapter 8 highlights the major findings and future directions of this research, and Chapter 9 lists the references used as support throughout the document.

Chapter 2 Introduction to Cancer Therapy

2.1 Current state of cancer therapies

Despite the fact that the “war on cancer” was waged over 40 years ago and significant time and resources have gone into researching cancer cures, cancer remains the second leading cause of death according to the World Health Organization, only slightly behind cardiovascular disease (12). The number of cancer cases are projected to double worldwide in the next 20-40 years, with cancer projected to overtake cardiovascular disease as the number one cause of death (2, 13). While some progress has been made in improving cancer prognosis, these improvements are limited to certain types of cancers such as breast, prostate, and colorectal (12). In many other cancers, prognosis remains grim despite constant efforts to develop new therapies and technologies. Cancer cells have evolved a variety of resistance mechanisms that allow them to overcome many of the treatments developed. Active pump mechanisms (14), apoptosis inhibitors (15, 16) and inhibition of signaling molecules (17) all allow cancer cells to acquire multiple drug resistance (MDR) to outlast many pharmaceutical treatments. Surgical resection is limited by both the morphology of the tumor and the location relative to sensitive structures. The most commonly used chemotherapies target a biological phenotype of cancer cells, specifically their highly proliferative nature. However, such therapies leave behind resistant sub-populations of quiescent cells that repopulate the tumor, while also resulting in toxicity to healthy proliferative cells. Physical therapies such as ionizing radiation have limited efficacy in part because of the molecular mechanisms developed by cancerous cells to inhibit apoptosis pathways (18). Recently, targeted therapies have been developed to overcome the shortcomings of traditional regimes. However, these therapies are plagued by their own shortcomings. Recent advancements in targeted therapy

typically focus on receptors that are upregulated in cancer. However, many of the receptors currently being targeted are also expressed in normal cell populations, leading to off-target effects and potential toxicity (19-22). With a current therapeutic focus on biological properties of neoplastic cells, which tend to have a high degree of variance due to the highly heterogeneous nature of tumors, tumor recurrence and metastasis continue to present major challenges.

2.1.1 Surgery

Surgical resection is often the first method of treatment for solid tumors. This treatment involves physically removing as much of the tumor as is safe for the patient through surgery. Surgical resection is a local treatment and therefore limited to solid tumors that have not metastasized. Often tumors with irregular shape or those surrounding critical structures cannot be removed fully with surgery and only part of the tumor will be removed. Surgical resection is often combined with radiation therapy and chemotherapy for full treatment of a tumor.

2.1.2 Radiation therapy

Radiation therapy uses high energy radiation in the form of X-rays, gamma rays, and charged particles, to induced DNA damage in cells aimed at killing a tumor. Radiation therapy induces DNA damage either by inducing ionization directly on the cellular molecules or through the creation of free radicals which can induce DNA damage within the cells. As in the case of chemotherapy, quickly dividing cells are more susceptible to DNA damage by radiotherapy due to the fact that they go through the cell cycle process at a more rapid rate creating more opportunities for critical damage. Unlike chemotherapy which is systemic, radiation therapy is

often delivered locally and pre-treatment planning is used to determine a delivery scheme that will target the tumor region and minimize exposure for healthy regions. Radiation is the most commonly used treatment with approximately 50% of all cancer patients receiving radiotherapy during their course of illness (23). It is often the only option for patients with inoperable tumors and is useful for patients with incompletely resected or recurrent tumors after surgery (24).

The efficacy of radiation therapy is limited by resistance of the targeted cells to DNA damage. DNA repair pathways, naturally present in cells to protect against cell killing and mutagenesis, present clinical challenges to tumor treatment with radiotherapy. Three DNA repair pathways in particular are considered to be responsible for removing the majority of the damage imparted by radiotherapy—base excision repair (BER), non-homologous end joining (NHEJ), and homologous recombination (HR). Radiation-induced cell death relies on high yields of single-strand breaks and double-strand breaks, which are repaired by BER and NHEJ, respectively. HR plays a significant role in double-strand breaks in replicating cells (25). Besides the DNA repair pathways, ionizing radiation also triggers cancer cells' adaptive cellular responses. Activated oncogenes induce signal transduction pathways to impart cells with either intrinsic or an acquired resistance during radiation treatment. Specifically problematic in radioresistance are signaling pathways that provide cancer cells with a proliferative advantage or allow them to evade the cell death. Signal transduction pathways such as those regulated by membrane-bound receptor tyrosine kinases (RTKs) can be activated in a ligand-independent manner to allow cells to acquire radioresistance (26). Important pathways downstream of epidermal growth factor receptor (EGFR), such as those involving the phosphatidylinositol 3-kinase (PI3K) and its downstream kinases such as AKT and mammalian target of rapamycin (mTOR), have been implicated in radioresistance. The pro-

survival PI3K-AKT-mTOR signaling pathway is frequently upregulated in human tumors and regarded as one of the most challenging pro-survival pathways involved in the resistance to cancer treatment (27). Signal transducer and activator of transcription (STAT) pathway and Ras-mitogen-activated protein kinase (MAPK) pathway have also been implicated in radioresistance (28, 29). Because these mechanisms of radioresistance cause decreased efficacy of a core treatment option, efforts are being made to increase radiosensitivity through inhibition of DNA repair proteins (30-32), the manipulation of apoptotic pathways (33), and the inhibition of oncogenic pathways (34-36).

2.1.3 Chemotherapy

Chemotherapy involves the use of a variety of drugs which have a cytotoxic effect on cells. These drugs preferentially, but not exclusively, target rapidly dividing cancer cells. Chemotherapy is mainly used to control the overt disseminated disease, though it is also used as adjuvant treatment for primary tumors. Because cancer cells are typically (though not always) quickly dividing with excessively active growth-signaling pathways, chemotherapeutic drugs target these features in a variety of ways. A wide range of drugs are used, which have a wide range of targets, such as growth-signaling molecules and processes involved in cellular replication and expression. However, as these processes also drive normal cells, the effect of chemotherapeutic drugs in not limited to cancer cells, which results in unwanted side-effects. Normal cells that are by nature quickly dividing, such as the bone marrow constituents and cells of the intestinal lining, are particularly susceptible to unwanted chemotherapy damage.

In addition to the limitations of chemotherapy due to off-target effects, many cells exhibit resistance to a large number of chemotherapy drugs. Some cancers exhibit intrinsic resistance to certain drugs, whereby the resistance-mediating factors that pre-exist in the bulk of tumor cells make the therapy ineffective before ever being exposed to the drug. Other cancer cells are initially sensitive to the drug but after being exposed to chemotherapy, develop acquired drug resistance. This resistance can be caused by mutations arising during treatment, as well as through other adaptive responses, such as activation of alternative compensatory signaling pathways (37). A tumor is composed of a heterogeneous population of cells, some of which are drug-sensitive and others of which are drug-resistant. Drug resistance can arise through therapy-induced selection of a resistant minor subpopulation of cells that was present in the original tumor (38). After the initial rounds of chemotherapy, drug-sensitive cells are killed and drug-resistant cells are left behind to repopulate the tumor. The tumor may respond to treatment initially, but as the chemotherapeutic regime persist, the remaining drug-resistant cells show a poor response, and the tumor displays acquired resistance. It is typical for 1 in 10^6 –10^7 cancer cells in a tumor to have inherent resistance against a particular drug. A clinically detectable tumor typically has around 10^9 cells. Therefore it can be expected that a typical tumor may to contain 10–1,000 drug-resistant cells, which have the potential to repopulate the tumor despite destruction of the sensitive cells (25). Therefore, the probability of cure with chemotherapy is directly related to the size of the tumor when treatment begins. Chemotherapy has shown promise at curing certain cancers, such as childhood leukemias, Hodgkin's disease or testicular cancers, because the few surviving drug-resistant cells may become susceptible to the immune system(25).

For many drug-resistant cells, their MDR is associated with expression of ATP binding cassette (ABC) transporters. ABC transporters, which are expressed in the plasma membrane to maintain physiological homeostasis, can efflux a wide range of drugs to below therapeutic levels regardless of the starting concentration (39). Three pumps commonly associated with poor response to chemotherapy are P-glycoprotein (P-gp), the multidrug resistance-associated protein (MRP), and breast cancer resistance protein (BCRP) (40, 41). The MDR1 gene which encodes P-gp expression is the most common observed mechanism in clinical MDR (39, 42-44). Commonly used chemotherapeutic drugs such as doxorubicin and paclitaxel can be expelled by the P-gp pump (25). ABC transporters are especially problematic in cancer treatment because they can translocate a large number of structurally diverse compounds, unlike classical transporters which are very selective to certain molecules. This allows ABC transporters to impart cells with cross-resistance to several chemically unrelated drugs. In addition to altered membrane transport, another mechanism of resistance is a response on the genetic level. Exposure to chemotherapeutic drugs can induce an expression of protective genes in the cancer cells, allowing them to escape the effect of the drugs (41). Drug resistant cell lines have been shown to undergo gene rearrangement resulting in increased expression of MDR1, the gene which encodes P-gp (45). Defects in or deletion the p53 gene, which regulates cell cycle and the apoptotic pathway, is also associated with MDR (46, 47). Other genes involved in the apoptotic pathway such as h-ras and bcl-2/bax have shown evidence of contributing to resistance (48). Another method of gaining resistance that cells employ is through the use of DNA repair proteins. For instance, in the case of treatment with cisplatin, a commonly used chemotherapeutic drug, cells can develop an enhanced ability to remove cisplatin-DNA adducts and to repair cisplatin-induced lesions through elevation of proteins such as Xeroderma pigmentosum group E binding factor(XPE-BF) and excision repair

cross-complementing protein (ERCC1) (49). All of these mechanisms of intrinsic and acquired resistance translate into treatment failure, with rates of treatment failure for cancers in the metastatic stage around 90% when treated only with chemotherapy (25). While the cancer cells gain a level of resistance and begin showing poor response to the drugs, the healthy cells often remain drug-sensitive thereby causing many negative side effects in the patient while not effectively treating the cancer (50).

2.1.4 Targeted molecular therapy

Due to the advancement in our understanding of molecular and cell biology and the alterations at the molecular level in cancer cells, targeted therapies have emerged as a relatively new treatment direction. Targeted therapies involve the use of pathway inhibitors, especially kinase inhibitors, monoclonal antibodies, and oncolytic viruses to target receptors or signaling pathways that are altered in cancerous cells. A major goal of these therapies is to find targets on cancer cells that are distinctive enough from normal cells to achieve selective therapeutic response from the malignant cells without affecting healthy cells. Cancer cells commonly express different proteins on their cell surface than normal cells, including receptors which make valuable therapeutic targets due to their natural affinity for their preferred ligand. Many different classes of receptors have been identified as overexpressed in a variety of different cancers. Such receptors commonly targeted by molecular therapies include G protein coupled receptors, integrins, folate receptors, transferrin receptors, growth factor receptors, and sigma receptors. Cell-surface growth factor receptors, such as epidermal growth factor receptor (EGFR), and fibroblast growth factors (FGFRs) are attractive targets because they are often amplified and highly expressed in malignancy, and because they activate signaling pathways that are critical for tumor growth and survival. These overexpressed

receptors can be directly modulated or inhibited by agents such as antibodies or antibody fragments. The receptors can also be targeted by other small chemicals that directly bind the receptors and block their activities. Cytotoxic drugs can be conjugated to the preferred ligand of a targeted receptor to improve selective drug delivery. Another key focus of small molecule targeted therapy is the inhibition of important oncolytic pathways. Such pathways that are common targets include the PTEN/Akt pathway and the RAS/MAPK pathways (27).

Though targeted therapies represent a promising area of cancer intervention, in many cancers their efficacy remains limited. Often receptors which are targeted may be also found on healthy cells, decreasing the selectivity of such therapies. These targeted methods also drive the evolution of resistant cells by causing changes in receptor expression, causing eventual treatment failure. It is possible during the course of treatment, that the target can become modified or decreased to a level where it is no longer a useful target for treatment. For example, in the treatment of breast cancer with anti-estrogen drugs such as tamoxifen, tumors often transition from a responsive state to an endocrine-resistant state due to a loss of estrogen receptors in the tumor (51, 52).

As with all pharmaceutical treatments, targeted therapeutics are only effective if they physically reach their targeted environments. The physical makeup of solid tumors provides barriers to therapeutics, as drugs cannot reach their target due to the altered physical microenvironment created in tumor development (53, 54). The rapid division and proliferation that characterizes cancer cells leads to increased mass in a confined volume and causes increased intratumoral pressure and compression of lymphatic and blood vessels within the tumor, effectively baring drugs from reaching their intended site (Figure 2.1) (55). Angiogenesis results in leaky and uneven

vasculature and poor lymphatic drainage which decreases the likelihood of drugs reaching the tumor (54). For the most successful of targeted drugs less than 5% of the drug reaches the tumor (56).

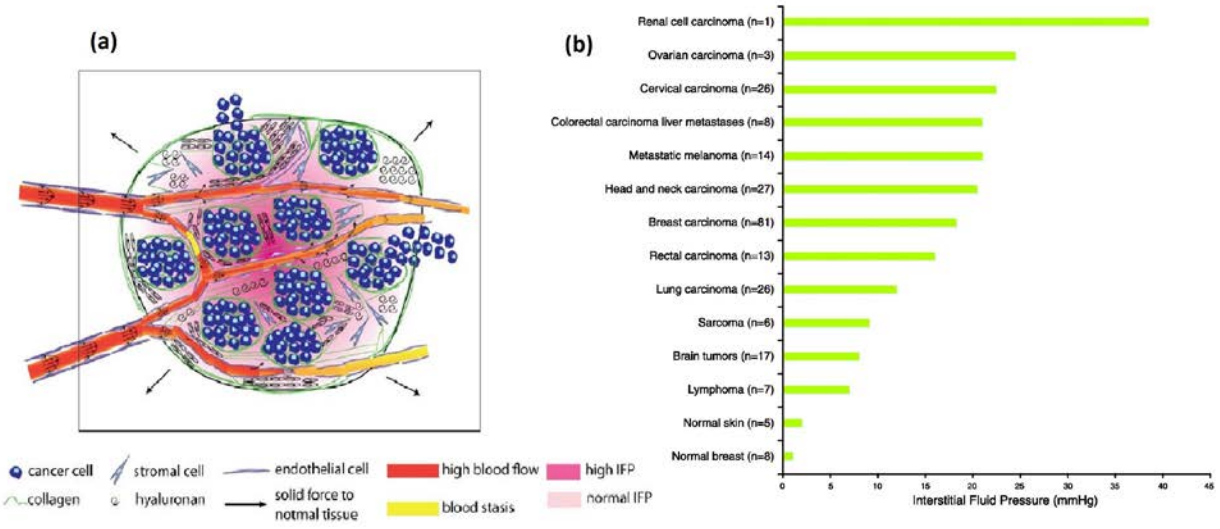

Figure 2.1 Major alterations in the mechanical tumor microenvironment that interfere with drug delivery to tumors. (a) *The rapid proliferation of cancer cells and stromal cells along with the deposition of collagen creates solid forces within the tumor. These forces cause compression of blood vessels, which leads to areas of high interstitial fluid pressure in the tumor (57).* ***(b)*** *A comparison of the interstitial fluid pressure in aggregated data collected from a variety of human tumors as compared to normal human tissues shows an often drastic increase in IFP in the tumor microenvironment (58). Data were collected from human patients using the wick-in-needle technique for measurement. Figure adapted from (59).*

One primary reason for the failure in current targeted treatment options is the highly heterogeneous nature of tumors (60). Not only does a given tumor vary greatly from other tumors (61-66) but also varies within a given tumor. The intra heterogeneity extends to nearly all phenotypic features, including cell morphology, gene expression, metabolism, migratory potential, and proliferative potential (67-70). A genetic analysis of multiple different regions in four different tumors of renal carcinoma and associated metastatic sites showed that all tumors had different somatic mutations and chromosomal imbalances in each different region that was biopsied, leading to a high degree of phenotypic diversity (71). This multi-scale heterogeneity drastically diminishes the treatment

efficacy of targeted therapies as a drug that may be successful in some cells is unlikely to affect all cells that make up the malignant neoplasm. Cells left behind due to this variable expression of targets can repopulate the tumor, resulting in overall treatment failure.

2.2 Glioblastoma multiforme

One such cancer that has had very little improvement in prognosis despite efforts at new interventions is glioblastoma multiforme (GBM) (72). Glioblastoma multiforme is a grade IV astrocytoma, caused by mutations to healthy astrocytes in the brain. GBM is the most common primary brain tumor as well as one of the most aggressive and invasive of all cancers. A person diagnosed with GBM has an average survival time of 14 months with intervention and an average survival time of less than 6 months without intervention (4). GBM tumors have been treated primarily with surgery followed by concurrent radiotherapy and adjuvant chemotherapy (73-75) Surgical protocols of maximal safe resection involve total resection only of the contrast enhancing component of the tumor to avoid removing tissue that will comprise neurological function (76). However, because of the highly invasive nature of GBM, to be sure to remove all cancerous cells would require removal of healthy brain tissue around the imaged tumor. Due to impossibility of this approach in the brain, surgery leaves behind cells that cause tumor relapse. The radiation regimes that follow surgery have limited specificity for cancerous cells and result in damage to normal cell types. Whole brain radiotherapy regimes cause radiation necrosis, pseudo-progression and cognitive defects in patients (77, 78), leading to a decrease in quality of life. Recently, adjuvant chemotherapy drugs have been used such as temozolomide (TMZ), but little improvements on survival have been achieved even with the adjuvant therapy due in part to the poor drug delivery in the brain. The blood brain barrier (BBB) represents a major challenge to delivery of therapeutics

in cancers such as GBM (79). Additionally, the epigenetic inactivation of the DNA repair enzyme methylguanin methyltransferatse (MGMT) in many cases of GBM causes alkylating compounds such as TMZ and nitrosourea to have limited efficacy. Chemoresistance in GBM has also been attributed to other DNA repair pathways such as DNA mismatch repair and the base excision repair pathways (80). Recent advancements in targeted therapies have had some success in certain cancers, such as targeting the Her2 receptor in breast cancer (81). However, the heterogeneity presented in GBM has restricted the success of such approaches for treatment of this cancer (82). GBM is characterized by distinct subclasses within an individual tumor (82-84). Many tyrosine kinases commonly used as receptor targets such as EGFR, PDGFRA, and MET have shown variable expression within a single tumor (85). As a result, response of cell lines derived from the same tumor exhibit different responses to growth factors (86) and therapeutics (87). Such a variable response in a single tumor poses great challenges for molecular targeting, as cells with lower receptor expressions will be left behind from these therapies to repopulate the tumor. The resistance response is complicated by the fact that rather than being a single resistance cancer clone, multiple clones with different genetic aberrations that allow survival after initial treatment may co-exist within the same cancer (84, 88). Driven by evolutionary selection pressures, heterogeneity becomes a survival advantage for the tumor in resisting treatment (70, 89).

Heterogeneity does not only extend to the molecular make-up of cells in this cancer. Rather, the tumor is characterized by a wide variety of phenotypic profiles, across varying microenvironmental niches (83, 90). This microenvironmental heterogeneity also manifests itself in physical differences in cells in the tumoral space. Some of these phenotypic profiles lead to resistance to current therapies. In particular, two classes of therapy resistant cells are prevalent in

GBM tumors, glioma stem cells and invasive glioma cells. Glioma stem cells (GSCs) are a subpopulation of cells in the tumor that have been shown to be responsible for tumor initiation and maintenance in GBM (91). These cells have a low proliferation rate, leading to escape from chemotherapy and radiation therapy. GSCs are not only quiescent but can repair damage done by radiation through DNA repair checkpoints (91). Because GSCs often share surface markers with normal brain tissue stem cells, molecular targeting cannot accomplish the selectivity necessary for non-toxic therapy. The characteristic resistance of GSCs, combined with their high tumorigenic potential, which allows them to repopulate the tumor after therapies have killed the tumor bulk, make them a highly important target for GBM therapies.

Invasive cells are also an important class of resistant cells that need to be targeted for GBM therapies to have high efficacy. GBM is characterized by an invasive front of cells that spread along white matter tracts and disseminate from the tumor, often several cm outside the lines of the visible tumor (92). These invasive cells take on a different morphology, as the dynamic process of invasion causes mechanical and structural changes in the cell (93). The invasion of malignant cells into the parenchyma of the brain makes surgery ineffective as a treatment method, as entire debulking of the tumor is impossible while still sparing brain function. Recurrence of GBM tumors is common with approximately 90% of GBM tumors returning after treatment (94). Recurrent tumors are found not only at the site of the initial tumor but also in distant parts of the brain, even the opposite hemisphere from the initial tumor location (95). These distant recurrences highlight the invasive potential of this tumor and the impossibility of full resection with surgery. There is no method to target these infiltrative cells preferentially without damaging critical surrounding structures such as astrocytes, neurons and blood vessels (96). In order to improve the efficacy of

GBM treatments it is necessary to develop selective treatments that can ablate the cells that escape current therapies.

2.2.1 Emerging strategies for GBM treatment

Targeting Growth Factor Receptors

The overexpression of the EGFR receptor is detected in nearly 50% of GBM cases, including over two-thirds of cases of primary GBMs (97). Therefore many efforts have been made for molecular therapies that target the EGFR receptor (98). Such treatment options include gefitnib (99, 100) and erlotinib (101, 102) which have both been evaluated in clinical trials and been shown to have modest efficacy. Additionally, a mutant EGFR receptor, *EGFRvIII*, which arises from genomic deletion of exons 2 to 7, is co-expressed in nearly 50% of GBMs with EGFR amplification (103). The presence of *EGFRvIII* is a reliable indicator of poor survival (104) and represents the most promising receptor target in GBM in terms of emerging therapies, due to the tumor-specific antigen's common expression by glioblastoma cells but not on normal tissue (105). Multiple different monoclonal anti-*EGFRvIII* antibodies have been generated for GBM therapy, with *in vivo* xenograft studies showing considerable efficacy (98, 106). An anti-*EGFRvIII* antibody fused to pseudomonas exotoxin A has shown to be an effective immunotoxin that may hold potential for GBM therapy (107). PDGFR is also an attractive target for GBM therapy. PDGFR signaling is associated with GBM proliferation and survival (108). Gleevec is an ATP competitive inhibitor of Abl that also has a high level of activity against PDGFR (108) (98) and has shown evidence of inhibiting the growth of GBM xenografts *in vivo* (109). Though these targeted methods have seen some success, the fact that these receptor targets have variable expression within a single tumor (85) causes these interventions to often have limited or variable efficacy (86, 87).

Antiangiogenic therapies

Therapies have also been developed to target the blood supply to the tumor in the form of antiangiogenic therapies. Glioblastoma promotes secretion of vascular endothelial growth factor (VEGF), which increases vascularization to provide nutrients to the tumor. Multiple steps in the angiogenesis process have been targets of drugs that have undergone clinical trials. Such drugs include monoclonal antibodies directed against VEGF or its receptors (110, 111), small molecule inhibitors of VEGRF-2 tyrosine kinas activity (112), and soluble decoy receptors created from VEGFR1 receptor that selectively inhibits VEGF (113). Antiangiogenic action through targeting integrin receptors on endothelial cells (114) has also seen early clinical trials. Though use of antiangiogenic drugs alone has shown little efficacy, some success has been seen with such drugs in combination with radiation and/or chemotherapy. Treatment for newly diagnosed glioblastoma with bevacizumab, a monoclonal antibody targeting VEGF, in combination with radiation and temozolomide was shown to prolong progression-free survival time and improve the performance status of patients. However, this combination therapy failed to extend overall survival time (9).

Immunotherapy

Immunotherapy has emerged as a promising therapeutic approach for GBM. Immunotherapy works by inducing or enhancing an immune response for the host's immune system to attack cancer cells. Cancer cells have a variety of mechanisms that allow them to evade the immune system. Passive immunotherapy involves the direct injection of monoclonal antibodies known to interact with an antigen specific to or associated with a tumor, or direct injection of stimulated immune effector cells, injection of cytokines to stimulate the immune system (115). In

glioblastoma, one humanized monoclonal antibody has been approved for treatment. Bevacizumab binds to and neutralizes the VEGF ligand to inhibit angiogenesis. This antibody has been used to treat recurrent GBM (9, 111, 116) and has shown contradictory results. Bevacizumab has been showed to decrease tumor size, but may promote a more invasive surviving tumor (117).

Attempts at active immunotherapy have also been developed for treatment of GBM in the form of vaccines to induce immune activation. As mentioned previously, one of the most common targets of selective therapy for GBM is *EGFRvIII*. PEP-3, a 14 amino acid peptide from *EGFRvIII* coupled with a foreign helper molecule has been used as a vaccine to generate *EGFRvIII* specific antibodies for GBM immunotherapy (105, 118, 119). Studies of the *EGFRvIII* peptide used in 18 glioma patients expressing *EGFRvIII* on their tumors showed an improved 6 month progression free survival and improved overall survival relative to controls (120). Additionally vaccines based on heat-shock proteins and dendritic cells have shown promise in clinical trials (121). The development of PVSRIPO, a synthetic form of the live polio vaccine, has been designated a breakthrough therapy by the FDA for its promising results in the treatment of GBM (122). PVSRIPO has a natural affinity for CD155 antigens, which are specific surface markers abundant on GBM cells, allowing it to achieve a level of selectivity. Additionally, the virus is attenuated which blocks the viral cytotoxicity in normal host cells. PVSRIPO is therefore capable of lysing cancerous cells without infecting and replicating in non-malignant host cells (123). Though immunotherapy holds promise as a treatment direction for GBM tumors these therapies are often highly aggressive and dangerous for older or immune-compromised patients. Tumor heterogeneity also presents problems for therapies aimed at tumor-specific antigens. For instance, as reported in a study using single-cell DNA analysis, only a subset of cells in the tumor may express *EGFRvII*

due to the intratumoral heterogeneity, and expression may be highly variable, resulting in survival and recurrence of the non-*EGFRvIII*-expressing cells when treated with EGFR vaccine therapy (124, 125). Additionally, *EGFRvIII* is only present in 20–30% of newly diagnosed GBM(104), highlighting the need to identify tumor-specific antigens and tumor-associated antigens with high levels of expression within a tumor and across multiple different tumors.

2.3 Cancer models for study and therapeutic testing

Tumor cells within the human body do not exist in isolation and bathed in nutrients, the way they are typically studied in lab settings *in vitro*. Rather, *in vivo* tumor cells exist within a complex milieu of both functional and abnormal tissue components, with heterogeneity operating at multiple length scales spanning molecular to tissue to entire organism. This integrated tumorous tissue is referred to as the tumor microenvironment (TME), and while the molecular (largely genetic) underpinnings of cancer have been the major scientific focus for the majority of the "war on cancer," the role of the TME in tumor initiation, progression, and therapy response is likely to be at least an equal contributor, and has received significantly less attention. While cancer is no longer thought of as a collection of aberrant genetic mutations but rather as a heterogeneous disease driven by and driving microenvironmental alterations, many of the models used to study cancer do not reflect this shift in disease understanding. The microenvironment evolves and changes as the tumor progresses acting in a two-way relationship with tumor cells, emphasizing the need to incorporate TME evolution as an active player in the dynamic process of cancer initiation and progression. The TME is composed of the extracellular matrix (ECM), the soluble factors (e.g., proteins) therein, and the adjacent cells (namely stromal cells and immune cells) (126). It has been established that each of these components, both separately and

in combination, contributes to both tumor initiation and progression, and may provide potential targets for or impediments to future cancer therapies.

Murine (generally mouse) tumor models are usually considered the gold standard preclinical models for the development of new cancer therapies. Yet due to the failure of the vast majority of therapies that show efficacy in mouse models, clearly these models are not ideal. The complexities of the *in vivo* environment often confound understanding of results and the large number of variables present in these models complicate the ability to isolate the impact of specific stimuli, such as cellular, chemical, and mechanical cues, during therapeutic testing (127). Due to the fact that the TME in small animal models is generally very different from that present in human disease , and the considerable differences between cancer progression in humans and animals (128, 129), these models often do not lead to a representative response to therapeutics (128, 130). Yet two-dimensional (2D) *in vitro* cultures, most often utilized in preclinical testing of therapeutics, rarely recapitulate the extracellular matrix components, cell-to-cell interactions and cell-to-matrix interactions that are crucial for differentiation, proliferation and cellular functions *in vivo* (131, 132). Three-dimensional (3D) cultures have, therefore, been created as a way to reconcile the pitfalls of animal and 2D culture models. 3D culture systems provide a more physiological response to therapeutics in the preclinical setting as well as insight into basic science mechanisms of tumor initiation and progression that would be hidden in the inherent complexity of *in vivo* models (130). 3D culture is defined, in the context of this dissertation, as a system in which cells are suspended in a tissue mimic and therefore retain the morphology and contacts similar to those seen *in vivo*. Generally, the tissue mimic is representative of the ECM in some characteristic that is the ECM stimulus of interest (i.e.,

protein concentration, mechanical properties). Several studies show that 3D organization of cells can reveal insight into the mechanism of tumorigenesis that 2D cultures cannot elucidate. When cells are grown in 3D gels, they have been showed to express a difference in importance signaling pathways compared to 2D cultures (133-135). 3D cultures allow for the modeling of cell-cell and cell-matrix interactions which are not present in monoculture models. Differences have been noted in the morphology of cells when grown as monolayers compared to 3D cultures, and these differences have been shown to affect cell behavior and response (128, 136-138). As 3D models improve, these models are beginning to restore the cellular morphologies and phenotypes seen during *in vivo* tumor development (139-143) . Additionally, 3D cancer models have been shown to more accurately predict the *in vivo* response to cytotoxic therapy (139, 144). Due to the ability of 3D models to produce consistent shape and morphology and model cell–cell and cell–matrix interactions in an environment which more accurately recapitulates therapeutic response *in vivo*, they are being increasingly adopted as a cost effective model for testing of cancer therapies.

In the studies informing this dissertation, a tissue-engineered 3D hydrogel platform is used for therapy testing. The hydrogels are composed of cells seeded within a system of type 1 collagen matrix. Type 1 collagen is commonly used as a matrix for 3D culture systems. It offers a number of advantages including ease of processing, low-cost, and flexibility for live cell manipulation. It is also an advantageous matrix for tissue engineering applications because the pore size, ligand density and stiffness can be varied by changing the concentration of collagen or by introducing chemical compounds to aid in cross-linking. Using these techniques, the structural properties of the gel can be manipulated (145). Additionally, cell-mediated degradation of collagen I through

the secretion of cleaving enzymes allows for remodeling of the matrix during proliferation, migration, and infiltration (146). These attributes of collagen allow for it to recapitulate aspects of pre-vascularized solid tumor growth, such as uninhibited 3D proliferative capacity, regions of hypoxia surrounding a necrotic core, and activation of genetic factors for self-sustaining angiogenesis, making it an attractive biomaterial for cancer models (138). For studies of the brain, collagen lacks physiological relevance as collagen is not largely prevalent in the brain microenvironment. However, it provides a consistent matrix to begin exploring the effects of a therapy on cells with a 3D morphology. In future studies stemming from the work reported here, more physiologically-relevant matrix materials will be explored such as hyaluronic acid, a major component of the brain microenvironment.

Chapter 3 Introduction to Electroporation Therapy

One approach that holds promise for overcoming some of the obstacles presented by current cancer therapy methods is physical disruption of the cell that does not depend on biological markers that tend to be highly heterogeneous in a tumor. One such method is electroporation, which uses high energy pulsed electric fields (PEFs) to form nanoscale pores in a cell lipid bilayer membrane (147). This electroporation phenomenon can be leveraged for cancer ablation.

3.1 Behavior of cell under external electric field

The internal compartment of a cell is separated from the external environment by a phospholipid bilayer that makes up the cell membrane. Embedded within the cell membrane are channel and gate proteins which allow for the exchange of molecules and ions across the membrane barrier. Cells use this exchange between external and internal compartments to maintain an electric potential gradient between the inner cell and the extracellular space. As a result of this gradient, a potential difference exists across the cell membrane. The phospholipid bilayer acts to maintain this potential difference at approximately -70 mV for mammalian cells (148). Simplifying the electric properties of the cell allows one to visualize the cell membrane as a dielectric capacitor separating a highly conductive inner fluid from a highly conductive outer fluid. The cell membrane acts as a dielectric at steady state as charges can be built up on either side of it but cannot cross as it maintains its electric potential across the membrane (Figure 3.1a). An external electric field applied across a cell will cause the ions in the highly conductive inner fluid to move in response to the polarity of the electric field with negative ions such as Cl^- building up on the inside of the membrane towards the positive direction of the field and positive ions such as Na^+ and K^+ building

up towards the negative direction of the field (149). On the outside of the cells, ions in the highly conductive external fluid also accumulate on the side of the cells corresponding to the electric field opposite of their charge. Because the cell membrane does not allow passage of these ions between the external and internal compartments, the charges accumulate at either side of the cell membrane to establish an electric potential across the membrane, termed a transmembrane potential (TMP) (Figure 3.1b). At a critical build-up of charge across the membrane, the induced TMP overcomes the required energy required to induce the rearrangement of the lipids in the membrane to such a point that they are able to form nanoscale hydrophilic pores (150, 151). This critical transmembrane potential for nanopore formation occurs at ~250 mV (151). Computational studies based on molecular dynamics have corroborated fundamental electroporation theory that states that as the voltage across the membrane increases, the rate of formation of aqueous passages in the membrane also increases (152-154). The formation of pores in the cell membrane increases the membrane permeability to ions and macromolecules, allowing for a redistribution of charge as a result (Figure 3.1c). The formation of pores removes the dielectric properties of the membrane and essentially establishes a short in the circuit of the cell at each pore. These pores allow the passage of many molecules to which the membrane is otherwise impermeable. This phenomenon known as electroporation, detected as a steep increase in electrical conductivity and permeability of the membrane, occurs within milliseconds of a cell being exposed to an electric field of sufficient amplitude (155, 156).

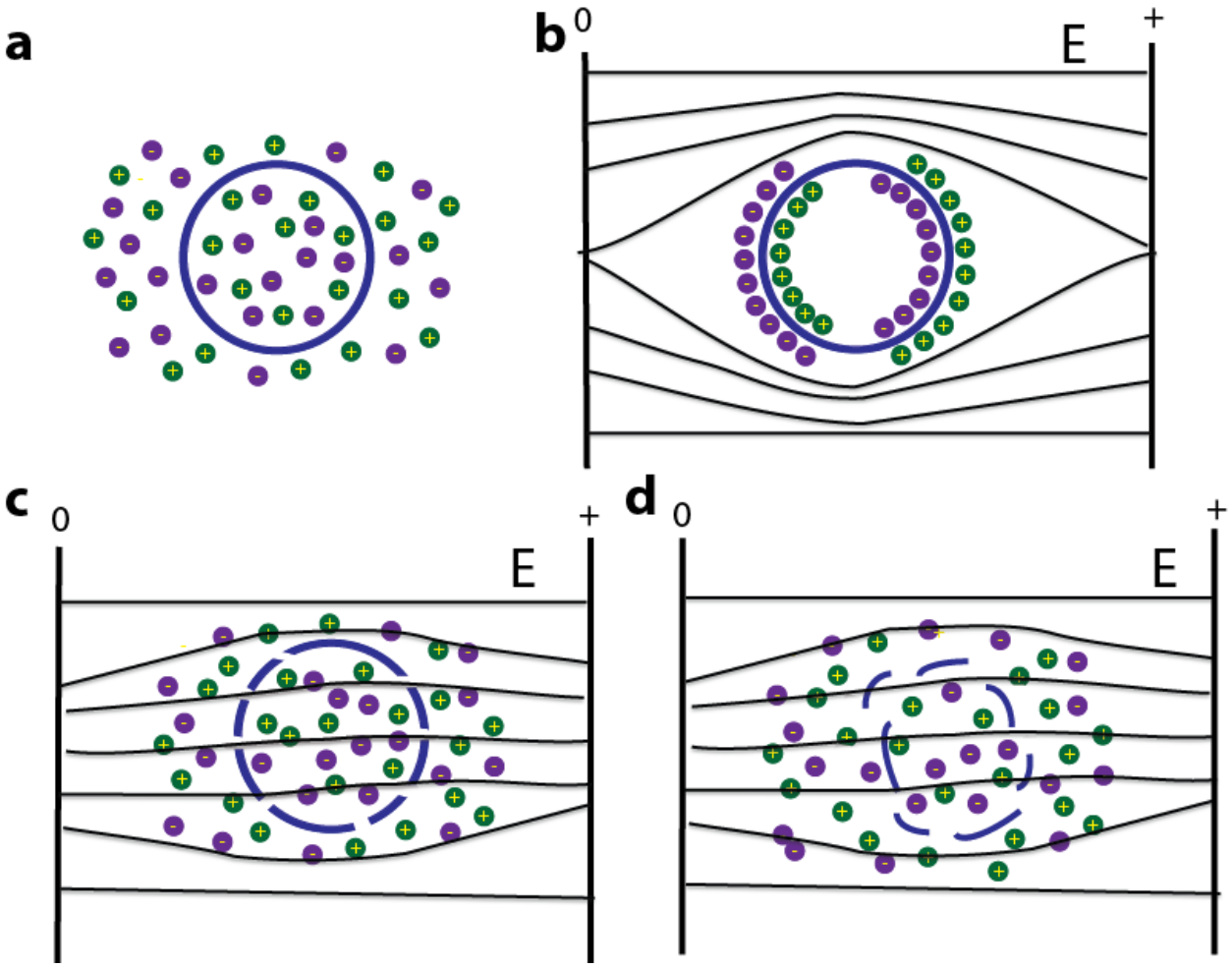

Figure 3.1 The behavior of a cell in an external electric field (a) *In the absence of an external electric field the cell membrane separates the internal and external environment to maintain an electric potential difference.* ***(b)*** *The cell polarizes in response to an applied constant or low frequency electric field, establishing an induced TMP across the membrane.* ***(c)*** *At sufficient amplitude, the electric field causes a TMP increase that leads to poration of the cell membrane.* ***(d)*** *At an induced TMP of approximately 1V, cell breakdown occurs due to irreparable damage to the cell membrane leading to cell death.*

This increase in membrane permeability has been utilized in medical applications in the form of reversible electroporation (RE). Reversible electroporation uses PEFs to form transient pores in the membrane to aid in the delivery of biological material normally restricted from entering the cell. Such materials that have been introduced to cells through RE include DNA for gene delivery and chemical therapeutics to aid in the efficacy of chemotherapy (157, 158).

Beyond a critical TMP threshold, typically 1V, the size and number of pores is so great that irreparable damage occurs (159) (Figure 3.1d). The pores are unable to reseal, which leads to cell death due to loss of homeostasis. This mechanism of cell death has been leveraged as a treatment modality known as irreversible electroporation (IRE). Comparison of SEM studies of pores induced on cell membranes in tissues treated with reversible electroporation and irreversible electroporation provide evidence for the increased size of pores associated with IRE relative to RE. Nanopores induced by both RE and IRE, observed by SEM, are round or oval-shaped, craterlike concaved, and dispersed throughout the cell surface (160). Comparing results of nanopores induced by reversible and irreversible electroporation suggests a significant size difference between RE-induced nanopores (average pore size 49.7 nm, range 10–120 nm) (161) and IRE- induced nanopores (average pore size 254.7 nm, range 40–490 nm) (160).

In 1967 Sale and Hamilton demonstrated the lethal effect of high electrical fields on different organisms (162-164) Since then, IRE has been leveraged in the food industry for sterilization and preprocessing of food (165, 166). IRE has also been used in decontaminating water from gram positive bacteria, gram negative bacteria, and amoebae (167-170). IRE most recently has been used as an ablation technique to treat a variety of cancers (171-176). In IRE cancer therapy, pulses are applied through electrodes inserted directly into a tumor, establishing an electric field across a well-defined tissue volume. This minimally invasive technique produces ablation of the tissue in a given tissue volume dependent on the electroporation parameters used.

3.2 IRE as a cancer treatment

Originally considered to be a downside of electroporation in transfection applications, IRE was first proposed as a theoretically feasible focal ablation method without the use of adjuvant drugs in 2005 by Davalos et al. (171). The first *in vivo* experiments demonstrated the feasibility of using IRE to produce a necrotic lesion with cell-scale resolution (177). Vascular effects of pulsed electric fields have been explored and IRE has been shown to be safe to use in close proximity to vasculature (178, 179). Immune response to IRE has also been studied for both healthy and tumorous tissue (180, 181). IRE has been shown to work on a mechanism not requiring an intact immune system, therefore making it a suitable treatment option for patients who are immunocompromised (180). Though IRE is not dependent on the immune system, there is evidence of an anti-tumor immune response so that IRE may be aided by the immune system in immunocompetent patients (180, 182, 183). Several pre-clinical trials on animal patients have since been completed (184, 185) as well as early stage human trials (173, 176). Safety studies have concluded that IRE can be used safely to treat a variety of tumors in different locations throughout the body (176). Recent data has shown the efficacy of IRE in stage III pancreatic cancer is drastically greater than all other treatment options for such patients. IRE has been shown to nearly double the median survival of these patients (186).

3.2.1 Clinical IRE

IRE has been used in clinical studies to treat a variety of cancers, including liver (187-191), prostate (192) , lung (193), brain (194), kidney (195-197) and pancreatic cancers (198-200). These studies have been conducted using the NanoKnife clinical device (Angiodynamics Inc, latham, NY). The clinical IRE procedure typically involves delivering a series of 50-100 µs pulses across

blunt tip electrode pairs which are typically 1 mm in diameter with spacing ranging from approximately 1.5-2.3 cm. These electrodes are inserted directly into or around the tumor and attached to a pulse generator which applies the desired voltage for treatment (Figure 3.2).

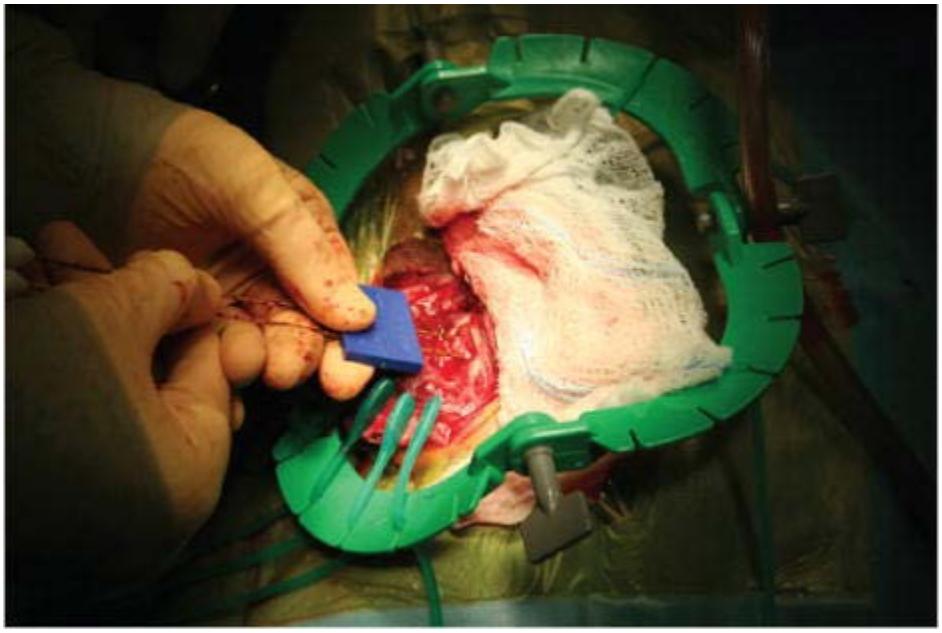

Figure 3.2. Clinical application of IRE therapy through electrodes inserted into a canine patient's brain. *Adapted from(201)*

The clinical pulse generator is programmed prior to treatment with the desired IRE pulse parameters including voltage, pulse waveform, and applied pulses. Electrode configuration and applied voltage are determined in pre-treatment planning with the goal of full tumor coverage and minimal ablation outside the target zone. For pre-treatment planning, MRI images are used to reconstruct the tumor along with surrounding important structures (Figure 3.3a). For the case of brain cancer this typically involves recontructing tumor volume, ventricles, major blood vessels, and surrounding brain tissue. The reconstructions are done in medical imaging programs such as OsiriX (Figure 3.3b). The 3D model (Figure 3.3c) is then imported into COMSOL for meshing

and finite element analysis (Figure 3.3d). By assigning physical characteristics to each material as well as setting applied voltage, a map of the electric field distribution across the tumor and surrounding brain can be predicted (Figure 3.3e). Ablation volume can be predicted based on predicted lethal thresholds for cells in the tumor. These lethal threshold predictions are informed by experiments testing cells cultured *in vitro* to determine pulse parameters that lead to cell ablation.

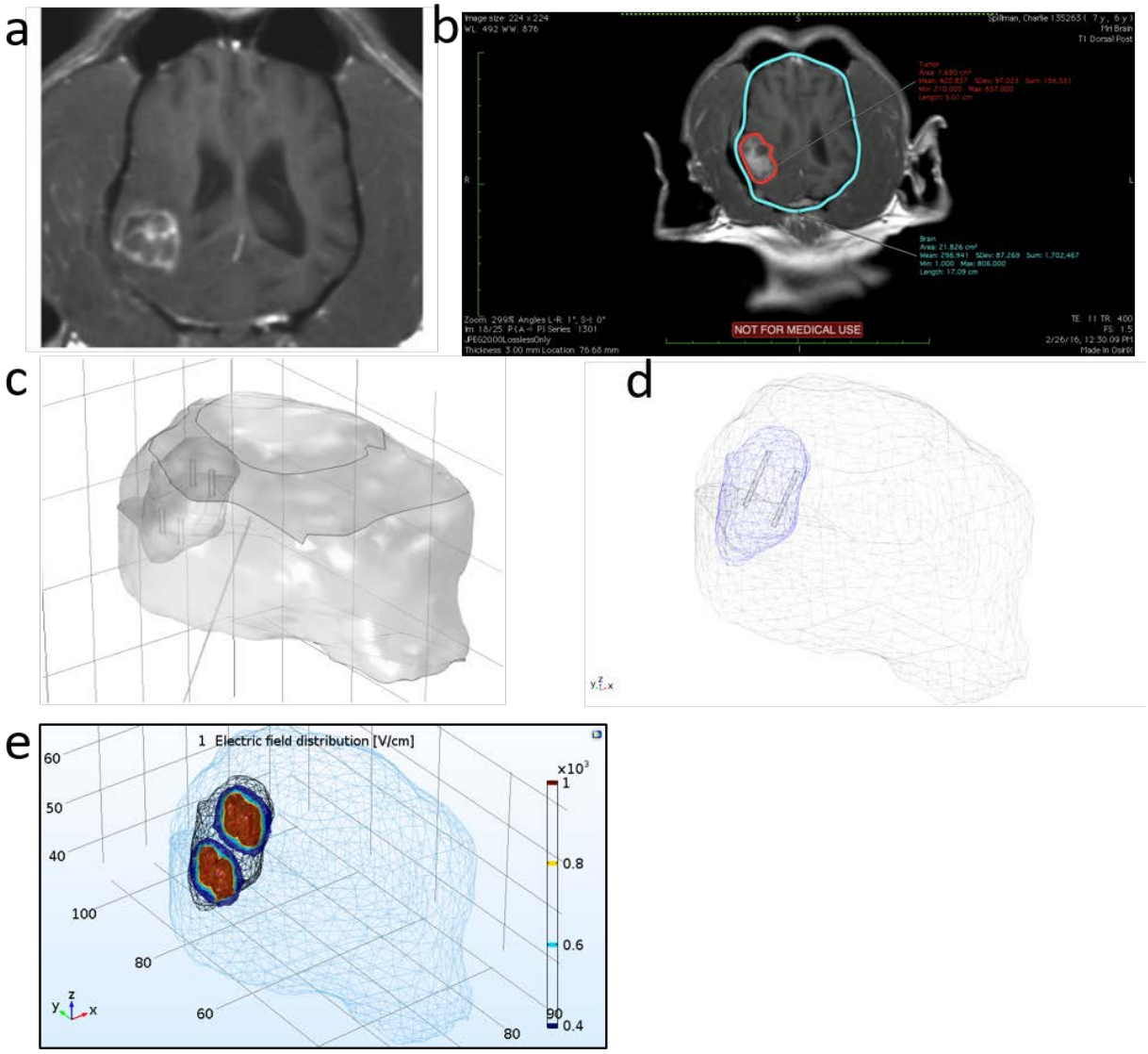

Figure 3.3. Pre-treatment planning for IRE application in the clinic. a) *An MRI image is taken and* ***b)*** *imported into OsiriX where it is reconstructed to form a* ***c)*** *3D model of the brain.* ***d)*** *The reconstruction is imported into COMSOL where it is meshed and* ***e)*** *the electric field distribution is determined through finite element analysis.*

For abnormally shaped tumors or tumors surrounding critical structures, often multiple different electrode insertions are needed to accomplish full ablation while confining damage to the target zone (Figure 3.4). Multiple insertion points for the electrodes can be used to avoid damage to critical structures, allowing IRE treatment the flexibility to treat tumors in locations that make

surgical resection difficult or impossible. The insertion points are determined in pre-treatment planning from a reference point in the brain so electrodes can be moved precisely and accurately during the course of the treatment.

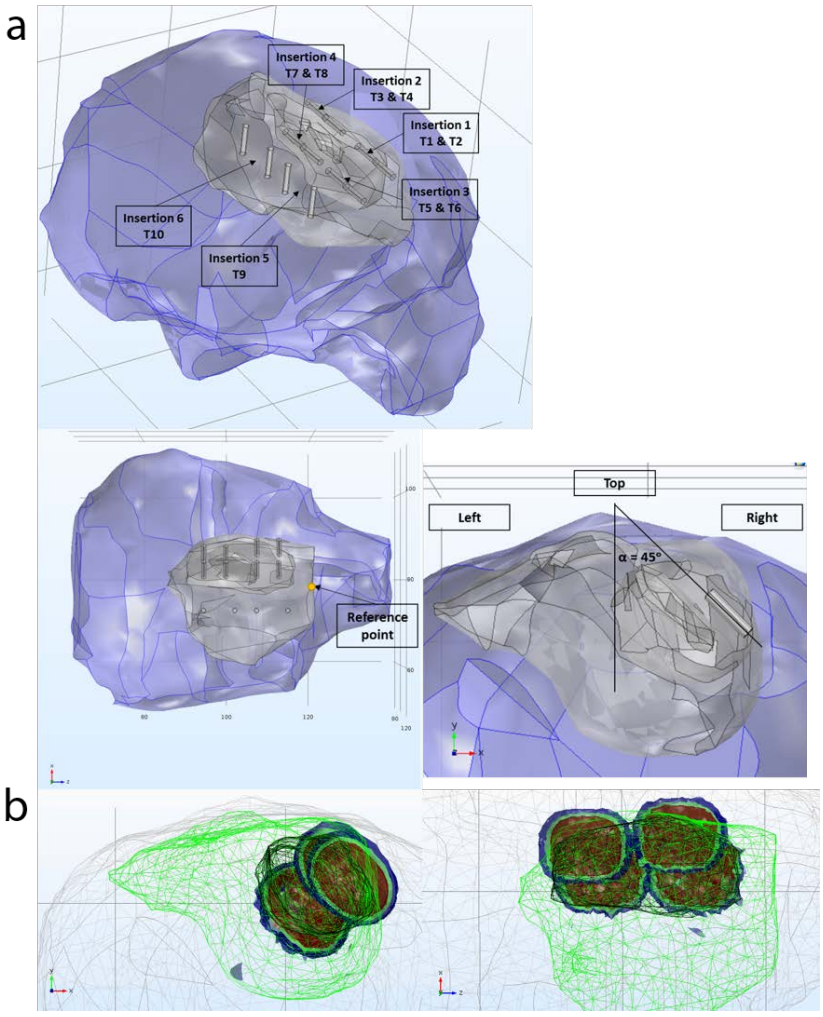

Figure 3.4. Treatment planning for a multiple insertion brain tumor ablation with IRE in a canine patient. a) *The tumor to be treated was surrounding multiple critical structures so six electrode insertion points, measured from a reference point, were used to deliver the ten ablations to the tumor without damaging the critical structures around which the tumor wrapped.* ***b)*** *Frontal (left) and top (right) views of predicted electric field distributions from ablations 1,3,5, and 7.*

3.2.2 Other energy based therapies

As imaging techniques have improved, physical ablation therapies have gained attention in cancer treatment due to their ability to concentrate treatment to a predefined region. Many thermal ablation techniques are in use as cancer therapies, such as radiofrequency ablation (RFA) (202), microwave ablation (203), cryoablation (204), laser interstitial thermal therapy (LITT) (205), and high intensity focused ultrasound(HIFU) (206). For most thermal therapies, the goal is to raise the temperature of the tissue to 50-100^{o}C, depending on the therapy (207).

Radiofrequency ablation

In RFA, an uninsulated electrode is inserted into the tumor and grounding pads are placed on the patient's thighs. An alternating current (AC) signal with a frequency of 460 kHz is delivered through the electrode. The alternating polarity of the AC signal causes ions in the tissue to switch direction very rapidly, leading to frictional or Joule heating (208, 209). The tissue is considered successfully ablated when its temperature exceeds 50 °C after one minute (210). Although minimally invasive and successful in ablating some tumors, lesion size is limited (< 3 cm) due to charring that prevents further movement of ions. Since the primary mechanism of ablation is heating, RFA therapy destroys healthy tissue along with the tumor. As a result, a severe immune response is possible and patients can experience flu-like symptoms for up to 3 weeks after treatment (211).

Microwave ablation

Similarly, microwave ablation (MWA) heats tissues using a single antenna through which an electromagnetic field is applied with a frequency at 900–2500 MHz. This alternating field causes polar molecules in the tissue, specifically water, to constantly realign and rotate with the field, producing thermal energy. MWA lesion size is not limited, as with RFA therapy, since microwaves can penetrate tissue that has been charred. This treatment also does not depend on the ionic conductivity or impedance of tissue therefore giving clinicians the ability to use MWA on difficult to treat organs such as the lungs (212). Although much larger lesions can be achieved using MWA (> 5 cm) (213), there is still no distinction made between healthy and tumorous tissue, therefore inducing a strong immune reaction. While RFA and MWA have experienced success in ablating tumors, these technologies are primarily focused on treating liver cancer and have not been attempted in brain since it is a relatively small and delicate organ.

Laser interstitial thermal therapy

Laser-interstitial thermal therapy (LITT) has been used to treat glioblastoma due to its ability to ablate precise volumes of tissue (214, 215). This technique delivers a laser pulse to the tissue, which absorbs the light energy and becomes heated. The main advantage of this technique, apart from precise ablation volumes, is that it is MRI compatible which gives clinicians the ability to monitor the treatment in real time. LITT can also be delivered laparoscopically and is much less invasive than RFA or MWA. A drawback to this therapy is that it may take upwards of several hours to treat a substantial volume of tissue and destroys healthy tissue in the process.

Thermal based therapies like RFA, MWA, and LITT have many pitfalls, especially in the complex environment of the brain. Because these techniques rely on thermal energy for cell death, they have had limited success in the brain primarily due to the heat sink effect associated with the vascular brain parenchyma (207). Cell ablation by thermal methods causes an increasing border of cell death with time as heat or cold dissipates from the source throughout the volume of the intended ablation zone. This gradual dissipation causes complications for predicting the treatment volume with a given set of parameters (216, 217). The elevated tissue temperatures associated with many thermal therapies cause coagulative necrosis of the affected tissue. The risk of harm to critical structures limits the locations these methods can be used. Tumors near or embedded in sensitive or critical structures are untreatable with thermal therapies. Thermal therapies are especially deleterious in GBM as tumor cells are known to surround blood vessels and neurons.

Tumor treating fields

Alternatively, there are energy based therapies that do not rely on heating of tissue and instead utilize low-level electric fields. FDA-approved tumor treating fields (TTFields, Novocure) apply an alternating current with low intensity (1-2 V/cm) and medium frequencies (100-300 kHz) through an insulating electrode cap that patients wear (218). Though the mechanism of action for TTFieldss is not completely understood, it is hypothesized that cell death occurs via two mechanisms of action—an antimicrotubule effect and a dielectrophoretic effect (219). At the cellular level, a non-uniform electric field is generated during treatment when a parent cell begins splitting into two daughter cells. The electric field is concentrated at the point between the two daughter cells as they continue to split apart. This area of high electric field induces a dielectrophoretic force on intracellular organelles causing premature separation. Tubulin subunits

are also polarized by the electric field causing them to align with the field, rather than aligning to form the mitotic spindle. This leads to unsuccessful replication and cell death (219). Preclinical data support these proposed mechanisms of action, as cells treated with TTFields have been shown to exhibit abnormal microtubule spindle assembly, evidence of mitotic arrest and subsequent apoptosis (220). While TTFields treatment has shown promise in prohibiting cell proliferation and cell division, it must be applied for 18 hours every day for a maximum of 18 months. It also may not be capable of targeting non-proliferating quiescent tumor cells that may remain after initial treatment and cause recurrence.

3.2.3 Advantages of IRE

Rather than rely on thermal energy, IRE uses electrical energy for cell death and therefore it does not require significant consideration for dissipation of thermal energy and causes less damage to normal soft tissue. As a cancer treatment IRE offers major advantages to thermal therapies, stemming in part from its ability to be tuned and optimized by design protocols. Treatment parameters can be designed in a way that Joule heating is minimized, thereby sparing sensitive structures such as blood vessels, nerves and the extracellular matrix (ECM) (183). By using treatment planning to minimize heating, IRE can achieve significant ablation volumes without detrimental heating of the surrounding tissue (177, 221, 222). The minimal heat generation (1-2 °C) as a result of treatment is especially beneficial for treatment in the brain. Protocols are designed to spare major blood vessels and avoid thrombogenesis so IRE can be used to ablate tumors surrounding structures critical for neurological or vascular function (171, 223, 224). IRE treatments produce ablations with a sub-millimeter transition between unaffected and necrotic tissue and the ablation area (201, 225). This allows ablations to be readily predicted through

mathematical modeling (226). In addition to mathematical predictions, it may be possible to monitor the treated area in real time with IRE to accurately treat the appropriate volume of tumor. Recent studies have shown that electroporation changes the electrical impedance spectrum of the tumor microenvironment (TME) (227), which could be used for monitoring the size of the ablated tissue (228). This would allow for precise ablation confined to the predetermined tumor area, by continued monitoring of the electro-physical properties of the TME during treatment.

Resistance methods are different with the physical disruption accomplished by IRE than drug resistance mechanisms. By targeting physical properties of the cells rather than the biology of neoplastic cells, the efficacy of these therapies is likely to depend on resistance processes that differ from those leading to the failure of radiation, chemotherapy, or molecular targeted therapies. These approaches will therefore complement more traditional treatments. Therapies can then be combined so that the resistant sub-populations are non-overlapping, helping to reduce tumor recurrence and increase survival times for patients.

3.2.4 Other uses of pulsed electric fields in tissue

Reversible electroporation involves applying pulsed electric fields to issues in which the magnitude of the applied filed does not exceed the threshold for formed pores to reseal. Electroporation is utilized as an important tool for basic research as well as for therapeutic intervention. In basic cell research, electroporation is used as a tool to introduce molecules such as dyes, tracers, antibodies, RNA, and DNA, and other such impermeable or mildly permeable molecules for cellular studies (229).

Therapeutically, reversible electroporation is used for delivery of chemicals into the cell such as in electrochemotherapy (ECT) to introduce chemotherapy drugs for the treatment of cancer. ECT utilizes pulsed electric fields to permeabilize cells to chemotherapeutic drugs that are otherwise unable to cross the cell membrane (158, 230). ECT pulses typically consist of a total of 8, 100 μs pulses delivered at 1 Hz. This ensures that the membrane reaches a transmembrane potential sufficient to permeabilize it, while avoiding the irreversible electroporation regime. This cancer therapy has the advantage over classic irreversible electroporation of being able to target quickly dividing cells. It allows for improved drug uptake compared to conventional chemotherapy. ECT has been shown to increase the mean survival time when used for treating brain tumors in a rat model when compared to untreated controls (231). Using both a four and eight electrode device, tumors in 9 out of the 13 rats treated with ECT were eliminated (69% regression rate) with minimal side effects (158). ECT has been used to treat both cutaneous and subcutaneous in humans (232-234).

Plasmid DNA can also be delivered to the inside of the cell by using electroporation. This non-viral delivery of plasmid DNA is termed electrogenetherapy. (235, 236). In order to achieve increased expression of a particular gene, electroporation is used to permeabilize cells to the plasmid DNA that codes the particular gene. EGT has been used in the growing field of immunotherapy for cancer as these genes, when introduced and expressed, can often activate a tumor antigen-specific response, affecting the immune response to cancer cells (237, 238).

Pulsed electric fields have also been investigated for increasing the permeability of the blood brain barrier for increased drug transport without compromising cell viability (239) . IRE therapies have been shown to enhance BBB transport *in vivo*. Garcia et al. found that the electric field threshold for BBB disruption is between 400 V/cm and 600 V/cm when delivering 90 pulses at a frequency of 1 Hz and pulse width of 50 μs (240). Hjouj et al. monitored electric field induced BBB disruption using MRI and found a similar threshold range between 330 V/cm and 500 V/cm using 50-70 μs pulses at a frequency of 4 Hz (241). Bonakdar et al. optimized pulse parameters to permeabilize the BBB safely using an *in vitro* microfluidic platform and observed an increase in cell uptake through the transcellular pathway (239). This application of PEFs may be useful for the delivery of chemotherapeutic agents for the treatment of brain cancer.

3.3 A second generation electroporation therapy

3.3.1 Pulse variables

The main variables that can be manipulated in designing IRE treatment regimens include pulse durations and pulse amplitudes. IRE treatments have ranged from durations on the order of nanoseconds to microseconds and amplitudes on the order of hundreds to thousands of volts per centimeter (242). As pulse duration is decreased, pulse amplitudes must be increased in order to achieve significant and lasting cellular effects.

It has been shown that by varying the pulse duration, IRE can achieve different cellular effects. Clinical IRE protocols use relatively long pulses, with pulse widths around 100 μs. These pulse widths have been shown to induce death through disruption of the cell membrane (242). In contrast, regimes using nanosecond pulsed electric fields (nsPEF) have been shown to cause

electroporation of the membranes of inner organelles (243, 244) as well as the outer cell membrane (245). An important difference in cellular effects with different pulse durations depends on the plasma membrane (PM) charging time. This PM charging time is the time it takes for ions to respond to the applied electric field to polarize the cell membrane and create the TMP increase necessary for electroporation of the PM. If the rise time of the pulsed electric field is slower than the membrane charging time, the cell will act as described above and the cellular membrane will be electroporated. If, however, the applied pulsed electric field has a rise time faster than the charging time of the plasma membrane, there is not enough time for the cell to shield its interior by charging the PM and the electric field will go through the PM into the cell interior (246). The charging time of an organelle is typically faster than the plasma membrane due to the smaller size of the organelle (247). If the amplitude of the field is high enough inside the cell, transmembrane voltages across intracellular membranes may reach threshold values, causing pore formation in those membranes rather than the plasma membrane of the cell (248).

As a result of this difference, the mechanism of cell death for nsPEFs may be distinct from IRE. *In vivo* results indicate that the death mechanism for nsPEFs involves predominantly apoptotic pathways (249-251) while longer IRE pulses may invoke death through necrosis (216, 252). Though some high amplitude nanosecond pulses have been categorized, short to mid-range pulses (0.1-10μs) remain largely unexplored for mammalian cells (Figure 3.5) (242). It is theorized that these pulses may provide access for electrically manipulating organelles while needing much lower amplitudes than nsPEFs to cause cell death. Because the plasma membrane charging time for mammalian cells are on the order of 1 μs, we investigated the use of pulse waveforms in the

range of this duration, termed high frequency irreversible electroporation (H-FIRE) to manipulate inner organelles.

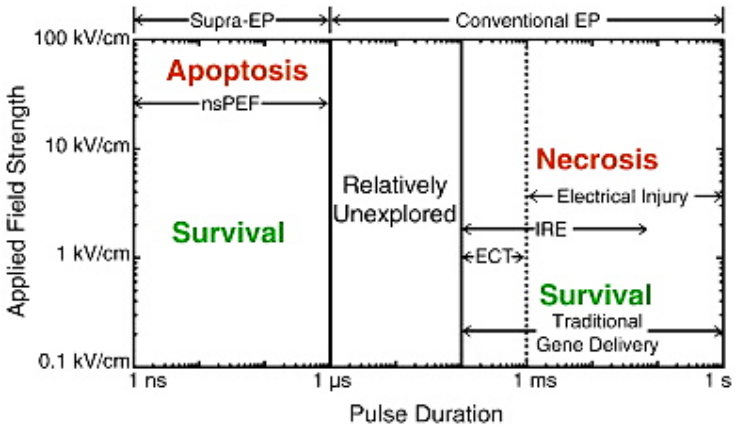

Figure 3.5 Map of effects and applications of electroporation in the pulse strength-duration space. *The unexplored region of the map is the targeted space of H-FIRE therapy. Adapted from (242).*

Some previous work has shown promise in using microsecond range pulses for manipulation of organelles. A series of 3 pulses with 5 µs pulse widths was shown to successfully induce uptake of DNA in mouse cells (253). Another study successfully achieved nucleofection, whereby DNA is delivered directly into the nucleus of eukaryotic cells by using pulsed electric fields. Nucleofection was successfully achieved by delivering pulses ranging from 10-200 µs followed by a long pulse of 100 ms maximum duration (254). Such studies suggest the possibility for inner organelle manipulation without using nanoscale pulse widths.

3.3.2 High frequency irreversible electroporation

High frequency irreversible electroporation was originally developed as a second generation form of IRE for cancer treatment. H-FIRE regimes use a pulse waveform that is bipolar with pulse

durations in the range of 500ns – 2 µs with a period of delay between each pulse to protect the electronics from the rapid pulsing (Figure 3.6b).

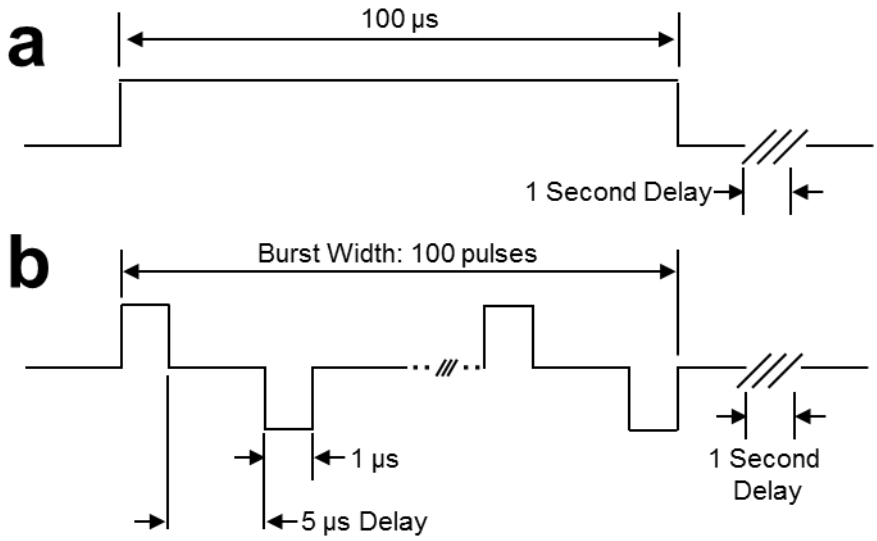

Figure 3.6 Schematic of typical IRE pulse and H-FIRE bursts ***(a)*** *The IRE therapy delivers a series of mono-polar pulses which are 100 µs in duration.* ***(b)*** *In H-FIRE, the mono-polar pulse is replaced by a rapid burst of bi-polar pulses 0.5-2 µs in duration. Displayed here is a 1 µs bipolar pulse with a 5 µs delay in between alternating pulses to protect the electronics from ringing.*

H-FIRE addresses two major short-comings of long unipolar pulse IRE protocols. Clinical applications of IRE, which use pulses of duration on the order of 100 µs (Figure 3.6a), cause muscle contractions during each pulse. As a result, these treatments require the administration of general anesthesia and paralytic agents to keep muscle contractions from interfering with therapy(173). Muscle contractions may cause carefully placed electrodes to move during treatment, therefore invalidating treatment planning efforts as well as endangering treatment outcome if electrodes hit sensitive structures. H-FIRE has the benefit of mitigating the muscle contractions seen with IRE due to its use of high frequency bipolar waveforms. As the frequency of bipolar waveforms is increased, the threshold for nerve stimulation is also increased (255),

thereby allowing H-FIRE to ablate tissue without causing problematic nerve stimulation (256). This is especially beneficial in debilitated patients where the use of anesthesia and neuroparalytic agents in combination becomes dangerous (173, 257).

Another benefit to H-FIRE bipolar pulse regimes is the possibility of more predictable electroporation lesions. The high frequency pulses eliminate some of the electroporation variability with cell size allowing for more consistent electroporation throughout a tissue volume (258). In addition to cell size dependence, IRE electric field distribution has variability based on heterogeneities in general tissue electrical properties as well. Areas of highly dense connective tissue or tissue-specific anisotropy introduce variability in IRE ablation (259). In contrast, the electric field distribution produced by the short bipolar pulses of H-FIRE does not depend as strongly on tissue homogeneity, suggesting H-FIRE can achieve more consistent ablation especially in anisotropic areas such as the white matter of the brain. This feature of H-FIRE becomes especially beneficial for treatment planning as more accurate predictions of ablation volumes can be achieved before therapy is delivered.

In addition to these benefits, we hypothesized H-FIRE may have capabilities for manipulating inner organelles in addition to electroporating the plasma membrane. As has been discussed above, changes in pulse duration have been shown to produce interesting differences in cell response to pulsed electric fields. Because H-FIRE uses square pulses of duration in the 500 ns-2 μs range, we hypothesized that this treatment regime may be able to target some larger organelles, specifically the cell nucleus. The charging time of a cell membrane for mammalian cells is typically approximately 1 μs (260). The time for the membrane to reach steady state in response to the

electric field is approximately 3 µs (261). On these time scales, the pulse duration of H-FIRE at 500 ns-2 µs with substantially faster rise times may allow for internal cell compartments to be exposed to electric fields while the plasma membrane is charging (Figure 3.7).

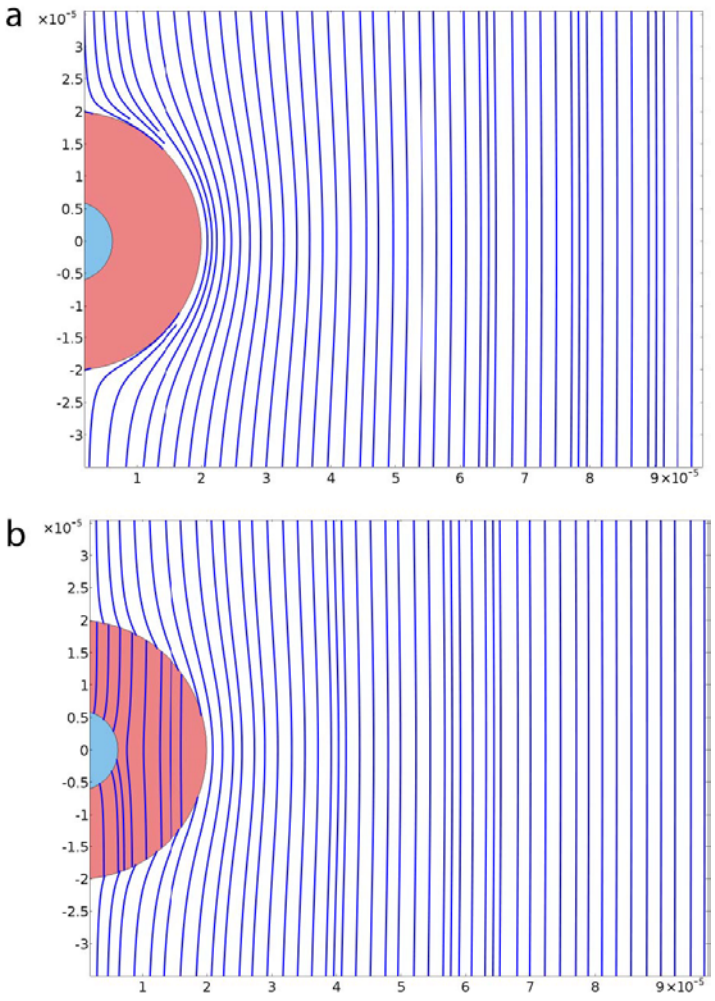

Figure 3.7 a) *The representative current density streamlines of a lower frequency (<100 kHz) electric field applied to a cell is distorted around the cell and confined to extracellular spaces. Current density lines modeled for a 10 kHz external electric field.* ***b)*** *The representative current density streamlines of a high frequency (>100 kHz) electric field applied to a cell is distorted around the cell much less than at lower frequencies, and some current bypasses the membrane to reach intracellular spaces of the cell. Current density lines modeled for a 1 MHz external electric field.*

3.3.3 Electromagnetism theory

The electroporation phenomenon in cells can be understood further by studying electromagnetism theory. Maxwell's equations describes the interaction of electromagnetic waves with solid objects, such as cells, by four equations. In the differential form, these are written as

$$\nabla \times H = J + \frac{\partial D}{\partial t} \quad (3.1) \qquad \text{Maxwell-Amperes law}$$

$$\nabla \times E = -\frac{\partial B}{\partial t} \quad (3.2) \qquad \text{Faradays law of induction}$$

$$\nabla \cdot D = \rho_e \quad (3.3) \qquad \text{Gauss's law}$$

$$\nabla \cdot B = 0 \quad (3.4) \qquad \text{Gauss's law for magnetism}$$

where H is the magnetic field (A/m), J is the current density (A/m^2), D is the electric displacement (C/m^2), E is the electric field (V/m), B is the magnetic flux density (T), and ρ_e is the electric charge density (C/m^3).

In order to model electroporation and arrive at a manageable analytical solution to Maxwell's equations a few simplifying assumptions are applied to the system. The electro-quasistatic approximation, which neglects magnetic induction, is valid if the electrical energy density exceeds the magnetic energy density. Assuming the magnetic flux density is negligible, Equation 3.2 is reduced to Maxwell's law of electrostatics

$$\nabla \times E = 0 \quad (3.5)$$

which, isolating the electric field expression, can be written in terms of the electric potential (Φ)

$$E = -\nabla \Phi \quad (3.6)$$

The constitutive relations for dielectric materials allow us to write D and J in terms of the electric field:

$$D = \varepsilon E \text{ (3.7)}$$

$$J = \sigma E \text{ (3.8)}$$

where ε is the dielectric permittivity and σ is the conductivity.

Therefore equation 3.1 can be written as

$$\nabla \times H = \sigma E + \frac{\partial \epsilon E}{\partial t} \text{ (3.9)}$$

Combining this with equation 3.6 gives

$$\nabla \times H = -\sigma \nabla \Phi - \epsilon \frac{\partial \nabla \Phi}{\partial t} \text{ (3.10)}$$

The magnetic field is not of interest in analyzing the motion of charges under the electro-quasistatic approximation so can be eliminated. By taking the divergence of both sides of Equation 3.10, a conditional equation for the spatial and temporal distribution of electric potential can be written as

$$0 = -\nabla \cdot (\sigma \nabla \Phi) - \epsilon \nabla \cdot (\frac{\partial \nabla \Phi}{\partial t}) \text{ (3.11)}$$

For steady state scenarios the time derivative vanishes, leaving

$$0 = -\nabla \cdot (\sigma \nabla \Phi) \text{ (3.12)}$$

Equation 3.12 is applicable for situations when the pulse duration is much larger than the membrane charging time. This is applicable for IRE applications using 100 µs pulse duration, compared to the ~1 µs charging time of the plasma membrane.

A cell can be simplified by considering it as three separate compartments. A dielectric spherical shell (plasma membrane) surrounds an electrolytic solution (cytoplasm). This sphere is surrounded itself by another electrolytic solution (extracellular space) (Figure 3.8a).

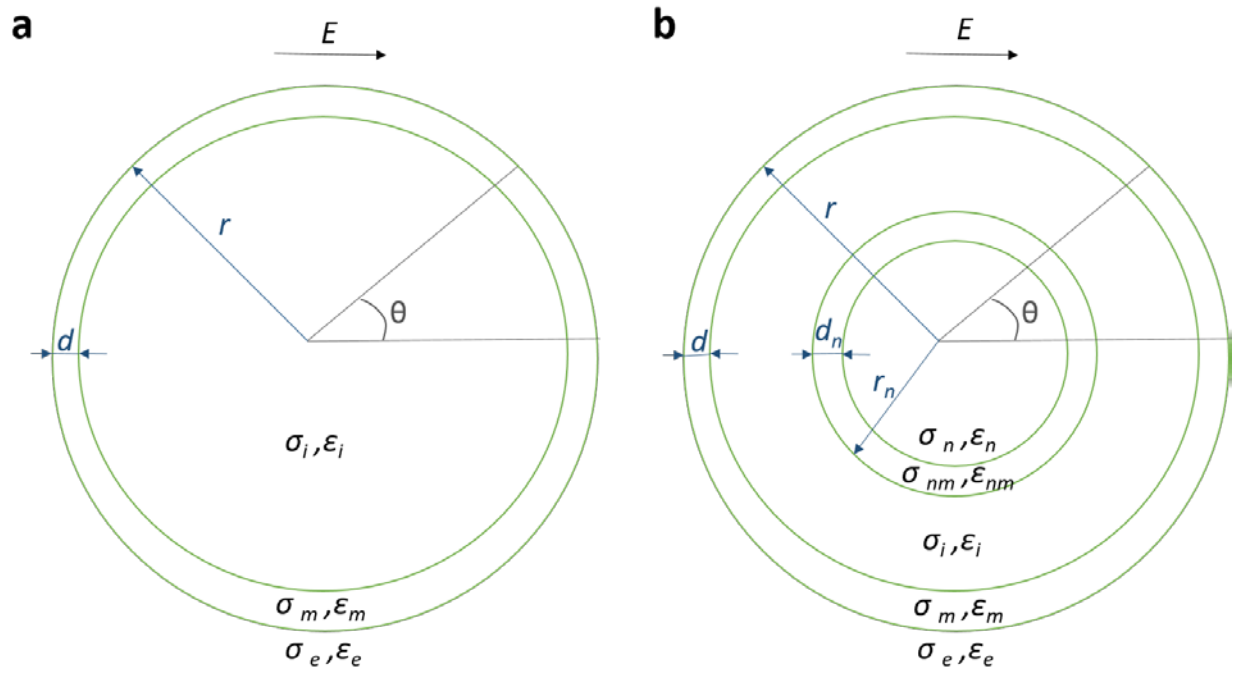

Figure 3.8 Model of spherical cell*. (a) Model of a spherical cell without any internal organelles. The model consists of three regions, the external environment (e), the membrane (m), and the cytosol (i). Each region characterized by an electric conductivity (σ, in S/m) and a dielectric permittivity (ε, in As/Vm). The cell radius is denoted by r and membrane thickness by d.* ***(b)*** *Model of a spherical cell with a spherical organelle such as a nucleus. The model consists of five regions, each characterized by an electric conductivity (σ, in S/m) and a dielectric permittivity (ε, in As/Vm). In addition to the external environment (e), the membrane (m), and the cytosol (i), the model includes a nuclear membrane (nm), and a nucleus (n). The nuclear membrane thickness is denoted by d_n and the nuclear radius by r_n.*

Considering this simplified cell, Equation 3.12 can be solved by separation of variables in spherical coordinates with the center of the cell aligned at the origin (262).

Ignoring inner organelles and permittivity terms, the steady state TMP of a cell in a uniform electric field E can be written as

$$\Delta\Phi = (\Phi_i - \Phi_o) = \lambda \cdot r \cdot E \cdot cos(\theta) \cdot (1 - e^{\frac{-t}{\tau}}) \quad (3.13)$$

where

$$\tau = r \cdot c_m(\frac{1}{\sigma_i} + \frac{1}{2\sigma_e}) \quad (3.14)$$

TMP ($\Delta\Phi$) is defined as the electric potential inside the cell membrane (Φ_i) minus the electric potential outside the cell membrane (Φ_o). λ is the shape factor of the cell and τ is the membrane relaxation time which is dependent on cell radius (r), membrane capacitance (c_m), the intracellular conductivity ($2\sigma_e$) and extracellular conductivity (σ_i).

When using an AC field of higher frequency, the Schwan equation applies(263):

$$\Delta\Phi = \lambda \cdot r \cdot E \cdot cos(\theta) \cdot (1 + (\omega\tau)^2)^{-0.5} \quad (3.15)$$

where ω is the angular frequency of the AC field.

For a spherical cell, the shape factor is approximately 1.5 and the equation can be reduced to

$$\Delta\Phi = \lambda \cdot r \cdot E \cdot cos(\theta) \cdot (1 + (\frac{f}{f_s})^2)^{-0.5} \quad (3.16)$$

where f_s is the frequency at which beta dispersion occurs. Beta dispersion describes the phenomenon where a biological cell is able to filter out low frequency currents and allow high frequency currents to pass through (264). For IRE pulses, the pulse duration is much greater than membrane charging time so the term $(\frac{f}{f_s})^2$ may be neglected. This leaves a steady-state equation for TMP.

$$\Delta\Phi = \lambda \cdot r \cdot E \cdot cos(\theta) \quad (3.17)$$

The maximum TMP will be reached when $\theta = 0\ or\ 180$, at the point where the cell membrane is directly perpendicular to the field.

$$\Delta\Phi_{max} = \lambda \cdot r \cdot E \quad (3.18)$$

This equation highlights the fact that for IRE, cell response to a constant electric field due to TMP change will be highly dependent on cell size, as TMP has a proportional relationship with cell

radius. The model of electric potential distribution of an insulating sphere in a conducting medium exposed to direct current (DC) fields is a classical model in electroporation theory (172, 265).

Because H-FIRE pulse frequencies approach the frequency at which beta dispersion occurs, the relationship between TMP and each variable becomes more complicated. As the frequency of the pulses increases, it becomes more likely that the electric field will at least partially bypass the plasma membrane and reach the inside of the cell, thereby decreasing the available field for plasma membrane charging.

An important consideration missing from these simplified dielectric models is the effect of the internal compartments of the cell. Organelles within the cell interior each have different conductivities and dielectric permittivities that cause the interior of the cell to be quite heterogeneous unlike the assumed homogeneous cytoplasm in the above derivation (Figure 3.8b). The electric field will therefore be distorted by the organelles. In order to accurately predict the transmembrane potentials both inside the cell and on the cell membrane, the influence of organelles on the electric field distribution must be considered. It is the subject of this work to experimentally investigate what affect internal organelles may have on practical outcomes of electroporation with a mind for how to leverage such effects for cancer therapy.

It is expected that for the electric field traversing the cell membrane and reaching the inside of the cell, the field will interact with the nuclear membrane in a way similar to its interaction with the plasma membrane. The potential across the nuclear membrane should be related to the equation

$$\Delta\Phi_n = 1.5 \cdot r_n \cdot E_i \cdot cos(\theta) \quad (3.19)$$

for the electric field (E_i) that reaches the inside of the cell.

It is therefore hypothesized that if a significant portion of the applied electric field traverses the cell membrane, the transmembrane potential change across the nuclear envelope should reflect nuclear size. This hypothesis, that H-FIRE can affect the inside of a cell in a way that nuclear size becomes an important variable in response, is to be investigated in proceeding chapters.

Chapter 4 IRE and H-FIRE Dependence on Cell Morphology[1]

4.1 Introduction

Cancer therapies have historically focused on targeting the bulk of a tumor with surgical resection, or the highly proliferative phenotypic characteristics of cancer cells with chemotherapy. These are generally combined with radiation therapy to induce physical damage to tumor cells. More recently molecularly targeted therapies have gained attention (266, 267) which target specific mutations such as Her2 overexpression in breast cancer. However each of these treatments has significant downsides for the quality of the patient's life and duration of survival. Chemotherapy and radiation result in relatively indiscriminant damage to normal cell types. In the case of brain cancer, this leads to radiation necrosis, pseudo-progression(77) and cognitive defects in 20-50% of patients undergoing whole brain radiotherapy(78). Surgery fails to remove disseminated invasive cells that lie beyond the surgical resection border, while targeted therapies place a selection pressure leading to the emergence of therapy-resistant cells, both of which may lead to tumor recurrence and ultimately patient death. Especially in the case of glioblastoma multiforme (GBM), a highly aggressive and invasive form of brain cancer, the tumor is characterized by multiple levels of heterogeneity (71, 83, 84), leading to predictable recurrence after initial treatment rounds.

[1] Chapter 4 is adapted from J.W. Ivey, E.L. Latouche, M.B. Sano, J.H. Rossmeisl, R.V. Davalos, S.S. Verbridge, Targeted cellular ablation based on the morphology of malignant cells, Scientific reports, 5 (2015).

The intratumoral heterogeneity of GBM is responsible, at least in part, for the failure of both conventional and targeted therapies to greatly extend the lifespan of patients diagnosed with GBM (10, 266-268). These tumors are made up of cells that vary greatly in their genetic, transcriptional, and phenotypic profiles, across varying microenvironmental niches (83, 90). This microenvironmental heterogeneity also manifests itself in physical differences in cells in the tumoral space. For example, GBM is characterized by an invasive front of cells that spread along white matter tracts, take on a different morphology, and perhaps also adopt a different mechanical phenotype to accomplish invasion (93). The extension of tumor cells into the surrounding brain parenchyma contributes significantly to the failure of surgery as a treatment method, however there is no method to target these infiltrative cells preferentially without damaging critical surrounding structures such as astrocytes, neurons and blood vessels(96). It remains an open challenge for GBM, as for all highly malignant tumors, to find a treatment that may preferentially target malignant cells, yet not succumb to resistance mechanisms that plague all existing therapies.

To address the need for a therapy to preferentially target malignant cells, we have developed a cellular ablation method using pulsed electric fields (PEFs). In PEF therapy, pulses are applied through electrodes inserted directly into a tumor, establishing an electric field across a well-defined tissue volume. Cells polarize in the presence of this external electric field resulting in an elevated transmembrane potential (TMP). If the TMP breaches a critical threshold, transient nanoscale pores form in the plasma membrane, which allow large molecules to traverse across the lipid bilayer (269). This phenomenon, known as reversible electroporation(270), is a well-established method used in aiding drug delivery, or for delivery of genetic material(157, 158). Beyond another critical TMP threshold, typically 1V, irreparable damage occurs, preventing the resealing of these

pores, which leads to cell death. This mechanism of cell death has been leveraged as a treatment modality known as irreversible electroporation (IRE), which has been applied to treat a variety of cancers(171, 172).

IRE offers the major advantages of sparing sensitive structures such as major blood vessels(172) and the extracellular matrix (ECM). IRE treatments produce ablations with a sub-millimeter transition between unaffected and necrotic tissue(201, 225) and the ablation area can be readily predicted through mathematical modeling(226). Treatments using long (~100µs) pulses have been shown to induce death through disruption of the cell membrane (242). However short to mid-range pulses (0.1-10µs) remain largely unexplored for mammalian cells, and it is theorized that these pulses may provide access for electrically manipulating organelles (242). For pulse lengths shorter than the plasma membrane charging time (~1µs) the majority of charge buildup is no longer confined to the plasma membrane(262). Instead, fast rise-times cause the potential drop to occur within the cell's interior. We have developed high-frequency irreversible electroporation (H-FIRE) (271, 272), which uses bipolar square waves of 1µs pulses delivered in a rapid burst, to explore the possibility of organelle targeting.

Despite the genetic heterogeneity within tumors that acts as a hindrance to most therapies, PEF treatments that target physical characteristics of malignant cells may provide a more effective means of targeting the most malignant sub-populations of such tumors. Cellular morphology, particularly cell size and nuclear-to-cytoplasm ratio (NCR) (273-275), as well as cellular electrical properties (276) are known to differ between normal and tumor cells. We hypothesize that phenotypic characteristics of malignant and normal cells present in the GBM microenvironment

vary sufficiently to provide targets for cell-specific ablation with properly tuned PEFs. Using 3D micro-engineered mimics of normal and malignant brain tissues, with experimentally defined ECM composition, we investigated cell-specific response to a range of pulse frequencies, to determine the extent to which either IRE or H-FIRE can target specific morphological cellular characteristics within a heterogeneous microenvironment.

4.2 Materials and methods

Cell culture

U-87 MG human glioblastoma cells (ATCC), D1TNC1 rat astrocyte cells (ATCC), and C6 rat glioblastoma cells (ATCC) were all cultured in Dulbecco's Modified Eagle Medium (DMEM) containing 10% fetal bovine serum (FBS) and 1% penicillin/streptomycin (PS). Normal Human Astrocyte (NHA) cells (Lonza) were cultured in Astrocyte Growth Media (Lonza). PC12 undifferentiated rat neurons (ATCC) were cultured in DMEM containing 5% horse serum, 5% calf serum and 1% PS. DBTRG human glioblastoma cells (ATCC) were cultured in RPMI medium containing 10% FBS, 2 mM L-glutamine, 1% PS and 0.1 mM non-essential amino acids. All cells were grown in culture at 37°C in 5% CO_2 in a humidified incubator. Cells were routinely passaged at 70-90% confluence. Prior to fabricating the 3D collagen scaffolds, cells were washed with PBS, removed from their flask using trypsin (Life Technologies) and centrifuged at 120*g* for six minutes. The supernatant was removed and the cell pellet was re-suspended in fresh medium and added to the collagen solution for a final concentration of $1x10^6$cells/mL. The hydrogels were submerged in appropriate growth media for the cell type at 37°C in 5% CO_2 in a humidified incubator and cell viability was maintained within hydrogels for up to 7 days (Figure 4.4a).

Collagen extraction

Collagen was extracted from the tendon of rat tail as described previously (277). Rat tails were dissected using scalpels under sterile conditions. The skin was removed and their tendons were extracted and dissolved in 0.1% acetic acid at 4°C for 48 hours. Dissolved collagen was centrifuged (Avanti J-25, Beckman Coulter, CA) at ×15,000*g* for 90 minutes in order to remove the insoluble contents such as residual fat and facia from the collagen solution. The solution was placed in a freezer overnight, and subsequently lyophilized for 48 h until complete dryness. Lyophilized collagen was kept in the freezer until ready for use.

Construction of 3D collagen scaffolds

Two different stock solution concentrations of collagen (4.5 mg/mL and 30 mg/mL) were created by dissolving concentrated lyophilized collagen in 0.1% acetic acid in the amounts necessary to achieve the desire stock concentration. Scaffolds with a final concentration of 2 mg/mL and 20 mg/mL were made from concentrated collagen stocks to create collagen gels of 0.2% (w/w) and 2% (w/w). Neutralized collagen solutions were created by mixing acid-dissolved collagen with 10X DMEM (10% of total collagen solution volume) and sufficient volumes of 1N NaOH until a pH in the range of 7.0-7.4 was achieved. pH was determined by a color change visible in the collagen solution calibrated by testing with a pH probe. The following steps were carried out under sterile conditions: (1) in a flat-bottomed microtube, the desired amount of collagen solution was added according to the desired final concentration, (2) in another microtube, the dilutant media consisting of Dulbecco's modification of eagles medium (DMEM) (Corning Cellgro, VA) 10× (0.1 final volume neutralized collagen), NaOH (volume of collagen × 0.02), DMEM 1× (as much as

necessary to adjust the final concentration) were pipetted, and (3) the dilutant media was pipetted in the collagen solution and gently mixed. All tubes and mixing hardware were kept on ice to prevent premature crosslinking of the collagen. The neutralized collagen was mixed with cells suspended in DMEM or NHA media to achieve a cell density of $1x10^6$ cells/mL in the final collagen mixture. Solutions were mixed carefully with a spatula to ensure homogenous distribution throughout the gel without damaging cells. Collagen solutions were then dispensed into a polydimethylsiloxane (PDMS) mold with a cut-out of 10 mm diameter and 1 mm depth and molded flat to ensure consistent scaffold geometry (Figure 4.1). Our previous mathematical modeling and experiments on oxygen (O_2) consumption rates by tumor cells (134) confirms that at this cell density and scaffold thickness, O_2 concentration is uniform throughout the scaffold depth. Collagen was allowed to polymerize at 37°C and 5% CO_2 for 30 minutes. A cell density of $1x10^6$ cells/mL was chosen as it gave us enough cells within the hydrogel to determine an accurate ablation area from a live/dead stain but was not a density high enough to establish a necrotic core in the hydrogel on the timescales of these experiments. It should be noted that experiments were conducted on a variety of cell densities, ranging from $5x10^5$ cells/mL to $5x10^6$ cells/mL and no difference was seen in electric field thresholds despite differences in cell densities. While the brain consists of relatively low amounts of fibrous proteins, collagen provides a convenient scaffold material that produces relevant 3D geometry, integrin engagement with surrounding extracellular matrix, and appropriate cell-cell interactions.

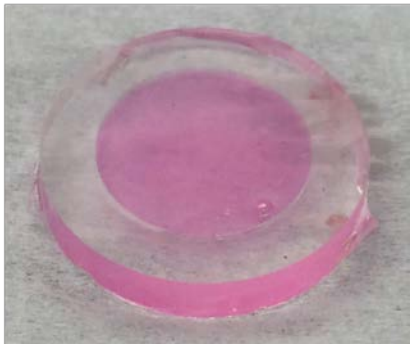

Figure 4.1 Cell-seeded collagen hydrogel maintained in PDMS well for controlled geometry.

Construction of 3D alginate scaffolds

Calcium alginate gels were created using the same PDMS molds as for collagen, creating discs 10 mm in diameter and 1 mm in thickness. Two alginate gel stock concentrations (0.4% and 4.0% (w/v) were prepared using powdered alginate (Protanal LF 10/60, FMC BioPolymer) that was dissolved in buffer, dialyzed, frozen and lyophilized, followed by re-constitution in serum-free DMEM, as we have previously reported(134). Alginate concentrations were chosen to span a wide range in mechanical stiffness, similar to the collagen concentrations used. Alginate solutions were mixed with cells at a density of $1x10^6$ cells/mL and dispensed into PDMS molds and molded flat with a porous membrane. Alginate hydrogels were cross-linked by submerging under 0.1M $CaCl_2$ dispensed over a porous membrane cover for 45 min. The alginate hydrogels were then cultured in 24 well plates with DMEM supplemented with 10% FBS and 1% PS at 37ºC, 5% CO_2.

Construction of co-culture scaffolds

Before seeding cells into collagen hydrogels, U87 cells were incubated for 30 minutes with calcein green, AM (Molecular Probes, Eugene, OR) and NHA cells were incubated for 30 minutes with calcein red-orange, AM (Molecular Probes, Eugene, OR) to distinguish cell populations from each other in co-culture. Importantly, calcein stains for flow cytometry were shown to be retained by cells for longer time periods of incubation in the hydrogel so these stains were used for co-culture experiments to maintain fluorescence on the timescales needed to allow for cell engagement with the matrix. After staining, cells were rinsed and seeded into collagen hydrogels at a totally density of $1x10^6$ cells/mL of collagen with each cell type making up half of the total cell density. Electroporation treatment was delivered 12 hours after seeding cells into collagen scaffolds. Upon electroporation treatment, calcein stains were no longer fluorescent in dead cells and lesion diameters were measured from the cells that were fluorescent 1 hour after treatment. Imaging for co-culture experiments were done 1 hour after electroporation treatment to ensure the fluorescent stains hadn't dissipated from the live cells.

Determination of shape factors

U-87 MG, DBTRG, C6, NHA, D1TNC1, and PC12 cells were individually seeded in hydrogels of one of the four conditions described previously (0.2%, 2% collagen, 0.4%, 4% alginate). After culturing the cells for 24 hours, the hydrogels were fixed using 4% formalin and blocked and permeabilized using 40 mg/mL bovine serum albumin (BSA) and 0.5% Triton-X. Cellular actin was stained with Alexa Flour 568 phalloidin (Life Technologies, Carlsbad, CA) while cell nuclei were stained with diaminophenylindole (DAPI; Sigma-Aldrich, St. Louis, MO). Cells were visualized using a Zeiss LSM510 (Carl Zeiss Microscopy LLC, Thornwood, NY) laser scanning confocal microscope. The stained cells were then used to determine cellular shape factors for cells

in each of the four conditions. Image analysis was done in Image J (NIH, Bethesda, MD) to determine the nuclear area, nuclear perimeter, cytoplasmic area, cytoplasmic perimeter, and longest and shortest diameter of the cell. Z-stack images were converted into 2D projection images and cell measurements were made from these projections. Measurements were made on at least four cells per hydrogel and at least 5 hydrogels were analyzed for each condition.

Live fluorescent imaging

U-87 MG cells were cultured under normal culture conditions and incubated for 16 hours with CellLight Nucleus-RFP, Bacman 2.0 (Molecular Probes, Eugene, OR) and CellLight Tubulin-GFP (Molecular Probes, Eugene, OR) added to the media at a concentration of 10 particles per cell. Cells were then passaged and seeded into hydrogels of a final concentration of 0.2% collagen at a density of $1x10^6$ cells/mL. After cells were cultured in collagen hydrogels for 24 hours, electroporation of hydrogels was performed on the stage of a Zeiss Observer Z1 microscope (Carl Zeiss Microscopy LLC, Thornwood, NY) to allow for imaging during treatment. Images were taken of single cells immediately before pulsing treatments were started and then every 30 seconds for 5 minutes after pulsing began. Cells were imaged upon exposure to IRE treatment or H-FIRE treatment. Cells that were not exposed to pulses were imaged as a control.

Electroporation of 3D scaffolds

Pulsed electroporation experiments were performed in hydrogels with constant electrical properties. The electrical conductivities of each of the gel-cell mixtures were measured with a conductivity meter to ensure similar electrical properties (0.98 ± 0.04 S/m). The IRE pulses were

generated using an ECM 830 pulse generator (Harvard apparatus, Holliston, MA) and delivered to the tissue through custom electrodes. High- frequency pulses were delivered using a custom-built pulse generation system (INSPIRE 2.0, VoltMed Inc., Blacksburg, VA). Two solid stainless steel cylinders with diameters of 0.87 mm, separated 3.3 mm edge-to-edge, were used as electrodes. A custom-made part housed the electrodes to ensure uniform spacing and placement in each collagen scaffold. Treatments were performed delivering a total of 50 square pulses (IRE) or 50 bursts of 1 µs pulses (H-FIRE). The IRE protocol delivered 100 µs pulses with a repetition rate of 1 pulse per second. In the H-FIRE protocol, a burst consisting of 100x 1µs pulses with a 5µs inter-pulse delay was delivered as shown in Figure 4.3a with a repetition rate of 1 burst per second. For IRE treatments, the pulse amplitude was set to 450 V_{peak} while for H-FIRE treatments 700 V_{peak} was used to produce ablations of approximately the same volume as the IRE group.

Determination of electric field distribution in hydrogels

Finite element models using COMSOL Multiphysics (Version 4.3, COMSOL Inc., Palo Alto, CA) were used to solve the Laplace equation to find the electric field distribution within the hydrogels for each different voltage used. COMSOL Multiphysics was also used to solve the Joule heating equation to calculate the temperature distribution in the hydrogel as a result of each treatment. The simulation geometry was modeled as a 10 mm diameter and 1 mm thick cylinder with two steel electrode cylinders (d = 0.87 mm) spanning the depth of the hydrogel. Thermal and electrical properties for each domain can be found in Table 4.1. The mesh was refined until error between successive refinements was less than 1%. The final mesh contained 47,438 elements and solutions were found in approximately 3 minutes on a Pentium i3 processor.

From Maxwell's equations, a relation for electric potential can derived that can be solved to calculate the electric field distribution across a given volume.

Combining equation 3.3 with equation 3.7, derived from Maxwell equations shown previously gives

$$\nabla \cdot E = \frac{\rho_e}{\varepsilon} \text{ (4.1)}$$

Combining equation 4.1 with equation 3.6 results in

$$\nabla \cdot \nabla \Phi = \nabla^2 \Phi = -\frac{\rho_e}{\varepsilon} \text{ (4.2)}$$

In a charge free region of space, $\rho_e = 0$ and equation 4.2 becomes

$$\nabla^2 \Phi = 0 \text{ (4.3)}$$

Equation 4.3 is known as Laplace's equation where Φ is the electric potential. This equation can be solved with appropriate initial and boundary conditions with finite element modeling to determine electric field distribution from pulsed electric fields (278). This solution depends only on the applied voltage, electrode geometry, and electrode placement. The boundaries of one electrode were set to the applied voltage ($\Phi = V_{applied}$) and the boundaries of the second were set to ground ($\Phi = 0$) while the initial voltage (V_0) for all subdomains were set to 0 V. All other external boundaries were set to electrical insulation ($-\boldsymbol{n} \cdot \boldsymbol{J} = 0$).

The experimental platform enables us to visualize a range of electric field magnitudes as opposed to a single value that is applied when testing cells in suspension using plate electrodes. In our numerical model of the collagen scaffolds, the electric field distribution throughout the hydrogel can be distinctly visualized. By bounding regions of different electric field magnitudes using a

contour plot, the model allows us to determine the field threshold that causes an equivalent area of cell death for each of our treatments. This highlights our ability to precisely predict ablation sizes.

Table 4.1 Physical properties used in finite element models of hydrogel treatments. * measured values, ‡ default material values in COMSOL

Parameter	Symbol	Value	Unit	Reference
IRE Voltage	V_{IRE}	450	[V]	*
H-FIRE Voltage	V_{HFIRE}	450-700	[V]	*
Electrode Density	ρ_e	7850	[kg/m^3]	‡
Electrode Specific Heat Capacity	Cp_e	475	[J/(kg·K)]	‡
Electrode Thermal Conductivity	k_e	44.5	[W/(m·K)]	‡
Electrode Conductivity	σ_e	4.03x10^6	[S/m]	‡
Electrode Permittivity	ε_e	1		‡
Hydrogel Density	ρ_h	997.8	[kg/m^3]	[18]
Hydrogel Specific Heat Capacity	Cp_h	4181.8	[J/(kg·K)]	[18]
Hydrogel Thermal Conductivity	k_h	0.6	[W/(m·K)]	[18]
Hydrogel Conductivity	σ_h	1.2	[S/m]	[18]
Hydrogel Permittivity	ε_h	0		[18]

Determination of Joule heating in hydrogels

Thermal effects on the scaffolds due to resistive losses were modeled by solving the Joule heating equation:

$$\nabla \cdot (k\nabla T) + \sigma|\nabla\phi|^2 \cdot \frac{d}{\tau} = \rho c_p \frac{\delta T}{\delta t} \quad (4.4)$$

where k is the thermal conductivity, T is the temperature, c_p is the specific heat capacity, and ρ is the density of the 3D scaffold. $\sigma|\nabla\phi|^2$ is the Joule heating term, which was simplified by using a scaling factor proportional to the ratio of pulse duration d and pulse interval τ. This duty cycle approach, in which the total energy delivered to the tissue is averaged throughout the duration of the treatment, has been shown to accurately reproduce experimental results in hydrogels (171) and tissue. Provided that the upper most boundary (perpendicular to electrodes) was exposed to the environment, it was assigned convective cooling properties ($-n \cdot (-k\nabla\mathrm{T}) = h(T_{ext} - T)$ with a coefficient value, h, of 50 W/m^2·K while the remaining external boundaries of the simulation domain were set to thermal insulation ($-n \cdot (-k\nabla\mathrm{T}) = 0$). The initial temperatures for all domains as well as the exterior temperature were set to 20°C.

Finite element analysis of individual cells

The transmembrane potentials across the cell membrane and nuclear envelope were modeled using a finite element model with an impedance boundary condition scheme(271). These finite element models were used to numerically investigate the response of representative cell geometries to simulated IRE and H-FIRE pulses (Figure 4.2). Cell geometry was determined based on average measurements made in ImageJ image analysis software (NIH, Bethesda, MD) from confocal microscopy images. Geometries for U-87 cells in two different collagen densities (0.2%, 2%) as well as four different cell types (U-87, NHA, C6, D1TNC1) in a 0.2% collagen matrix were used. All models were solved using a 2D-axisymmetric platform in COMSOL Multiphysics. A large media domain, with sides of 300 µm, was used to avoid any significant boundary effects. The cell and the nucleus were modeled as half-ovals where their lengths and widths were varied according

to measurements from confocal microscopy images (Table 4.2). Simulations were solved in the time-domain using an electric currents module. To account for the resistance and capacitance posed by the cell membrane and the nuclear envelope the boundaries of the nucleus and cytoplasm were assigned impedance properties based on the existing literature, as summarized in Table 4.2. For most single cell simulations the final mesh contained around 3,000 elements and solutions were found in no longer than 1 minute on a Pentium i3 processor. For each domain (media, cytoplasm, nucleoplasm), a separate Electric Currents physics module was used and the dependent electric potential variables ϕ_{media},ϕ_{cyto}, ϕ_{nuc} for the media, cytoplasm, and nucleoplasm domains were defined, respectively. These variables were then defined to calculate the voltage across the cell membrane (ϕ_m) and nuclear envelope (ϕ_n)

$$\phi_m = \phi_{media} - \phi_{cyto} \qquad (4.5)$$

$$\phi_n = \phi_{cyto} - \phi_{nuc} \qquad (4.6)$$

In each Electric Currents module, the boundaries representing membranes were defined as impedance boundary conditions with reference potentials prescribed as the electric potential in the adjacent (φ_{ref}) domain

$$\boldsymbol{n} \cdot (\boldsymbol{J}_1 - \boldsymbol{J}_2) = \frac{1}{d}\left(\sigma\left(\phi - \phi_{ref}\right) + \varepsilon_0 \varepsilon_m \frac{\partial}{\partial t}\left(\phi - \phi_{ref}\right)\right) \qquad (4.7)$$

where σ is the conductivity, ε_0 is the permittivity of free space, ε_m is the relative permittivity, and d is the thickness of the cell membrane or nuclear envelope. The boundary was defined as a 'thin layer' and the electrical conductivity, relative permittivity, and surface thickness were defined

using the values presented in Table 4.2. Domain boundaries perpendicular to the z-axis (z = ±150 µm) were defined as time domain voltages (ϕ = V(t)) simulating the 1 or 100 µs pulses with rise times of 16 ns or 10 µs, respectively. The remaining external boundary was given electrically insulating properties ($-\boldsymbol{n} \cdot \boldsymbol{J} = 0$). To simplify the model, these simulations do not take into account the rapid change in membrane conductivity which occurs when cells become electroporated by pulsed electric fields. Incorporating these changes in conductivity would require us to experimentally quantify the dielectric response of the cell membrane and nuclear envelope to the H-FIRE pulse parameters used, which goes beyond the scope this study.

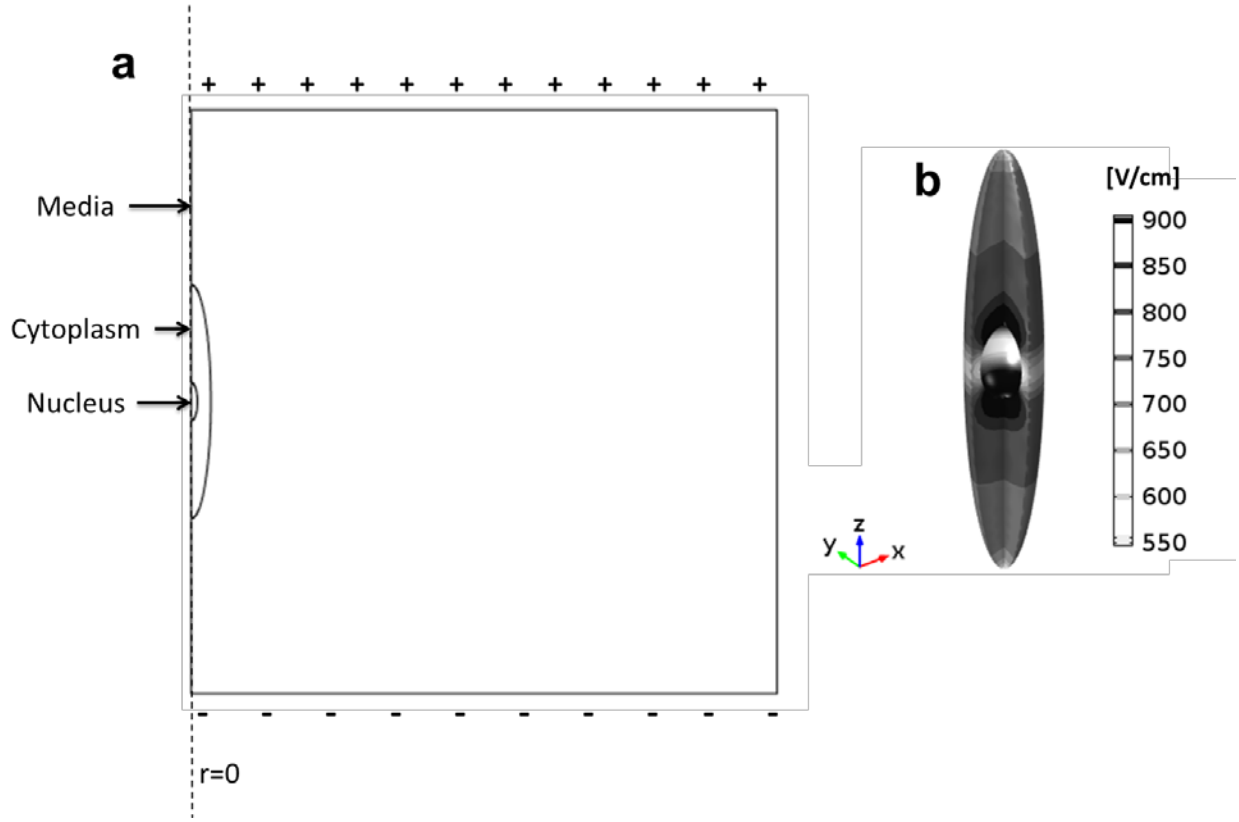

Figure 4.2. Individual cells modeled in a large 2D axisymmetric domain. *(**a**) For numerical modeling of a single cell an electric field is applied across a block of media and a cell centered within. Changes in TMP and nTMP are calculated from time-dependent solutions. (**b**) Electric field isocontours in cytoplasm for H-FIRE therapy (700V) of glioma cell model*

Table 4.2. Physical properties used in finite element models of single cells. * measured values, ‡ approximation based on water composition

Parameter	Symbol	Value	Units	Reference
Media Conductivity	σ_m	0.98	[S/m]	*
Media Permittivity	ε_m	$80\varepsilon_0$	[F/m]	‡
Cytoplasm Conductivity	σ_{cyt}	0.3	[S/m]	(279)
Cytoplasm Permittivity	ε_{cyt}	$154.4\varepsilon_0$	[F/m]	(280)
Nucleoplasm Conductivity	σ_{nuc}	1.35	[S/m]	(279)
Nucleoplasm Permittivity	ε_{nuc}	$52\varepsilon_0$	[F/m]	(279)
Cell Membrane Thickness	t_{mem}	$5x10^{-9}$	[m]	(281)
Nuclear Membrane Thickness	t_{Nmem}	$40x10^{-9}$	[m]	(279)
Cell Membrane Conductivity	σ_{mem}	$3x10^{-7}$	[S/m]	(282)
Cell Membrane Permittivity	ε_{mem}	$8.57\varepsilon_0$	[F/m]	(283)
Nuclear Membrane Conductivity	σ_{Nmem}	$6x10^{-3}$	[S/m]	(279)
Nuclear Membrane Permittivity	ε_{Nmem}	$28\varepsilon_0$	[F/m]	(279)
Domain Side Length	L_d	$300x10^{-6}$	[m]	-
Benign Cell Length	L_c	$60x10^{-6}$	[m]	*
Benign Cell Width	w_c	$20x10^{-6}$	[m]	*
Benign Nuclear Length	L_n	$19.7x10^{-6}$	[m]	*
Benign Nuclear Width	w_n	$6.2x10^{-6}$	[m]	*
Malignant Cell Length	L_c	$120x10^{-6}$	[m]	*
Malignant Cell Width	w_c	$20x10^{-6}$	[m]	*
Malignant Nuclear Length	L_n	$20.4x10^{-6}$	[m]	*
Malignant Nuclear Width	w_n	$14.7x10^{-6}$	[m]	*

Determination of lethal thresholds

The thresholds for cell death were determined by first performing a live-dead stain on the hydrogels 24 hours after delivering treatment. It has been reported that this is sufficient time to allow transient pores formed in the cell membrane to recover (284). Live cells were stained with Calcein AM (Biotium, Hayward, CA) and fluoresced as green while dead cells were stained with ethidium homodimer III (Biotium, Hayward, CA) and fluoresced as red. The diameter of the red-stained dead region was measured using ImageJ image analysis software. Geometric measurements of the ablation zones were mapped to a finite element model to calculate the electric field during treatments of the scaffolds (Figure 4.4). The electric field magnitude at the edge of the live and dead regions was considered the electric field threshold for cell death for the given cell type. Imaging of samples presented some background noise mainly due to debris from the remaining 3D microenvironment and re-seeding of detached cells post-treatment.

In vivo canine treatment

All canine *in vivo* studies were approved by the institutional animal care and use committee (08-218-CVM). IRE treatments were performed in the brains of anesthetized normal canine subjects, and in dogs with spontaneous malignant gliomas according to previously described methods (184, 226, 285). In tumor-bearing dogs, biopsy of the brain lesion was performed prior to IRE ablation to allow for histopathological diagnosis and grading of tumors, and an additional biopsy of the ablated region obtained within 24 hours of the IRE to characterize the effects of the IRE treatment.

Histomorphological staining

Archived, paraffin embedded, transversely oriented brain sections from normal and tumor-bearing dogs treated with IRE were retrieved, cut at 5 µm thickness, mounted on positively charged slides, and stained routinely with hematoxylin and eosin(226, 285). Digital photomicrographs of regions of interest representing IRE ablated regions of cerebral cortex, subcortical white matter, contralateral homologous cortical and white matter controls, and a canine GBM pre- and post-IRE treatment were captured with charge-coupled device digital camera (Nikon DS-Fi1c, Nikon, Japan) and commercial imaging analysis software system (NIS Elements AR, Nikon, Japan).

Statistical Analysis

Statistical significance was determined by a two-tailed *t*-test performed in Prism Statistical Software (Version 6, Graphpad, La Jolla, CA). A 95% confidence interval was used with significance defined as $p<0.05$. All numerical results are reported as the mean and the standard deviation of all experimental measurements. No outliers were excluded.

4.3 Results

4.3.1 Cell size selectivity of pulsed electric fields

Single cell responses to electric field pulses were simulated with finite element modeling. Simulated TMP changes in response to modeled IRE pulses (Figure 4.3a) are highly dependent on cell size (Figure 4.3b). In contrast, cells exposed to H-FIRE pulses do not show significant TMP variation with cell size in these models (Figure 4.3c). It should be noted that the maximum TMP reached by both cell types when exposed to H-FIRE pulses is significantly lower than the TMP for IRE pulses. This is because the 1 µs H-FIRE pulse durations are shorter than the cell membrane

charging time. If the pulse duration was progressively increased, the TMP would approach the values calculated in the IRE case (271).

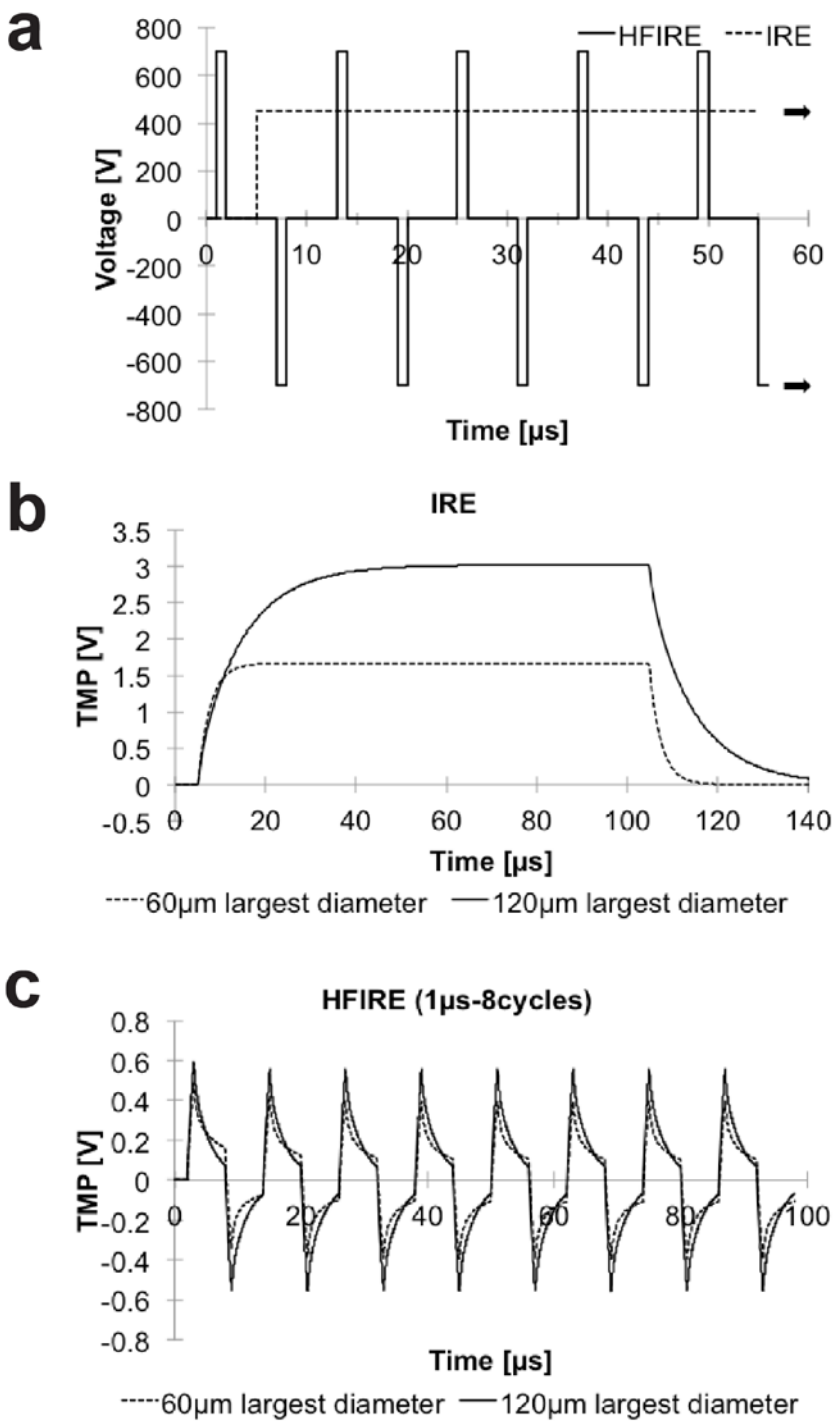

Figure 4.3. Finite element modeling using two pulse waveforms predicts IRE is cell size depended while H-FIRE is cell size independent (a) *Simulated unipolar 100 µs IRE waveform and bipolar 1 µs H-FIRE waveform.* ***(b)*** *Calculated cellular TMP response for two different cell sizes exposed to an IRE waveform applying 500 V/cm shows TMP size dependence.* ***(c)*** *H-FIRE pulse waveform response shows no TMP cell size dependence at 500 V/cm. TMP values were calculated at a point where the cell membrane is perpendicular to the direction of the electric field.*

To experimentally explore the effect of cell size on electric field thresholds for cell death, we tuned the mechanical and chemical structure of the tumor microenvironment using a three-dimensional GBM hydrogel tumor model (Figure 4.4a) to then be used as a therapy-testing platform (Figure 4.4b). We determined the lethal electric field threshold by simulating the electric field within the hydrogels during pulse exposure, at the two experimental voltages, using finite element modeling (Figure 4.4c-d). These simulations reveal the change in expected lesion shape as a function of voltage, evolving from a peanut to a circular shape as the electric field magnitude increases. Finite element modeling of treatment-induced temperature distribution in the hydrogel demonstrates that cellular damage does not occur through thermal effects, as cells are not exposed to temperatures above physiological levels (Figure 4.4e), with no long-term temperature increases evident (Figure 4.4f).

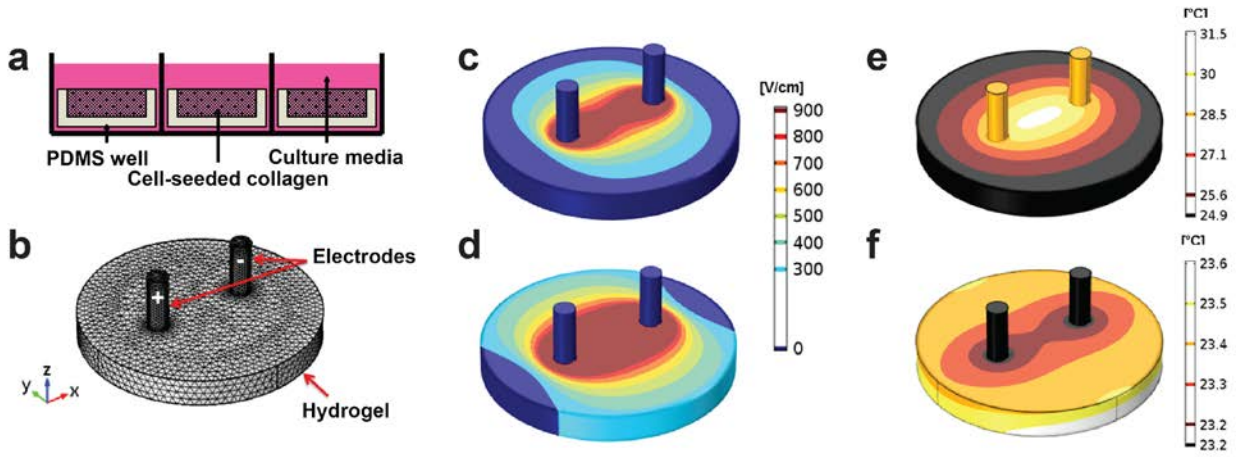

Figure 4.4. Finite element models predict the electric field and thermal distributions within hydrogel platforms. *(**a**) Engineered 3D collagen hydrogels are made by adding cell-seeded collagen (0.2% or 2% w/w) into PDMS wells of controlled geometry. They are kept in a well plate under cell culture conditions with nutrients supplied by culture media. (**b**) Mesh used to calculate the electric field distribution within the tissue mimics illustrates the experimental setup for therapy testing. Electric field (V/cm) isocontours when (**c**) 450 V and (**d**) 700 V pulses are simulated. (**e**) Temperature isocontours immediately post-therapy (50 pulses of 700 V) show a maximum temperature rise of 12 °C above room temperature. (**f**) Temperature isocontours one minute post-therapy confirm that cells are not exposed to any long-term thermal effects as a result of IRE or H-FIRE pulses.*

Cell size and shape within hydrogel scaffolds are functions of scaffold density; by varying collagen density in the tissue model we were able to control cell size and outer membrane perimeter for a single cell type. U-87 MG human GBM cells exhibited a significantly smaller area ($p=0.005$) in the higher density (2% w/w) collagen ($920 \pm 249\ \mu m^2$) as compared with lower density (0.2% w/w) collagen ($1572 \pm 503\ \mu m^2$) (Figure 4.5a). Using this *in vitro* model we then determined that these cell geometries determined lethal thresholds for IRE but not for H-FIRE pulses. As predicted by the model, IRE lesions for cells in 0.2% collagen were larger than the lesions for cells in 2.0% collagen (Figure 4.5b, $p<0.0001$). The larger cells were killed by IRE pulses with amplitude exceeding 428 ± 47 V/cm**,** while the smaller cells required a larger field for cell death (492 ± 41 V/cm). In contrast, H-FIRE treatments did not result in statistically significant differences in lesion size, corresponding to an average lethal threshold of 601 ± 65 V/cm that was independent of collagen density (Figure 4.5c). The electrical conductivity for the two scaffolds was experimentally comparable, and cell densities were identical in the two conditions.

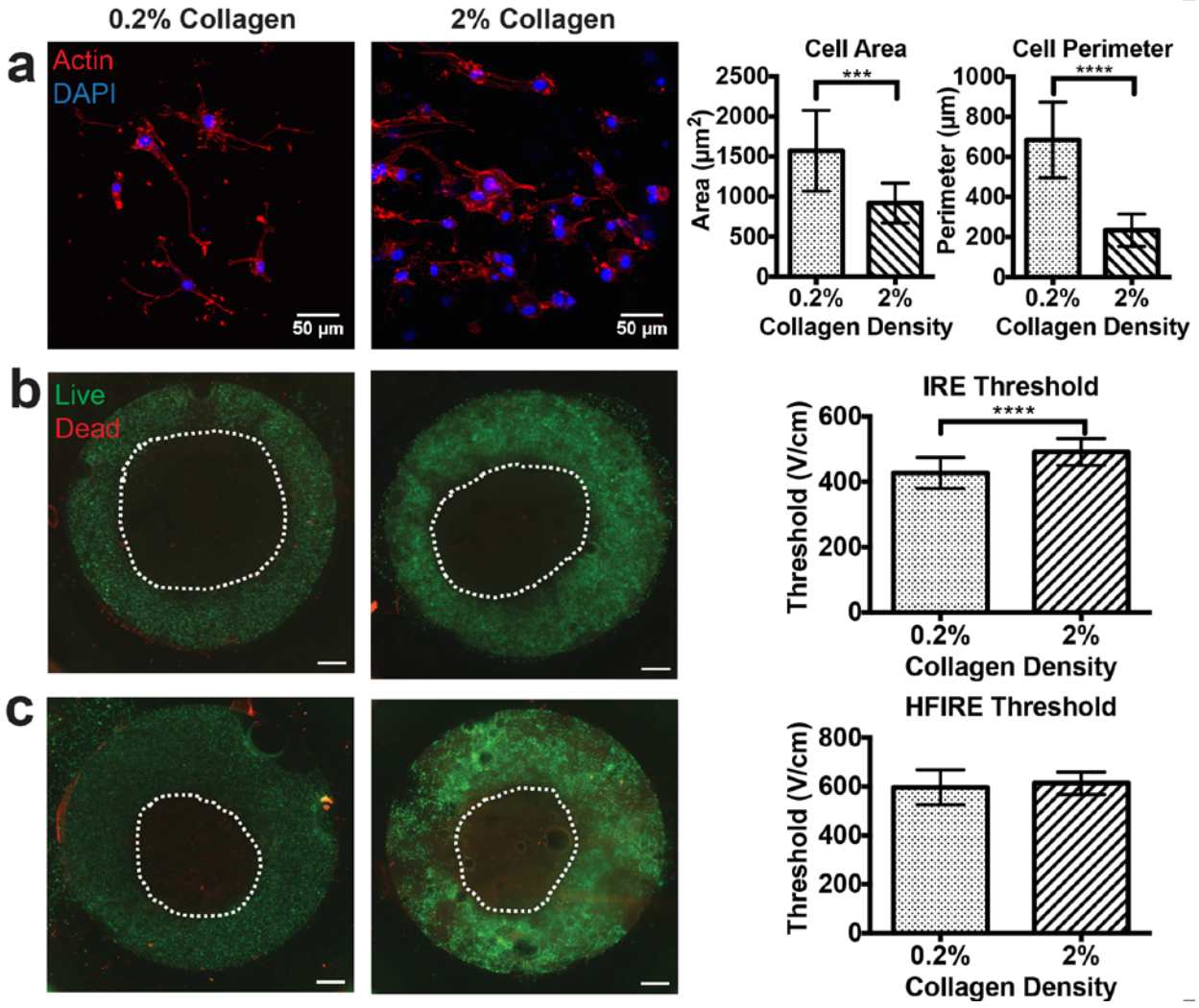

Figure 4.5. ECM-tuned hydrogels reveal cell size dependent IRE lesions and cell size independent H-FIRE lesions. ***(a)*** *Altered cell morphology and overall cell size results from changing density of hydrogel matrix from 0.2% to 2.0% collagen (n = 25, scale bar 50 µm)* ***(b)*** *Comparison of IRE treatment for larger cells in 0.2% collagen reveals larger lesion and thus lower death threshold than for smaller cells in 2% collagen (n = 20, $p < 0.001$) (scale bar 1 mm)* ***(c)*** *Comparison of H-FIRE treatment in 0.2% and 2% collagen reveals uniform lesions and thus equivalent death thresholds despite cell size differences. (n = 20, $p \geq 0.1$) (scale bar 1 mm). (***$p \leq 0.0005$ and ****$p \leq 0.0001$).*

We performed additional experiments in calcium alginate hydrogels, in which cell morphology is relatively constant for different scaffold densities due to the lack of cell-ECM binding sites (Figure

4.6a). In alginate hydrogels, lesion sizes and lethal thresholds were independent of polymer concentration for both IRE (Figure 4.6b) and H-FIRE (Figure 4.6c).

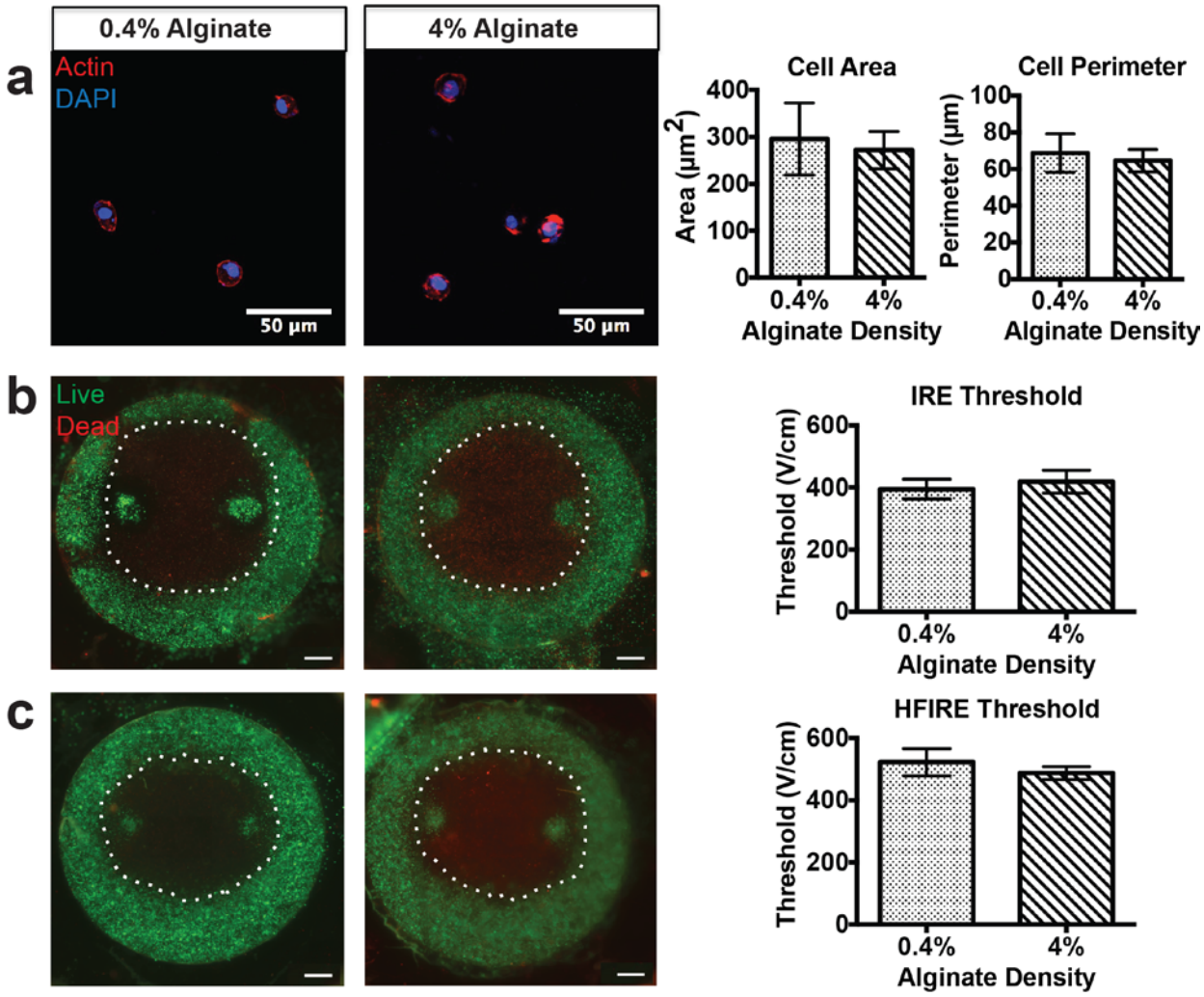

Figure 4.6. Constant cell morphology with changing stiffness results in equivalent lethal thresholds for IRE and H-FIRE. *(**a**) Changing the density of alginate does not change cell morphology due to lack of cell-ECM binding sites, allowing for isolating the effect of stiffness on treatments (n = 25) (**b**) IRE lesions and lethal thresholds are equivalent across stiffness differences for equivalent cell morphology (n = 20, $p \geq 0.1$) (scale bar 1 mm) (**c**) H-FIRE lesions and lethal thresholds are equivalent across alginate stiffness differences (n = 20, $p \geq 0.1$) (scale bar 1 mm).*

4.3.2 Lack of selectivity of IRE

We previously treated canine patients with naturally occurring malignant gliomas using IRE (184). Histology from this treatment provides an important comparison point between our 3D *in vitro* ablation results presented here, and the *in vivo* outcome in a context that is highly representative of the human GBM phenotype. When untreated cerebrocortical grey matter (Figure 4.7a) was exposed to IRE treatment, non-discriminate cell death occurred as both neuronal and glial cells were ablated (Figure 4.7b). Similarly, untreated white matter of the internal capsule (Figure 4.7c) treated with IRE resulted in glial death in addition to vacuolization and axonal loss (Figure 4.7d). Though malignant glioblastoma cells (Figure 4.7e) were ablated with IRE treatment (Figure 4.7f), so too is the stromal cytoarchitecture. Based on these *in vivo* results demonstrating the relatively non-selective nature of IRE ablation in canine GBM, combined with our *in vitro* studies demonstrating statistically significant yet small differences in IRE threshold based on cell size, we next focused on the potential for pulsed electric fields to exert cell-specific targeting. Histology images from canine patients illustrate the well-known tumor cell phenotype characterized by the enlarged nuclei of GBM cells (Figure 4.7e) compared to healthy tissue (Figure 4.7a,c), therefore motivating our hypothesis that intracellular localization of treatment electric fields may enable tumor cell targeting due to nuclear size differences.

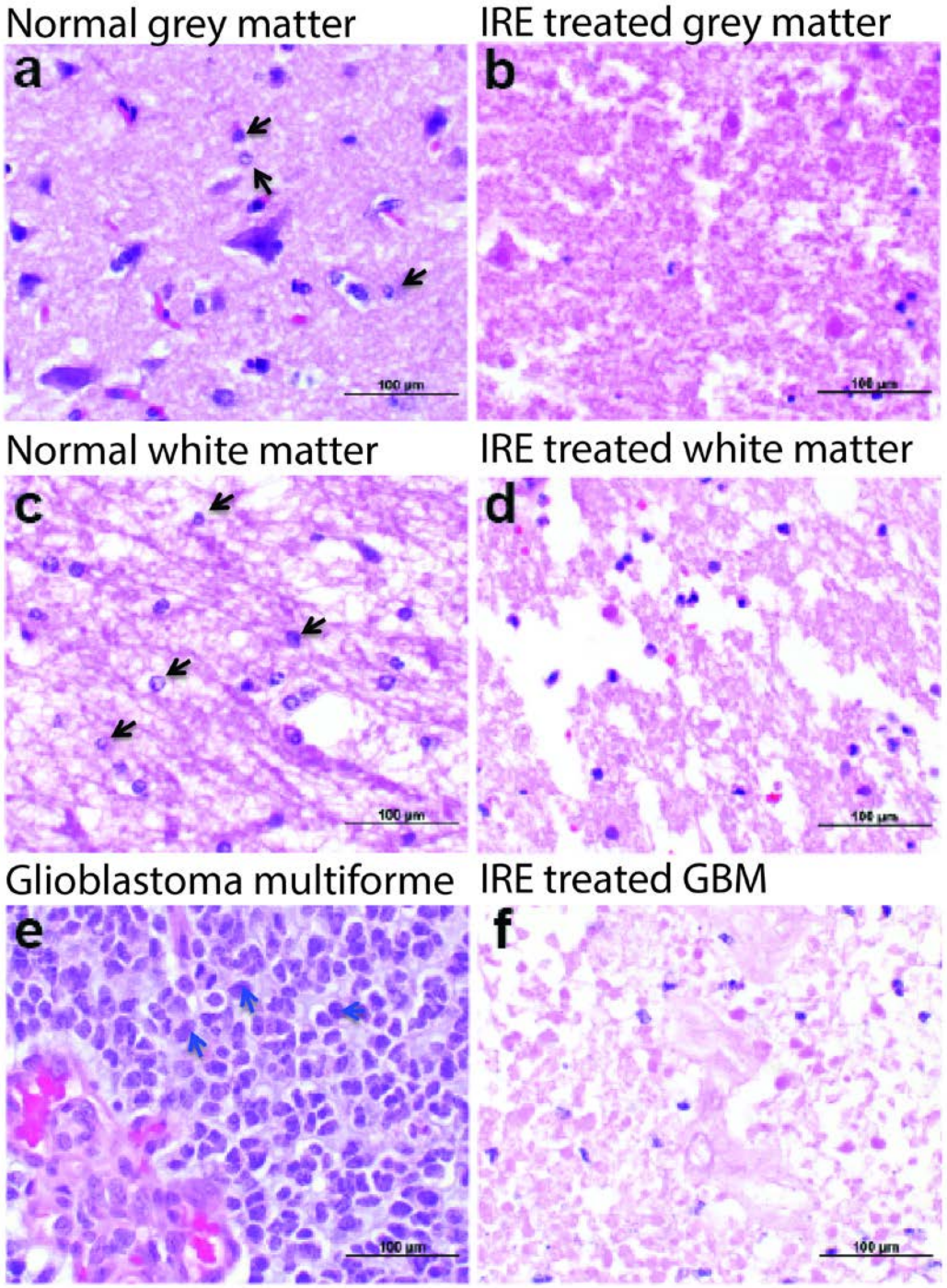

Figure 4.7. Histomorphology of normal and neoplastic canine brain tissues ablated with IRE. *(**a**) Normal, untreated cerebrocortical grey matter (**c**) and white matter of the internal capsule. IRE ablation results in neuronal (**b**) and glial death (**b**,**d**), as well as vacuolization and axonal loss (**d**). Biopsy of glioblastoma multiforme before (**e**) and after (**f**) IRE ablation. The IRE treatment causes disruption of tumor and stromal cytoarchitecture, and tumor cell death. All sections stained with hematoxylin and eosin.*

4.3.3 Intracellular effect of pulsed electric fields

To examine the potential for H-FIRE pulses to exert their effect *via* intracellular localization of electric fields, we performed finite element modeling of field distribution across a single cell (Figure 4.2). This model predicts that for a simulated IRE pulse with an electric field magnitude of 500 V/cm applied for 100 μs, only 14% of the external electric field traverses the cell membrane and is present in the cytoplasm (Figure 4.8a). In contrast, H-FIRE pulses deliver most of their energy to the inside of the cell (Figure 4.8b). The cytoplasm is charged over 400 V/cm for the entire duration of each 1μs H-FIRE pulse while the same is true for only 8% of each 100 μs IRE pulse.

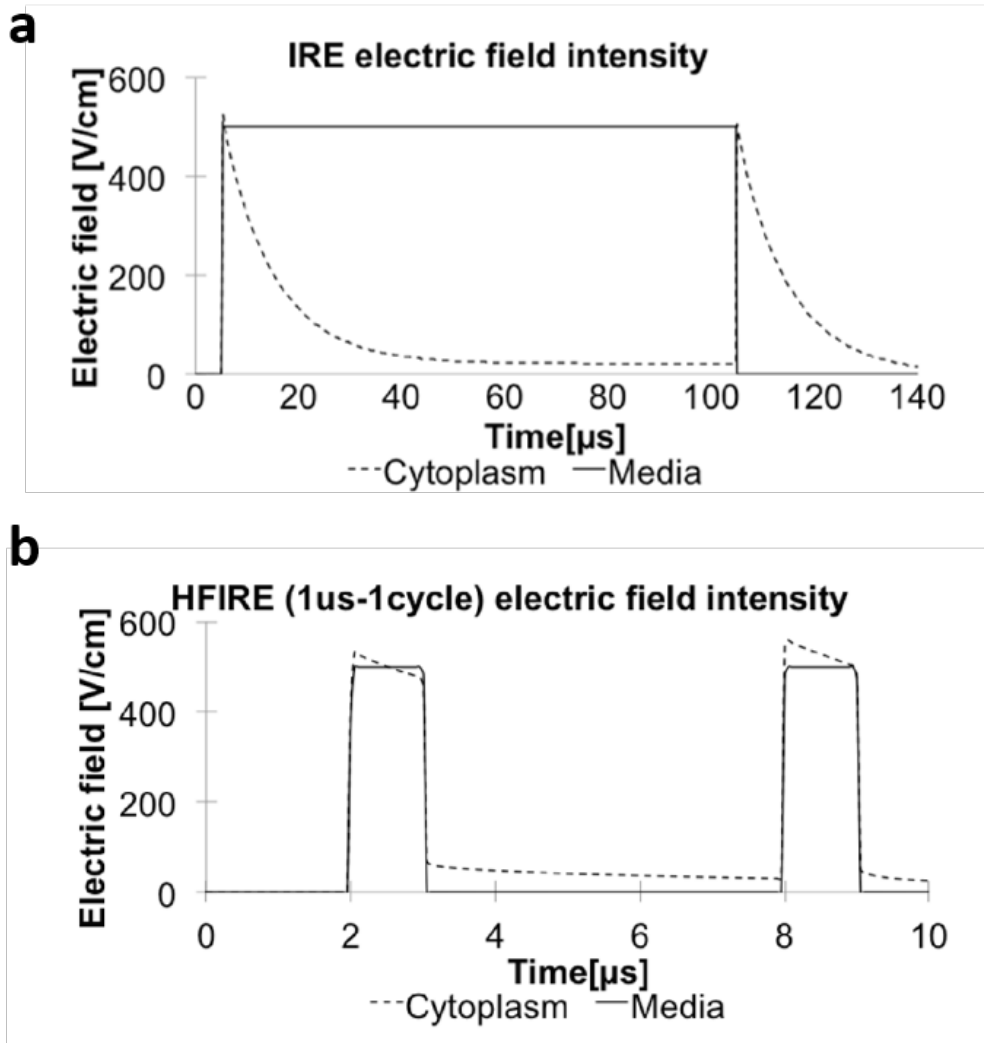

Figure 4.8 The electric field produced by H-FIRE can penetrate the cell membrane while the inside of the cell is mostly shielded from IRE electric fields *(**a**) Numerical modeling of the electric field produced by IRE pulses predicts the electric field reaches the cytoplasm inside the cell for only a short duration of the pulse time while the majority of the electric field is retained in the media where it aggregates around the cell membrane. (**b**) Numerical modeling of the electric field distribution predicts the electric field produced by H-FIRE pulses penetrates through the plasma membrane into the cytoplasm for the entire duration of the pulse on-time.*

To test the implications of effects on tumor cell nuclei for this prediction of a strong intracellular field created by H-FIRE, we constructed 3D models using six different cell types (Figure 4.9a), chosen to include multiple malignant versus normal cell comparisons. Malignant cell types include two human malignant glioma cell lines (U-87 and DBTRG) and a rat glioblastoma line (C6). Non-

malignant cell types include primary normal human astrocytes (NHA), normal rat astrocytes (D1TNC1), and undifferentiated rat neurons (PC12). These 3D cultured cells exhibited no significant difference in cell area (Figure 4.9b), but did exhibit significant differences in nuclear area (Figure 4.9c). All three tumor cell populations that we cultured exhibited enlarged nuclei when compared with each of the normal cell populations.

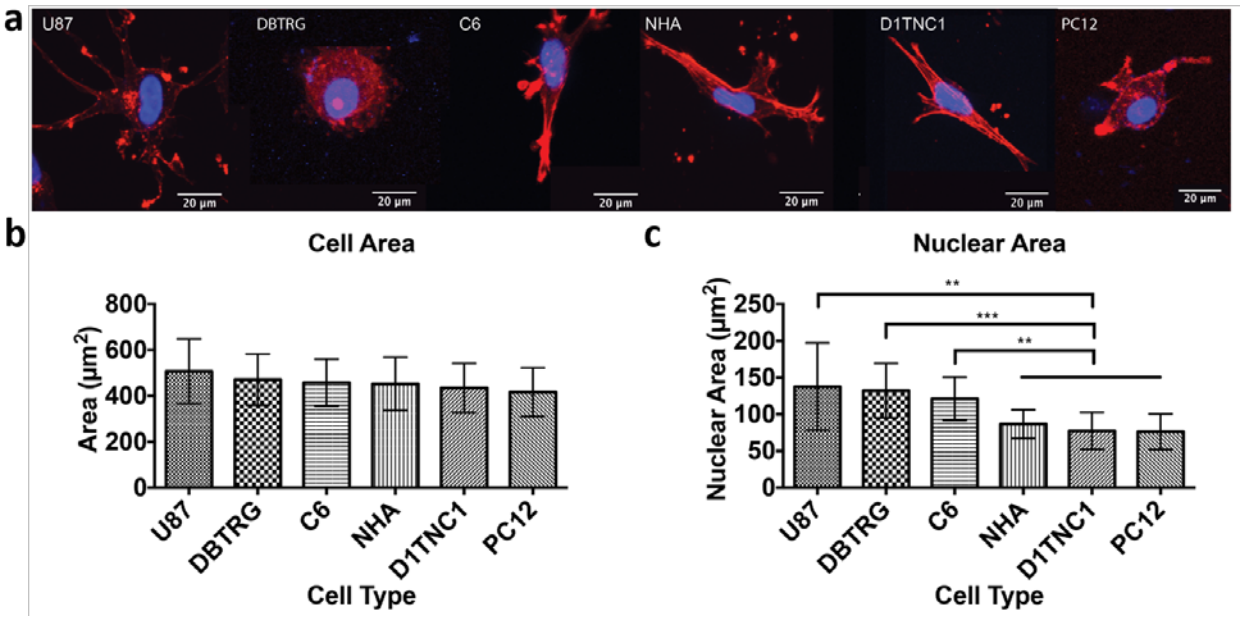

Figure 4.9. Inner organelle effect of H-FIRE predicted to allow for cell-selective differences between malignant and non-malignant cell types by affecting nuclear transmembrane potential. *(**a**) Fluorescent imaging of U-87, DBTRG, C6, NHA, D1TNC1, and PC12 cells allows for determination of shape factors to be used in modeling and to correlate to experimental lesion results. (**b**) U-87, DBTRG, C6, NHA, D1TNC1, and PC12 cells show no significant difference ($p \geq 0.1$) in overall cell area ($n = 20$). (**c**) Nuclear area of malignant glioma cells (U-87, DBTRG, and C6) is greater than for non-malignant cells (NHA, D1TNC1, and PC12) ($n = 20$, $^{**}p \leq 0.005$ and $^{***}p \leq 0.0005$).*

Consistent with model predictions of IRE cell size dependence and nuclear size independence, the four cell types exhibited similar IRE lesions (Figure 4.10a). In contrast, H-FIRE lesions in the tissue mimics with GBM cells were significantly larger than lesions with non-transformed cell

types (Figure 4.10b). The similar lethal IRE thresholds across cell types (Figure 4.10c) is consistent with the fact that all four cell types have similar outer membrane areas. H-FIRE experimental results, however, reveal a lower lethal threshold for malignant cells (Figure 4.10d), which have larger nuclei compared with their normal cell counterparts. For H-FIRE treatments, U87 human glioblastoma cells were killed at a threshold of 601 +/- 71 V/cm, DBTRG human glioblastoma cells were killed at a threshold of 720 +/- 67 V/cm, and C6 rat glioblastoma cells were killed at a threshold of 752 +/- 58 V/cm. All normal cell types tested had a significantly larger lethal threshold than any of the malignant cell types tested ($p<0.0001$). NHAs were killed at a threshold of 1006 +/- 81 V/cm, D1TNC1 cells had a lethal threshold of 1107 +/- 106 V/cm, and PC12 cells had a lethal threshold of 1076 +/- 57 V/cm.

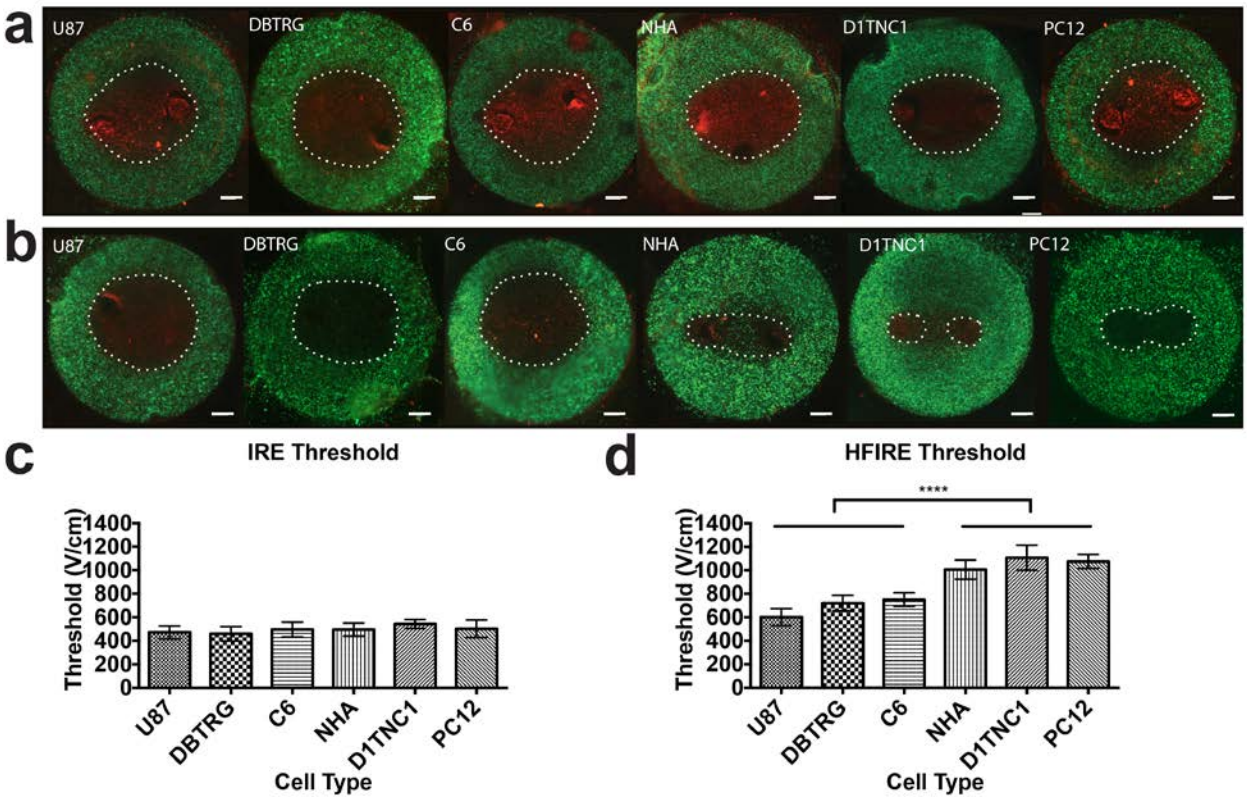

Figure 4.10. H-FIRE threshold is dependent on nuclear size, resulting in cell selective targeting. *(**a**) IRE lesion sizes have no significant difference across different cell types (n = 10, $p \geq 0.1$). (**b**) H-FIRE lesion size for malignant glioma cells (U-87, DBTRG, and C6) is greater than non-malignant astrocytes (NHA and D1TNC1) and neurons (PC12) (n = 10). (**c**) COMSOL modeling relating lesion size to death thresholds shows no significant difference between IRE thresholds for different cell types (n = 10, $p \geq 0.1$), confirming the hypothesis that IRE thresholds are primarily dependent on cell size. (**d**) Death thresholds for malignant cells are smaller than normal cells with H-FIRE treatment suggesting a range of electric field values that will kill malignant cells without killing healthy cells (n = 10, ****$p \leq 0.0001$).*

As in mono-culture hydrogels, equivalent lesions were achieved for U87 and NHA cells in co-culture hydrogels treated with IRE (Figure 4.11a). Selective killing of malignant cells was demonstrated using H-FIRE in a co-culture environment, as U87 lesions were significantly larger than NHA lesions within the same hydrogel (Figure 4.11b). H-FIRE and IRE lethal thresholds for each cell type in co-culture were unchanged from those in monoculture. The selective killing in co-culture demonstrated by H-FIRE further supports the feasibility of selective targeting in a complex environment with multiple cell types such as at the periphery of a tumor.

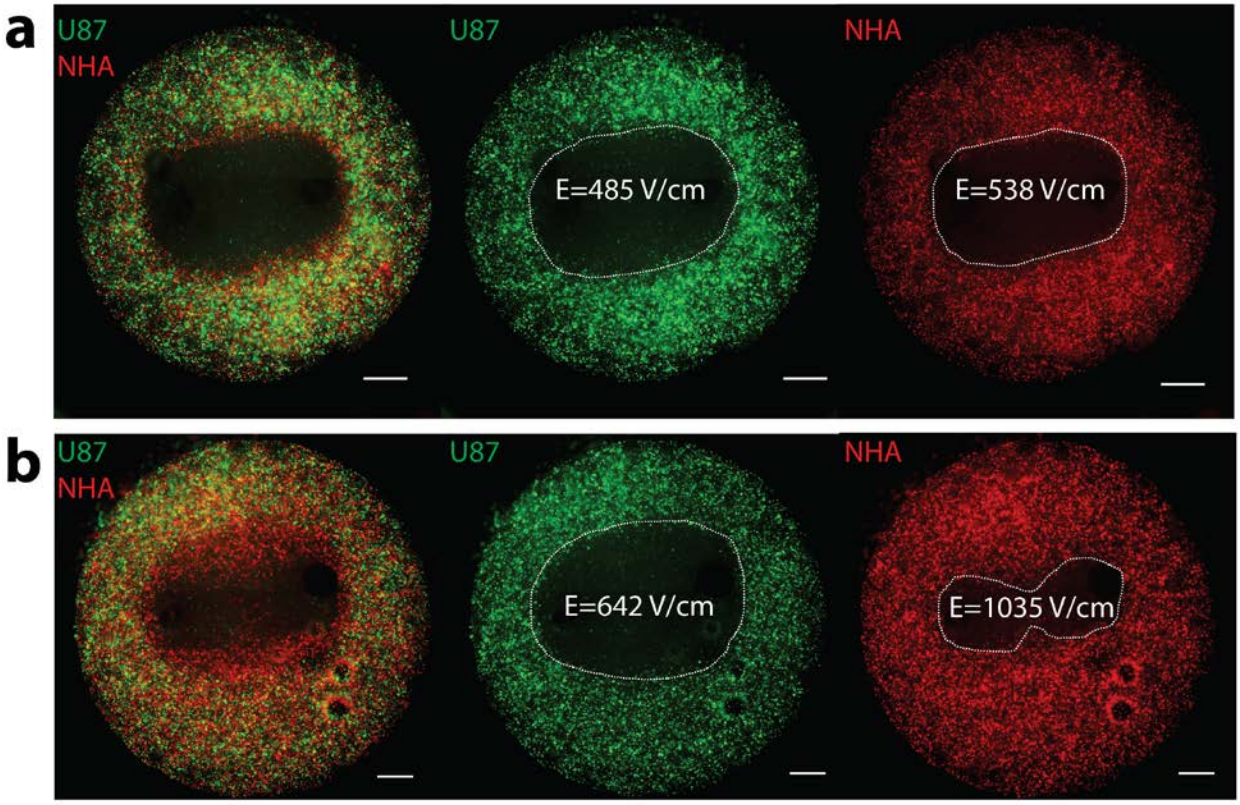

Figure 4.11. Co-culture treatment demonstrates equivalent lesions with IRE and selective targeting of malignant cells with H-FIRE. *(**a**) U87 cells (green) and NHA cells (red) co-cultured in a hydrogel and treated with IRE show lethal thresholds in co-culture that match the lethal thresholds seen in monoculture with the lethal threshold of the two cell types being equivalent (scale bar 1 mm). (**b**) U87 cells (green) and NHA cells (red) treated with H-FIRE show lethal thresholds in co-culture that match the lethal thresholds seen in monoculture with the lethal threshold of malignant U87 cells being significantly lower than that of the NHA cells resulting in a larger lesion (scale bar 1 mm).*

4.3.4 Death mechanisms of IRE and H-FIRE

To investigate the differences between the mechanism of death with IRE and H-FIRE we performed single cell imaging upon exposure to each treatment regime. Cell nuclei and tubulin were stained by live fluorescent stain and cultured in 3D collagen hydrogels. Fluorescent imaging *in situ* within these hydrogels was performed directly before, and then at 30-second intervals after exposure to IRE, revealing an outward diffusion of dye from the cell membrane within 1 minute after pulsing (Figure 4.12a). By 5 minutes after treatment the tubulin dye had diffused almost

entirely out of the cell while the nuclear dye showed a disruption of the integrity of the nucleus. In contrast, cells exposed to H-FIRE showed a strong inward collapse of the nucleus followed by a collapse of the tubulin stained cytoplasm on the 5-minute timescale (Figure 4.12b). A control cell that was not exposed to either treatment imaged over the same time course confirms that treatment-induced changes are not related to photo-bleaching (Figure 4.12c). The marked increase in cytoplasm area with time after IRE treatment is different from the small decrease in cytoplasm area as a result of H-FIRE treatment ($p<0.0001$) (Figure 4.12d). The H-FIRE response shows a consistent decrease of the nuclear area with time after treatment that is significantly greater than the decrease in nuclear area evident after IRE treatment ($p=0.0066$) (Figure 4.12e).

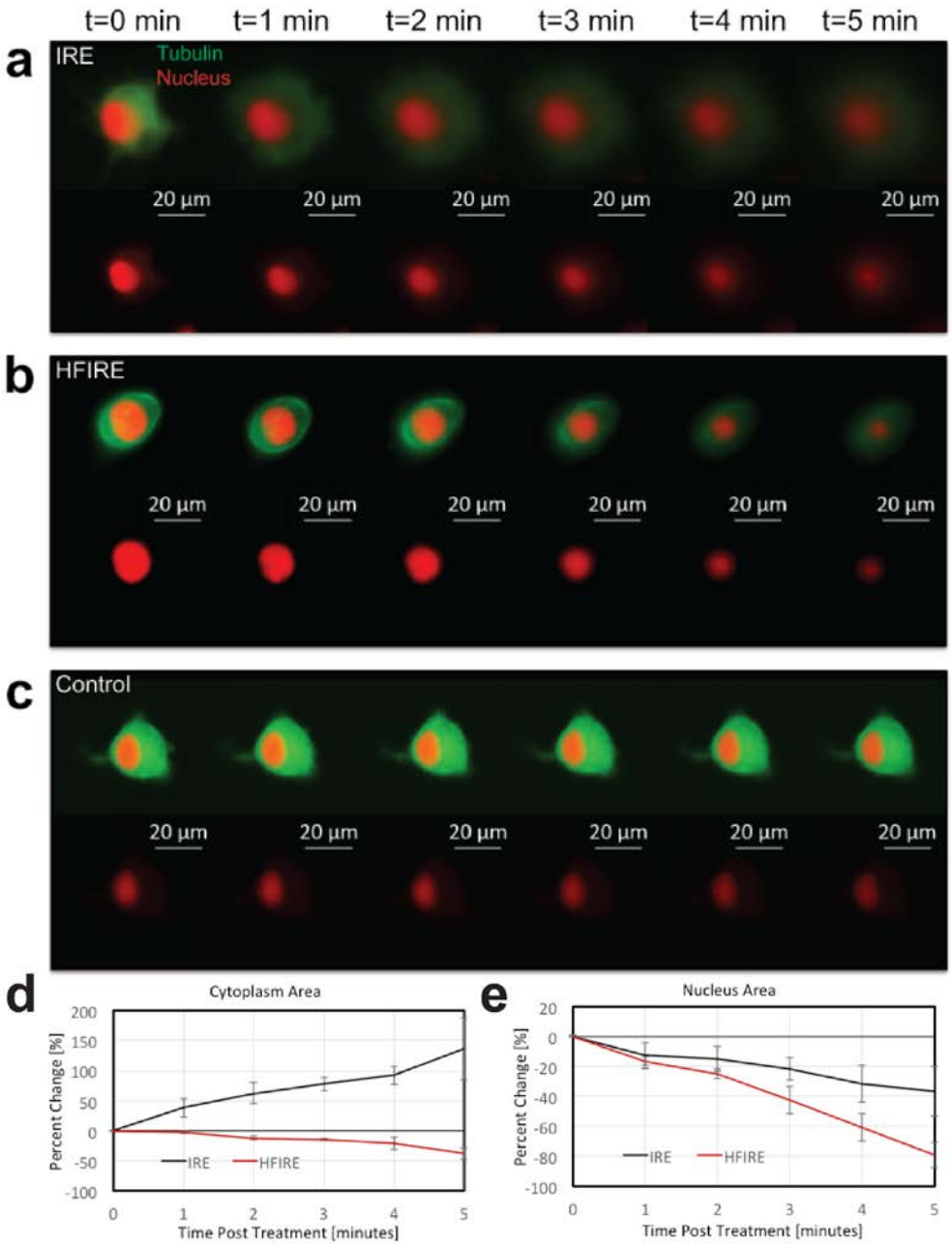

Figure 4.12. Cell responses after treatment show difference in IRE and H-FIRE mechanism. ***(a)*** *Cell exposed to IRE treatment shows a diffusion of stained tubulin from the cell cultured in a 3D hydrogel over a 5-minute time course, suggesting a disruption of the outer cell membrane as a result of pulses.* ***(b)*** *Cell exposed to H-FIRE treatment shows a sharp collapse of the nucleus, and while tubulin staining dims, it does not clearly diffuse outside of original cell membrane area as in the IRE case. This suggests a different effect on both the nucleus and cell between IRE and H-FIRE.* ***(c)*** *Cell not exposed to any pulses acts as a control to ensure no photo-bleaching effects from imaging over 5-minute time course.* ***(d)*** *Change of cytoplasm area in response to IRE and H-FIRE shows a significant difference in the cytoplasmic response to therapy ($n = 3$, $p \leq 0.0001$). Cytoplasm area increases in response to IRE as a result of tubulin diffusion, which is not present with H-FIRE.* ***(e)*** *Change in nuclear area in response to IRE and H-FIRE shows a significant difference in nuclear response to therapy ($n = 3$, $p = 0.0066$). The more drastic collapse of the nucleus with H-FIRE supports a nuclear effect in H-FIRE that isn't present with IRE.*

4.3.5 Estimate of lethal threshold for nuclear disruption

We next further explored the relationship between H-FIRE lethal thresholds and nuclear size, leveraging our experimental data as input for subsequent mathematical models. We hypothesized that cell death occurs at a critical nTMP disruption that is independent of cell type, whereas the external field required for this nuclear disruption scales inversely with nucleus size. Using experimental findings for lethal thresholds, nuclear geometries, and idealized cell geometries for glioma cells and astrocytes, we performed finite element modeling of single cell response to minimum lethal electric fields for each cell type. In search for the potential mechanism of action for H-FIRE, we simulated electric field magnitudes of 1006 V/cm for NHA cells and 601 V/cm for U-87 cells. We found a larger increase in TMP for the astrocyte than for the glioma cell (Figure 4.13a), however these TMPs were significantly below the anticipated 1 V instantaneous lethal threshold for IRE. In contrast, simulation of nTMP response across the entire area of the nuclear envelope predicts similar increases in nTMP for both cell types, indicating that irreversible electroporation is occurring at a common value (~130 mV) of nTMP for both cells (Figure 4.13b).

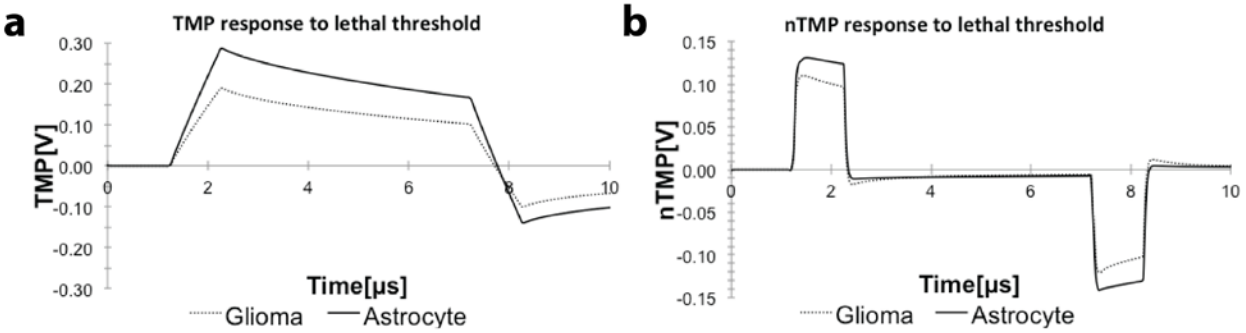

Figure 4.13. Predicted TMP and nTMP response to H-FIRE experimental lethal thresholds for modeled glioma and astrocyte cells suggests a nTMP effect. *(**a**) Modeled cells with experimental geometries for glioma cell and astrocytes exposed to simulated H-FIRE experimental lethal electric field thresholds for the given cell type show a difference in TMP increase in response. (**b**) Modeled cells with experimental geometries for glioma cell and astrocytes exposed to simulated H-FIRE experimental lethal electric field thresholds for the given cell type show a similar nTMP increase in response, suggesting a value for nTMP increase that will cause cell death. TMPs and nTMPs presented in this figure correspond to the surface average.*

4.4 Discussion

The overall goal of our current study was to leverage tissue engineered models of tumor versus normal brain microenvironments, based on our previously published methods(134), to investigate the response of representative cell geometries to IRE and H-FIRE pulses. These platforms critically provide a three-dimensional physiological tissue context in which to explore the effects of 3D cell morphology on response to electric fields, not possible with 2D experiments, while eliminating other confounding variables found *in vivo*. Hydrogels have been previously established as a relevant platform to test tissue responses to IRE pulses(225), while such models have also been demonstrated to better recapitulate human tumor physiology and therapy response as compared with 2D models(139, 286). With the ability to easily tune targeting parameters and microenvironment, these models provide a valuable tool for measuring the impact of cell morphology and tissue physics on therapy response broadly, and more specifically on response to therapeutic electric fields, which are the focus of this study.

It is important to note that our work is informed by, and builds on our experience in treating spontaneous GBM in canine patients. Spontaneous, primary brain tumors are only relatively common in two species – dogs and humans. Human and canine brain tumors share many features, including histopathologic and diagnostic imaging characteristics, which allows application of World Health Organization pathologic classification and imaging based therapeutic response assessment schemes used in human clinical practice. Canine and human brain tumors have also been demonstrated to have similar expression patterns of growth factor receptors, chromosomal deletions, and losses of function of tumor suppressor genes. As tumors progress 5- to 7-fold faster in dogs relative to humans, dogs with spontaneous brain tumors are an attractive model for the

faithful and rapid evaluation and translation of novel brain tumor therapeutics(287). While our *in vivo* work in treating primary canine GBM tumors demonstrates the great potential for IRE for the treatment of human GBM, this work also demonstrates a limitation inherent in IRE in terms of its potential for tumor cell specific ablation. However our 3D models are significantly more amenable to exploring cell-level responses and death mechanisms, needed to advance electric field ablation to a more cell-targeted modality.

Size selective ablation using PEFs has been previously reported, both on the single cell level in 2D culture(288), and in cell suspensions for the application of differentiating tumor from blood cells based on large differences in size (289), but has yet to be demonstrated for cells cultured in physiologically-relevant tissues. Our experiments support the concept that IRE results in cell size-selective lethal thresholds in 3D tissues. The bulk electrical resistance properties of the cell-seeded hydrogels did not vary as a function of collagen density, and we therefore believe differences measured are a result of cell morphology rather than altered tissue electrical properties. Control experiments performed in alginate further support this hypothesis that the differences observed in collagen resulted from cell size variations rather than additional factors such as direct sensing of matrix density. Although this finding does not eliminate the possibility that variables such as variation in binding ligand density, matrix structure, and matrix mechanics may also impact lesion size, this size dependence is consistent with previously published data on cells in solution (289). Furthermore this correlation of threshold with altered matrix density is absent for H-FIRE, suggesting a cellular effect rather than a matrix effect. We hypothesize that this is due to the H-FIRE field primarily interacting with the inner organelles of the cell. There is the possibility that the IRE changes are related to cell-ECM interaction changes that are sensed for IRE response,

which effects the outer membrane, but not H-FIRE, which is hypothesized to be enhanced by differences in intracellular structures. However, because the effect here is so small over a large ECM density range, we don't believe this will impact therapy. Our finite element modeling supports the hypothesis that H-FIRE can induce intracellular effects as a single H-FIRE burst applied to a single cell model produces a much higher field inside the cell than a simulated IRE burst. H-FIRE treatment delivers a rapid burst of over 100 of these 1µs pulses. This allows H-FIRE pulses to preferentially charge intracellular membranes, which we anticipated would have profound effects on cell death as a function of cell type.

Our *in vitro* 3D model results demonstrate a statistically significant dependence of field threshold on cell size, however the narrow range of selectivity evident along with the degree of cell size heterogeneity observed *in vivo* may prevent this dependence from being leveraged for targeting specificity. A much more obvious difference between cell types, clearly evident in our H&E staining of tumorous and healthy canine brain samples, is the enlarged nuclei of cancer cells compared to healthy brain tissue. Therefore, enlarged nuclei of cancerous cells represent the metric we explored for selective targeting. Used as an pathological indicator of cancer, enlarged nuclei compared with their non-malignant counterparts is one of the most reliable distinguishing characteristics of tumor cells(290), however the targeting of anti-cancer therapy against this hallmark has never been demonstrated. We justified our assumption in using enlarged nuclei as a predictor of malignancy because it is a fundamental morphologic marker for cancer, and is nearly universally applied when diagnosing cancers, including brain tumors. Although it is not as important in brain malignancies compared to some other cancers, nuclear pleomorphism is a criteria used when grading brain tumors as described by the WHO(291). The exuberant giant,

multinucleated features present in some glioblastomas provide an excellent example of the extreme nuclear pleomorphism that can be present in cancer. It is true that histologic and other morphologic criteria are gradually being supplemented and improved when complemented with genetic and other diagnostic criterion towards the development of personalized medicine. However, as the WHO classification system is currently an accepted and the most widely used gold standard, and histological diagnosis remains a primary method of cancer diagnosis, the nuclear pleomorphism and NCR are still a valid surrogate of malignancy.

The nucleus is typically the largest contiguous intracellular feature and a likely target for damage by the high intracellular fields produced by H-FIRE. To experimentally test the effect of nuclear area on treatments, we chose different cell types, which exhibited differences in nuclear sizes without significant differences in plasma membrane area, allowing us to eliminate confounding effects due to cell size. Numerical simulations identified increased nuclear size as an important variable for increased nTMP. We hypothesized that an increase in nTMP could trigger cell death above a specific threshold, and therefore malignant cells with enlarged nuclei should have a lower H-FIRE lethal threshold than normal cells, in contrast with IRE, which would not exhibit nuclear selectivity. The similarity of IRE thresholds is consistent with the fact that there was no significant difference in plasma membrane areas. The differences in H-FIRE lesion sizes supports the hypothesis that H-FIRE threshold differences are related to nucleus area as opposed to overall cell area, with lower lethal thresholds corresponding to larger nuclei. The intracellular field produced from H-FIRE seems to affect the nucleic membrane in a way at least partially analogous to the way IRE affects the plasma membrane, as a larger membrane exposed to the majority of the electric field is easier to affect than a smaller membrane. Our main goal in this work is to demonstrate that

enlarged nuclei may provide a viable target for H-FIRE therapies. A critical point for the purpose of this study is that the cell populations we have chosen exhibit significant differences in the morphological features we are interested in, namely enlarged nuclei. Here we show a relationship between enlarged nuclei and lower lethal thresholds with H-FIRE treatment, which we believe we will be able to leverage in future work *in vivo* due to the known enlargement of NCR in cancer. It may be possible to sort malignant populations based on marker expression and to then establish a robust understanding of the connection between H-FIRE lethal thresholds and molecular signatures. Our continuing work will follow this important line of study, specifically involving the H-FIRE response of glioma cells expressing differing levels of known cancer stem cells markers.

By varying collagen matrix density we show that GBM cells in 0.2% collagen demonstrate a more elongated morphology than in 2% collagen, which may be similar to the morphology changes seen in invasive cells, which tend to elongate and lose bulk in the cytoplasm surrounding the nucleus. However, no experimental steps were taken to specifically induce an invasive phenotype in these cells. Based on histological examination of invasive cells, it appears that an enlarged nucleus in malignant cells is conserved even during the dynamic process of invasion. Though further investigation is necessary, the results presented here indicate that H-FIRE should be capable of targeting these invasive cells.

Time-course images of single cells exposed to each treatment show a distinct difference in mechanism of killing between H-FIRE and IRE, consistent with the findings that different cellular characteristics are important variables with the two treatments. The time-course of cell death after

IRE treatment strongly implicates the immediate disruption of the cell membrane as a cause of cell death, as tubulin proteins originally confined in the cell by the cell membrane begin diffusing out of the cell upon exposure to IRE. In contrast, cells exposed to H-FIRE show no diffusion from the outer cell membrane but rather a nuclear collapse while the tubulin is retained within the original cell area. These findings suggest that while the outer membrane may be subject to a small degree of electroporation, it does not play as much of a role in the mechanism of cell death in H-FIRE, but rather that the primary effect is on the nucleus.

Given our results, we hypothesize that H-FIRE is acting on the biophysical structure of the cells in a way that nuclear area becomes a key variable. When glioma and astrocyte cells were simulated at their respective lethal H-FIRE thresholds (601 V/cm vs. 1006 V/cm), we found similar TMP and nTMP ranges of approximately 150-250 mV and 100-130 mV, respectively. These simulations did interestingly predict a small difference in outer TMP as a function of nuclear size. However the magnitude of this TMP, approximately 150 mV, was significantly lower than the anticipated instantaneous threshold (1 V) for cell death by irreversible electroporation. This supports the hypothesis that the primary mechanism of death with H-FIRE is not an increase in cell TMP, but rather is related to intracellular effects. For glioma and astrocyte cells, the maximum simulated nTMP of 130 mV is also well below the lethal threshold for death resulting from outer membrane disruption, suggesting that small disruptions of nTMP may significantly impact cell survival. It is unclear whether the pathway to cell death is dominated by effects on the nuclear envelope alone, versus in combination with cell membrane disruption, or a separate cascade of intracellular effects. However, the correlation of nTMP values between the two different cell types, at different lethal

electric field strengths, indicates that nuclear area impacts the cell death process after H-FIRE treatment.

Our mathematical model does have limitations, as outer cell membranes are approximated as elliptical, and do not account for the irregular shape of physiological cells, or heterogeneity in electrical properties of individual cells. Inclusion of membrane conductivity changes due to electroporation effects would also enhance the accuracy of our simulations. While IRE models accounting for such effects do exists, these have not been characterized for H-FIRE pulses. Characterization of the cell membrane response to H-FIRE pulses (e.g., conductivity, porosity) is beyond the scope of this project thus both models are presented with non-dynamic cell membrane properties. As pulse-width of H-FIRE pulses increases TMP values start approaching those of IRE. It is important to note that the cell-specific thresholds presented in this paper may no longer hold for different pulse widths.

While experimental evidence also suggests that outer membrane electroporation is occurring during H-FIRE, our experimental results and model findings strongly suggest an active role for nTMP effects in the H-FIRE mechanism of action. It is widely recognized that the mechanism of death in irreversible electroporation using short pulses is complex, poorly understood, and can follow multiple different pathways (242). Furthermore, nuclear poration may be aided not only by increased nuclear size of cancer cells but also other abnormalities of the nucleus such as reduced nucleus stiffness necessary for invasion(292). Another possibility is an amplification of the electric field applied to the cytoplasm caused by distortion around an enlarged nucleus. This may result in other inner organelles, such as mitochondria, being disrupted by H-FIRE pulses. Future work will

be needed to explore these additional effects, however our results highlight the importance of TMP increases in both IRE and H-FIRE and nTMP increases specifically associated with H-FIRE, in determining cell death PEF thresholds.

It is important to note, the electric field therapies explored in these studies differ from the alternating electric field treatments being used clinically (218). These tumor treating fields (TTFields), such as the Optune^{TM} system (Novocure, Saint Helier, Jersey), have specific inhibitory effects on dividing cells, while H-FIRE and IRE target the physical properties of cells through membrane disruption. While having the benefit of being less invasive than H-FIRE treatment, TTFields rely on targeting the properties of highly proliferative cells, and would leave behind the quiescent tumor initiating cells that cause recurrence. Because IRE and H-FIRE operate *via* a different mechanism, they should elicit a death response through membrane disruption for both bulk tumor cells and non-dividing tumor initiating cells. In addition, it is unlikely that this physical death mechanism result in the emergence of resistant subpopulations on short timescales, because a large number of genetic mutations would likely be required to render a cell resistant to electric field-induced damage.

Because an enlarged nucleus is a conserved phenotype in malignant cells and H-FIRE is not dependent on cell size, it is hypothesized that consistent and tunable lesions can be achieved in heterogeneous tumors so as not to leave behind cells that will repopulate the tumor. There is certainly heterogeneity in nuclear size of cells in malignant tumors and therefore H-FIRE will not be perfectly able to selectively kill all malignant cells. However, when H-FIRE is used as a supplement to current therapies, any cells left behind from H-FIRE due to nuclear area

heterogeneity are unlikely to also be resistant to the adjunctive therapies as these therapies operate by different mechanisms. Because malignancy correlates with altered nuclear morphology, the malignant selection mechanisms should be different with this method than other treatment methods and should not leave behind highly malignant cells. A major difference between H-FIRE and other therapies that select out resistant populations is that H-FIRE acts on physical aspects of the cell, which are highly conserved in malignant populations. Based on our results, we also show H-FIRE selectivity may be beneficial because there is no associated dose limiting toxicity (DLT) to normal tissues. DLT, biological resistance/escape, and off target effects are major problems associated with chemotherapy, radiotherapy, and molecular immunotherapies, which may not be an issue with a treatment based on physical properties of cells. However, all these hypotheses will need to be tested in more complex models of disease.

It is important to note that the results reported here were obtained in an *in vitro* model of disease, which was intended to maximally replicate *in vivo* morphological features, by tuning matrix conditions, while also minimizing confounding factors. It is likely that local and systemic immune effects will be observed when this therapy is implemented *in vivo.* It is unclear if a differential immune effect between H-FIRE and IRE treatments will be observable due to the relative intracellular and membrane targeting processes and future studies in appropriate *in vivo* models of disease will be necessary to optimize protocols which result in targeting of malignant cells.

Though the exact mechanism of cell killing with H-FIRE is not yet known, our modeling and experimental data suggest a mechanism that is different than that of long IRE pulses which target the plasma membrane, and that, unlike for IRE, is cell type dependent among cells of similar size.

The H-FIRE killing mechanism is such that the biophysical structure of malignant cells allows for the selective targeting of these cells using a range of electric field distributions that induce no damage to the healthy cells studied but elicit a death response in malignant cells. Though it is unlikely that 100% selective killing of malignant cells can be achieved due to the heterogeneity that does exist in physical properties of cells, H-FIRE can be used to ablate all cells within the tumor margin and pulse parameters can be tuned to achieve preferential killing of a significant fraction of the malignant cells past the tumor margin. Because malignant cells that comprise the tumor have a lower death threshold (~530-810 V/cm) than normal astrocytes (~930-1200 V/cm) surrounding the tumor, it follows that a treatment regime delivering a voltage between these two thresholds to the edge of the tumor may result in ablation of tumor cells while sparing healthy astrocytes. While the response of other cell types and structures within the brain parenchyma must be investigated in future work, a threshold in such a range at the edge of the tumor may be effective at killing the invasive glioblastoma cells that render surgery to be an ineffective treatment for GBM, and infiltrative tumors more broadly.

Chapter 5 Using Targeted Molecular Therapy to Enhance the Selectivity of H-FIRE[2]

5.1 Introduction

The high rate of tumor recurrence in many cancers including GBM, has motivated research into a new class of therapies that may eliminate the more resistant sub-clones when used alone or in combination with other treatments. One such class of therapies is irreversible electroporation (IRE), which uses high intensity but low energy electric fields to disrupt the integrity of cell membranes, causing cell death. Treatment with IRE involves exposing cells to a series of pulsed electric fields delivered through electrodes inserted into the tissue. The electric field causes a buildup of charge across the cell membrane, and a subsequent increase in the transmembrane potential (TMP) of the cell. Once the transmembrane potential reaches a critical value of ~250 mV, transient nanoscale pores form in the membrane allowing the passage of otherwise excluded molecules through the membrane barrier (151). This reversible electroporation technique has been used for gene transfection, gene therapy, and cancer electrochemotherapy (ECT) (157, 158). When the transmembrane potential reaches another critical value of ~ 1 V, the cell cannot recover from the pore formation and dies due to loss of homeostasis (171). This method of cell ablation, termed irreversible electroporation (IRE), has been used for the treatment of a variety of cancers including prostate, pancreas, and liver cancers (186, 187, 192, 293). While the benefits of this treatment modality have underpinned its successful use for a variety of cancers, invasive cancers such as glioblastoma (GBM) still present challenges. IRE methods do not allow for the treatment of diffuse

[2] Chapter 5 is adapted from J.W. Ivey, E.L. Latouche, M.L. Richards, G.J. Lesser, W. Debinski R.V. Davalos, S.S. Verbridge, Enhancing Irreversible Electroporation by Manipulating Cellular Biophysics with a Molecular Adjuvant, Biophysical Journal, 113, 472-480 (2017).

cells outside the tumor margin without ablation of healthy tissue, a situation especially problematic in the brain. To address these challenges and improve selectivity outside the tumor margin, investigators have begun studying combination therapies such as IRE used with ECT (294).

A parallel and promising direction for glioma treatment has been provided by molecularly-targeted therapies. These involve identifying either receptors or signaling pathways that are altered in cancerous cells, which can then be used to target drug-carrying particles (295, 296), or else provide a target through pathway manipulation *via* a molecular drug (297, 298). The EphA2 receptor, a member of the largest class of receptor tyrosine kinases, has been identified as overexpressed in a large number of cancers (299, 300), including GBM (301). While GBM tumors have demonstrated high expression of EphA2, normal brain does not express appreciable levels of the receptor (301). GBM cell lines have also been shown to over-express EphA2 compared to normal cell lines (301). In general, Eph receptors and ephrin ligands seem to have a physiological role in development, as the proteins are expressed at the highest level during this time are at low levels in normal adult tissue (302, 303). In the brain, Eph and ephrin gene expression seems to be mostly confined to specific cell populations involved in processes such as remodeling and the formation of new neuronal connections (304). Contrary to normal physiological levels, EphA2 is highly overexpressed in the majority of patient tumors and is highly overexpressed in terms of the percentage of cells within a given tumor(305). Additionally, EphA2 plays an important role in tumor progression and has been linked to tumor grade and poor prognosis (306, 307). The overabundance of EphA2 receptor is correlated with lesser presence of ephrinA1 (eA1), the preferred ligand for EphA2 (308, 309). eA1 has been explored as a therapeutic option due to its ability to decrease invasion and proliferation of malignant cells (301, 309). EphA2 makes for an

attractive target as it is a plasma membrane–localized receptor that can internalize on ligand binding (310).

In order to increase the selective capabilities of IRE treatment, here we investigate a new combinatorial treatment concept, combining electroporation with a molecular therapy that we hypothesized would act in a synergistic manner to the physical treatment. Our previous research efforts have identified the receptor EphA2 as a promising target for selective molecular treatment for GBM (301). Our research efforts have shown that exogenous soluble eA1 is a functional ligand for EphA2 (311) and progress has been made in creating ephrin-based therapeutic agents through conjugation of a bacterial toxin protein to soluble eA1 that selectively targets GBM cells (312). From this work developing an ephrin-based molecular targeted therapy, we noted a selective morphology change in GBM cells upon exposure to eA1. This physical response, characterized by a rounding of the cell and a shrinking of the cell cytoplasm (311, 313, 314), formed the basis of the currently presented investigation into a combinatorial treatment with IRE therapies.

In considering IRE, the physical attributes of a cell are important, as electroporation is dependent on both cell size and morphology. The effect of cell size on electroporation has been demonstrated for a variety of pulse widths ranging from a few microseconds (289) to hundreds of milliseconds (288). The steady-state scenario is valid for the understanding of electroporation phenomenon involved in typical IRE protocols used in the treatment of cancer. These protocols involve the application of around 90 pulses of 50-100 μs duration delivered through electrodes inserted into the tissue (187, 315). We have shown that by reducing the duration of the electric field pulses to be shorter than the charging time of the cell membrane, the field can penetrate the cell interior, and

the dependence of electroporation on cell size is reduced (256, 316). This shorter pulse technique, termed high-frequency IRE (H-FIRE), which uses trains of $\leq 2\mu s$ duration bipolar pulses, exposes inner organelles to large electric fields. H-FIRE acts on cells in a way that nuclear size becomes a more important predictor of cell death than cell size, with a lower electric field needed to kill cells with a higher nuclear to cytoplasm ratio (NCR) (316). However a major limitation remains the relatively small size of resulting lesions, and methods to extend the field-induced damage into the infiltrative niche are greatly needed in order to translate this specificity in the treatment of clinically relevant tumors.

Despite some efforts to predict the TMP of cells exposed to PEFs on the order of a few microseconds no mathematical models for cells of a high NCR have been developed (272, 317). In this study we look further into the impact of cell size and morphology on electroporation phenomenon at short pulse lengths, where the steady-state electroporation equation breaks down and frequency is known to play an important role in predicting induced TMP. Equipped with the finding that NCR is an important predictor of electroporation using H-FIRE pulse lengths, we investigated the NCR effect on H-FIRE ablation by combining H-FIRE therapy with a molecular intervention using eA1 to increase NCR.

The overabundance of EphA2 receptor and diminished presence of eA1 in GBM tissue open up this receptor ligand interaction as a unique method for selectively tuning cell morphology to isolate the NCR effect on H-FIRE. These biological cell manipulations allow us to discover electroporation behaviors in the pulse space where traditional analytical model predictions do not

apply. Additionally, this work highlights a novel correlation—an increase in electroporation efficacy due to decreasing cell size—thereby highlighting the complexities ignored by the Schwan equation in describing cell response to electric fields with short pulses.

5.2 Materials and methods

Cell culture

U-87 MG human glioblastoma cells (ATCC) were cultured in Dulbecco's Modified Eagle Medium (DMEM) containing 10% fetal bovine serum (FBS) and 1% penicillin/streptomycin (PS). Normal Human Astrocyte (NHA) cells (Lonza) were cultured in Astrocyte Growth Media (Lonza). U-251 MG human glioblastoma cells (ATCC) cells were grown in DMEM containing 10% FBS, 1% PS, and 0.1 mM non-essential amino acid. DBTRG human glioblastoma cells (ATCC) were culture in RPMI medium containing 10% FBS, 2 mM L-glutamine, 1% PS and 0.1 mM non-essential amino acids. All cells were grown in culture at 37 °C in 5% CO2 in a humidified incubator. Cells were seeded in hydrogels at a density of 1×10^6 cells/mL. The hydrogels were submerged in appropriate growth media for the cell type at 37 °C in 5% CO2 in a humidified incubator and cell viability was maintained within hydrogels for up to 7 days.

Construction of collagen scaffolds

Stocks of type I collagen were prepared by dissolving rat tail tendon in acetic acid, followed by freezing and lyophilization as described previously (140). Stock solution concentrations of collagen were created at a density of 10 mg/mL. Scaffolds with a final concentration of 5 mg/mL were made from concentrated collagen stocks to create collagen gels of 0.5% (w/w). Neutralized collagen solutions were created by mixing acid-dissolved collagen with 10X DMEM (10% of total

collagen solution volume) and sufficient volumes of 1N NaOH until a pH in the range of 7.0–7.4 was achieved. The neutralized collagen was mixed with cells suspended in DMEM or NHA media to achieve a cell density of 1×10^6 cells/mL in the final collagen mixture. Solutions were mixed carefully with a sterilized spatula to ensure homogenous distribution throughout the gel without damaging cells. Collagen solutions were then dispensed into a polydimethylsiloxane (PDMS) mold with a cut-out of 10 mm diameter and 1 mm depth and molded flat to ensure consistent scaffold geometry. Our previous mathematical modeling and experiments on oxygen (O_2) consumption rates by tumor cells(140) confirms that at this cell density and scaffold thickness, O_2 concentration is uniform throughout the scaffold depth. Collagen was allowed to polymerize at 37 °C and 5% CO_2 for 30 minutes.

Treatment with ephrinA1

Cells seeded in collagen hydrogels were cultured for 24 hours after seeding to allow for cells to engage the collagen and achieve a physiologically relevant morphology. After 24 hours, hydrogels in the ephrin A1 treated condition were cultured in serum-free cell culture media with 1µg/mL ephrin A1-FC (R&D Systems) added to the media for 12 hours prior to electroporation treatment or fixation for immunofluorescence staining. Control cells were cultured in hydrogels submerged in serum-free culture media without the added ephrin A1-FC for 12 hours prior to use in experiments. The 12-hour time point was chosen because a full morphological change of the cells within the hydrogels was seen by 12 hours and no further changes were observed at longer exposure times. The concentration of 1µg/mL ephrin A1 was chosen because it has been shown previously to induce a collapse of the cytoplasm. Experiments with 2 µg/mL ephrin A1 showed no further morphological change past that observed with 1µg/mL ephrin A1. No difference was

seen in viability between hydrogels cultured in ephrin A1-FC conditioned media and control media before exposure to electroporation therapy.

Fluorescent staining

U-87, U251, DBTRG, and NHA cells were individually seeded in hydrogels described previously. After culturing the cells for 24 hours for engagement with the matrix and then an addition 12 hours after treatment, the hydrogels were fixed using 4% formalin and blocked and permeabilized using 40 mg/mL bovine serum albumin (BSA) and 0.05% Triton-X. Cellular F-actin was stained with Alexa Flour 568 phalloidin (Life Technologies, Carlsbad, CA) while cell nuclei were stained with diaminophenylindole (DAPI; Sigma-Aldrich, St. Louis, MO). Cells were visualized using a Zeiss LSM880 (Carl Zeiss Microscopy LLC, Thornwood, NY) laser scanning confocal microscope.

Determination of NCR

Untreated hydrogels seeded at the same cell density and collagen conditions as treated hydrogels were fixed and fluorescently stained to determine overall cell area and nuclear area for cells in the control condition and in the ephA1 treated condition. Measurements were made on at least four cells per hydrogel and at least 5 hydrogels were analyzed for each condition so at least 20 cells were used to determine average NCR for each cell type in each condition. Image analysis was done in Image J (NIH, Bethesda, MD. Z-stack images were converted into 2D projection images and cell measurements were made from these projections. NCR was calculated from the measured cell area (A_C) and nuclear area (A_N) as follows:

$$NCR = \frac{A_N}{A_C - A_N} \quad (5.1)$$

Finite element analysis in hydrogels

Finite element models using COMSOL Multiphysics (Version 4.3, COMSOL Inc., Palo Alto, CA) were used to solve the Laplace equation to find the electric field distribution within the hydrogels for each different voltage used. The electric field distribution within the hydrogel was found by solving the Laplace Equation:

$$\nabla^2 \phi = 0 \quad (5.2)$$

where ϕ is the electrical potential. The boundaries of one electrode were set to the applied voltage ($\phi = V_{applied}$) and the boundaries of the second were set to ground ($\phi = 0$) while the initial voltage (V_0) for all subdomains were set to 0V. All other external boundaries were set to electrical insulation ($-\boldsymbol{n} \cdot \boldsymbol{J} = 0$). The mesh was refined until error between successive refinements was less than 1%. The final mesh contained 47,438 elements and solutions were found in approximately 3 minutes on a Pentium i3 processor.

Finite element analysis of individual cells based on NCR

The electrodynamic solutions of interest were reached by modeling a spherical cell membrane and nuclear envelope and solving a finite element model with an impedance boundary condition scheme as previously described (271, 316). The models used in to investigate the membrane response to different pulse parameters changed its NCR based on representative cell geometries determined based on average measurements made in ImageJ image analysis software (NIH, Bethesda, MD) from confocal microscopy images. In order to better understand the effect of high frequency components of H-FIRE on individual cells a frequency-dependent module was used to mimic the increase in frequency for different H-FIRE pulse lengths and IRE-type pulses. The geometry and physical properties of the cell can be found in Table 5.1.

Simulations were solved in the frequency-domain using an electric currents module, which has been previously shown to correlate well for spherical cells exposed to rectangular pulses in the order of 1-2μs (272). To account for the impedance posed by the membranes of the cell and nucleus their boundaries were assigned impedance properties found in literature (Table 5.1).

Table 5.1 Physical properties used in single cell analysis for H-FIRE + eA1 treatment. * measured values, ‡ approximation based on water composition

Parameter	Symbol	Value	Units	Reference
Media Conductivity	σ_m	0.98	[S/m]	*
Media Permittivity	ε_m	$80\varepsilon_0$	[F/m]	‡
Cytoplasm Conductivity	σ_{cyt}	0.3	[S/m]	(279)
Cytoplasm Permittivity	ε_{cyt}	$154.4\varepsilon_0$	[F/m]	(280)
Nucleoplasm Conductivity	σ_{nuc}	1.35	[S/m]	(279)
Nucleoplasm Permittivity	ε_{nuc}	$52\varepsilon_0$	[F/m]	(279)
Cell Membrane Thickness	t_{mem}	$5x10^{-9}$	[m]	(281)
Nuclear Membrane Thickness	t_{Nmem}	$40x10^{-9}$	[m]	(279)
Cell Membrane Conductivity	σ_{mem}	$3x10^{-7}$	[S/m]	(282)
Cell Membrane Permittivity	ε_{mem}	$8.57\varepsilon_0$	[F/m]	(283)
Nuclear Membrane Conductivity	σ_{Nmem}	$6x10^{-3}$	[S/m]	(279)
Nuclear Membrane Permittivity	ε_{Nmem}	$28\varepsilon_0$	[F/m]	(279)
Domain Side Length	L_d	$300x10^{-6}$	[m]	-
Benign Cell Radius	R_c	$20x10^{-6}$	[m]	*
Benign Nuclear Radius	R_n	$6.2x10^{-6}$	[m]	*
Malignant Cell Radius	R_{mc}	$20x10^{-6}$	[m]	*
Malignant Nuclear Radius	R_{mn}	$14.7x10^{-6}$	[m]	*
Malignant Cell Radius (post-ephrin)	R_{mce}	$16.7x10^{-6}$	[m]	*
Malignant Nuclear Radius (post-ephrin)	R_{mne}	$14.7x10^{-6}$	[m]	*

While some equations such as the one presented by Huang *et al* have been useful for calculating the TMP for cells exposed to an AC signal, further development of the model needs to be done (318). Our group developed an equivalent circuit model considering the general dimensions, conductivity, and permittivity of the cell membrane, cytoplasm, nucleic envelope, and nucleus.

While the equation describing this model can be further refined it provides evidence that changes to the NCR mostly affect the capacitive component representing the cytoplasm.

5.3 Results

5.3.1 EphA2 activation by eA1 induces a targeted morphology change in malignant cells

To investigate the dynamics of eA1 induced morphology changes, we cultured malignant GBM and normal brain cells in 3D hydrogels and exposed them to eA1. EphA2 activation by eA1 in malignant cell lines (U-87 MG, U-251 MG, and DBTRG) led to visible cell morphology changes characterized by cell rounding and a collapse of the cytoplasm (Figure 5.1a). Cell rounding was visible after 6 hours of culture in media containing eA1 (1 μg/mL) with the full morphological change accomplished by 12 hours (Figure 5.2). In normal human astrocyte (NHA) cells, no morphological change was observed at any time point out to 48 hours when culturing hydrogels in eA1 media. For the malignant cell lines, the cytoplasm collapse upon EphA2 activation resulted in a significant change in the NCR of the cells (Figure 5.1b). NHA cells showed no significant change in NCR under these treatment conditions. No morphology change was observed in control tumor cells cultured in media without eA1 present.

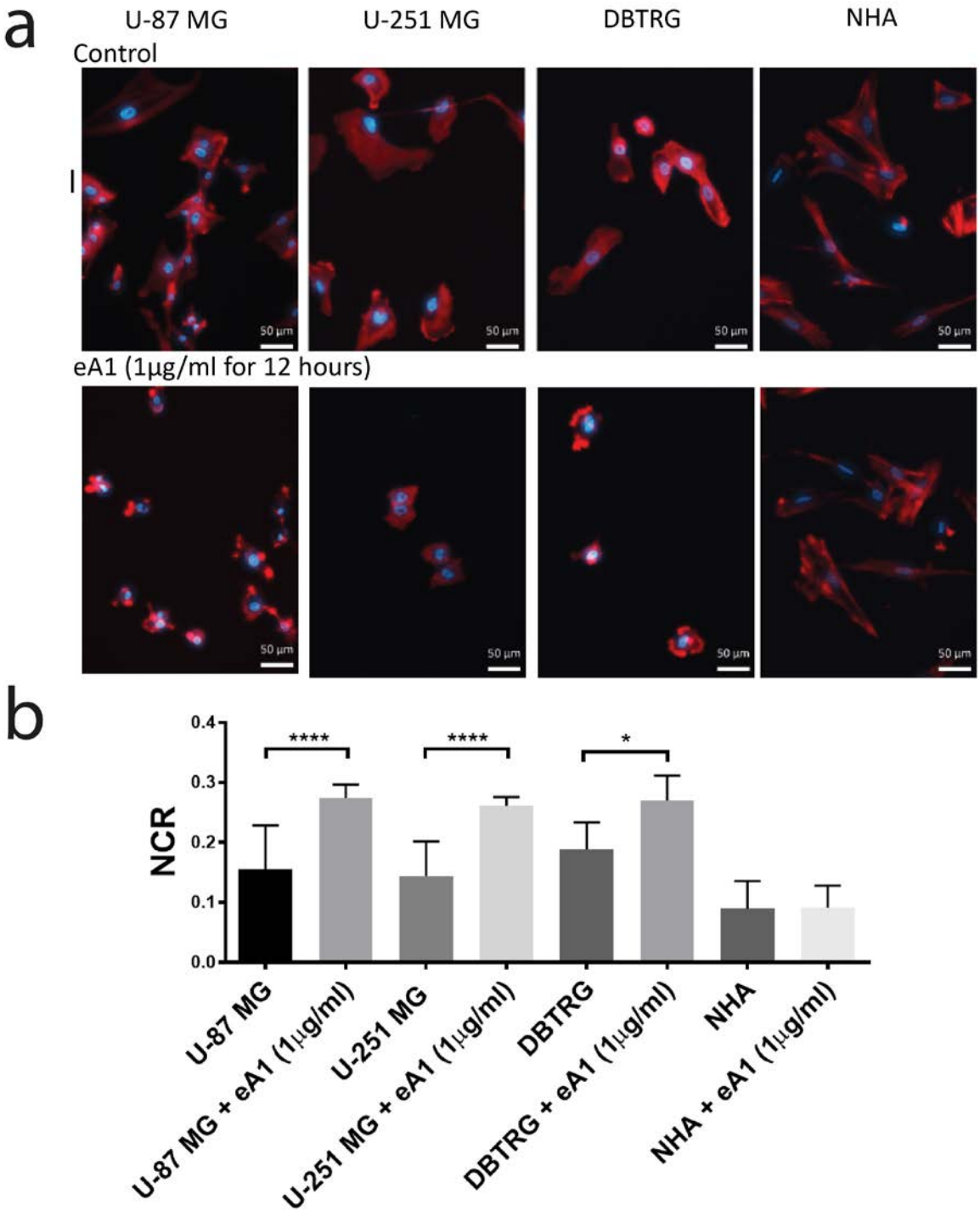

Figure 5.1. Treatment with soluble ephrin A1 causes glioma morphology change, while not altering NCR for astrocytes. (a) *Malignant cells stain with DAPI (blue) and phalloidin (red) cultured in media with 1µg/mL eA1 for 12 hours exhibit cell rounding and a collapse of the cytoplasm around the nucleus while healthy cell morphology remains unchanged upon exposure to eA1. Scale bar 50µm* ***(b)*** *eA1 induced morphology change results in a quantitative increase in NCR for malignant cells while NCR remains unchanged for normal astrocytes.(n=20) ****$p \leq 0.0001$, *$p=0.027$*

The longer-term dynamics of eA1 activation and morphology change were studied by observing cells cultured with 1 µg/mL eA1 over a time course of 14 days. After the initial 12 hours, no additional morphology changes were observed up to an additional 12 hours of culture with 1 µg/mL eA1. We replaced eA1 media with basal media after 24 hours and cultured cells out to 14 days in basal media to determine the reversibility of the morphology change. Cells activated by eA1 did not return to their original morphology after 14 days of culture in basal media. A visual comparison on images, presents evidence that cells remained viable but with a reduced proliferation rate after activated with eA1 for 24 hours and cultured in basal media out to 14 days compared to control cultures (Figure 5.2). After activation with eA1 cells have reduced actin as seen by the diminished phalloidin stain.

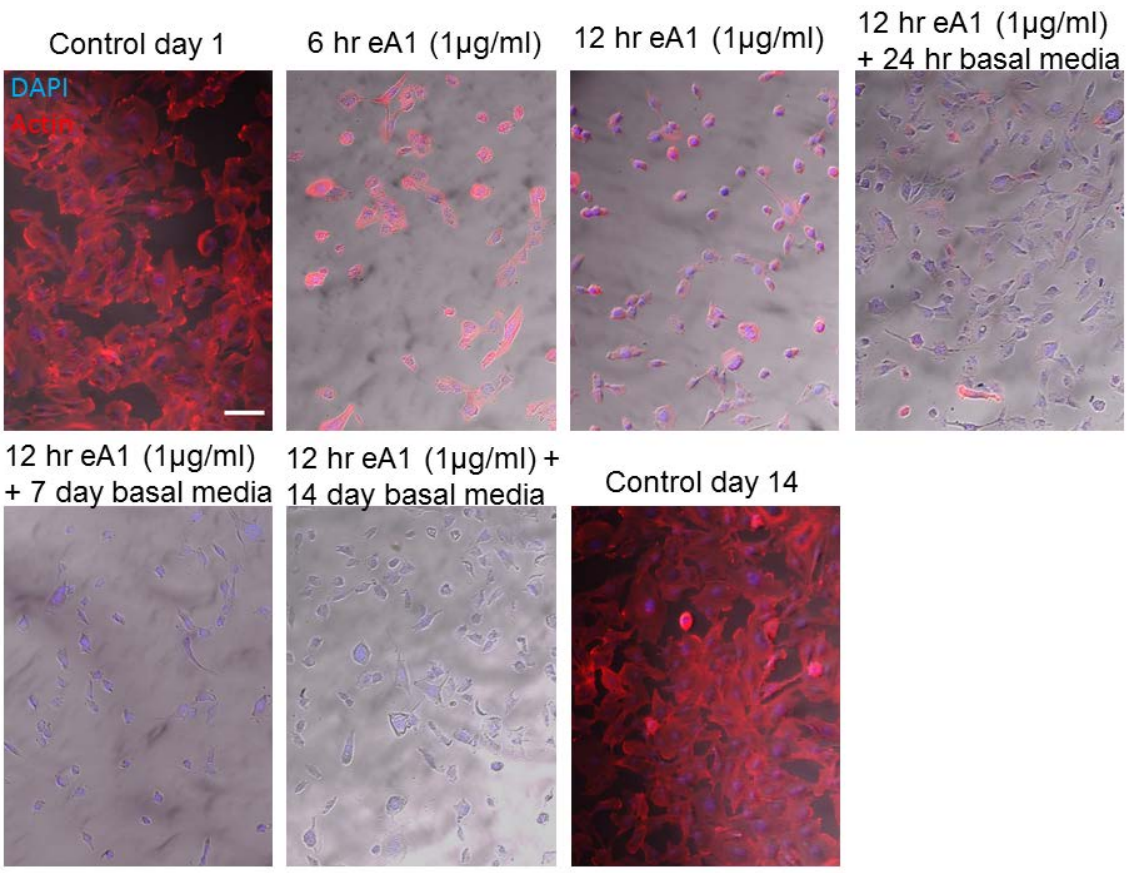

Figure 5.2. Time course of U-251 cells cultured with eA1 (1 µg/mL) which is removed after induced morphology change. *U-251 cells stain with DAPI (blue) and phalloidin (red) undergo a full morphology change after 12 hours in culture with 1 µg/mL eA1. Upon removal of eA1 media and replacement with normal culture media, U-251 cells do not return to normal morphology after 14 days in culture. Cells remain viable with reduced proliferation rates and reduced actin compared to cells cultured only with normal culture media. Scale bar 100 µm.*

5.3.2 Extent of electroporation for different cell morphologies is dependent on frequency of electric field

Finite element modeling was used to predict the induced TMP on a variety of cell morphologies as a function of the frequency of a steady-state, AC electric field. Characteristic morphologies determined from experimental culture of glioma cells, normal astrocytes, and glioma cells treated with eA1 were used. At lower frequencies, characteristic of IRE pulse waveforms, larger cells experience a greater induced transmembrane potential compared with a glioma cell that shrinks in volume due to treatment with eA1. At a frequency of approximately 10 kHz, the enlarged nucleus

of the glioma cell causes it to experience a greater transmembrane potential than the astrocyte of the same size but smaller nucleus. This trend continued throughout higher frequencies of electric field, suggesting that fields of frequency higher than 10 kHz can be used to accomplish greater electroporation on cells with a larger nucleus than in cells with a smaller nucleus. At an electric field frequency of approximately 100 kHz the smaller cell experiences a larger induced transmembrane potential than the larger cells, suggesting a greater extent of electroporation of smaller cells than larger cells.

As the duration of the applied pulse is decreased, a greater proportion of the power is concentrated in higher frequency signal content. The experimental pulse train of 1 μs bipolar pulses with a 5 μs delay between pulses (Figure 5.3a), delivers the majority of its power between 100 kHz and 1000 kHz (Figure 5.3b). Interestingly, these frequencies correspond to the frequencies predicted to allow for a cross-over in TMP for the eA1-induced cell morphologies when exposed to an AC signal (Figure 5.3c).

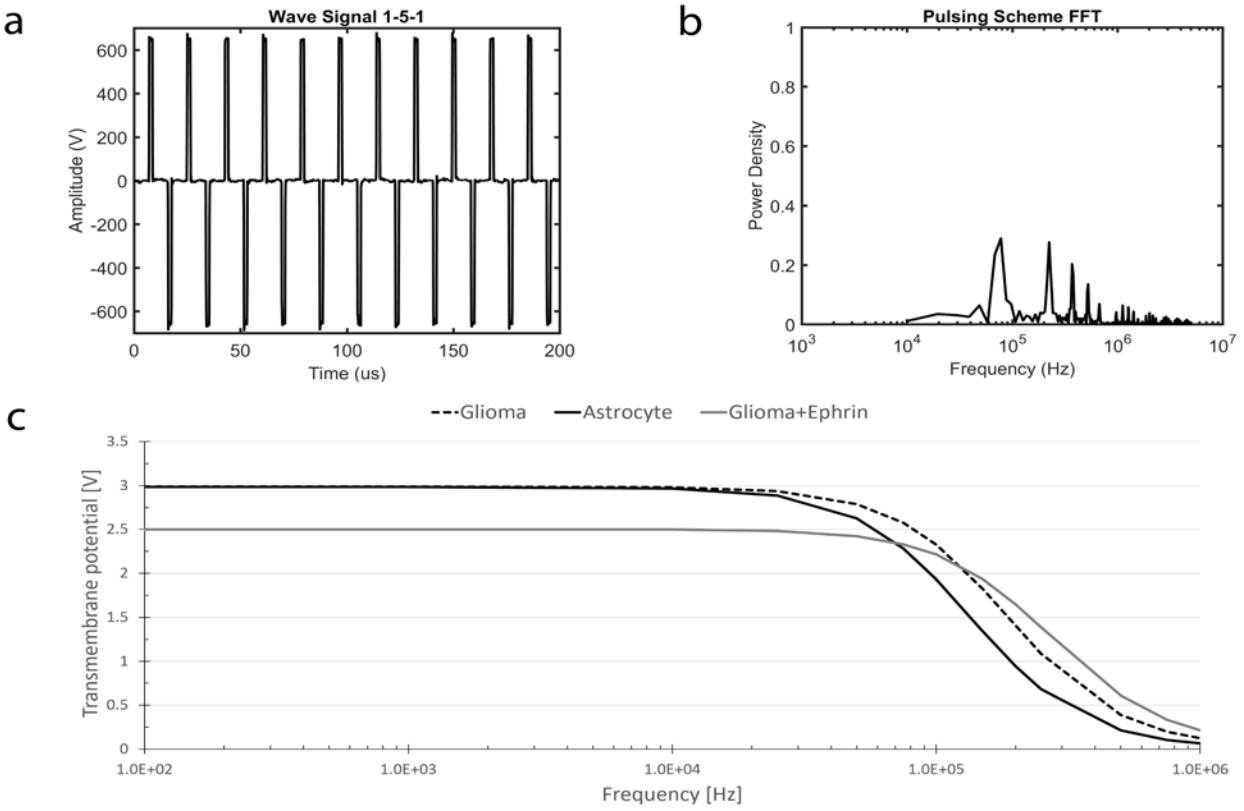

Figure 5.3. a) Experimental pulse waveform applied to hydrogels*. A bipolar waveform of 1 us pulses separated by a 5 us delay was used to accomplish electroporation in hydrogel platform* ***b) Power spectrum analysis of experimental pulse train.*** *Amplitude frequency distribution found by Fast Fourier Transform of experimental pulse trains shows that the pulse train of 1us bipolar pulses separated by a 5us delay delivers the majority of its power in the frequencies around 100 kHz.* ***c) Single cell steady-state response to electric field of 1000V/cm applied as AC signal****. As expected, larger cells (U87 and Astrocyte) present larger TMP's at lower frequencies. However, cells of higher NCR will have larger TMP's at higher frequencies (>100kHz).*

5.3.3 Morphology change impacts lethal thresholds for electroporation of malignant cells

To determine if the increase in NCR in malignant cells led to a change in H-FIRE threshold as predicted by finite element modeling, eA1 treated hydrogels were exposed to a regimen of H-FIRE treatment and compared with control hydrogels. Malignant hydrogels treated with eA1 had significantly larger lesions than control hydrogels while non-malignant hydrogels had no significant difference between conditions (Figure 5.4a). The increase in NCR for malignant cells corresponded to a smaller lethal threshold for H-FIRE while the lethal threshold did not change

for non-malignant cells (Figure 5.4b). For U87 cells, under normal conditions the lethal threshold is 603 ± 65 V/cm (n=8) while treated with eA1 the lethal threshold is 446 ± 55 V/cm (n=8). For U-251 cells, under normal conditions the lethal threshold is 662 ± 57 V/cm (n=8) while treated with eA1 the lethal threshold is 415 ± 48 V/cm (n=8). For DBTRG cells, under normal conditions the lethal threshold is 712 ± 68 V/cm (n=6) while treated with eA1 the lethal threshold is 532 ± 48 V/cm (n=6). Lethal thresholds for non-malignant cell types remained unchanged. Control NHA cells are killed at a threshold of 1028 ± 47 V/cm (n=6) and eA1 treated NHA cells have a lethal threshold of 1032 ± 82 V/cm (n=6). For the most responsive cell type, U-251 cells, eA1 treatment resulted in a 37% decrease in lethal threshold for H-FIRE therapy.

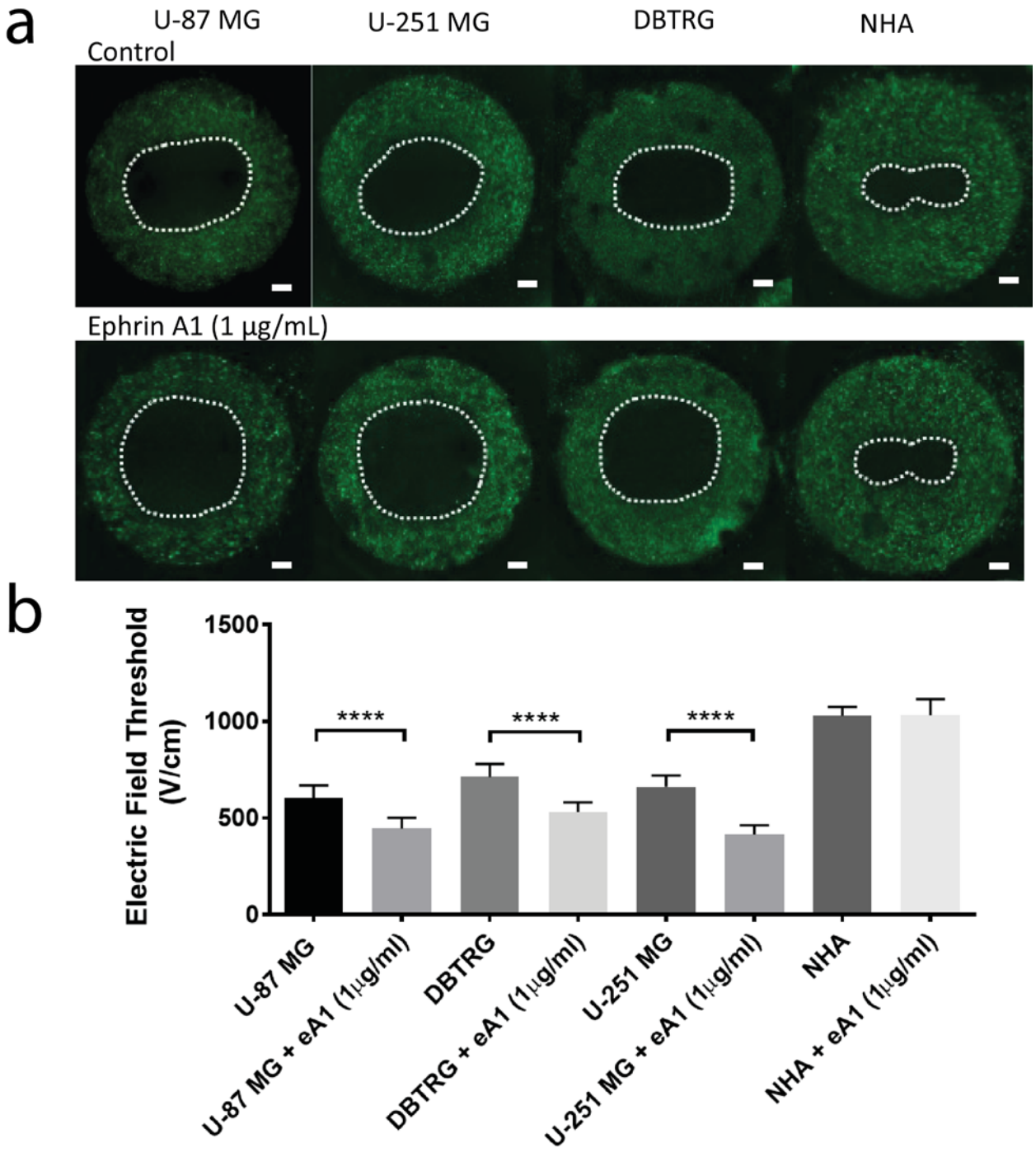

Figure 5.4. NCR change induced by ephrinA1 enhances H-FIRE lesions in malignant cells. (a) *H-FIRE lesion size for malignant glioma cells (U-87, U-251, and DBTRG) is increased from control when hydrogels are cultured with eA1 ligand. H-FIRE lesions in non-malignant astrocytes (NHA) remain unchanged with eA1 exposure. Scale bar 1 mm* ***(b)*** *COMSOL modeling relating lesion size to lethal thresholds shows a significant decrease in H-FIRE lethal threshold for malignant cells when treated with eA1 prior to electroporation exposure. H-FIRE lethal threshold for non-malignant cells remains unchanged with eA1 exposure.*

The correlation between NCR and lethal electric field threshold is summarized in Figure 5.5. Healthy cells are unaffected by eA1 in terms of an NCR change so the lethal threshold remains the same for healthy cells treated with eA1 and H-FIRE and those treated with only H-FIRE. Malignant cells have an inherent larger NCR than healthy cells which corresponds to a lower lethal electric field threshold when treated with H-FIRE. This difference in NCR between healthy and malignant cells is increased even more when cells are treated with eA1 before H-FIRE. Malignant cells treated with H-FIRE + eA1 have a larger NCR than cells not treated with eA1 and therefore have a lower electric threshold for cell death.

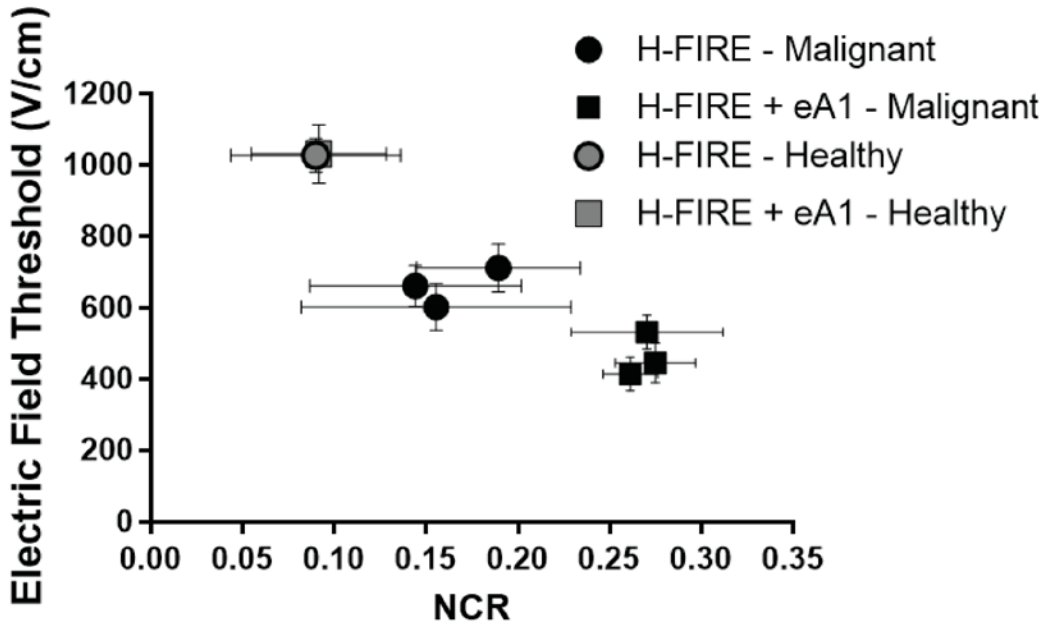

Figure 5.5. Lethal threshold is correlated with NCR. *Summary of data shows a correlation between average NCR of a given cell type in the hydrogel and the lethal electric field threshold for that cell type in the hydrogel. Healthy astrocytes (gray markers) show no change with eA1 treatment while malignant cells (black markers) show a decreased lethal electric field threshold when treated with eA1 to induce an NCR increase. ****$p \leq 0.0001$*

Similarly, eA1 treated hydrogels were exposed to traditional IRE pulses of 100 µs pulse width to determine if these lesions would change as a result of the eA1-induced morphology change in

treated cells. In contrast to the trend seen using H-FIRE pulses, IRE lesions of eA1-treated U-251 cells are significantly smaller than control hydrogels of U-251 cells cultured in normal media (Figure 5.6). U-251 cells cultured in normal media within the hydrogels had an IRE lethal threshold of 517 ± 45 V/cm (n=6). U-251 cells cultured with media containing 1 µg/mL eA1 within the hydrogels had an IRE lethal threshold of 684 ± 44 V/cm (n=6).

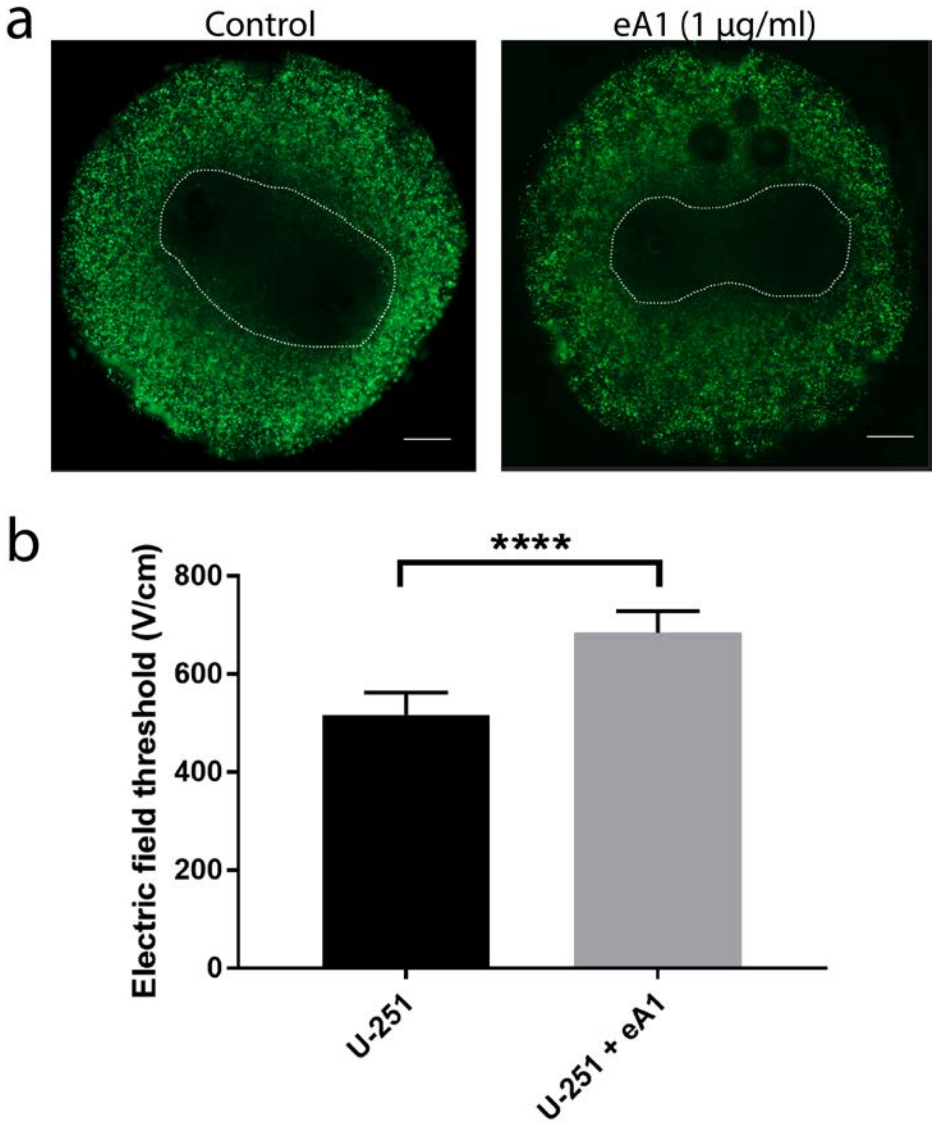

Figure 5.6. NCR change induced by ephrinA1 results in smaller IRE lesions. (a) *IRE lesion size for U-251 glioma cells is smaller compared to the control when hydrogels are cultured with eA1 ligand. Scale bars 1 mm.* ***(b)*** *COMSOL modeling relating lesion size to lethal thresholds shows a significant increase in IRE lethal threshold for U-251 cells when treated with eA1 prior to electroporation exposure.(n=6) ****$p \leq 0.0001$*

5.3.4 eA1 treatment enhances malignant cell selectivity of H-FIRE

To demonstrate the enhanced selectivity of malignant cells possible with combination H-FIRE and eA1 treatment, we performed co-culture experiments. Hydrogels of NHAs and U-87 GBM cells were cultured in media containing eA1 and then exposed to a regime of H-FIRE pulses. While selective killing of U87 cells and not NHA cells is achieved in the control condition, the region of U87 killing is significantly enlarged while the NHA lesion remains the same for cells exposed to eA1 (Figure 5.7).

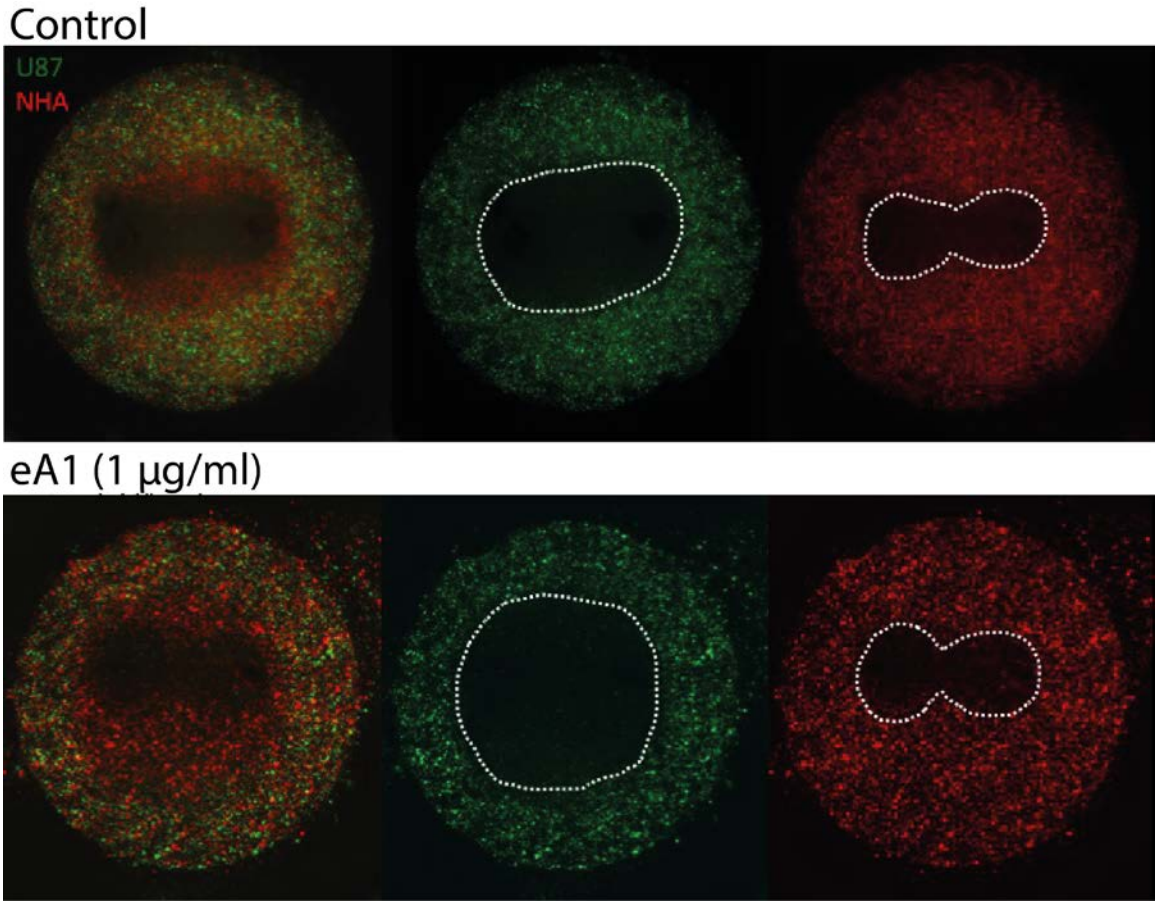

Figure 5.7. Treatment with eA1 enhances selectivity of H-FIRE for malignant cells in co-culture. *The area of ablated malignant cells and live healthy cells in extended by treating co-culture hydrogels with eA1 prior to H-FIRE exposure. Scale bars 1 mm.*

5.3.5 eA1 at nonlethal doses is effective at enhancing H-FIRE

To determine if the enhancement seen with the use of eA1 was due entirely to its synergistic action with H-FIRE or if the eA1 was having an effect on viability on its own we cultured hydrogels in basal media and eA1 media for 14 days without exposing them to H-FIRE therapy. eA1 treated gels were submerged in eA1 media for 12 hours as done in the H-FIRE experiments. Media was removed and replaced with basal culture media after 12 hours and the hydrogels were cultured out to 14 days. A comparison of live/dead stain between eA1 treated hydrogels and control hydrogels cultured only in basal media shows no difference in overall cell viability (Figure 5.8). Therefore, it can be concluded that the concentration of eA1 used to induce the morphology change (1 µg/mL) is not lethal for these cells at the timescales they are exposed to treatment. This will be important in designing treatments *in vivo*. If non-lethal concentrations can be used, then the control of diffusion of the ligand need not be strict for the safety of the healthy tissues. Rather a large area surrounding the tumor can safely be exposed to eA1 pre-treatment while still accomplishing the necessary morphology change in malignant cells to lower the required electric field threshold for cell ablation.

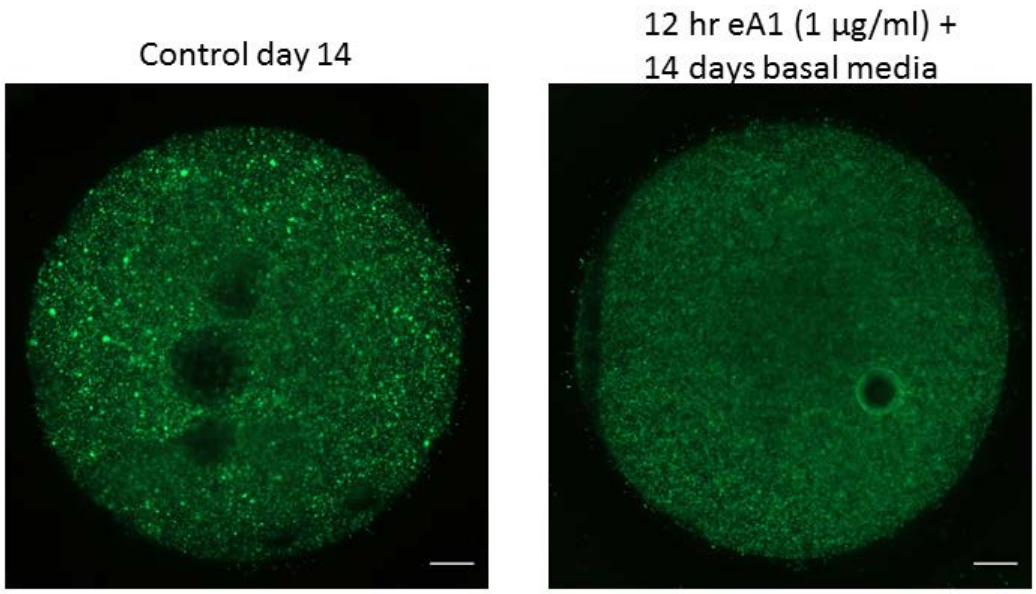

Figure 5.8. Live dead staining of cells cultured with eA1 in hydrogels. *Cells were cultured in collagen hydrogels with 1 µg/mL eA1 media for 12 hrs which was then replaced with basal media and cells were cultured out to 14 days. Calcien AM staining of the live cells (green) and ethD-III staining of dead cells (red) shows no visible cell death for eA1 treatment. Scale bar 1 mm.*

5.3.6 Predicted clinical effects of eA1

A canine patient brain was used as a theoretical model for testing the effect of combination H-FIRE and eA1 therapy on clinical electroporation regimes (Figure 5.9a). Finite element modeling was used to determine the electric field distribution in the canine patient's brain upon receiving electroporation therapy. Using experimental thresholds for cell death for healthy cells and malignant cells for each treatment regime (IRE, H-FIRE, or H-FIRE + eA1) we were able to map out which areas of the brain experienced cell death due to the treatment. Distinguishing healthy cell death from tumor cell death by the segmentation of the tumor in the MRI, we can determine what percentage of the tumor would be ablated and what percentage of the healthy brain would be ablated with a given electroporation regime. The extent of ablation for tumorous and healthy tissue for IRE, H-FIRE, and H-FIRE and eA1 combination therapy are plotted in Figure 5.9b. As applied

voltage increases, the volume of tumor treated increases but so do damage to healthy cells. H-FIRE treatment causes significantly less healthy brain damage than IRE due to the ability to ablate malignant cells at a lower threshold than healthy brain cells. Combining H-FIRE treatment with eA1 allows for a greater extent of tumor ablation without increasing healthy tissue damage due to the decrease in lethal threshold for eA1 treated malignant cells.

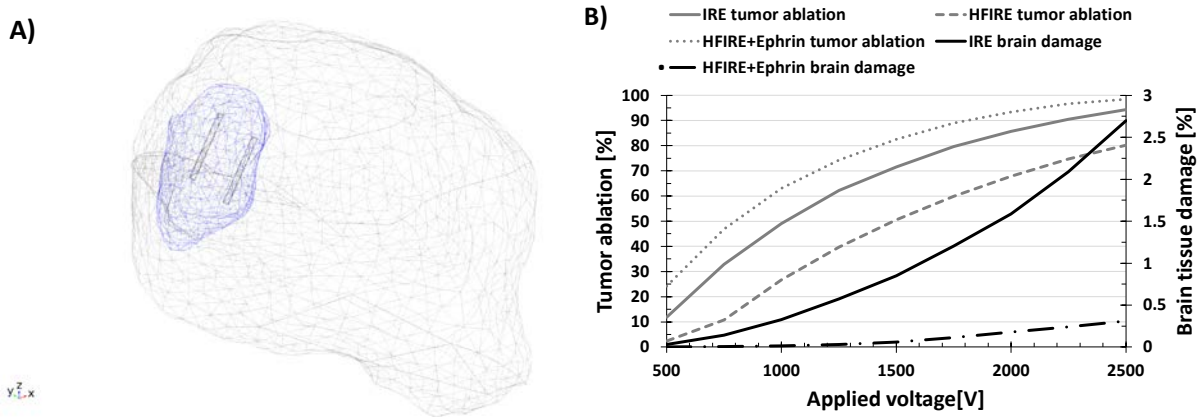

Figure 5.9. Treatment planning comparison across proposed therapies. a) *Canine patient anatomy consisting of brain (V = 64.56cm^3), tumor (V = 2.32 cm^3), and electrodes in gray, blue, and black meshes, respectively.* ***b)*** *Expected therapeutic impact of IRE, H-FIRE, and H-FIRE+eA1 at different applied voltages for patient in* ***a)****. Best coverage with least damage to healthy tissue is achieved through combinatorial H-FIRE and eA1 therapy.*

5.3.7 Analytical cell circuit model

The TMP response of the cell follows the form of a low pass filter where the effect on TMP decreases as frequency is increased due to the electric field passing through the cell membrane at high frequencies. The gain for a low pass filter takes the general form of

$$g = \frac{V_{out}}{V_{in}} = \frac{1}{\sqrt{1+(\omega * R * C)^2}} \quad (5.4)$$

A modified low pass filter equation can be used to illustrate the important variables in predicting response to different frequencies. Each component of the cell—cell membrane, cytoplasm, and nuclear membrane—has a characteristic impedance that affects the TMP response of the cell to

varying degrees depending on the cell morphology. As the cell shrinks the cytoplasm can be modeled as a third membrane, having a resistance and capacitance. As the capacitance of each section of the cell is dependent on the surface area, the change in morphology induced by eA1 treatment will produce changes in cell capacitance, which shifts the curve of the low pass filter plot. The equivalent circuit model of a cell can contain capacitive and resistive components for the cell membrane, cytoplasm, and nucleus. We derived an equation in order to calculate the transmembrane potential of the cell when exposed to AC fields at different frequencies. Equations 5.5-5.8 relate the induced TMP on a cell to the resistances of the cell, nucleus and cytoplasm (R_m, R_n, and R_{cyt} respectively) and the capacitances of the cell, nucleus and cytoplasm (C_c, C_n, and C_{cyt} respectively). Each component of the cell is modeled as a capacitor and a resistor in parallel (Figure 5.10a).

$$TMP = 1.5 * r * E * \cos(\theta) * g \quad (5.5)$$

where g is the gain across the cell membrane, a function of the impedance of the cellular components, defined as

$$g = \frac{Z_m}{Z_m + Z_{cyt} + Z_n} \quad (5.6)$$

Where Z is the impedance of a component calculated as

$$Z_{(a=m,cyt,n)} = \frac{R_a * X_a}{\sqrt{R_a^2 + X_a^2}} \quad (5.7)$$

Impedance of each component a is a function of the resistance of the component (R_a) and the reactance of each component (X_a) defined as

$$X_a = \frac{1}{\omega * C_a} \quad (5.8)$$

The equation presented in this study, while subject to further refinement, predicts that changes to the NCR result in higher order changes in the overall capacitance of the cell. This can be explained by the dependence of capacitance to surface area, which in turn is dependent on a cell's NCR. Also predicted by FEA at higher frequencies, the equation shows that the TMP of a smaller cell can exceed that of a larger cell if the NCR of the smaller cell is larger than that of the large cell (Figure 5.10b), which has been not previously described in electroporation theory.

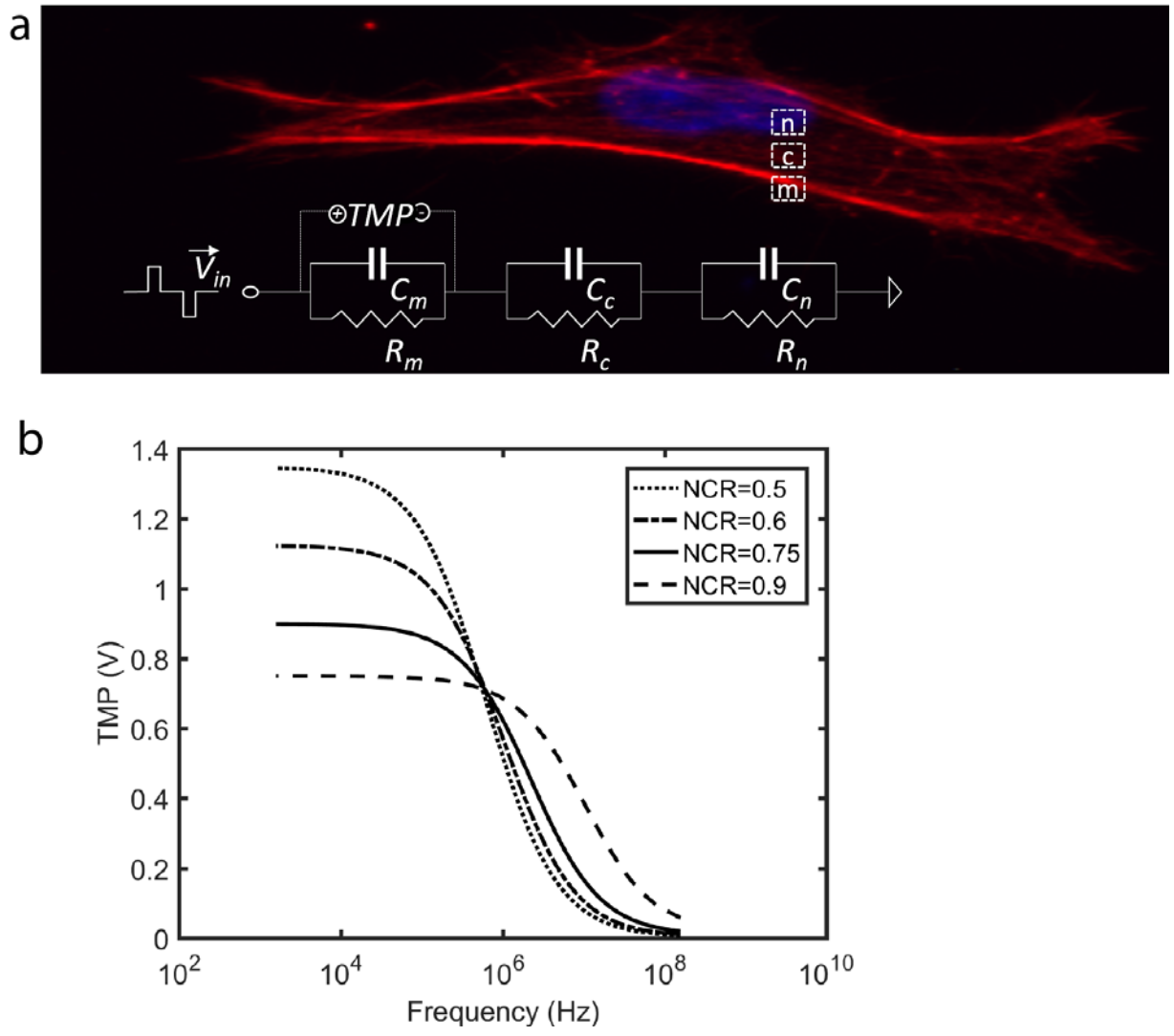

Figure 5.10. Cell circuit model predictions. (a) *Cell circuit model with 3 components including cell membrane, cytoplasm, and nuclear membrane.* ***(b)*** *Three shell model of a cell as a low pass filter predicts pulse frequency affects relationship between TMP and cell NCR. Cell NCR changes reflect a varied cell size of a cell with a constant nuclear size.*

5.4 Discussion

The steady-state Schwan equation describing TMP change in an external field (eq 3.17) is valid for the understanding of electroporation phenomenon involved in typical IRE protocols used in the treatment of cancer. These protocols involve the application of around 90 pulses of 50-100 μs duration delivered through electrodes inserted into the tissue (187, 315). As seen from equation 3.17, the cell shape and cell radius are important predictors of the induced transmembrane potential. The effect of cell size on electroporation, as predicted by equation 3.17, has been demonstrated for a variety of pulse widths ranging from a few microseconds (289) to hundreds of milliseconds (288). This variance of extent of electroporation with cell size can cause uncertainty in planning the application of treatment pulses. Cell size and morphology have been shown to vary depending on many factors including the stage in the cell growth cycle (319) and active process such as invasion (93). In cancer especially, many of these processes are dysregulated resulting in a large variance in cell size and morphology, which could cause uncertainty and discrepancies between IRE treatment planning and actual tumor coverage. This remains a major limitation to traditional IRE protocols for ablation of highly heterogeneous or infiltrative tumor tissues.

We have demonstrated that the cell size dependence for electroporation-induced cell death depends critically on frequency range. Each component of the cell—membrane, cytoplasm, and nuclear membrane—has a characteristic impedance that affects the TMP response to varying degrees depending on the cell morphology. As the capacitance of each part of the cell is dependent on the surface area, the change in morphology induced by eA1 treatment will produce changes in cell capacitance, which shifts the TMP curve of our analytical model. Using a simplified three

component circuit model of the cell, we predict a pulse frequency region that can achieve greater electroporation for smaller cells (Figure 5.10).

We hypothesize that the effect demonstrated here of high frequency pulses preferentially ablating cells of smaller volume but higher NCR may be due to changes in impedance of the cytoplasm. For AC fields, a frequency-dependent model takes into account the capacitance of the cell membrane in determining TMP. If part of the external field is able to bypass the cell membrane and interact with internal components of the cell, the impedance of the cytoplasm and nucleus become important factors. This effect will be magnified as the volume of the cytoplasm is decreased, which can be exploited through treatment with eA1. Therefore, for high frequency pulses, the NCR of a cell becomes a significant variable in predicting electroporation response. This finding is significant for the understanding of electroporation theory because it clearly illustrates that the relationship between cell size and electroporation is closely dependent on waveform frequency, which would impact electroporation protocols both for research as well as therapeutic applications.

As the association between cell morphology change and response to electric fields cannot be directly investigated *in vivo* due to the many confounding variables, three dimensional tissue engineered models become an invaluable resource in this study. Within hydrogels, cells take on a physiologically relevant three-dimensional morphology, not possible with two-dimensional experiments. The hydrogel experimental platform allows for tuning of the tissue microenvironment while allowing for real time observation of morphology change upon ephrinA1

treatment. In addition, hydrogels have been established as a relevant platform for testing of pulsed electric field therapies(225).

We have shown for the first time that molecular targeting with ensuing changes in GBM cell morphology may be used to enhance the selectivity of PEFs to induce tumor cell death. Selectivity, regulated by NCR, opens up the possibility of enhanced targeted cancer therapy, as malignant cells are known to often have increased NCR compared to normal cells (273, 274). Because the EphA2 receptor is overexpressed specifically on malignant cells in adulthood, the induced morphology change can be exploited in developing combinatorial targeted therapies using H-FIRE. The ability to selectively target cells with increased NCR is significant for the future of GBM treatment because it may allow for the treatment of diffuse malignant cells that have invaded into normal brain tissue. Invasive cells should be particularly susceptible to this combinatorial therapy because of their consistent over-expression of the EphA2 receptor in a variety of cancers (320-323). Binding of eA1 decreases invasion (301, 309), suggesting that highly invasive cells exist in an environment of low eA1 with an abundance of unbound EphA2 receptors, making them especially susceptible to effects induced by local delivery of soluble ephrinA1. By lowering the lethal threshold for malignant cells in the outermost regions of the tumor where selectivity is most important, eA1 treatment can increase the margin of tumor that can safely be ablated with H-FIRE therapy regimes.

We have shown that the morphology change induced by treatment with eA1 remains after removal of eA1 (Figure 5.2). This morphology change that sensitizes cells to H-FIRE damage will therefore be amenable to clinical application as the timing between eA1 activation and H-FIRE treatment

does not need to be precise. The long-term implications of eA1 exposure have been relatively unexplored and our initial investigations suggest cells exposed to this molecular treatment exhibit sustained effects that should be investigated in the future.

The failure of molecular targeting therapeutics is often attributed to the heterogeneous expression of receptors both within a single tumor and across different tumors. Heterogeneous expression of EphA2 has indeed been seen in resected human glioma tissues (308). However, because the EphA2 targeting used in this combination therapy is used for enhancement, even cells that do not overexpress the receptor will be susceptible to H-FIRE targeting. Because the two therapies work on different mechanisms, the resistant populations to each therapy should not overlap. Though many attempts have been made to use EphA2 as a direct therapeutic target (312, 324), this work is the first to our knowledge that utilizes a resulting morphological change to enhance targeting by combination with a physical therapy in the form of PEFs. We furthermore note that high frequency (~100 kHz) pulses in particular are necessary to induce this synergistic tumor cell death response, as we have demonstrated that lower frequency IRE pulses of the sort most commonly used for clinical tumor ablation (186, 187) become less effective in combination with sub-lethal eA1 treatment in our studies.

The EphA2 receptor has been identified as overexpressed in various cancers (299, 300, 325-327) in addition to GBM, suggesting the broader application of our results for treatments in other tumor sites for which more traditional surgical or radiotherapy options may be limited, for example tumors that surround sensitive nerve or vascular structures. Areas of increased EphA2 expression are important therapy targets as elevated EphA2 expression has been correlated with higher

pathological grade (306) and poor prognosis (307, 328). EphA2 is an important target for this synergistic therapy for another important reason, specifically that it may allow for the targeting of highly tumorigenic glioma stem cells (GSCs), which ECT combinatorial treatments may leave behind due to their highly chemo-resistant nature (329). EphA2 receptors have been found to be expressed most highly on tumor initiating cells with the highest levels of expression in the most aggressive, stem cell-like mesenchymal subtype (330). Though the EphA2/ephrinA1 interaction has been the subject of our study, multi-ligand cocktails can also be explored to capitalize on the other ephrin interactions in cancer.

The findings presented here highlight the importance of considering the physical phenotypes of cells both for treatment planning and for exploitation to improve treatment efficacy. The classical understanding of electroporation simplifies the relationship between TMP and cell shape and size. However, we have shown that the relationship is more complex, and the vast pulse frequency parameter space should be further explored to identify novel therapeutic synergies of the sort that we have demonstrated here. Taking into account the complex relationship between these variables may open up the possibility for significantly improved cancer therapies by targeting the physical hallmarks of tumor cells with next generation combinatorial therapies. Though our findings are presented here in the context of tumor ablation, the importance of considering cellular biophysics extends to other applications of electroporation as well. Applications such as genetic engineering may benefit from manipulating cellular biophysics to more effectively deliver intracellular cargo both in therapy applications but also as a practice in basic research.

Chapter 6 Towards Optimizing Pulse Parameters for Selectivity

6.1 Introduction

Malignant gliomas and other such aggressive tumors present a challenging problem from a therapeutic perspective with limited treatment options due to their infiltrative nature. In the case of GBM, cells possess a myriad of resistance mechanism that allow them to escape radiation and chemotherapy. Surgery is limited to the bulk tumor volume as removal of tissue outside of the tumor boundary is especially deleterious in the brain. Therefore the invasive front of the GBM tumor, which can extend cm into the healthy brain tissue, represents an important target for next-generation GBM treatments. In order to target cells at the margin of the tumor and beyond, a selective therapy for malignant cells must be developed. We have previously shown that H-FIRE therapy exhibits an inherent selectivity for malignant cells due to their increased NCR compared to healthy cells. Though this selectivity is important, the margin of safe treatment achieved by selectively killing malignant cells with H-FIRE when applied to a clinical tumor is likely to be only a few mm. However other aspects of the pulse parameters may be optimized to further extend the margin past the tumor where safe treatment may be applied.

When treating tissue with IRE, a number of conditions determine the extent of electroporation. While the primary predictor of electroporation is local electric field strength, the electric field distribution as well as the tissue response to the electric field depends on the tissue type and intrinsic structure of the tissue (331). Additionally, pulse parameters greatly affect the response of the tissue, as demonstrated by the different response of a single cell to H-FIRE pulse durations (1 µs) and IRE pulse durations (100 µs) (316, 332). In addition to pulse duration, other pulse

parameters such as pulse number, pulse shape, pulse amplitude, and pulse repetition rate all have an influence on the extent a tissue is electroporated. Electric field distribution depends highly on the electrode geometry, as well as tissue conductivity. Therefore, in designing a clinical IRE therapy, there are more variables affecting tissue response than can reasonably be completely studied. In H-FIRE therapy, an added variable of the delay between the bipolar pulses is likely to play an important role in tissue response. In this study we attempt to determine the effect of some of these variables—specifically pulse number, pulse duration, and inter-pulse delay—in the context of malignant cell selectivity, with the goal of finding pulse parameters for further *in vitro* studies as well as possibly informing *in vivo* treatments.

6.2 Materials and methods

Cell culture

U-87 MG human glioblastoma cells (ATCC) were cultured in Dulbecco's Modified Eagle Medium (DMEM) containing 10% fetal bovine serum (FBS) and 1% penicillin/streptomycin (PS). Normal Human Astrocyte (NHA) cells (Lonza) were cultured in Astrocyte Growth Media (Lonza). All cells were grown in culture at 37 °C in 5% CO2 in a humidified incubator. Cells were seeded in hydrogels at a density of 1×10^6 cells/mL. The hydrogels were submerged in appropriate growth media for the cell type at 37 °C in 5% CO2 in a humidified incubator and cell viability was maintained within hydrogels for up to 7 days.

Construction of collagen scaffolds

Stocks of type I collagen were prepared by dissolving rat tail tendon in acetic acid, followed by freezing and lyophilization as described previously (140). Stock solution concentrations of

collagen were created at a density of 10 mg/mL. Scaffolds with a final concentration of 5 mg/mL were made from concentrated collagen stocks to create collagen gels of 0.5% (w/w). Neutralized collagen solutions were created by mixing acid-dissolved collagen with 10X DMEM (10% of total collagen solution volume) and sufficient volumes of 1N NaOH until a pH in the range of 7.0–7.4 was achieved. The neutralized collagen was mixed with cells suspended in DMEM or NHA media to achieve a cell density of 1×10^6 cells/mL in the final collagen mixture. Solutions were mixed carefully with a sterilized spatula to ensure homogenous distribution throughout the gel without damaging cells. Collagen solutions were then dispensed into a polydimethylsiloxane (PDMS) mold with a cut-out of 10 mm diameter and 1 mm depth and molded flat to ensure consistent scaffold geometry. Our previous mathematical modeling and experiments on oxygen (O_2) consumption rates by tumor cells (140) confirms that at this cell density and scaffold thickness, O_2 concentration is uniform throughout the scaffold depth. Collagen was allowed to polymerize at 37 °C and 5% CO_2 for 30 minutes.

Finite element analysis in hydrogels

Finite element models using COMSOL Multiphysics (Version 4.3, COMSOL Inc., Palo Alto, CA) were used to solve the Laplace equation to find the electric field distribution within the hydrogels for each different voltage used. The electric field distribution within the hydrogel was found by solving the Laplace Equation:

$$\nabla^2 \phi = 0 \quad (6.1)$$

where ϕ is the electrical potential. The boundaries of one electrode were set to the applied voltage ($\phi = V_{applied}$) and the boundaries of the second were set to ground ($\phi = 0$) while the initial voltage (V_0) for all subdomains were set to 0V. All other external boundaries were set to electrical

insulation ($-\boldsymbol{n} \cdot \boldsymbol{J} = 0$). The mesh was refined until error between successive refinements was less than 1%. The final mesh contained 47,438 elements and solutions were found in approximately 3 minutes on a Pentium i3 processor.

Electroporation techniques

Pulsed electroporation experiments were performed in collagen hydrogels with constant electrical properties. High- frequency pulses were delivered using a custom-built pulse generation system (INSPIRE 2.0, VoltMed Inc., Blacksburg, VA). Pulses were delivered through custom-built electrodes composed of two solid stainless steel cylinders with diameters of 0.87 mm, separated 3.3 mm edge-to-edge, with spacing and geometry maintained by a 3D printed electrode holder. In the H-FIRE pulsing protocol, treatments were performed delivering a variety of pulses ranging from 10 bursts to 200 bursts. Pulse numbers of 10, 25, 40, 50, 100, and 200 bursts were studied. For pulse number studies, a burst consisted of 1 μs pulses of alternating polarity with a 5 μs inter-pulse delay delivered with a repetition rate of 1 burst per second. Voltage output was set to 700 V to achieve measurable lesions within the hydrogel geometry. To determine the effect of pulse width on selectivity, pulses of varying waveforms were used. H-FIRE pulse waveforms studied included 10 x 5 μs pulses of alternating polarity with a 5 μs inter-pulse delay, 25 x 2 μs pulses of alternating polarity with a 2 μs inter-pulse delay, 50 x 1 μs pulses of alternating polarity with a 5 μs inter-pulse delay, and 50 x 1 μs pulses of alternating polarity with a 1 μs inter-pulse delay. Conventional IRE pulse waveforms of unipolar 100 μs pulses were also studied. All pulses were delivered with a pulse number of 50 and a repetition rate of 1 burst per second. The total on-time of the electric field was constant at 100 μs per burst across all pulse widths studied. Conventional IRE pulses were delivered

using an ECM 830 pulse generator (Harvard apparatus, Holliston, MA) through the same custom-built electrodes. IRE voltage output was set to 350 V to achieve measurable lesions within the hydrogel geometry.

Determination of lethal threshold in hydrogels

The thresholds for cell death were determined by first performing a live-dead stain on the hydrogels 24 hours after delivering treatment. Live cells were stained with Calcein AM (Biotium, Hayward, CA) and fluoresced as green while dead cells were stained with ethidium homodimer III (Biotium, Hayward, CA) and fluoresced as red. The size of the red-stained dead region was measured using ImageJ image analysis software. Geometric measurements of the ablation zones were mapped to a finite element model to calculate the electric field during treatments of the scaffolds. The electric field magnitude at the edge of the live and dead regions was considered the electric field threshold for cell death for the given cell type. Each individual hydrogel exposed to either H-FIRE or IRE therapy that was measured to determine the lethal electric field for the cell type was considered an independent sample representing the response of approximately 125,000 cells. For each condition, hydrogels were pulsed in at least 3 different independent experiments on different days.

Power spectral analysis

A power spectral analysis was conducted by running a Fast Fourier Transform (FFT) on the experimental H-FIRE pulses. The pulse waveform of 1 µs positive pulse, 5 µs inter-pulse delay, and 1 µs negative pulse was analyzed as was the pulse waveform of 1 µs positive pulse, 1 µs inter-pulse delay, and 1 µs negative pulse. The power spectral analysis was used to determine the

dominant frequencies a cell is exposed to upon treatment as demonstrated elsewhere as a tool for understanding bipolar pulses (333).

Quantification of selectivity

Selectivity was quantified by measuring the area of ablation of malignant cells (A_M) and the area of ablation (A_H) for healthy cells in the hydrogel using ImageJ image processing software. Percent selective ablation area was calculated according to the formula

$$\%\ Selective\ Ablation\ Area = \frac{A_M - A_H}{A_M} * 100\% \quad (6.2)$$

Statistical analysis

Statistical significance was determined by a two-tailed *t*-test performed in Prism Statistical Software (Version 6, Graphpad, La Jolla, CA). A 95% confidence interval was used with significance defined as $p < 0.05$. All numerical results are reported as the mean and the standard deviation of all experimental measurements. No outliers were excluded.

6.3 Results

6.3.1 Pulse duration and inter-pulse delay affect malignant cell selectivity

In order to determine the pulse duration that achieves treatment with the most selectivity for malignant cells, co-culture hydrogels of malignant U87-MG cells and normal human astrocytes were treated. Co-culture hydrogels were exposed to a range of pulse durations ranging from 100 µs unipolar IRE pulses to 1 µs H-FIRE pulses. As seen in Figure 6.1, increasing selectivity is achieved with decreasing pulse width. This finding is consistent with the hypothesis that the shorter pulses are able to penetrate the cell membrane and interact with the abnormal inner organelles in

malignant cells. A comparison of 5µs-5µs-5µs, 2µs-2µs-2µs, and 1µs-1µs-1µs pulses shows that decreasing the pulse width of a symmetric bipolar pulse allows for greater selective ablation of malignant cells. In order to investigate the impact on inter-pulse delay, co-culture hydrogels pulsed with 1µs-5µs-1µs pulses can be compared to co-culture hydrogels pulsed with 1µs-1µs-1µs pulses. The range of electric field thresholds for selective ablation of malignant cells increases with decreasing pulse width and decreases with decreasing inter-pulse delay.

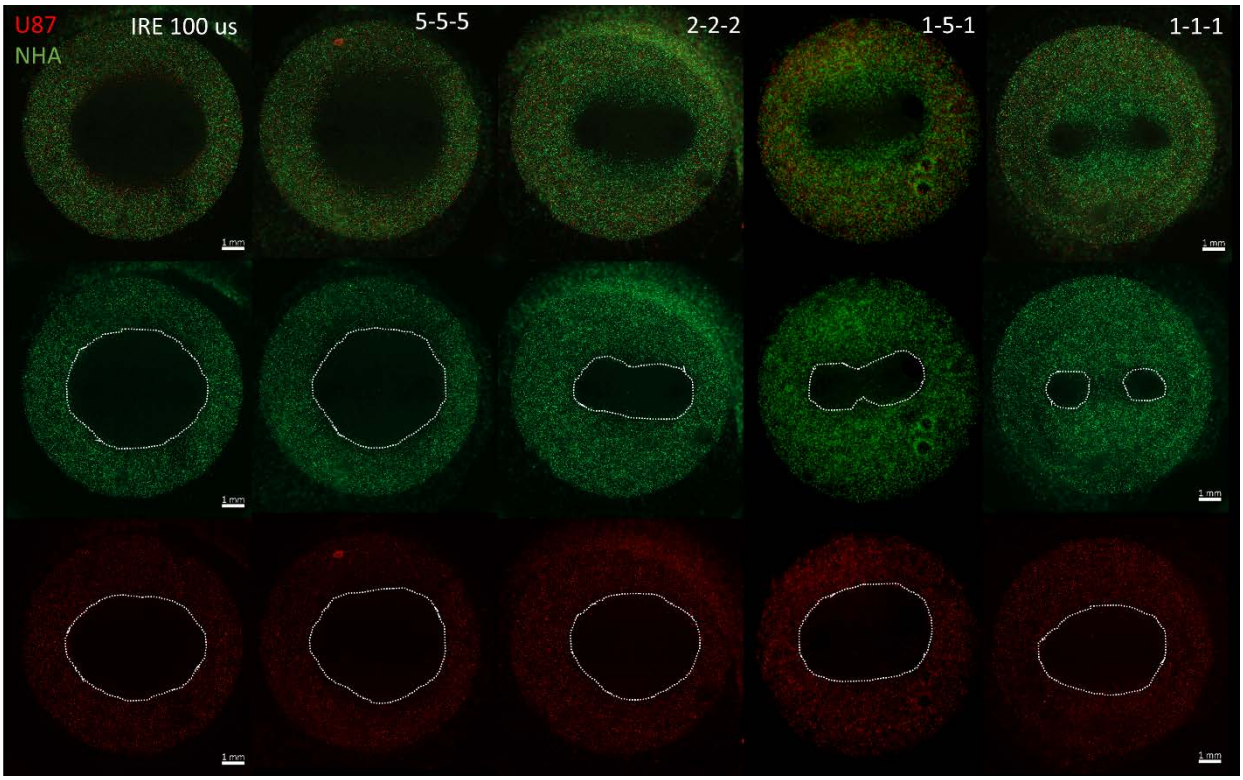

Figure 6.1. Co-culture of malignant U87 cells and healthy NHA treated with H-FIRE show that increasing selectivity is achieved as pulse width and inter-pulse delay are decreased. *As pulse width is decreased from 100 µs to 1 µs the healthy astrocytes (green) display a smaller ablation area relative to the ablation area of malignant glioma cells (red). Comparison of a 5 µs and 1 µs inter-pulse delay shows greater selectivity with the shorter delay.*

To quantify the selectivity of each pulse waveform, we calculated the percentage of total ablation volume that was selective ablation of malignant cells. As seen in Figure 6.2a, with decreasing pulse width comes an increasing degree of selectivity achieved for malignant cell death. A comparison

between the 1µs-5µs-1µs waveform and 1µs-1µs-1µs waveform shows a significantly (p=0.005) greater degree of selectivity with the 1µs-1µs-1µs waveform. From this it can be concluded that by shortening the inter-pulse delay, we can achieve a higher degree of selectivity. A comparison between the selectivity achieved by the 1µs-5µs-1µs waveform and the 2µs-2µs-2 µs waveform shows a significantly (p=0.04) greater percentage selectivity with the 1µs-5µs-1µs waveform, suggesting that though inter-pulse delay plays a role in selectivity, the pulse width is the dominating variable. As pulse width is decreased the range between which malignant cells can be killed while healthy cells remain alive is widened (Figure 6.2b).

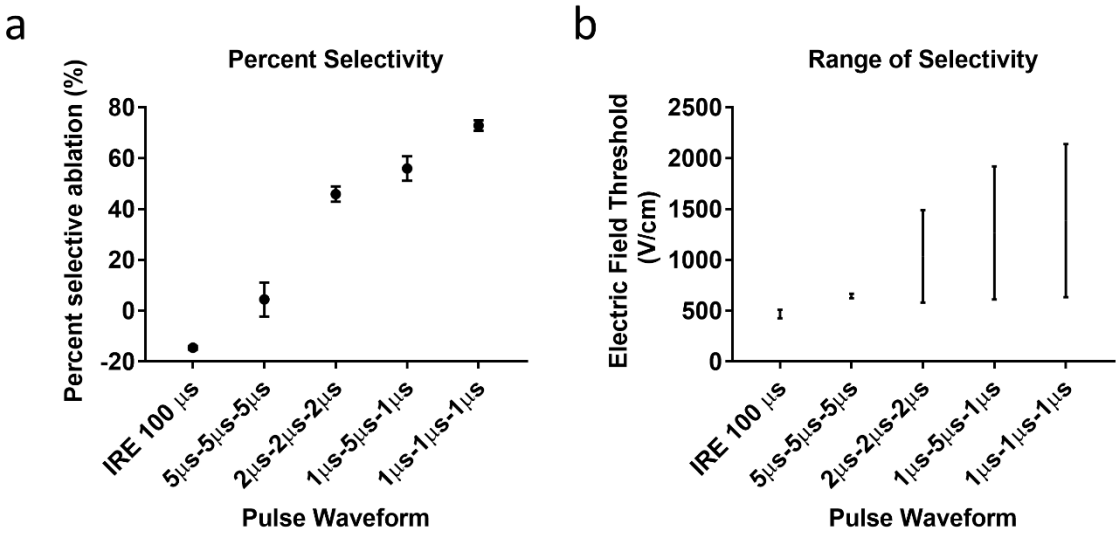

Figure 6.2. Quantification of selectivity from co-culture hydrogels. ***a)*** *Percent selective ablation, defined as the percent of total cell ablation area that is solely ablation of malignant cells and not healthy cells is increased with decreasing pulse width. Decreasing inter-pulse delay from 5 µs to 1 µs in the 1 µs bipolar pulse form also increases percent selectivity.* ***b)*** *The increasing selectivity seen with decreasing pulse width and decreasing inter-pulse delay results in a greater range of electric fields that are lethal for malignant cells but safe for healthy cell exposure.*

In order to understand the effect of changing pulse width and inter-pulse delay, it is useful to understand the frequency components involved in the individual pulse waveform. As demonstrated in the previous chapter and displayed in Figure 5.3, as frequency of the applied waveform is

increased, the induced TMP on the cell with the geometry of a glioma cell increases more than the TMP on the cell with healthy cell geometry. This effect is hypothesized to be due to the effect of the enlarged nucleus interacting with the electric field that bypasses the cell membrane in high frequency applied fields. This predicted selectivity begins at frequencies slightly greater than 10^4 Hz but becomes most pronounced at frequencies between 10^5 to 10^6 Hz. Both decreasing the pulse width and decreasing the delay between the bipolar pulses effectively pushes more of the delivered power into higher frequencies. For 1 μs bipolar pulses, changing the inter-pulse delay from 5 μs to 1 μs pushes the majority of the power delivered into the range between 10^5-10^6 Hz that is predicted to be optimal for achieving selectivity (Figure 6.3).

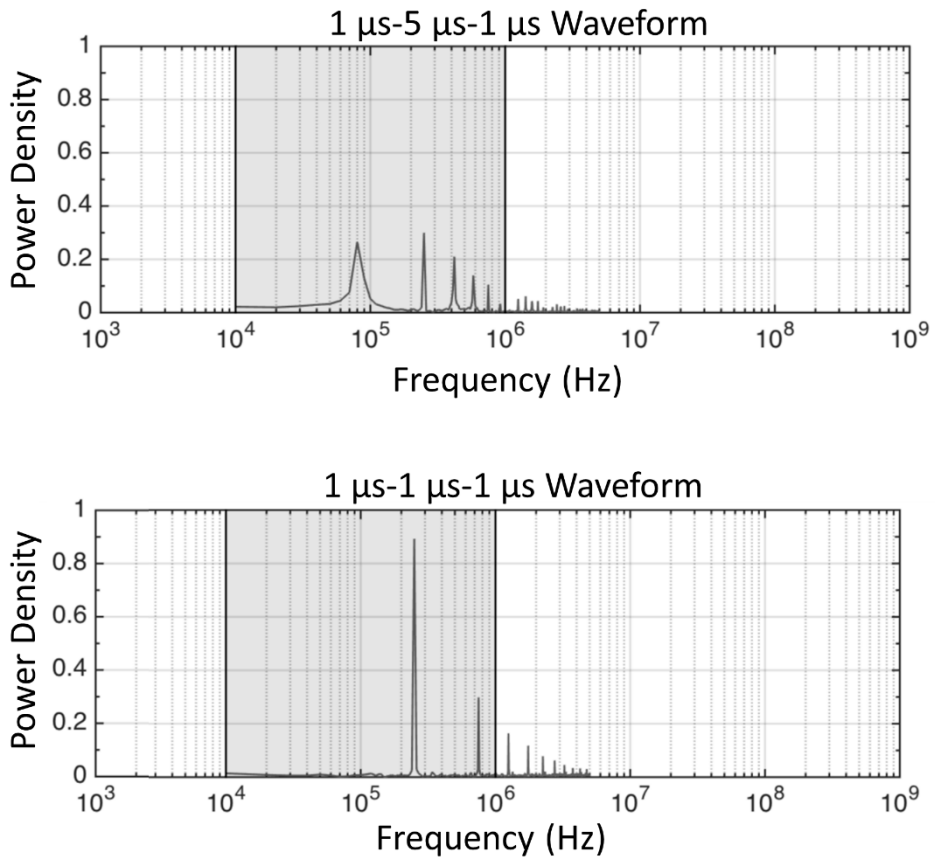

Figure 6.3 Power spectral analysis for experimental pulses. *The FFT performed on the experimental pulsing schemes 1-5-1 (top) and 1-1-1 (bottom) show the frequency at which the majority of the power is delivered for each waveform. By decreasing inter-pulse delay, the majority of the power delivered is shifted into the higher frequency range.*

6.3.2 Number of applied pulses affects malignant cell selectivity

Another parameter that is important in determining the electroporation response of a cell is the number of applied pulses. In order to determine the effect of pulse number on selectivity we exposed U87 malignant glioma cells and healthy NHAs to treatments with a range of pulse numbers applied to the hydrogel tissue mimic (Figure 6.4).

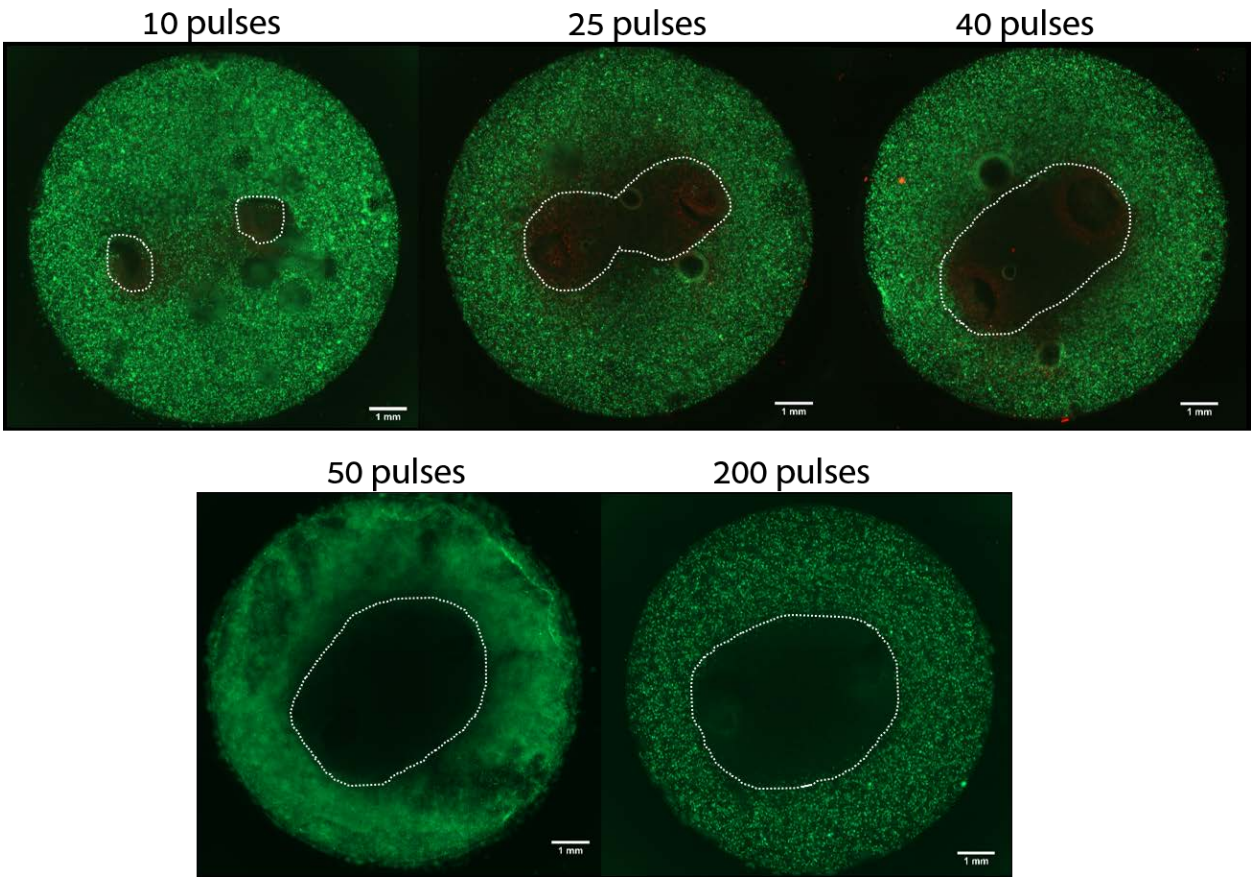

Figure 6.4 Number of applied pulses affects ablation in hydrogel tumor mimics. *Increasing pulse number applied to the hydrogel increases the ablation area for U87 cells.*

As seen in Figure 6.5, the drop in lethal electric field threshold with increasing pulse number follows a rough exponential trend. Importantly, the dynamics of the changing lethal electric field threshold with pulse number differ across the two cell types. This creates an optimal separation between lethal electric field thresholds around 50 pulses before the lethal electric field thresholds for the two cell types begin to converge at higher pulse numbers.

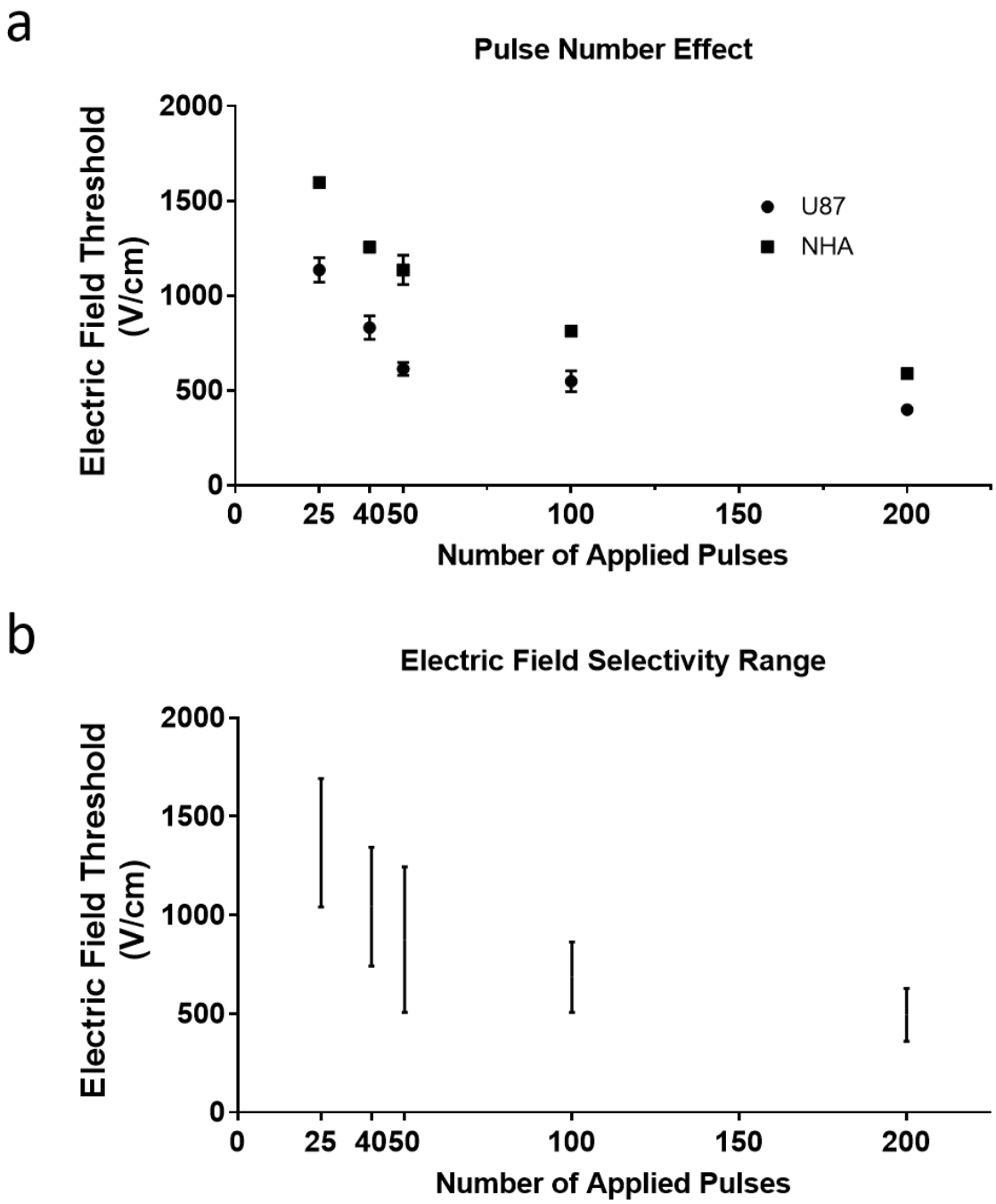

Figure 6.5 Effect of pulse number on selective malignant cell killing compared to healthy astrocytes*. a) As the number of pulses applied to cells increases, the lethal electric field thresholds drops at a diminishing rate for both malignant U87 cells and healthy NHAs. The dynamics of the change in lethal electric field threshold with pulse number are different for U87 and NHAs b) Changing the number of applied pulses changes the range of electric field thresholds that can be used to ablate malignant U87 cells while sparing NHAs.*

6.4 Discussion

This work represents an attempt to inform both future *in vitro* hydrogel experiments as well as *in vivo* clinical application. These findings suggest that to achieve optimal selectivity, shorter waveforms with short inter-pulse delays are preferable. Decreasing pulse width as well as decreasing inter-pulse delay results in a larger range of selectivity for PEFs targeting malignant cells. Electric fields within this range of selectivity can be used at the tumor edge to ablate malignant cells while sparing healthy brain tissue. Thus tuning these variables allows for a greater possibility for safely treating the invasive cells of a tumor.

It is important to note that the conclusions here apply specifically to the two cell types tested. However, all our previous research on the effect of H-FIRE on cells has shown trends that support the grouping of cells into categories of malignant and healthy. For all cell types tested, malignant cell lines show a similar electroporation response to other malignant cell lines tested. Similarly, healthy cell lines all exhibit similar responses to H-FIRE therapy. These responses differ between these two classes of cell type designation. Therefore, it is reasonable to assume the selectivity achieved between U87 cells and NHA with give pulse parameter results that can be extended to other malignant and healthy cell types within the GBM tumor.

There remains an important balance between pulse duration and voltage, thereby limiting the degree to which pulse duration can be decreased without sacrificing other aspects of a successful therapeutic regime. As pulse duration is decreased, voltage must be increased in order to achieve similar ablation volumes. Additionally there is theoretically a limit to decreasing pulse duration to

achieve the electroporation effects on the same scale as is demonstrated in these experiments. For instance, as pulse durations reach into the ns range, a new mechanism of action comes into play and cell response may differ from pulses in the μs range (334, 335). The current experimental waveforms used by us are limited by the capabilities of the electronics used for pulse generation. For our custom-built pulse generator, a 1 μs pulse width is the minimal width that can safely be delivered at the voltages necessary to cause ablation without damage to the electronics. Further studies are warranted for pulse durations less than 1 μs to determine the optimal pulse waveform for selectivity. For the current capabilities of the electronics studied, a 1μs-1μs-1μs waveform is a preferable output for achieving selectivity between U87 cells and NHAs. Similarly, a regime that delivers 50 pulses is preferable for achieving selectivity within this system. The optimal pulse number is likely to vary for different cell types and almost certainly to be different in the context of *in vivo* ablation of tumors. Despite this likely variance across different context, these findings confirm the importance of pulse number is designing electroporation regimes for selectivity. Further studies must be conducted to determine the optimal pulse number for clinical use. As pulse number is decreased, voltage must be increased to achieve similar ablation volumes so there exist an important balance between these variables in designing electroporation regimes. As voltage is increased, not only is the burden on the electronics greater, but greater thermal damage will occur. For safe application of H-FIRE in the brain, thermal damage should be minimized so the applied voltage that can be safely delivered to the brain has an upper limit. These variables should all be taken into account when designing a clinical protocol for selective ablation in the brain. Therefore, many further safety studies are warranted to explore the dynamics of these pulse variables in an *in vivo* context.

The studies on pulse number are also important for informing treatments for optimizing electrode configuration. For instance, by designing an electrode configuration with 4 spaced electrodes where the healthy cells on the edge of the ablation area only receive 25 pulses and the malignant cells in the center receive 100 pulses, the difference in lethal electric field for selectivity increases from 461 V/cm (if all cells received 25 pulses) or 253 V/cm (if all cells received 100) to 1037 V/cm (if malignant cell receive 100 pulses and astrocytes receive 25). However if this same 4 electrode configuration were treated with 50 pulses delivered to each electrode so that healthy cells received 50 pulses and malignant cells received 200 pulses, the difference in lethal electric field exposure falls from 1037 V/cm to 738 V/cm, suggesting that fewer pulses at a higher voltage may be able to achieve greater depth of safe ablation at the tumor edges.

For the particulars of this *in vitro* experimental set up, the degree of separation between the average lethal threshold for malignant GBM cells and the average lethal threshold for normal astrocytes is greatest with a 1µs-1µs-1µs waveform and 50 applied pulses. Though the optimal pulse parameters may be different in the clinical context due to larger ablation volumes, more connected tissue, and limited electrode configurations due to sensitive structures, it is important to note, pulse number and pulse duration represents an important variable in malignant cell selectivity. In clinical regimes, treatment planning is aimed primarily at ablating the largest volume of bulk tumor with a safe voltage. In clinical practice, we often use more pulses in order to keep the applied voltage to a level that avoids sparking from the electrodes. As the technology improves and the interaction between pulse parameters becomes better understood, there will undoubtedly be an aspect of treatment planning directed at optimizing electrode configuration, pulse width, pulse number, and voltage in a way to improve selectivity, especially when treating the edge of a tumor. The range

of separation, seen to vary across both variables studied, gives us information on how far past the tumor margin it is safe to treat with a given waveform, highlighting the importance of both pulse duration and pulse number as variables to optimize in a given system.

Chapter 7 Testing the Efficacy of H-FIRE Therapy on Glioma Stem Cells[3]

7.1 Introduction

Central to the highly heterogeneous makeup of a glioblastoma tumor are its initiator cells that are the progenitors from which the many subclasses of cells that make up a tumor are derived. The search for a subclass of cells at the top of the hierarchy, responsible for initiation or recurrence of tumor has brought an intersection between stem cell biology and oncology. It was hypothesized that just as an organ develops from stem cells, a tumor is similarly derived from a set of stem-like cells that make up a small percentage of the tumor but drive its development and progression (336). These cells are able to maintain a tumor despite multimodal assaults by chemotherapies and radiation therapies. Though this theory of tumor origin through cancer stem cells has been controversial, as more evidence is found of cells with surface markers similar to known stem cell markers, the hierarchical model of tumor development has gained traction and esteem. This model implies that tumors are derived from a small population of cells that are capable of self-renewal and initiation while the rest of the cells that make up the tumor, the bulk tumor cells, represent a type of differentiated cancer cell population that cannot form new tumors. There is still some speculation over whether these cancer stem cells are originator cells, responsible for the initiation and progression of the tumor or whether they are a product of tumor formation(337). However, regardless of their standing in the hierarchy of the tumor, they possess two characteristics that

[3] This work was done in collaboration with Dr. Akanksha Kanitkar, Dr. Zhi Sheng, and Dr. Scott Verbridge and is in preparation for publication.

make them very important to the study of cancer therapies—their ability to initiate new tumors and their ability to resist current cancer therapies.

In a seminal study identifying cancer stem cells in the brain, it was found that a small population (100 cells) of glioma stem cells, identified as such by the CD133 surface marker characteristic of embryonic stem cells, were able to recapitulate the heterogeneity of entire tumors in immunocompromised mice (91). In contrast, 10,000 CD133- cells never became tumorigenic, suggesting that only certain cells had the potential to initiate tumor growth and these cells share surface markers with embryonic stem cells. Since this discovery with regard to CD133+ cells, others have identified cancer initiating cells in the brain based on other stem cell markers or the ability of cells to form neurospheres, another characteristic of stem cells (338-340). What have come to be known as glioma stem cells (GSCs) or brain tumor initiating cells (BTICs) are a class of cells that express high levels of stem cell markers involved in self-renewal as well as genes involved in neural stem cell proliferation and differentiation.

In addition to their self-renewal properties, cancer stem cells have another important characteristic central to their role in the tumor hierarchy. That is, their high degree of resistance and repair mechanisms. A population of GBM cells exposed to a lethal dose of 1,3-bis(2-chloroethyl)-1-nitrosourea (BCNU) chemotherapy produced a resistant subpopulation of cells with stem-like properties, stem cell surface markers, and the ability to produce tumors in immunocompromised mice brains (341). Lineage tracing studies in mouse models have shown that brain tumors treated with TMZ produce a resistant line of GSCs which repopulate the tumor (342). Similarly, a resistant

subpopulation emerges when GBM cells are exposed to radiotherapy that can initiate tumorigenesis when implanted into SCID mice (343). These cells have high levels of stem cell markers as well as the ability for self-renewal and pluripotency (343). GSCs have been shown to have a variety of resistance mechanisms including a variety of drug resistant genes (BCRP, MDR1), MGMT activity for DNA repair as well as other DNA repair capacity such as increased damage checkpoints, and a variety of apoptosis inhibitors (329, 344-347). Multiple molecular mechanisms have been identified in GSCs to mediate therapeutic resistance to cytotoxic therapies such as Notch (348), NF-κB (349), EZH2 (350), and PARP (351). Additional mechanisms of resistance may evolve from exposure to microenvironmental factors such as hypoxia (352, 353) and metabolic stress (354, 355). In general, cells are characterized as GSCs based on five criteria—ability for self-renewal, differentiation potential, high tumorigenicity, drug resistance, and radio-resistance (356, 357). Together, these features of GSC make them highly likely to be responsible for GBM recurrence.

Because many methods of cancer treatment are ineffective for GSCs and because they are important in tumor progression and recurrence, a large need exists for a different class of therapies that can work effectively against GSCs. Conventional therapy regimes often eliminate the bulk tumor while increasing the pool of GSCs that can propagate a tumor, resulting in near universal recurrence in GBM tumors (358). Irreversible electroporation is a therapy that holds promise for the treatment of GSCs as it works on a physical mechanism that should not be overcome by drug resistance and DNA repair mechanisms. Irreversible electroporation ablates cells through the formation of defects in the membranes of the cells, making it likely to be an effective therapy for GSC ablation. In addition, our previous studies have shown that by using high frequency

irreversible electroporation, the efficacy of the treatment is enhanced for cells with a higher nuclear to cytoplasm ratio. Previous studies of the structural characterization of glioma stem cells have reported atypical and enlarged nuclei in GSCs as well as irregular physical structure in other organelles (356, 359, 360). The purpose of this study is to determine the ability of H-FIRE therapy to ablate GSCs and the possibility of selective targeted of these cells due to any structural differences they may possess.

7.2 Materials and methods

Cell culture

GBM 10, VTC061, and VTC064 patient-derived glioma stem cells were received from the lab of Dr. Zhi Sheng. These cells were isolated from resected tumor tissue as described previously (361). MES 326 patient derived glioma stem cells were received from the lab of Dr. Ichiro Nakano. These cells were isolated from resected tumor tissue as described previously (349). GBM 10, VTC061, VTC064 and MES 326 were cultured as free-floating neurospheres in Dulbecco's Modified Eagle Medium (DMEM) supplemented with B27, 20 ng/mL epidermal growth factor (EGF), 20 ng/mL basic fibroblast growth factor (bFGF), 1% L-glutamine, and 1% Penicillin/Streptomycin (PS). U-87 MG human glioblastoma cells (ATCC) were cultured in DMEM containing 10% fetal bovine serum (FBS) and 1% (PS). Normal Human Astrocyte (NHA) cells (Lonza) were cultured in Astrocyte Growth Media (Lonza). U-251 MG human glioblastoma cells (ATCC) cells were grown in DMEM containing 10% FBS, 1% PS, and 0.1 mM non-essential amino acid. DBTRG human glioblastoma cells (ATCC) were culture in RPMI medium containing 10% FBS, 2 mM L-glutamine, 1% PS and 0.1 mM non-essential amino acids. PC12 rat cells (ATCC) were cultured in DMEM containing 5% horse serum, 5% calf serum and 1% PS. PC12 cells were differentiated into

neuron-like cells by adding 50 ng/mL nerve growth factor (NGF) to the culture media every other day for 14 days. All cells were grown in culture at 37 °C in 5% CO2 in a humidified incubator. Cells were seeded in hydrogels at a density of 1×10^6 cells/mL. The hydrogels were submerged in appropriate growth media for the cell type at 37 °C in 5% CO2 in a humidified incubator and cell viability was maintained within hydrogels for up to 14 days

Construction of collagen scaffolds

Stocks of type I collagen were prepared by dissolving rat tail tendon in acetic acid, followed by freezing and lyophilization as described previously (140). Stock solution concentrations of collagen were created at a density of 10 mg/mL. Scaffolds with a final concentration of 5 mg/mL were made from concentrated collagen stocks to create collagen gels of 0.5% (w/w). Neutralized collagen solutions were created by mixing acid-dissolved collagen with 10X DMEM (10% of total collagen solution volume) and sufficient volumes of 1N NaOH until a pH in the range of 7.0–7.4 was achieved. The neutralized collagen was mixed with cells suspended in DMEM, NHA, or GSC media to achieve a cell density of 1×10^6 cells/mL in the final collagen mixture. Solutions were mixed carefully with a sterilized spatula to ensure homogenous distribution throughout the gel without damaging cells. Collagen solutions were then dispensed into a polydimethylsiloxane (PDMS) mold with a cut-out of 10 mm diameter and 1 mm depth and molded flat to ensure consistent scaffold geometry. Our previous mathematical modeling and experiments on oxygen (O_2) consumption rates by tumor cells (134) confirms that at this cell density and scaffold thickness, O_2 concentration is uniform throughout the scaffold depth. Collagen was allowed to polymerize at 37 °C and 5% CO_2 for 30 minutes. For testing of GSCs neurosphere morphology,

hydrogels were seeded with single cells at a cell density of 1×10^5 cells/mL and maintained in culture for 9 days to allow time for large neurospheres to grow from the individual cells.

Fluorescent staining

GBM 10, VTC064, VTC061, MES 326, U87, U251, DBTRG, NHA, and PC12 cells were individually seeded in hydrogels described previously. After culturing the cells for 24 hours, the hydrogels were fixed using 4% formalin and blocked and permeabilized using 40 mg/mL bovine serum albumin (BSA) and 0.05% Triton-X. Cellular F-actin was stained with Alexa Flour 568 phalloidin (Life Technologies, Carlsbad, CA) while cell nuclei were stained with diaminophenylindole (DAPI; Sigma-Aldrich, St. Louis, MO). Cells were visualized using a Zeiss LSM880 (Carl Zeiss Microscopy LLC, Thornwood, NY) laser scanning confocal microscope.

Determination of NCR

Fluorescent stained cells were used to determine overall cell area and nuclear area for cells. Image analysis was done in Image J (NIH, Bethesda, MD. Z-stack images were converted into 2D projection images and cell measurements were made from these projections. Measurements were made on at least four cells per hydrogel and at least 5 hydrogels were analyzed for each condition. NCR was calculated from the measured cell area (A_C) and nuclear area (A_N) as follows:

$$NCR = \frac{A_N}{A_C - A_N} \quad (7.1)$$

Electroporation of 3D scaffolds

Pulsed electroporation experiments were performed in hydrogels with constant electrical properties. The electrical conductivities of each of the gel-cell mixtures were measured with a conductivity meter to ensure similar electrical properties (0.98 ± 0.04 S/m). H-FIRE pulses were delivered using a custom-built pulse generation system (INSPIRE 2.0, VoltMed Inc., Blacksburg, VA). Two solid stainless steel cylinders with diameters of 0.87 mm, separated 3.3 mm edge-to-edge, were used as electrodes. Treatments were performed delivering a total of 50 bursts of 500 ns pulses. In the H-FIRE protocol, a burst consisting of 100 x 500 ns pulses with a 2μs inter-pulse delay was delivered with a repetition rate of 1 burst per second. In H-FIRE treatments 800 V_{peak} was used to produce ablations in the hydrogel large enough for distinct electric field lines to be measured but small enough that boundary effects of the hydrogel edge didn't interfere with the electric field distribution at the lethal threshold. As the hardware has improved throughout the course of the experiments presented in this document, the pulse waveform used in this study used 500 ns pulses as that is the shortest pulse duration safely delivered by the pulse generator.

Finite element analysis in hydrogels

Finite element models using COMSOL Multiphysics (Version 4.3, COMSOL Inc., Palo Alto, CA) were used to solve the Laplace equation to find the electric field distribution within the hydrogels for each different voltage used. COMSOL Multiphysics was also used to solve the Joule heating equation to calculate the temperature distribution in the hydrogel as a result of each treatment. The simulation geometry was modeled as a 10 mm diameter and 1 mm thick cylinder with two steel electrode cylinders (d = 0.87 mm) spanning the depth of the hydrogel. Thermal and electrical properties for each domain can be found in Table 4.1. The mesh was refined until error between

successive refinements was less than 1%. The final mesh contained 47,438 elements and solutions were found in approximately 3 minutes on a Pentium i3 processor.

Determination of lethal threshold

The thresholds for cell death were determined by analyzing images taken of live-dead stain on the hydrogels 24 hours after delivering treatment. Live cells were stained with Calcein AM (Biotium, Hayward, CA) and fluoresced as green while dead cells were stained with ethidium homodimer III (Biotium, Hayward, CA) and fluoresced as red. The diameter of the red-stained dead region was measured using ImageJ image analysis software. Geometric measurements of the ablation zones were mapped to a finite element model to calculate the electric field during treatments of the scaffolds. The electric field magnitude at the edge of the live and dead regions was considered the lethal electric field threshold for the given cell type.

Statistical analysis

Statistical significance was determined by a two-tailed *t*-test performed in Prism Statistical Software (Version 6, Graphpad, La Jolla, CA). A 95% confidence interval was used with significance defined as $p < 0.05$. All numerical results are reported as the mean and the standard deviation of all experimental measurements. No outliers were excluded.

7.3 Results

7.3.1 GSCs exhibit enlarged nuclei compared to healthy brain cells

The GSCs tested all grow as non-adherent neurospheres, a common morphological marker of stem cells (Figure 7.1a). To confirm that GSCs follow the trend of enlarged nuclear to cytoplasm ratio that many other cancerous cells have been shown to exhibit, we used confocal imaging to determine the nuclear and cell size of GSCs in three dimensional hydrogels (Figure 7.1b).

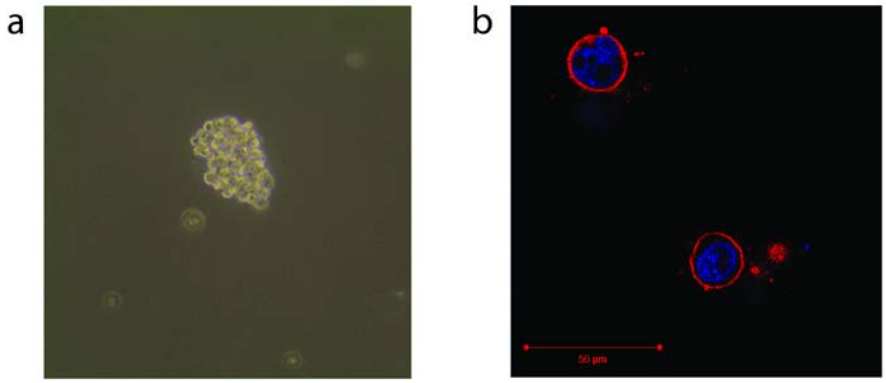

Figure 7.1 Glioma stem cell morphology (a) *GSCs grow as spherical cells into large free-floating neurospheres in normal culture conditions.* ***(b)*** *Confocal images of GSCs show a spherical cell with a large nucleus and a small volume of cytoplasm surrounding the nucleus.*

As seen in Figure 7.2a, within the platform of collagen hydrogels, the nuclear sizes of the GSC populations (GBM10, VTC064, and MES 326) are significantly larger than the healthy cell types measured (NHA, D1TNC1, and PC12). The GSCs have a nuclear size similar to those of a variety of glioblastoma cell lines (U87, DBTRG, and U251). Because of their spherical shape, the GSCs have substantially less spreading and therefore a smaller cytoplasmic area. This morphological feature is reflected in their nuclear to cytoplasm ratio, which is significantly greater than that of either bulk tumor cells or healthy cells (Figure 7.2b).

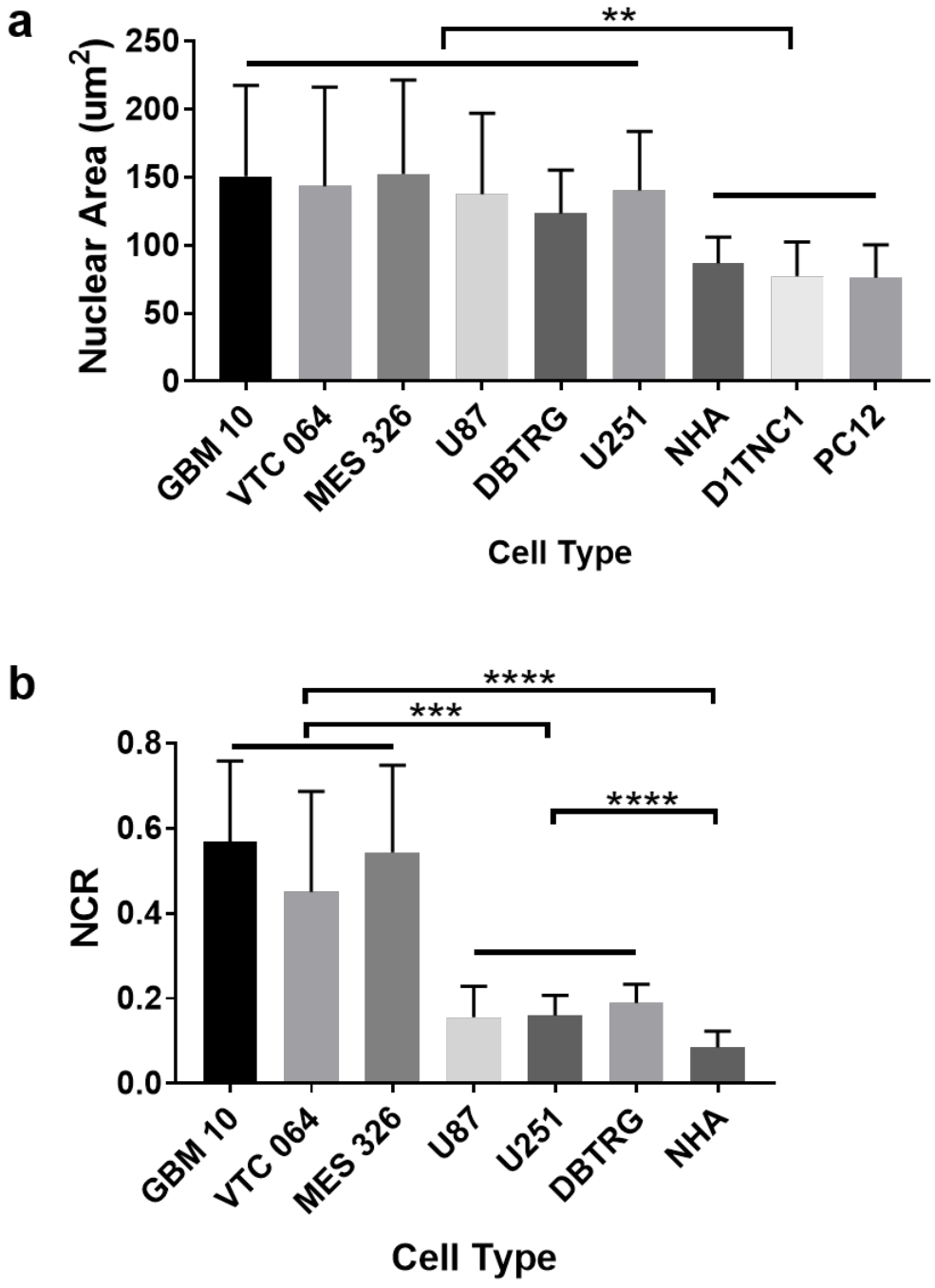

Figure 7.2 Glioma stem cells exhibit a cell morphology characterized by an enlarged nuclear area and enlarged nuclear to cytoplasm ratio compared to healthy brain cells. (a) *Comparison of the nuclear size of GSCs with other cell times shows a trend of enlarged nuclei for malignant cells compared to healthy brain cells* ***(b)*** *GSCs exhibit an enlarged NCR compared to both bulk tumor cells and healthy astrocytes due to their spherical morphology.*

7.3.2 GSCs are successfully ablated with H-FIRE therapy

Four different populations of patient derived stem cells (GBM 10, VTC061, VTC064 and MES 326) were seeded in 3D hydrogels and exposed to H-FIRE therapy with pulse waveforms of 0.5µs-2µs-0.5µs. For all GSC populations a noticeable lesion was produced by exposing the hydrogel to H-FIRE pulses (Figure 7.3a). To understand the efficacy of H-FIRE on GSC populations, these ablation areas were compared to the ablation areas for U251 bulk tumor cells (Figure 7.3b) and normal healthy astrocytes (NHA) (Figure 7.3c). The ablation areas of all four GSC populations tested were significantly greater than the ablation area of U251 ($p=0.002$) (Figure 7.3d). Both the GSCs and the bulk tumor cells exhibited significantly greater ablation areas than NHAs ($p<0.0001$).

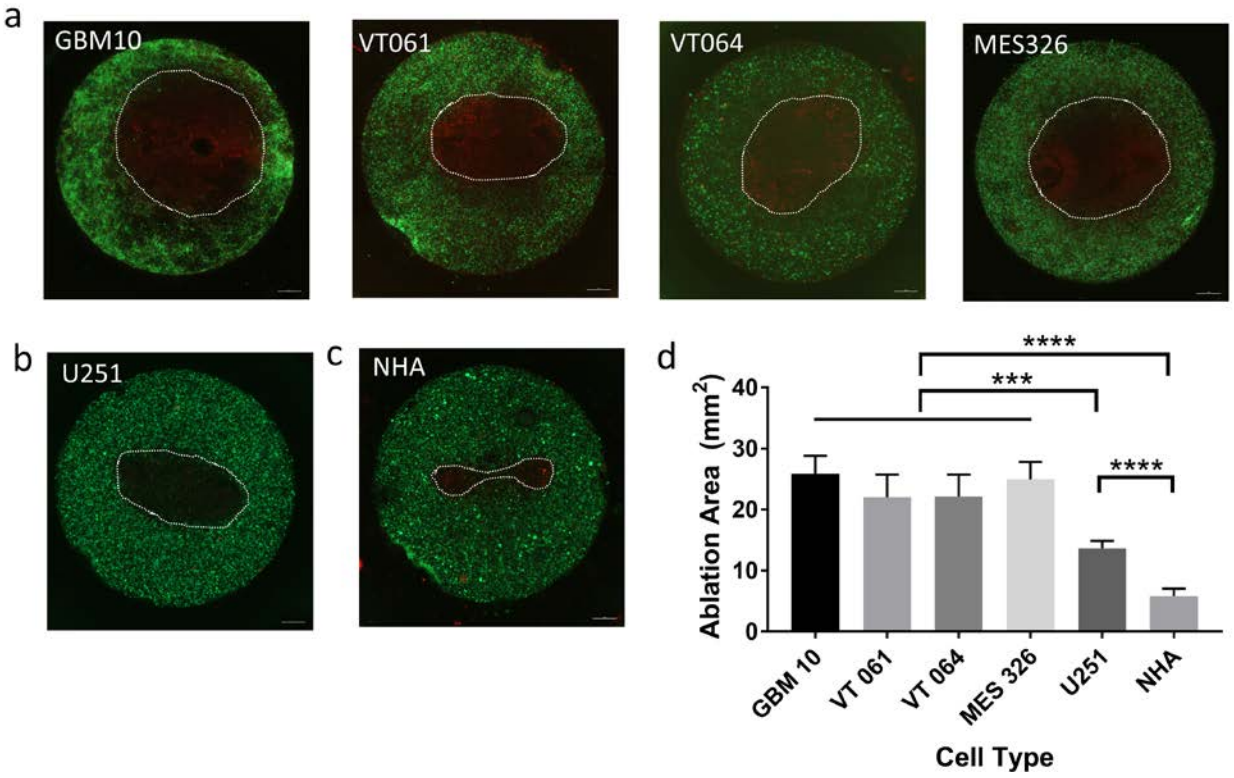

Figure 7.3 Populations of patient derived glioma stem cells are successfully ablated by H-FIRE therapy at lower thresholds than bulk tumor cells or healthy astrocytes. *Comparison of lesion sizes shows* ***(a)*** *four GSC populations have greater lesion sizes to* ***(b)*** *than bulk tumor cells or* ***(c)*** *healthy astrocytes for the same pulse parameters* ***(d)*** *GSC populations have a lower lethal threshold than bulk tumor cells or healthy astrocytes when exposed to H-FIRE pulses. ***p=0.002, ****p<0.0001*

7.3.3 GSC selectivity is dependent on pulse waveform

As seen in Figure 7.4a, the larger ablation areas of GSC correspond to lower lethal electric field thresholds for GSCs compared to both bulk U251 glioma cells and healthy astrocytes. For the GBM 10 population treated with H-FIRE delivering a 0.5µs-2µs-0.5µs waveform, the lethal threshold is 1020 ± 73 V/cm. For VTC061 cells, the lethal threshold is 1088± 32 V/cm. For VTC064 cells the lethal threshold is 1018 ± 30 V/cm. MES 326 cells are killed at a lethal threshold of 987 ± 61 V/cm. The lethal threshold for all four GSC populations treated with a 0.5µs-2µs-

0.5µs waveform is significantly lower than U251 bulk cells, which have a lethal threshold of 1285 ± 148 V/cm. The lethal threshold for NHA is significantly greater than the thresholds for both GSCs and U251s at 1610 ± 140 V/cm ± 140 V/cm.

In order to compare the results presented in this chapter with previous experimental results, we tested GSC ablation with the 1µs-5µs-1µs waveform we have used previously. As seen in Figure 7.4b, when cells were treated with a 1µs-5µs-1µs waveform, all cell types exhibit a lower lethal electric field threshold than when treated with a 0.5µs-2µs-0.5µs waveform. GBM 10 cells treated with a 1µs-5µs-1µs waveform are killed at an electric field distribution of 722 ± 98 V/cm. MES 326 cells have a lethal electric field distribution of 660 ± 27 V/cm. U251 cells are ablated when exposed to electric fields of 690 ± 44 V/cm while NHAs require 1125 ± 74 V/cm for ablation. Importantly, while the selective killing of GSCs and bulk tumor cells relative to healthy astrocytes remains, the selectivity between GSCs and U251 cells is not achieved. While GSCs are ablated at lower electric field thresholds than U251s with the 0.5µs-2µs-0.5µs, the lethal thresholds for the GSCs and U251 is not significantly different when the frequency of the pulse duration is increased by using a 1µs-5µs-1µs waveform.

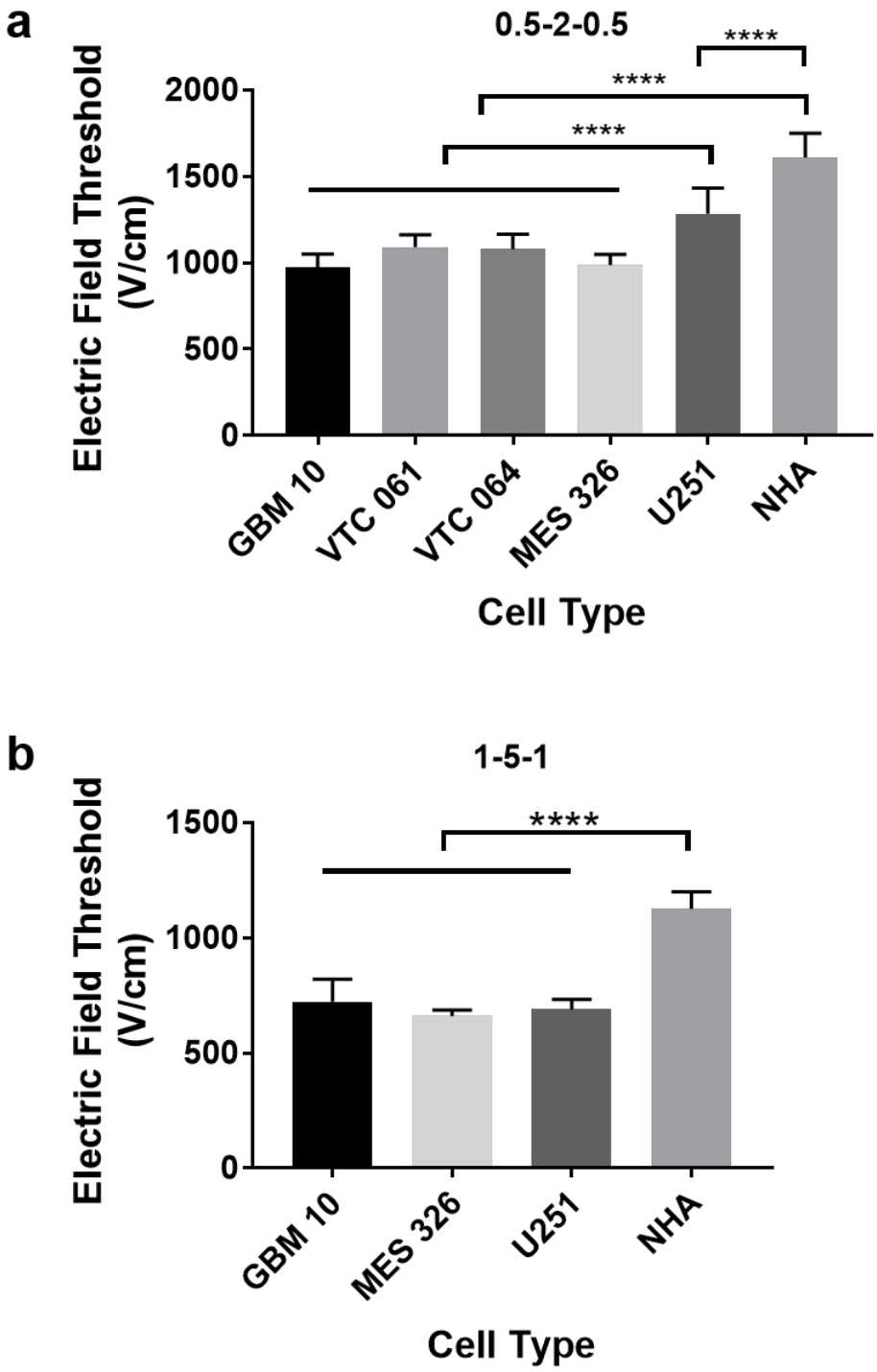

Figure 7.4 GSC selective killing with H-FIRE is improved with higher frequency pulses. a) *When treated with a 0.5µs-2µs-0.5µs H-FIRE pulseform, all four GSC populations tested had significantly lower lethal electric field thresholds than bulk tumor cells or healthy astrocytes. Bulk tumor cells had significantly lower lethal electric field thresholds than healthy astrocytes.* ***b)*** *When treated with a 1µs-5µs-1µs waveform, GSC populations have a significantly lower lethal electric field thresholds than healthy astrocytes but the difference between GSC and bulk GBM cell line ablation thresholds is not significant.*

Because GSCs grow in neurospheres (Figure 7.1a) that can reach hundreds of cells in diameter, we next determined the lethal threshold of cells in large neurospheres to determine if the bunched cell morphology changes response to H-FIRE. GSCs were cultured in hydrogels for 9 days and exposed to H-FIRE pulses. This time-scale allowed cells to grow into large neurospheres within the collagen hydrogels. The spheroid clusters exhibit lethal thresholds with no significant difference from single cell GSC hydrogels. From these results it can be concluded that the growth of spheroids does not affect GSC cell response to H-FIRE treatment.

7.4 Discussion

The results of this study show that H-FIRE can be an effective therapy for the ablation of GSCs. Though these cells may be resistant to other therapies, they are susceptible to H-FIRE ablation on a similar scale to bulk tumor cells and significantly more susceptible than healthy astrocytes. Interestingly, two of the GSC populations tested (VTC061 and VTC064) have been shown previously to be resistant to chemotherapeutics (362) while another (MES 326) has been shown to be resistant to radiation therapy (349). Therefore, the ablation of these cell populations represents a successful treatment of therapy-resistant cells that may repopulate tumors if found *in vivo*. The nuclear size of GSCs is enlarged as seen in other malignant cells, and our measurements on H-FIRE thresholds are consistent with the hypothesis that NCR is an important predictor of cell response to H-FIRE. It is important to note that while the GSCs presented here exhibit the enlarged NCR seen *in vivo* (359), the morphology of these cells in the collagen hydrogel does not reflect the morphology of these cells *in vivo*. Importantly for this study, the hydrogel platform was able to provide a 3D environment where enlarged nuclei could be confirmed in patient derived cells and this variable could be correlated to lethal electric field threshold. However, collagen is not an

ideal material for recapitulating stem cell properties found *in vivo*. Future work will explore hydrogels composed of more physiologically relevant materials such as hyaluronic acid. Recreating the morphology of GSCs using *in vitro* models remains a challenge. Future work will be done where H-FIRE ablation is tested on biopsies of canine patient tissues in which the response of an *in vivo* morphology can be compared to the responses seen *in vitro*. Despite any lack of physiological relevance for GSC morphology in hydrogel tissue mimics, the high nuclear to cytoplasmic ratio of GSCs has been confirmed *in vivo* (359, 360, 363). The experimental evidence presented throughout this dissertation suggests a strong correlation between NCR and lethal electric field threshold for H-FIRE treatment that is expected to extend to *in vivo* morphologies, suggesting that the results of GSC ablation presented here should be applicable to more physiologically relevant morphologies of GSCs as well.

Informed by our experiments carried out in Chapter 6, we used the shortest pulse width and pulse duration possible while maintaining the stability of the electronics. As these experiments progress, so too have the capabilities of the electronics as we continually improve the pulse generator used for H-FIRE delivery. For the experiments performed in this chapter, a pulse waveform of 0.5µs-2µs-0.5µs was used. In the experiments presented in Chapters 4 and 5, a 1µs-5µs-1µs pulse waveform of was used, as this was the shortest pulse width and inter-pulse delay available to us at the time of these experiments. Consistent with the results presented in Chapter 6, changing the pulse waveform resulted in a change in the selectivity accomplished by H-FIRE. Decreasing the pulse wave length improves the ability of H-FIRE to selectively target GSCs over both healthy astrocytes and bulk tumor cells. This is hypothesized to be due to the enhanced NCR in GSCs relative to the bulk tumor cells and healthy astrocytes. As the waveform shifts to one of shorter

pulse duration and shorter inter-pulse delay, the majority of the power is delivered at a higher-frequency. This allows more of the electric field to bypass the cell membrane and interact with the enlarged nucleus. As the capabilities of the electronics in the pulse generator continue to improve, it will be important to further optimize these pulse parameters for malignant cell selectivity.

The results of this study confirm and expand on previous results demonstrating a lower H-FIRE threshold is required for ablation of malignant cells than for healthy cells. The results of this study add robustness to this conclusion as all previous malignant cells used were immortalized cell lines. The use of patient derived cells in this study adds a degree of clinical relevance to the conclusions regarding the relationship between lethal threshold and malignancy. This study demonstrates the feasibility of using patient derived cells for therapy testing if different thresholds are found for different patient samples. This use of patient-specific cells could be expanded for determination of lethal thresholds for personalized treatment of individual tumors.

The results of this study may be of high clinical relevance because they suggest an option for treatment of cells currently considered therapy-resistant. Assuming that there may be a subclass of cells that have some degree of resistance to H-FIRE therapy, there is no reason to believe these populations would overlap with populations resistant to other therapies. We have demonstrated successful and selective ablation of a population of cells previously shown to be highly resistant to radiotherapy (MES 326) and chemotherapy (VTC064 and VTC061) (349, 362). These results suggest H-FIRE may be a valuable therapy to be used in conjunction with more traditional therapies to reduce the population of resistant cells that may be left behind to cause tumor

recurrence. Studies have shown cancer stem cells usually exist in a quiescent state but the population may grow exponentially when stimulated by surgery, chemotherapy, and radiotherapy (364). Further studies must be done to ensure H-FIRE does not produce an increase in growth kinetics of these GSCs. If no such effect is found, it may be a valuable practice to follow surgery, chemotherapy, and radiotherapy used in GBM treatment with a regime of H-FIRE pulses. This may protect against GSCs causing a recurrent tumor as the result of therapy resistance and increased growth.

Chapter 8 Summary

8.1 Introduction

Irreversible electroporation is a form of pulsed electric field therapy used for ablating tissue in a minimally invasive non-thermal manner. Useful in the clinical setting for treatment of cancer, IRE involves introducing electrodes into and around a tumor and delivering a train of pulses of relatively high amplitude and low duration. This technique is currently used clinically for the treatment of several types of cancers, including with liver, kidney, pancreatic, and prostate cancer (187, 195, 198, 199, 365). Additionally the safe and effective IRE treatment of spontaneous canine gliomas has been demonstrated (184).

High-frequency irreversible electroporation is a second generation form of IRE which was developed primarily as a means to mitigate muscle contractions upon treatment with the goal of reducing the need for general anesthesia and neuroparalytic agents. Beyond these features, H-FIRE has important differences from IRE on the level of cellular response that we hypothesized could make it useful as a selective therapy.

The goal of this dissertation was to describe the development and testing of high-frequency irreversible electroporation as a selective therapy for the treatment of brain cancer. To accomplish this we performed experiments testing the effect of H-FIRE on a variety of cells representative of those found in the brain tumor microenvironment, including bulk glioblastoma cells, healthy astrocytes, healthy neurons, and glioma stem cells. These cell responses were compared to responses achieved with IRE treatment. Through manipulating both the biophysics of the cell and

the pulse parameters of the treatment, we have made progress towards enhancing the selectivity of electroporation therapy for malignant cell ablation.

8.2 What this dissertation accomplished

In this dissertation, we hypothesized that by lowering the pulse duration of a classical irreversible electroporation treatment, in the form of high-frequency irreversible electroporation, we could induce selective malignant cell killing through interaction with the altered inner organelles in cancer cells. Because cancer cells often exhibit morphological alterations from normal cells, such as enlarged nuclei, we hypothesized that we could use H-FIRE to target these alterations in a way that may produce a selective therapy.

In Chapter 4, our finite element models of experimental cell morphologies exposed to experimental electric field distributions confirmed that the electric fields, though confined to the cell membrane in IRE pulses, should be able to partially bypass the outer membrane with H-FIRE pulses to interact with the inner organelles. H & E staining of canine patients' tumor tissue and healthy tissue showed that enlarged nuclear to cytoplasm ratio is a marker of cancerous cells in glioblastoma multiforme. Culture of a number of different cell types, including multiple human and rat glioblastoma lines, human and rat healthy astrocytes, and healthy neuron-like cells, confirmed the trend of enlarged nuclear to cytoplasm ratio in malignant cells compared to healthy cells when cultured in 3D hydrogel tissue mimics. Tissue engineering methods for hydrogel construction allowed for the isolation of nuclear size as the key morphological variable across cell types cultured in collagen hydrogels. Within the hydrogel platform, the responses of multiple cell

types to IRE (100 µs) and H-FIRE (1 µs) pulses were studied. Live/dead staining of electroporation treated hydrogels was used to determine ablation area which was correlated to a lethal electric field threshold using COMSOL modeling of the electric field distribution within the treated hydrogel. An important trend emerged from these studies. Consistent with previous studies and classical electroporation theory, IRE lesions were similar across all cell types with similar cell area. Interestingly, cell-seeded hydrogels treated with H-FIRE pulses differed in lesion size depending on the size of the nucleus in the particular cell line. Cell lines with larger nuclei—the malignant cells tested—displayed greater ablation areas and thus lower lethal electric field thresholds than cell lines with smaller relative nuclei—the healthy cell lines tested. This correlation strengthens our hypothesis informed by mathematical modeling that electric fields created by H-FIRE pulses may bypass the cell membrane to target altered morphological structures inside the cancerous cell such as enlarged nuclei. Fluorescent microscopy of single cells undergoing treatment with either IRE or H-FIRE showed a difference in death mechanism between the two treatments. Upon exposure to IRE a cell is likely to experience the dissipation of cytoplasm from the outer membrane as defects form, while cells treated with H-FIRE exhibit a consistent decrease of stained nuclear area. Though these differences have been observed, the specific mechanism of cell death with H-FIRE has yet to be characterized.

We demonstrated the inherent selectivity of H-FIRE for ablation of malignant cells at an electric field range of approximately 600 V/cm to 1000 V/cm for the pulse parameters studied. This finding is significant as it increases our understanding of the complexity of electroporation phenomenon past the simplified rule of electroporation theory that maintains electroporation extent at a given voltage depends primarily on cell size. Additionally, this finding represents the identification and

targeting of a conserved alteration in glioblastoma cells—enlarged nuclear to cytoplasm ratio—that has not previously been used as a therapeutic target, though it represents a key diagnostic phenotype used routinely by pathologists. Despite the importance of the inherent selectivity of H-FIRE demonstrated in Chapter 4, this range of selective malignant cell killing achieved with high-frequency pulses, when translated into a clinical ablation, only allows for safe ablation of millimeters past the visible tumor margin. Therefore, attempts were made in Chapters 5 and 6 to extend the region of selectivity achieved by H-FIRE by manipulating cell biophysics and manipulating pulse parameters, respectively.

In Chapter 5, we demonstrated that the biophysics of a cell can be externally manipulated in a way that allows for greater malignant cell selectivity to be achieved with H-FIRE pulses. Using the same H-FIRE pulse waveform as used in the studies in Chapter 4, a 1 μs bipolar pulse separated by a 5 μs delay, we were able to extend ablation area of malignant cells by around 30% while avoiding an extension of healthy cell ablation areas. This was accomplished by using a targeted molecular therapy to shrink the cytoplasm of malignant cells. The EphA2 receptor which is overexpressed on glioblastoma cells compared to healthy brain cells, when bound by its preferred ligand, eA1, induces a morphology change characterized by a shrinking of the cytoplasm, which effectively induces an increase in NCR. This molecular therapy was used to confirm the importance of NCR as a variable in predicting electroporation response, demonstrate an external manipulation of cellular biophysics, and improve selectivity for malignant cell ablation. We confirmed that within the hydrogel platform, malignant glioma cells treated with eA1 ligand underwent a morphology change that produced an increased NCR. Healthy astrocytes kept a similar morphology to that seen before treatment, unaffected by eA1 presumably due to the low

level of EphA2 receptors on the astrocytes. The morphology change induced in malignant cells resulted in enlarged ablation area in the hydrogels, corresponding to significantly lower lethal electric field thresholds. Alternatively, healthy cells treated with eA1 and H-FIRE exhibited no change in ablation area. Because of the selectivity of the eA1-induced morphology change for malignant cells, inherent in the natural expression of EphA2, this combination treatment resulted in greater selective malignant cell killing compared to H-FIRE alone. This selectivity enhancement was demonstrated in co-culture hydrogels of malignant U87 cells and healthy NHAs. Using experimentally-determined lethal electric field thresholds, we predicted the effect of this enhanced selectivity *in vivo* using finite element modeling of a canine patient's brain tumor. Finite element models predicted that by using combination eA1 and H-FIRE treatment we can safely treat significantly more of a patient tumor than with either H-FIRE or IRE alone.

To understand the effect demonstrated in these experiments, which is contrary to classical electroporation theory which holds larger cells will experience greater electroporation at the same applied voltage, we looked at the effect of frequency on cell response using finite element modeling. Experimental cell morphologies of both healthy astrocytes and malignant glioma cells, both untreated and treated with eA1 were used in mathematical models. Our findings showed that at a pulse frequency of around 10^4 Hz, a glioma cell with the enlarged nucleus compare to the healthy cell, will experience a greater induced TMP on the cell membrane. At a slightly higher pulse frequency, around 10^5 Hz, the eA1 treated glioma cell with an enlarged nucleus and reduced cell size will experience a greater induced TMP than either the untreated glioma cell or the treated or untreated healthy cell. These results highlight the importance of pulse frequency in predicting electroporation response of a cell. Additionally they inform general electroporation theory as to

the complexities involved in the relationship between electroporation, pulse frequency, cell size, and the effect of inner organelles.

In Chapter 6, we explored how different pulse variables affect malignant cell selectivity with electroporation therapy. The number of variables that can be explored in a given electroporation regime are numerous, highlighting the importance of vitro 3D hydrogel platforms for testing. In this chapter we explored the effect of pulse duration, inter-pulse delay and pulse number on the ablation of malignant cells and healthy astrocytes with the goal of achieving maximum selectivity within the experimental system. We showed that malignant cell selectivity increases as pulse width decreases, with the greatest selectivity achieved for the shortest pulse duration studied—1 μs. Similarly, selectivity increases as the delay between pulses is decreased with the greatest selectivity in our system achieved for the shortest inter-pulse delay studied—again 1 μs. Of the two, we showed that pulse duration seems to have a greater effect on selectivity than inter-pulse delay. Our studies on the effect of changing pulse number showed evidence that there is an optimal pulse number for selectivity, beyond which the lethal electric field thresholds for malignant cells and healthy cells begin to converge. For the system studied, the optimal pulse number was 50 pulses, information which is important for informing future studies. These findings highlight the importance of pulse variables in determining electroporation response and could be useful for informing the design of electrode configuration in clinical regimes using multiple electrode insertions.

In Chapters 4-6, the focus is the ablation of bulk malignant cells. The motivation for the selective ablation achieved and enhanced in these chapters is primarily focused on the invasive cells that spread past the tumor margin and escape surgical resection. In Chapter 7, we focus on the second class of therapy-resistant cells problematic in glioma recurrence—glioma stem cells. In this Chapter, we demonstrate that the selective ablation of H-FIRE extends to patient-derived glioma stem cells. Interestingly, H-FIRE is more effective at ablating the GSCs studied than the bulk tumor cells or healthy cells studied when using 500ns pulses. Within the culture of the hydrogel, the GSCs exhibit enlarged nuclear to cytoplasm ratio to an even greater extent than bulk glioma cells. This correlates with lower electric field thresholds for cell death. The selectivity of GSCs, then, extends beyond that of bulk glioma cells. Importantly, we demonstrated effective ablation of two cell populations previously determined to be resistant to chemotherapeutics and one population previously determined to be resistant to radiotherapies, suggesting the ability to ablate cells that are likely responsible for recurrence *in vivo*. Glioma stem cells are an important class of cells given much attention in current research into glioblastoma treatments. The results presented in this chapter represent an exciting extension of the selective capabilities of H-FIRE therapy to another highly problematic class of cells.

Overall, the goals of this work were to demonstrate the selectivity of an electroporation therapy for two important class of cells considered problematic in a glioblastoma tumor. To that end, we have been successful in demonstrating inherent selectivity of IRE by decreasing pulse duration to fall in the high-frequency range, specifically prevalent with pulses of 0.5 -1 μs duration. We have successfully extended the margin of selectivity achieved by H-FIRE both by tuning pulse parameters, and by using a combination therapy with molecular targeted eA1 ligand to enhance

the enlarged NCR of cancer cells. Finally, we have demonstrated successful ablation of therapy-resistant GSCs. This dissertation represents the beginnings of the development of a selective therapy for GBM that has promise for use in the clinic. Additionally, the thorough exploration of cellular response in the frequency range of H-FIRE pulses, a range previously minimally explored, has helped to inform electroporation theory. Many of the predictions of steady-state electroporation theory do not hold for H-FIRE length pulses, a fact that should be considered when exploring these pulses for treatment of tissue *in vivo*. Additionally, an understanding of the complexitity of electroporation phenomenon in these frequency ranges may be valuable for electroporation tools in basic research, such as gene transfection applications. Many pulse parameters remain to be explored and further efforts to enhance the selectivity margin will prove useful in translating this therapy to the clinic for treatment of brain cancer.

8.3 Future work

Two important questions remain to be explored as extensions of this dissertation work. The first is what the specific mechanism of cell death is with H-FIRE treatment. By gaining knowledge of the mechanism by which H-FIRE induces cell death, we hope to be able to gain better ideas on methods to enhance the malignant cell selectivity demonstrated in this work. Understanding the mechanism of H-FIRE and the differences of the death response at the cellular level when treated with H-FIRE and IRE is the next step in propelling investigations of other interventions and manipulations that may be useful for improving the efficacy of the therapy. Secondly, though *in vitro* studies are invaluable in the early stages of developing this treatment method, ultimately the goal is to develop the treatment to be used clinically for the treatment of glioblastoma. There are a multitude of variables found *in vivo* that may diminish the selectivity demonstrated here *in vitro*.

Our next efforts in the course of developing this selective treatment is to test the findings presented here in an *in vivo* context to confirm the ability to translate these findings to the clinic.

8.3.1 Mechanism of H-FIRE

Future work on this project will include a further investigation of the mechanism of both H-FIRE and IRE at the cellular and subcellular level. Because pulse duration determines how the cell interacts with the electric field, many results reported may not hold for different regimes that use different pulse parameters. For pulse durations longer than 10 μs, poration of the cell membrane seems to be a consistent response to treatment. Cells exposed to 100 μs IRE pulses were observed using scanning electron microscopy and were seen to exhibit nanometer sized pores in the cell membrane (160). However, reports have stated that nanosecond pulses can affect intracellular structures without first electroporating the outer membrane (248). Though other groups have suggested that even at pulse widths of 2ns small pores form in the plasma membrane (243). The conflicting results reported are compounded by the fact that membrane charging times are not set properties of the cell but are sensitive to differences in geometric and dielectric properties of the cell and surrounding environment.

Membrane poration

Our own work comparing the mechanism of IRE and H-FIRE has shown cell membrane permeabilization with all pulse durations tested, from the 100 μs pulse IRE case down to the 500 ns H-FIRE pulses. The plasma membrane permeabilization was observed as the fluorescence of propidium iodide (PI) entering the cell immediately upon pulsing. Thus, we know that even the pulse trains of the shortest duration tested (500 ns) are affecting the plasma membrane. It will be

a priority in future work to determine if any inner organelle membranes are also being affected. Our previous finite element modeling has predicted that a larger portion of the electric field reaches the inside of the cell with H-FIRE pulses. It has been theorized that the threshold value for electroporation may be less for inner organelles, because these membranes have greater curvature than the plasma membrane (262, 366). The possibility of inner organelle electroporation should be explored with unbound stains for internal organelles of interest, such as the nucleus and mitochondria.

Apoptosis vs. necrosis vs. autophagy

In addition to evidence of inner membrane permeabilization, a priority of future work will be on characterizing the necrotic, apoptotic, or autophagic death response that occurs after treatment by IRE or H-FIRE. There have been a variety of conflicting results reported as to how IRE induces cell death. Cell death by apoptosis (367, 368) and by necrosis (369, 370) have both been reported. Despite the challenges and complications involved in determining the mechanistic pathway of cell death with IRE and H-FIRE, it is an important path to pursue in future work. It seems likely that the two regimes will fall on different places on the apoptosis-necrosis spectrum. Whereas necrotic cell death has been reported for IRE pulses in the 100 microsecond pulse duration range (369, 370), most groups investigating nsPEF have reported cell death by apoptosis while the evidence for necrotic cell death with nsPEFs seems to be limited. Two hypothesis for the mechanism of necrotic cell death with IRE seem likely. The first is that IRE treatment causes the formation of a population of pores in such significant numbers and/or size that pores become held open permanently. This permanent pore could be due to the interaction between a formed pore and a channel or other structures within the membrane. The irreversible trapping of pores then causes a

lethal biochemical imbalance leading to cell death. The second hypothesis attributes cell death to internal cellular compartments which are exposed to a lethal biochemical change even if the initial pores reseal after a short time (159). For nsPEFs, it is generally assumed initial pores in the plasma membrane reseal and death is a product of chemical imbalances in cellular compartments, such as the release of calcium activating apoptotic pathways (334, 335). Because H-FIRE pulse regimes lie somewhere in between the spectrum of cellular response of IRE and nsPEFs, the death mechanism for H-FIRE remains largely unexplored.

In order to further investigate the question of how IRE and H-FIRE induce cell death, Western blotting can be used to determine protein levels for common apoptotic and autophagic markers. These markers include pro/p17-caspase 3, cleaved PARP, muscle actin for apoptosis and LC3A/B, P62, Atg5, and Beclin 1 for autophagy. By comparing the level of apoptotic and autophagic markers in cells exposed to different pulse regimes, it should be possible to determine if shorter pulses may invoke more of an apoptotic response while longer pulses cause more necrosis to occur. If caspase activation is observed, a further mechanistic understanding can be found by looking at calcium release using calcium indicators such as Fura-2 or Calcium Green, loaded into cells before treatment.

The determination of H-FIRE mechanism is important for both clinical application as well as for guiding further experimental investigations. Necrotic and apoptotic cell death mechanisms manifest differently in clinical response as necrosis has been shown to induce an inflammatory response while apoptosis has not (371). Therefore, answering the question of H-FIRE mechanism

may lead to measures to improve clinical outcomes. Additionally, by understanding the lethal mechanism of H-FIRE, we may gain knowledge that would help pinpoint variables to be manipulated to optimize cell death.

8.3.2 Determination of selectivity *in vivo*

The ultimate goal of this work is to form a basis for developing a therapy to be used for the treatment of human glioblastoma. The next major step along that path is to test the therapy *in vivo*. This *in vivo* testing will happen in two stages, first in a rat model of glioblastoma followed by testing on canine patients with spontaneous brain tumors.

Though mouse models are the most common *in vivo* cancer model, for this application a rat model is preferable due to the limitations associated with the surgery and electrode insertion in a model as small as a mouse. The larger size of the rat model is more appropriate for these studies. Human malignant glioma cells will be implanted in anesthetized rats using sterile, stereotactic surgery to accomplish injection of cells into the brain via a needle. The model will be of human glioma cells seeded in a rat brain in order to maintain the brain tumor microenvironment, which is integral in establishing physiological relevance for glioma treatment testing. After treatment with H-FIRE, alone or in combination with eA1, rat brains can be sectioned and submitted for histological analysis. A variety of standard (HE) and immunohistochemical stains will be used to facilitate observation of treatment-related effects. This model can be used for studying the selective abilities of H-FIRE alone and in combination with eA1. Additionally, this model will give us information about how the lethal thresholds change from *in vitro* platforms to *in vivo* platforms.

After H-FIRE efficacy is established in the rat brain tumor model, testing will be done in canine patients, to further improve the relevance to humans. Canine patients are an ideal model for testing next generation GBM therapies because dogs are the only species other than humans in which spontaneous primary brain tumors are common. These tumors are three times more common in dogs, making them a relatively readily available model (372, 373). Additionally, it has been demonstrated that EphA2 is overexpressed in canine gliomas as in human gliomas (374), opening up this model for testing biophysics manipulation with eA1. Unlike rodent models where injected tumors are often small and treatment application must be scaled down, spontaneous brain tumors of dogs are large enough to allow for testing of devices, concentrations, and pulse parameters that can be easily scaled to human patients.

We have previously treated 3 canine patients diagnosed with meningiomas with H-FIRE therapy and have demonstrated the feasibility of the treatment for spontaneous brain tumors in canines. The treated patients exhibited no signs of muscle contractions during treatment, sharp delineation between treated and untreated regions in biopsied samples, and no adverse effects. However, we have yet to demonstrate selective killing of malignant cells. The demonstration of selective malignant cell killing at the tumor margin is a goal of future work. In order to inform canine treatment, it will be valuable to treat biopsies of canine tumor tissue and healthy tissue to determine lethal electric field thresholds relevant to the *in vivo* canine model. Additionally, a demonstration of the ablation of GSCs in a canine patient is a necessary part of future work.

8.4 Published work

J.W. Ivey, E.L. Latouche, M.L. Richards, G.J. Lesser, W. Debinski, R.V. Davalos, S.S. Verbridge, Enhancing Irreversible Electroporation by Manipulating Cellular Biophysics with a Molecular Adjuvant, *Biophysical Journal*, 113, 472-480 (2017).

J.W. Ivey, E.L. Latouche, M.B. Sano, J.H. Rossmeisl, R.V. Davalos, S.S. Verbridge, Targeted cellular ablation based on the morphology of malignant cells, *Scientific reports*, 5, (2015).

J.W. Ivey, M. Bonakdar, A. Kanitkar, R.V. Davalos, S.S. Verbridge, Improving cancer therapies by targeting the physical and chemical hallmarks of the tumor microenvironment, *Cancer Letters* (2015).

E.M. Wasson, J.W. Ivey, S.S. Verbridge, R.V. Davalos, The feasibility of enhancing susceptibility of glioblastoma cells to IRE using a calcium adjuvant, *Annals of Biomedical Engineering*:1-13 (2017).

B. Balhouse, J. Ivey, S.S. Verbridge, "Engineering microenvironments for cancer study." *Three-Dimensional Microfabrication Using Two-Photon Polymerization.* Ed. Tommaso Bladacchini, Elsevier (2015).

E.L. Latouche, C.B. Arena, J.W. Ivey, P.A. Garcia, T.E. Pancotto, S.S. Verbridge, J.H Rossmeisl, and R.V. Davalos, High-frequency irreversible electroporation for the ablation of brain tumors: A feasibility study. (Submitted)

Chapter 9 References

1. Torre LA, Bray F, Siegel RL, Ferlay J, Lortet-Tieulent J, & Jemal A (2015) Global cancer statistics, 2012. *CA: A Cancer Journal for Clinicians* 65(2):87-108.
2. Jemal A, Center MM, Desantis C, & Ward EM (2010) Global patterns of cancer incidence and mortality rates and trends. *Cancer Epidemiology and Prevention Biomarkers* 19(8):1893-1907.
3. Arora RS, Alston RD, Eden TO, Estlin EJ, Moran A, & Birch JM (2009) Age-incidence patterns of primary cns tumors in children, adolescents, and adults in england. *Neuro Oncology* 11(4):403-413. Epub 2008 Nov 2024.
4. Stupp R, Mason WP, Van Den Bent MJ, Weller M, Fisher B, Taphoorn MJ, *et al.* (2005) Radiotherapy plus concomitant and adjuvant temozolomide for glioblastoma. *New England Journal of Medicine* 352(10):987-996.
5. Berger MS (1994) Malignant astrocytomas: Surgical aspects. *Seminars in Oncology* 21(2):172-185.
6. Shaw EJ (2000) Central nervous system overview. *Clinical Radiation Oncology*, eds Gunderson LL & Tepper JE (Churchill-Livingstone, Philadelphia, PA), pp 314-354.
7. Lesser GJ & Grossman S (1994) The chemotherapy of high-grade astrocytomas. *Seminars in Oncology* 21(2):220-235.
8. Bock HC, Puchner MJA, Lohmann F, Schütze M, Koll S, Ketter R, *et al.* (2010) First-line treatment of malignant glioma with carmustine implants followed by concomitant radiochemotherapy: A multicenter experience. *Neurosurgical Review* 33(4):441-449.
9. Vredenburgh JJ, Desjardins A, Herndon JE, Dowell JM, Reardon DA, Quinn JA, *et al.* (2007) Phase ii trial of bevacizumab and irinotecan in recurrent malignant glioma. *Clinical Cancer Research* 13(4):1253-1259.
10. Gilbert MR, Dignam JJ, Armstrong TS, Wefel JS, Blumenthal DT, Vogelbaum MA, *et al.* (2014) A randomized trial of bevacizumab for newly diagnosed glioblastoma. *New England Journal of Medicine* 370(8):699-708.
11. Paszek MJ, Zahir N, Johnson KR, Lakins JN, Rozenberg GI, Gefen A, *et al.* (2005) Tensional homeostasis and the malignant phenotype. *Cancer Cell* 8(3):241-254.
12. Siegel RL, Miller KD, & Jemal A (2016) Cancer statistics, 2016. *CA: A Cancer Journal for Clinicians* 66(1):7-30.
13. Thun MJ, Delancey JO, Center MM, Jemal A, & Ward EM (2009) The global burden of cancer: Priorities for prevention. *Carcinogenesis* 31(1):100-110.
14. Szakács G, Paterson JK, Ludwig JA, Booth-Genthe C, & Gottesman MM (2006) Targeting multidrug resistance in cancer. *Nature Reviews Drug discovery* 5(3):219-234.
15. Dean M, Fojo T, & Bates S (2005) Tumour stem cells and drug resistance. *Nature Reviews Cancer* 5(4):275-284.
16. Putt KS, Chen GW, Pearson JM, Sandhorst JS, Hoagland MS, Kwon J-T, *et al.* (2006) Small-molecule activation of procaspase-3 to caspase-3 as a personalized anticancer strategy. *Nature Chemical Biology* 2(10):543-550.
17. Sebolt-Leopold JS & English JM (2006) Mechanisms of drug inhibition of signalling molecules. *Nature* 441(7092):457-462.
18. Galluzzi L, Vitale I, Vacchelli E, & Kroemer G (2011) Cell death signaling and anticancer therapy. *Frontiers in Oncology* 1:5.

19. Malik IA, Naz N, Sheikh N, Khan S, Moriconi F, Blaschke M, *et al.* (2011) Comparison of changes in gene expression of transferrin receptor-1 and other iron-regulatory proteins in rat liver and brain during acute-phase response. *Cell and Tissue Research* 344(2):299-312.
20. Di Fiore PP, Pierce JH, Fleming TP, Hazan R, Ullrich A, King CR, *et al.* (1987) Overexpression of the human egf receptor confers an egf-dependent transformed phenotype to nih 3t3 cells. *Cell* 51(6):1063-1070.
21. Kraus MH, Popescu N, Amsbaugh S, & King CR (1987) Overexpression of the egf receptor-related proto-oncogene erbb-2 in human mammary tumor cell lines by different molecular mechanisms. *The EMBO Journal* 6(3):605.
22. Hynes NE & Lane HA (2005) Erbb receptors and cancer: The complexity of targeted inhibitors. *Nature Reviews Cancer* 5(5):341-354.
23. Delaney G, Jacob S, Featherstone C, & Barton M (2005) The role of radiotherapy in cancer treatment. *Cancer* 104(6):1129-1137.
24. Durante M & Loeffler JS (2010) Charged particles in radiation oncology. *Nature Reviews Clinical Oncology* 7(1):37-43.
25. Luqmani Y (2005) Mechanisms of drug resistance in cancer chemotherapy. *Medical Principles and Practice* 14(Suppl. 1):35-48.
26. Rodemann HP, Dittmann K, & Toulany M (2007) Radiation-induced egfr-signaling and control of DNA-damage repair. *International Journal of Radiation Biology* 83(11-12):781-791.
27. Engelman JA (2009) Targeting pi3k signalling in cancer: Opportunities, challenges and limitations. *Nature Reviews Cancer* 9(8):550-562.
28. Khodarev NN, Beckett M, Labay E, Darga T, Roizman B, & Weichselbaum RR (2004) Stat1 is overexpressed in tumors selected for radioresistance and confers protection from radiation in transduced sensitive cells. *Proceedings of the National Academy of Sciences of the United States of America* 101(6):1714-1719.
29. Skvortsova I, Skvortsov S, Stasyk T, Raju U, Popper BA, Schiestl B, *et al.* (2008) Intracellular signaling pathways regulating radioresistance of human prostate carcinoma cells. *Proteomics* 8(21):4521-4533.
30. Busby EC, Leistritz DF, Abraham RT, Karnitz LM, & Sarkaria JN (2000) The radiosensitizing agent 7-hydroxystaurosporine (ucn-01) inhibits the DNA damage checkpoint kinase hchk1. *Cancer Research* 60(8):2108-2112.
31. Veuger SJ, Curtin NJ, Richardson CJ, Smith GC, & Durkacz BW (2003) Radiosensitization and DNA repair inhibition by the combined use of novel inhibitors of DNA-dependent protein kinase and poly (adp-ribose) polymerase-1. *Cancer Research* 63(18):6008-6015.
32. Hickson I, Zhao Y, Richardson CJ, Green SJ, Martin NM, Orr AI, *et al.* (2004) Identification and characterization of a novel and specific inhibitor of the ataxia-telangiectasia mutated kinase atm. *Cancer Research* 64(24):9152-9159.
33. Mi J, Bolesta E, Brautigan DL, & Larner JM (2009) Pp2a regulates ionizing radiation–induced apoptosis through ser46 phosphorylation of p53. *Molecular cancer therapeutics* 8(1):135-140.
34. Gupta AK, Bakanauskas VJ, Cerniglia GJ, Cheng Y, Bernhard EJ, Muschel RJ, *et al.* (2001) The ras radiation resistance pathway. *Cancer Research* 61(10):4278-4282.

35. Brach M, Hass R, Sherman M, Gunji H, Weichselbaum R, & Kufe D (1991) Ionizing radiation induces expression and binding activity of the nuclear factor kappa b. *Journal of Clinical Investigation* 88(2):691.
36. Criswell T, Leskov K, Miyamoto S, Luo G, & Boothman DA (2003) Transcription factors activated in mammalian cells after clinically relevant doses of ionizing radiation. *Oncogene* 22(37):5813-5827.
37. Longley D & Johnston P (2005) Molecular mechanisms of drug resistance. *The Journal of Pathology* 205(2):275-292.
38. Swanton C (2012) Intratumor heterogeneity: Evolution through space and time. *Cancer Research* 72(19):4875-4882.
39. Gottesman MM, Fojo T, & Bates SE (2002) Multidrug resistance in cancer: Role of atp–dependent transporters. *Nature Reviews Cancer* 2(1):48-58.
40. Kibria G, Hatakeyama H, & Harashima H (2014) Cancer multidrug resistance: Mechanisms involved and strategies for circumvention using a drug delivery system. *Archives of Pharmacal Research* 37(1):4-15.
41. Persidis A (1999) Cancer multidrug resistance. *Nature biotechnology* 17(1):94-95.
42. Higgins CF (1992) Abc transporters: From microorganisms to man. *Annual review of cell biology* 8(1):67-113.
43. Endicott JA & Ling V (1989) The biochemistry of p-glycoprotein-mediated multidrug resistance. *Annual review of biochemistry* 58(1):137-171.
44. Gottesman MM, Pastan I, & Ambudkar SV (1996) P-glycoprotein and multidrug resistance. *Current opinion in genetics & development* 6(5):610-617.
45. Mickley LA, Spengler BA, Knutsen TA, Biedler JL, & Fojo T (1997) Gene rearrangement: A novel mechanism for mdr-1 gene activation. *Journal of Clinical Investigation* 99(8):1947.
46. Petty R, Evans A, Duncan I, Kurbacher C, & Cree I (1998) Drug resistance in ovarian cancer—the role of p53. *Pathology & Oncology Research* 4(2):97-102.
47. Johnson KR & Fan W (2002) Reduced expression of p53 and p21waf1/cip1 sensitizes human breast cancer cells to paclitaxel and its combination with 5-fluorouracil. *Anticancer research* 22(6A):3197-3204.
48. Burger H, Nooter K, Boersma AW, Van Wingerden KE, Looijenga LH, Jochemsen AG, *et al.* (1999) Distinct p53-independent apoptotic cell death signalling pathways in testicular germ cell tumour cell lines. *International Journal of Cancer* 81(4):620-628.
49. Rosell R, Taron M, Ariza A, Barnadas A, Mate JL, Reguart N, *et al.* (2004) Molecular predictors of response to chemotherapy in lung cancer. *Seminars in Oncology*, (Elsevier), pp 20-27.
50. Wright JA, Smith HS, Watt FM, Hancock MC, Hudson DL, & Stark GR (1990) DNA amplification is rare in normal human cells. *Proceedings of the National Academy of Sciences* 87(5):1791-1795.
51. Miller W (2004) Biological rationale for endocrine therapy in breast cancer. *Best Practice & Research Clinical Endocrinology & Metabolism* 18(1):1-32.
52. Campos SM (2004) Aromatase inhibitors for breast cancer in postmenopausal women. *The oncologist* 9(2):126-136.
53. Minchinton AI & Tannock IF (2006) Drug penetration in solid tumours. *Nature Reviews Cancer* 6(8):583-592.

54. Jain RK (2005) Normalization of tumor vasculature: An emerging concept in antiangiogenic therapy. *Science* 307(5706):58-62.
55. Stylianopoulos T, Martin JD, Chauhan VP, Jain SR, Diop-Frimpong B, Bardeesy N, *et al.* (2012) Causes, consequences, and remedies for growth-induced solid stress in murine and human tumors. *Proceedings of the National Academy of Sciences* 109(38):15101-15108.
56. Bae YH & Park K (2011) Targeted drug delivery to tumors: Myths, reality and possibility. *Journal of Controlled Release* 153(3):198.
57. Jain RK, Martin JD, & Stylianopoulos T (2014) The role of mechanical forces in tumor growth and therapy. *Annual Review of Biomedical Engineering* 16:321.
58. Goel S, Duda DG, Xu L, Munn LL, Boucher Y, Fukumura D, *et al.* (2011) Normalization of the vasculature for treatment of cancer and other diseases. *Physiological Reviews* 91(3):1071-1121.
59. Ivey JW, Bonakdar M, Kanitkar A, Davalos RV, & Verbridge SS (2015) Improving cancer therapies by targeting the physical and chemical hallmarks of the tumor microenvironment. *Cancer Letters*.
60. Fisher R, Pusztai L, & Swanton C (2013) Cancer heterogeneity: Implications for targeted therapeutics. *British Journal of Cancer* 108(3):479-485.
61. Jones S, Zhang X, Parsons DW, Lin JC-H, Leary RJ, Angenendt P, *et al.* (2008) Core signaling pathways in human pancreatic cancers revealed by global genomic analyses. *Science* 321(5897):1801-1806.
62. Parsons DW, Jones S, Zhang X, Lin JC-H, Leary RJ, Angenendt P, *et al.* (2008) An integrated genomic analysis of human glioblastoma multiforme. *Science* 321(5897):1807-1812.
63. Sjöblom T, Jones S, Wood LD, Parsons DW, Lin J, Barber TD, *et al.* (2006) The consensus coding sequences of human breast and colorectal cancers. *Science* 314(5797):268-274.
64. Varela I, Tarpey P, Raine K, Huang D, Ong CK, Stephens P, *et al.* (2011) Exome sequencing identifies frequent mutation of the swi/snf complex gene pbrm1 in renal carcinoma. *Nature* 469(7331):539-542.
65. Mardis ER, Ding L, Dooling DJ, Larson DE, Mclellan MD, Chen K, *et al.* (2009) Recurring mutations found by sequencing an acute myeloid leukemia genome. *New England Journal of Medicine* 361(11):1058-1066.
66. Network CGaR (2011) Integrated genomic analyses of ovarian carcinoma. *Nature* 474(7353):609-615.
67. Fidler IJ & Hart IR (1982) Biological diversity in metastatic neoplasms: Origins and implications. *Science* 217(4564):998-1003.
68. Nicolson GL (1984) Generation of phenotypic diversity and progression in metastatic tumor cells. *Cancer and Metastasis Reviews* 3(1):25-42.
69. Heppner GH (1984) Tumor heterogeneity. *Cancer Research* 44(6):2259-2265.
70. Marusyk A & Polyak K (2010) Tumor heterogeneity: Causes and consequences. *Biochimica et Biophysica Acta (BBA)-Reviews on Cancer* 1805(1):105-117.
71. Gerlinger M, Rowan AJ, Horswell S, Larkin J, Endesfelder D, Gronroos E, *et al.* (2012) Intratumor heterogeneity and branched evolution revealed by multiregion sequencing. *New England Journal of Medicine* 366(10):883-892.

72. Grossman SA, Ye X, Piantadosi S, Desideri S, Nabors LB, Rosenfeld M, *et al.* (2010) Survival of patients with newly diagnosed glioblastoma treated with radiation and temozolomide in research studies in the united states. *Clinical Cancer Research* 16(8):2443-2449.
73. Clarke J, Butowski N, & Chang S (2010) Recent advances in therapy for glioblastoma. *Archives of Neurology* 67(3):279-283.
74. Stupp R, Hegi ME, Mason WP, Van Den Bent MJ, Taphoorn MJ, Janzer RC, *et al.* (2009) Effects of radiotherapy with concomitant and adjuvant temozolomide versus radiotherapy alone on survival in glioblastoma in a randomised phase iii study: 5-year analysis of the eortc-ncic trial. *The Lancet Oncology* 10(5):459-466.
75. Stupp R, Tonn J-C, Brada M, Pentheroudakis G, & Group EGW (2010) High-grade malignant glioma: Esmo clinical practice guidelines for diagnosis, treatment and follow-up. *Annals of Oncology* 21(suppl 5):v190-v193.
76. Perry J, Okamoto M, Guiou M, Shirai K, Errett A, & Chakravarti A (2012) Novel therapies in glioblastoma. *Neurology Research International* 2012.
77. Siu A, Wind JJ, Iorgulescu JB, Chan TA, Yamada Y, & Sherman JH (2012) Radiation necrosis following treatment of high grade glioma—a review of the literature and current understanding. *Acta Neurochirurgica* 154(2):191-201.
78. Crossen JR, Garwood D, Glatstein E, & Neuwelt EA (1994) Neurobehavioral sequelae of cranial irradiation in adults: A review of radiation-induced encephalopathy. *Journal of Clinical Oncology* 12(3):627-642.
79. Van Tellingen O, Yetkin-Arik B, De Gooijer M, Wesseling P, Wurdinger T, & De Vries H (2015) Overcoming the blood–brain tumor barrier for effective glioblastoma treatment. *Drug Resistance Updates* 19:1-12.
80. Sarkaria JN, Kitange GJ, James CD, Plummer R, Calvert H, Weller M, *et al.* (2008) Mechanisms of chemoresistance to alkylating agents in malignant glioma. *Clinical Cancer Research* 14(10):2900-2908.
81. Phillips GDL, Li G, Dugger DL, Crocker LM, Parsons KL, Mai E, *et al.* (2008) Targeting her2-positive breast cancer with trastuzumab-dm1, an antibody–cytotoxic drug conjugate. *Cancer Research* 68(22):9280-9290.
82. Bonavia R, Cavenee WK, & Furnari FB (2011) Heterogeneity maintenance in glioblastoma: A social network. *Cancer Research* 71(12):4055-4060.
83. Sottoriva A, Spiteri I, Piccirillo SGM, Touloumis A, Collins VP, Marioni JC, *et al.* (2013) Intratumor heterogeneity in human glioblastoma reflects cancer evolutionary dynamics. *Proceedings of the National Academy of Sciences* 110(10):4009-4014.
84. Patel AP, Tirosh I, Trombetta JJ, Shalek AK, Gillespie SM, Wakimoto H, *et al.* (2014) Single-cell rna-seq highlights intratumoral heterogeneity in primary glioblastoma. *Science* 344(6190):1396-1401.
85. Snuderl M, Fazlollahi L, Le LP, Nitta M, Zhelyazkova BH, Davidson CJ, *et al.* (2011) Mosaic amplification of multiple receptor tyrosine kinase genes in glioblastoma. *Cancer Cell* 20(6):810-817.
86. Szerlip NJ, Pedraza A, Chakravarty D, Azim M, Mcguire J, Fang Y, *et al.* (2012) Intratumoral heterogeneity of receptor tyrosine kinases egfr and pdgfra amplification in glioblastoma defines subpopulations with distinct growth factor response. *Proceedings of the National Academy of Sciences* 109(8):3041-3046.

87. Meyer M, Reimand J, Lan X, Head R, Zhu X, Kushida M, *et al.* (2015) Single cell-derived clonal analysis of human glioblastoma links functional and genomic heterogeneity. *Proceedings of the National Academy of Sciences* 112(3):851-856.
88. Sottoriva A, Verhoeff JJ, Borovski T, Mcweeney SK, Naumov L, Medema JP, *et al.* (2010) Cancer stem cell tumor model reveals invasive morphology and increased phenotypical heterogeneity. *Cancer Research* 70(1):46-56.
89. Sottoriva A, Vermeulen L, & Tavaré S (2011) Modeling evolutionary dynamics of epigenetic mutations in hierarchically organized tumors. *PLoS Comput Biol* 7(5):e1001132.
90. Navin N, Kendall J, Troge J, Andrews P, Rodgers L, Mcindoo J, *et al.* (2011) Tumour evolution inferred by single-cell sequencing. *Nature* 472(7341):90-94.
91. Singh SK, Hawkins C, Clarke ID, Squire JA, Bayani J, Hide T, *et al.* (2004) Identification of human brain tumour initiating cells. *nature* 432(7015):396-401.
92. Hochberg FH & Pruitt A (1980) Assumptions in the radiotherapy of glioblastoma. *Neurology* 30(9):907-907.
93. Cuddapah VA, Robel S, Watkins S, & Sontheimer H (2014) A neurocentric perspective on glioma invasion. *Nature Reviews Neuroscience* 15(7):455-465.
94. Wen PY & Kesari S (2008) Malignant gliomas in adults. *New England Journal of Medicine* 359(5):492-507.
95. Lefranc F, Brotchi J, & Kiss R (2005) Possible future issues in the treatment of glioblastomas: Special emphasis on cell migration and the resistance of migrating glioblastoma cells to apoptosis. *Journal of Clinical Oncology* 23(10):2411-2422.
96. Giese A, Bjerkvig R, Berens M, & Westphal M (2003) Cost of migration: Invasion of malignant gliomas and implications for treatment. *Journal of Clinical Oncology* 21(8):1624-1636.
97. Frederick L, Wang X-Y, Eley G, & James CD (2000) Diversity and frequency of epidermal growth factor receptor mutations in human glioblastomas. *Cancer Research* 60(5):1383-1387.
98. Traxler P, Bold G, Buchdunger E, Caravatti G, Furet P, Manley P, *et al.* (2001) Tyrosine kinase inhibitors: From rational design to clinical trials. *Medicinal research reviews* 21(6):499-512.
99. Rich JN, Reardon DA, Peery T, Dowell JM, Quinn JA, Penne KL, *et al.* (2004) Phase ii trial of gefitinib in recurrent glioblastoma. *Journal of Clinical Oncology* 22(1):133-142.
100. Franceschi E, Cavallo G, Lonardi S, Magrini E, Tosoni A, Grosso D, *et al.* (2007) Gefitinib in patients with progressive high-grade gliomas: A multicentre phase ii study by gruppo italiano cooperativo di neuro-oncologia (gicno). *British Journal of Cancer* 96(7):1047-1051.
101. Van Den Bent MJ, Brandes AA, Rampling R, Kouwenhoven MC, Kros JM, Carpentier AF, *et al.* (2009) Randomized phase ii trial of erlotinib versus temozolomide or carmustine in recurrent glioblastoma: Eortc brain tumor group study 26034. *Journal of Clinical Oncology* 27(8):1268-1274.
102. Brown PD, Krishnan S, Sarkaria JN, Wu W, Jaeckle KA, Uhm JH, *et al.* (2008) Phase i/ii trial of erlotinib and temozolomide with radiation therapy in the treatment of newly diagnosed glioblastoma multiforme: North central cancer treatment group study n0177. *Journal of Clinical Oncology* 26(34):5603-5609.

103. Kuan C, Wikstrand C, & Bigner D (2001) Egf mutant receptor viii as a molecular target in cancer therapy. *Endocrine-related cancer* 8(2):83-96.
104. Pelloski CE, Ballman KV, Furth AF, Zhang L, Lin E, Sulman EP, *et al.* (2007) Epidermal growth factor receptor variant iii status defines clinically distinct subtypes of glioblastoma. *Journal of Clinical Oncology* 25(16):2288-2294.
105. Choi BD, Archer GE, Mitchell DA, Heimberger AB, Mclendon RE, Bigner DD, *et al.* (2009) Egfrviii-targeted vaccination therapy of malignant glioma. *Brain Pathology* 19(4):713-723.
106. Mishima K, Johns TG, Luwor RB, Scott AM, Stockert E, Jungbluth AA, *et al.* (2001) Growth suppression of intracranial xenografted glioblastomas overexpressing mutant epidermal growth factor receptors by systemic administration of monoclonal antibody (mab) 806, a novel monoclonal antibody directed to the receptor. *Cancer Research* 61(14):5349-5354.
107. Lorimer IA, Keppler-Hafkemeyer A, Beers RA, Pegram CN, Bigner DD, & Pastan I (1996) Recombinant immunotoxins specific for a mutant epidermal growth factor receptor: Targeting with a single chain antibody variable domain isolated by phage display. *Proceedings of the National Academy of Sciences* 93(25):14815-14820.
108. Lokker NA, Sullivan CM, Hollenbach SJ, Israel MA, & Giese NA (2002) Platelet-derived growth factor (pdgf) autocrine signaling regulates survival and mitogenic pathways in glioblastoma cells. *Cancer Research* 62(13):3729-3735.
109. Kilic T, Alberta JA, Zdunek PR, Acar M, Iannarelli P, O'reilly T, *et al.* (2000) Intracranial inhibition of platelet-derived growth factor-mediated glioblastoma cell growth by an orally active kinase inhibitor of the 2-phenylaminopyrimidine class. *Cancer Research* 60(18):5143-5150.
110. Winkler F, Kozin SV, Tong RT, Chae S-S, Booth MF, Garkavtsev I, *et al.* (2004) Kinetics of vascular normalization by vegfr2 blockade governs brain tumor response to radiation: Role of oxygenation, angiopoietin-1, and matrix metalloproteinases. *Cancer Cell* 6(6):553-563.
111. Kreisl TN, Kim L, Moore K, Duic P, Royce C, Stroud I, *et al.* (2008) Phase ii trial of single-agent bevacizumab followed by bevacizumab plus irinotecan at tumor progression in recurrent glioblastoma. *Journal of Clinical Oncology* 27(5):740-745.
112. Batchelor TT, Sorensen AG, Di Tomaso E, Zhang W-T, Duda DG, Cohen KS, *et al.* (2007) Azd2171, a pan-vegf receptor tyrosine kinase inhibitor, normalizes tumor vasculature and alleviates edema in glioblastoma patients. *Cancer Cell* 11(1):83-95.
113. Folkman J (2007) Angiogenesis: An organizing principle for drug discovery? *Nature Reviews Drug discovery* 6(4):273-286.
114. Nabors LB, Mikkelsen T, Rosenfeld SS, Hochberg F, Akella NS, Fisher JD, *et al.* (2007) Phase i and correlative biology study of cilengitide in patients with recurrent malignant glioma. *Journal of Clinical Oncology* 25(13):1651-1657.
115. Rosenberg SA, Yang JC, & Restifo NP (2004) Cancer immunotherapy: Moving beyond current vaccines. *Nature medicine* 10(9):909-915.
116. Cohen MH, Shen YL, Keegan P, & Pazdur R (2009) Fda drug approval summary: Bevacizumab (avastin®) as treatment of recurrent glioblastoma multiforme. *The oncologist* 14(11):1131-1138.

117. De Groot JF, Fuller G, Kumar AJ, Piao Y, Eterovic K, Ji Y, *et al.* (2010) Tumor invasion after treatment of glioblastoma with bevacizumab: Radiographic and pathologic correlation in humans and mice. *Neuro-Oncology* 12(3):233-242.
118. Heimberger AB & Sampson JH (2009) The pepviii-klh (cdx-110) vaccine in glioblastoma multiforme patients. *Expert opinion on biological therapy* 9(8):1087-1098.
119. Del Vecchio CA, Li G, & Wong AJ (2012) Targeting egf receptor variant iii: Tumor-specific peptide vaccination for malignant gliomas. *Expert review of vaccines* 11(2):133-144.
120. Sampson JH, Heimberger AB, Archer GE, Aldape KD, Friedman AH, Friedman HS, *et al.* (2010) Immunologic escape after prolonged progression-free survival with epidermal growth factor receptor variant iii peptide vaccination in patients with newly diagnosed glioblastoma. *Journal of Clinical Oncology* 28(31):4722-4729.
121. Terasaki M, Shibui S, Narita Y, Fujimaki T, Aoki T, Kajiwara K, *et al.* (2010) Phase i trial of a personalized peptide vaccine for patients positive for human leukocyte antigen–a24 with recurrent or progressive glioblastoma multiforme. *Journal of Clinical Oncology* 29(3):337-344.
122. Dobrikova EY, Broadt T, Poiley-Nelson J, Yang X, Soman G, Giardina S, *et al.* (2008) Recombinant oncolytic poliovirus eliminates glioma in vivo without genetic adaptation to a pathogenic phenotype. *Molecular therapy* 16(11):1865-1872.
123. Brown MC & Gromeier M (2015) Oncolytic immunotherapy through tumor-specific translation and cytotoxicity of poliovirus. *Discovery medicine* 19(106):359.
124. Del Vecchio C, Giacomini C, Vogel H, Jensen K, Florio T, Merlo A, *et al.* (2013) Egfrviii gene rearrangement is an early event in glioblastoma tumorigenesis and expression defines a hierarchy modulated by epigenetic mechanisms. *Oncogene* 32(21):2670-2681.
125. Francis JM, Zhang C-Z, Maire CL, Jung J, Manzo VE, Adalsteinsson VA, *et al.* (2014) Egfr variant heterogeneity in glioblastoma resolved through single-nucleus sequencing. *Cancer discovery* 4(8):956-971.
126. Shieh AC (2011) Biomechanical forces shape the tumor microenvironment. *Annals of biomedical engineering* 39(5):1379-1389.
127. Kim JB, Stein R, & O'hare MJ (2004) Three-dimensional in vitro tissue culture models of breast cancer—a review. *Breast Cancer Research and treatment* 85(3):281-291.
128. Yamada KM & Cukierman E (2007) Modeling tissue morphogenesis and cancer in 3d. *Cell* 130(4):601-610.
129. Rangarajan A & Weinberg RA (2003) Opinion: Comparative biology of mouse versus human cells: Modelling human cancer in mice. *Nature Reviews. Cancer* 3(12):952.
130. Buchanan C & Rylander MN (2013) Microfluidic culture models to study the hydrodynamics of tumor progression and therapeutic response. *Biotechnology and bioengineering* 110(8):2063-2072.
131. Yoon S, Kim JA, Lee SH, Kim M, & Park TH (2013) Droplet-based microfluidic system to form and separate multicellular spheroids using magnetic nanoparticles. *Lab on a Chip* 13(8):1522-1528.
132. Mazzoleni G, Di Lorenzo D, & Steimberg N (2009) Modelling tissues in 3d: The next future of pharmaco-toxicology and food research? *Genes & nutrition* 4(1):13.
133. Lee GY, Kenny PA, Lee EH, & Bissell MJ (2007) Three-dimensional culture models of normal and malignant breast epithelial cells. *Nature methods* 4(4):359.

134. Verbridge SS, Choi NW, Zheng Y, Brooks DJ, Stroock AD, & Fischbach C (2010) Oxygen-controlled three-dimensional cultures to analyze tumor angiogenesis. *Tissue Engineering. Part A* 16(7):2133-2141.
135. Muthuswamy SK (2011) 3d culture reveals a signaling network. *Breast Cancer Research* 13(1):103.
136. Kenny PA, Lee GY, Myers CA, Neve RM, Semeiks JR, Spellman PT, *et al.* (2007) The morphologies of breast cancer cell lines in three-dimensional assays correlate with their profiles of gene expression. *Molecular Oncology* 1(1):84-96.
137. Smith BH, Gazda LS, Conn BL, Jain K, Asina S, Levine DM, *et al.* (2011) Three-dimensional culture of mouse renal carcinoma cells in agarose macrobeads selects for a subpopulation of cells with cancer stem cell or cancer progenitor properties. *Cancer Research* 71(3):716-724.
138. Szot CS, Szot CS, Buchanan CF, Freeman JW, & Rylander MN (2011) 3d in vitro bioengineered tumors based on collagen i hydrogels. *Biomaterials* 32(31):7905-7912.
139. Fischbach C, Chen R, Matsumoto T, Schmelzle T, Brugge JS, Polverini PJ, *et al.* (2007) Engineering tumors with 3d scaffolds. *Nat Meth* 4(10):855-860.
140. Cross VL, Zheng Y, Choi NW, Verbridge SS, Sutermaster BA, Bonassar LJ, *et al.* (2010) Dense type i collagen matrices that support cellular remodeling and microfabrication for studies of tumor angiogenesis and vasculogenesis in vitro. *Biomaterials* 31(33):8596-8607.
141. Nelson CM & Bissell MJ (2005) Modeling dynamic reciprocity: Engineering three-dimensional culture models of breast architecture, function, and neoplastic transformation. *Seminars in cancer biology*, (Elsevier), pp 342-352.
142. Raof NA, Raja WK, Castracane J, & Xie Y (2011) Bioengineering embryonic stem cell microenvironments for exploring inhibitory effects on metastatic breast cancer cells. *Biomaterials* 32(17):4130-4139.
143. Kim JB (2005) Three-dimensional tissue culture models in cancer biology. *Seminars in cancer biology*, (Elsevier), pp 365-377.
144. Dit Faute MA, Laurent L, Ploton D, Poupon M-F, Jardillier J-C, & Bobichon H (2002) Distinctive alterations of invasiveness, drug resistance and cell–cell organization in 3d-cultures of mcf-7, a human breast cancer cell line, and its multidrug resistant variant. *Clinical & experimental metastasis* 19(2):161-167.
145. Baker EL, Bonnecaze RT, & Zaman MH (2009) Extracellular matrix stiffness and architecture govern intracellular rheology in cancer. *Biophysical Journal* 97(4):1013-1021.
146. Ala-Aho R & Kähäri V-M (2005) Collagenases in cancer. *Biochimie* 87(3):273-286.
147. Weaver JC (1994) Molecular basis for cell membrane electroporationa. *Annals of the New York Academy of Sciences* 720(1):141-152.
148. Lodish H (2008) *Molecular cell biology* (Macmillan).
149. Cosman ER (2005) Electric and thermal field effects in tissue around radiofrequency electrodes. *Pain Medicine* 6(6):405-424.
150. Neu JC & Krassowska W (1999) Asymptotic model of electroporation. *Physical review E* 59(3):3471.
151. Weaver JC & Chizmadzhev YA (1996) Theory of electroporation: A review. *Bioelectrochemistry and Bioenergetics* 41(2):135-160.

152. Tieleman DP, Leontiadou H, Mark AE, & Marrink S-J (2003) Simulation of pore formation in lipid bilayers by mechanical stress and electric fields. *Journal of the American Chemical Society* 125(21):6382-6383.
153. Tieleman DP (2004) The molecular basis of electroporation. *BMC biochemistry* 5(1):1.
154. Tarek M (2005) Membrane electroporation: A molecular dynamics simulation. *Biophysical Journal* 88(6):4045-4053.
155. Hibino M, Shigemori M, Itoh H, Nagayama K, & Kinosita Jr K (1991) Membrane conductance of an electroporated cell analyzed by submicrosecond imaging of transmembrane potential. *Biophysical Journal* 59(1):209.
156. Hibino M, Itoh H, & Kinosita Jr K (1993) Time courses of cell electroporation as revealed by submicrosecond imaging of transmembrane potential. *Biophysical Journal* 64(6):1789.
157. Mir LM (2001) Therapeutic perspectives of in vivo cell electropermeabilization. *Bioelectrochemistry* 53(1):1-10.
158. Agerholm-Larsen B, Iversen HK, Ibsen P, Moller JM, Mahmood F, Jensen KS, *et al.* (2011) Preclinical validation of electrochemotherapy as an effective treatment for brain tumors. *Cancer Research* 71(11):3753-3762.
159. Weaver JC (2003) Electroporation of biological membranes from multicellular to nano scales. *Dielectrics and Electrical Insulation, IEEE Transactions on* 10(5):754-768.
160. Lee EW, Wong D, Prikhodko SV, Perez A, Tran C, Loh CT, *et al.* (2012) Electron microscopic demonstration and evaluation of irreversible electroporation-induced nanopores on hepatocyte membranes. *Journal of Vascular and Interventional Radiology* 23(1):107-113.
161. Chang D & Reese TS (1990) Changes in membrane structure induced by electroporation as revealed by rapid-freezing electron microscopy. *Biophysical Journal* 58(1):1-12.
162. Sale A & Hamilton W (1967) Effects of high electric fields on microorganisms: I. Killing of bacteria and yeasts. *Biochimica et Biophysica Acta (BBA)-General Subjects* 148(3):781-788.
163. Hamilton W & Sale A (1967) Effects of high electric fields on microorganisms: Ii. Mechanism of action of the lethal effect. *Biochimica et Biophysica Acta (BBA)-General Subjects* 148(3):789-800.
164. Sale A & Hamilton W (1968) Effects of high electric fields on micro-organisms: Iii. Lysis of erythrocytes and protoplasts. *Biochimica et Biophysica Acta (BBA)-Biomembranes* 163(1):37-43.
165. Doevenspeck H (1961) Influencing cells and cell walls by electrostatic impulses. *Fleischwirtschaft* 13(12):968-987.
166. Toepfl S, Mathys A, Heinz V, & Knorr D (2006) Review: Potential of high hydrostatic pressure and pulsed electric fields for energy efficient and environmentally friendly food processing. *Food Reviews International* 22(4):405-423.
167. Vernhes M, Benichou A, Pernin P, Cabanes P, & Teissie J (2002) Elimination of free-living amoebae in fresh water with pulsed electric fields. *Water Research* 36(14):3429-3438.
168. Joshi R & Schoenbach K (2002) Mechanism for membrane electroporation irreversibility under high-intensity, ultrashort electrical pulse conditions. *Physical review E* 66(5):052901.

169. Rowan N, Macgregor SJ, Anderson J, Fouracre R, & Farish O (2000) Pulsed electric field inactivation of diarrhoeagenic bacillus cereus through irreversible electroporation. *Letters in applied microbiology* 31(2):110-114.
170. Schoenbach KH, Peterkin FE, Alden Iii RW, & Beebe SJ (1997) The effect of pulsed electric fields on biological cells: Experiments and applications. *Plasma Science, IEEE Transactions on* 25(2):284-292.
171. Davalos RV, Mir L, & Rubinsky B (2005) Tissue ablation with irreversible electroporation. *Annals of biomedical engineering* 33(2):223-231.
172. Rubinsky B (2007) Irreversible electroporation in medicine. *Technology in Cancer Research & Treatment* 6(4):255-259.
173. Ball C, Thomson KR, & Kavnoudias H (2010) Irreversible electroporation: A new challenge in "out of operating theater" anesthesia. *Anesthesia & Analgesia* 110(5):1305-1309.
174. Daud AI, Deconti RC, Andrews S, Urbas P, Riker AI, Sondak VK, *et al.* (2008) Phase i trial of interleukin-12 plasmid electroporation in patients with metastatic melanoma. *Journal of Clinical Oncology* 26(36):5896-5903.
175. Garon EB, Sawcer D, Vernier PT, Tang T, Sun Y, Marcu L, *et al.* (2007) In vitro and in vivo evaluation and a case report of intense nanosecond pulsed electric field as a local therapy for human malignancies. *International Journal of Cancer* 121(3):675-682.
176. Thomson KR, Cheung W, Ellis SJ, Federman D, Kavnoudias H, Loader-Oliver D, *et al.* (2011) Investigation of the safety of irreversible electroporation in humans. *Journal of Vascular and Interventional Radiology* 22(5):611-621.
177. Edd JF, Horowitz L, Davalos RV, Mir LM, & Rubinsky B (2006) In vivo results of a new focal tissue ablation technique: Irreversible electroporation. *Biomedical Engineering, IEEE Transactions on* 53(7):1409-1415.
178. Maor E, Ivorra A, Leor J, & Rubinsky B (2007) The effect of irreversible electroporation on blood vessels. *Technology in Cancer Research & Treatment* 6(4):307-312.
179. Maor E, Ivorra A, & Rubinsky B (2009) Non thermal irreversible electroporation: Novel technology for vascular smooth muscle cells ablation. *PLoS One* 4(3):e4757.
180. Al-Sakere B, Bernat C, Andre F, Connault E, Opolon P, Davalos RV, *et al.* (2007) A study of the immunological response to tumor ablation with irreversible electroporation. *Technology in Cancer Research & Treatment* 6(4):301-305.
181. Lee EW, Loh CT, & Kee ST (2007) Imaging guided percutaneous irreversible electroporation: Ultrasound and immunohistological correlation. *Technology in Cancer Research & Treatment* 6(4):287-293.
182. Al-Sakere B, André F, Bernat C, Connault E, Opolon P, Davalos RV, *et al.* (2007) Tumor ablation with irreversible electroporation. *PLoS One* 2(11):e1135.
183. Onik G, Mikus P, & Rubinsky B (2007) Irreversible electroporation: Implications for prostate ablation. *Technol Cancer Res Treat* 6(4):295-300.
184. Garcia PA, Pancotto T, Rossmeisl JH, Henao-Guerrero N, Gustafson NR, Daniel GB, *et al.* (2011) Non-thermal irreversible electroporation (n-tire) and adjuvant fractionated radiotherapeutic multimodal therapy for intracranial malignant glioma in a canine patient. *Technology in Cancer Research & Treatment* 10(1):73-83.
185. Neal RE, Rossmeisl JH, Garcia PA, Lanz OI, Henao-Guerrero N, & Davalos RV (2011) Successful treatment of a large soft tissue sarcoma with irreversible electroporation. *Journal of Clinical Oncology* 29(13):e372-e377.

186. Martin RC, Kwon D, Chalikonda S, Sellers M, Kotz E, Scoggins C, *et al.* (2015) Treatment of 200 locally advanced (stage iii) pancreatic adenocarcinoma patients with irreversible electroporation: Safety and efficacy. *Annals of surgery* 262(3):486-494.
187. Cannon R, Ellis S, Hayes D, Narayanan G, & Martin RC (2013) Safety and early efficacy of irreversible electroporation for hepatic tumors in proximity to vital structures. *Journal of Surgical Oncology* 107(5):544-549.
188. Cheung W, Kavnoudias H, Roberts S, Szkandera B, Kemp W, & Thomson K (2013) Irreversible electroporation for unresectable hepatocellular carcinoma: Initial experience and review of safety and outcomes. *Technology in Cancer Research & Treatment* 12(3):233.
189. Narayanan G, Froud T, Lo K, Barbery KJ, Perez-Rojas E, & Yrizarry J (2013) Pain analysis in patients with hepatocellular carcinoma: Irreversible electroporation versus radiofrequency ablation-initial observations. *Cardiovasc Intervent Radiol* 36(1):176-182.
190. Niessen C, Jung EM, Wohlgemuth WA, Trabold B, Haimerl M, Schreyer A, *et al.* (2013) Irreversible electroporation of a hepatocellular carcinoma lesion adjacent to a transjugular intrahepatic portosystemic shunt stent graft. *Korean J Radiol* 14(5):797-800.
191. Silk MT, Wimmer T, Lee KS, Srimathveeravalli G, Brown KT, Kingham PT, *et al.* (2014) Percutaneous ablation of peribiliary tumors with irreversible electroporation. *Journal of Vascular and Interventional Radiology* 25(1):112-118.
192. Onik G & Rubinsky B (2010) Irreversible electroporation: First patient experience focal therapy of prostate cancer. *Irreversible electroporation*, (Springer), pp 235-247.
193. Usman M, Moore W, Talati R, Watkins K, & Bilfinger TV (2012) Irreversible electroporation of lung neoplasm: A case series. *Medical Science Monitor* 18(6):CS43-CS47.
194. Garcia PA, Rossmeisl Jr JH, Ellis TL, & Davalos RV (2014) Nonthermal irreversible electroporation as a focal ablation treatment for brain cancer. *Tumors of the central nervous system, volume 12*, (Springer), pp 171-182.
195. Pech M, Janitzky A, Wendler JJ, Strang C, Blaschke S, Dudeck O, *et al.* (2011) Irreversible electroporation of renal cell carcinoma: A first-in-man phase i clinical study. *Cardiovascular and interventional radiology* 34(1):132-138.
196. Wendler JJ, Pech M, Blaschke S, Porsch M, Janitzky A, Ulrich M, *et al.* (2012) Angiography in the isolated perfused kidney: Radiological evaluation of vascular protection in tissue ablation by nonthermal irreversible electroporation. *Cardiovascular and interventional radiology* 35(2):383-390.
197. Olweny EO, Kapur P, Tan YK, Park SK, Adibi M, & Cadeddu JA (2013) Irreversible electroporation: Evaluation of nonthermal and thermal ablative capabilities in the porcine kidney. *Urology* 81(3):679-684.
198. Martin RC, Mcfarland K, Ellis S, & Velanovich V (2013) Irreversible electroporation in locally advanced pancreatic cancer: Potential improved overall survival. *Annals of Surgical Oncology* 20(3):443-449.
199. Martin RC, Mcfarland K, Ellis S, & Velanovich V (2012) Irreversible electroporation therapy in the management of locally advanced pancreatic adenocarcinoma. *Journal of the American College of Surgeons* 215(3):361-369.
200. Bower M, Sherwood L, Li Y, & Martin R (2011) Irreversible electroporation of the pancreas: Definitive local therapy without systemic effects. *Journal of Surgical Oncology* 104(1):22-28.

201. Ellis TL, Garcia PA, Rossmeisl Jr JH, Henao-Guerrero N, Robertson J, & Davalos RV (2011) Nonthermal irreversible electroporation for intracranial surgical applications: Laboratory investigation. *Journal of neurosurgery* 114(3):681-688.
202. Cosman E, Nashold B, & Bedenbaugh P (1983) Stereotactic radiofrequency lesion making. *Stereotactic and Functional Neurosurgery* 46(1-4):160-166.
203. Martin RC, Scoggins CR, & Mcmasters KM (2010) Safety and efficacy of microwave ablation of hepatic tumors: A prospective review of a 5-year experience. *Annals of Surgical Oncology* 17(1):171-178.
204. Tacke J (2001) Thermal therapies in interventional mr imaging. Cryotherapy. *Neuroimaging clinics of North America* 11(4):759-765.
205. Atsumi H, Matsumae M, Kaneda M, Muro I, Mamata Y, Komiya T, *et al.* (2001) Novel laser system and laser irradiation method reduced the risk of carbonization during laser interstitial thermotherapy: Assessed by mr temperature measurement. *Lasers in surgery and medicine* 29(2):108-117.
206. Ter Haar G (1995) Ultrasound focal beam surgery. *Ultrasound in medicine & biology* 21(9):1089-1100.
207. Goldberg SN, Gazelle GS, & Mueller PR (2000) Thermal ablation therapy for focal malignancy: A unified approach to underlying principles, techniques, and diagnostic imaging guidance. *American Journal of roentgenology* 174(2):323-331.
208. Lencioni R, Cioni D, Crocetti L, Franchini C, Pina CD, Lera J, *et al.* (2005) Early-stage hepatocellular carcinoma in patients with cirrhosis: Long-term results of percutaneous image-guided radiofrequency ablation 1. *Radiology* 234(3):961-967.
209. Mcgahan JP & Dodd Iii GD (2001) Radiofrequency ablation of the liver: Current status. *American Journal of Roentgenology* 176(1):3-16.
210. Goldberg SN, Gazelle GS, Halpern EF, Rittman WJ, Mueller PR, & Rosenthal DI (1996) Radiofrequency tissue ablation: Importance of local temperature along the electrode tip exposure in determining lesion shape and size. *Academic radiology* 3(3):212-218.
211. Curley SA, Marra P, Beaty K, Ellis LM, Vauthey JN, Abdalla EK, *et al.* (2004) Early and late complications after radiofrequency ablation of malignant liver tumors in 608 patients. *Annals of surgery* 239(4):450-458.
212. Lubner MG, Brace CL, Hinshaw JL, & Lee FT (2010) Microwave tumor ablation: Mechanism of action, clinical results, and devices. *Journal of Vascular and Interventional Radiology* 21(8):S192-S203.
213. Yu Z, Liu W, Fan L, Shao J, Huang Y, & Si X (2009) The efficacy and safety of percutaneous microwave coagulation by a new microwave delivery system in large hepatocellular carcinomas: Four case studies. *International Journal of Hyperthermia* 25(5):392-398.
214. Carpentier A, Chauvet D, Reina V, Beccaria K, Leclerq D, Mcnichols RJ, *et al.* (2012) Mr-guided laser-induced thermal therapy (litt) for recurrent glioblastomas. *Lasers in surgery and medicine* 44(5):361-368.
215. Riordan M & Tovar-Spinoza Z (2014) Laser induced thermal therapy (litt) for pediatric brain tumors: Case-based review. *Translational pediatrics* 3(3):229.
216. Jourabchi N, Beroukhim K, Tafti BA, Kee ST, & Lee EW (2014) Irreversible electroporation (nanoknife) in cancer treatment. *Gastrointestinal Intervention* 3(1):8-18.
217. Chang I (2003) Finite element analysis of hepatic radiofrequency ablation probes using temperature-dependent electrical conductivity. *Biomedical engineering online* 2(1):12.

218. Kirson ED, Dbalý V, Tovaryš F, Vymazal J, Soustiel JF, Itzhaki A, *et al.* (2007) Alternating electric fields arrest cell proliferation in animal tumor models and human brain tumors. *Proceedings of the National Academy of Sciences* 104(24):10152-10157.
219. Davies AM, Davies AM, Weinberg U, & Palti Y (2013) Tumor treating fields: A new frontier in cancer therapy. *Annals of the New York Academy of Sciences* 1291(1):86-95.
220. Kirson ED, Gurvich Z, Schneiderman R, Dekel E, Itzhaki A, Wasserman Y, *et al.* (2004) Disruption of cancer cell replication by alternating electric fields. *Cancer Research* 64(9):3288-3295.
221. Neal RE, 2nd & Davalos RV (2009) The feasibility of irreversible electroporation for the treatment of breast cancer and other heterogeneous systems. *Ann Biomed Eng* 37(12):2615-2625.
222. Garcia P, Rossmeisl J, Neal R, Ellis T, Olson J, Henao-Guerrero N, *et al.* (2010) Intracranial nonthermal irreversible electroporation: In vivo analysis. *J Membr Biol* 236(1):127-136.
223. Thomson K (2010) Human experience with irreversible electroporation. *Irreversible electroporation*, ed Rubinsky B (Springer Berlin, Heidelberg), pp 249-254.
224. Mir LM & Orlowski S (1999) Mechanisms of electrochemotherapy. *Adv Drug Deliv Rev* 35:107-118.
225. Arena CB, Szot CS, Garcia PA, Rylander MN, & Davalos RV (2012) A three-dimensional in vitro tumor platform for modeling therapeutic irreversible electroporation. *Biophysical Journal* 103(9):2033-2042.
226. Edd JF & Davalos RV (2007) Mathematical modeling of irreversible electroporation for treatment planning. *Technology in Cancer Research & Treatment* 6(4):275-286.
227. Davalos RV, Otten DM, Mir LM, & Rubinsky B (2004) Electrical impedance tomography for imaging tissue electroporation. *Biomedical Engineering, IEEE Transactions on* 51(5):761-767.
228. Bonakdar M, Latouche EL, Mahajan RL, & Davalos RV (2015) The feasibility of a smart surgical probe for verification of ire treatments using electrical impedance spectroscopy. *Biomedical Engineering, IEEE Transactions on* 62(11):2674-2684.
229. Chang D (1991) *Guide to electroporation and electrofusion* (Academic Press).
230. Jaroszeski MJ, Gilbert R, & Heller R (1997) Electrochemotherapy: An emerging drug delivery method for the treatment of cancer. *Advanced drug delivery reviews* 26(2):185-197.
231. Salford LG, Persson B, Brun A, Ceberg C, Kongstad PC, & Mir LM (1993) A new brain tumor therapy combining bleomycin with in vivo electropermeabilization. *Biochemical and biophysical research communications* 194(2):938-943.
232. Belehradek M, Domenge C, Luboinski B, Orlowski S, Belehradek J, & Mir LM (1993) Electrochemotherapy, a new antitumor treatment. First clinical phase i-ii trial. *Cancer* 72(12):3694-3700.
233. Gothelf A, Mir LM, & Gehl J (2003) Electrochemotherapy: Results of cancer treatment using enhanced delivery of bleomycin by electroporation. *Cancer treatment reviews* 29(5):371-387.
234. Mir L, Glass L, Serša G, Teissie J, Domenge C, Miklavčič D, *et al.* (1998) Effective treatment of cutaneous and subcutaneous malignant tumours by electrochemotherapy. *British Journal of Cancer* 77(12):2336-2342.

235. Andre F & Mir L (2004) DNA electrotransfer: Its principles and an updated review of its therapeutic applications. *Gene therapy* 11:S33-S42.
236. Heller LC & Heller R (2006) In vivo electroporation for gene therapy. *Human Gene Therapy* 17(9):890-897.
237. Forde PF, Hall L, De Kruijf M, Bourke M, Doddy T, Sadadcharam M, *et al.* (2015) Non-viral immune electrogene therapy induces potent antitumour responses and has a curative effect in murine colon adenocarcinoma and melanoma cancer models. *Gene therapy* 22(1):29-39.
238. Cemazar M, Jarm T, & Sersa G (2010) Cancer electrogene therapy with interleukin-12. *Current gene therapy* 10(4):300-311.
239. Bonakdar M, Wasson EM, Lee YW, & Davalos RV (2016) Electroporation of brain endothelial cells on chip toward permeabilizing the blood-brain barrier. *Biophysical Journal* 110(2):503-513.
240. Garcia PA, Rossmeisl Jr JH, Robertson JL, Olson JD, Johnson AJ, Ellis TL, *et al.* (2012) 7.0-t magnetic resonance imaging characterization of acute blood-brain-barrier disruption achieved with intracranial irreversible electroporation. *PLOS ONE* 7(11):e50482.
241. Hjouj M, Last D, Guez D, Daniels D, Sharabi S, Lavee J, *et al.* (2012) Mri study on reversible and irreversible electroporation induced blood brain barrier disruption. *PLOS ONE* 7(8):e42817.
242. Weaver JC, Smith KC, Esser AT, Son RS, & Gowrishankar TR (2012) A brief overview of electroporation pulse strength-duration space: A region where additional intracellular effects are expected. *Bioelectrochemistry* 87:236-243.
243. Vernier PT, Sun Y, & Gundersen MA (2006) Nanoelectropulse-driven membrane perturbation and small molecule permeabilization. *BMC cell biology* 7(1):1.
244. Frey W, White JA, Price RO, Blackmore PF, Joshi RP, Nuccitelli R, *et al.* (2006) Plasma membrane voltage changes during nanosecond pulsed electric field exposure. *Biophysical Journal* 90(10):3608-3615.
245. Pakhomov AG, Kolb JF, White JA, Joshi RP, Xiao S, & Schoenbach KH (2007) Long-lasting plasma membrane permeabilization in mammalian cells by nanosecond pulsed electric field (nspef). *Bioelectromagnetics* 28(8):655-663.
246. Esser AT, Smith KC, Gowrishankar TR, Vasilkoski Z, & Weaver JC (2010) Mechanisms for the intracellular manipulation of organelles by conventional electroporation. *Biophysical Journal* 98(11):2506-2514.
247. Schoenbach KH, Joshi RP, Kolb JF, Chen N, Stacey M, Blackmore PF, *et al.* (2004) Ultrashort electrical pulses open a new gateway into biological cells. *Proceedings of the IEEE* 92(7):1122-1137.
248. Schoenbach KH, Beebe SJ, & Buescher ES (2001) Intracellular effect of ultrashort electrical pulses. *Bioelectromagnetics* 22(6):440-448.
249. Beebe SJ, Fox P, Rec L, Somers K, Stark RH, & Schoenbach KH (2002) Nanosecond pulsed electric field (nspef) effects on cells and tissues: Apoptosis induction and tumor growth inhibition. *Plasma Science, IEEE Transactions on* 30(1):286-292.
250. Beebe SJ, Fox PM, Rec LJ, Willis ELK, & Schoenbach KH (2003) Nanosecond, high-intensity pulsed electric fields induce apoptosis in human cells. *The FASEB Journal* 17(11):1493-1495.

251. Long G, Shires PK, Plescia D, Beebe SJ, Kolb JF, & Schoenbach KH (2011) Targeted tissue ablation with nanosecond pulses. *Biomedical Engineering, IEEE Transactions on* 58(8):2161-2167.
252. Cheng RG, Bhattacharya R, Yeh MM, & Padia SA (2015) Irreversible electroporation can effectively ablate hepatocellular carcinoma to complete pathologic necrosis. *Journal of Vascular and Interventional Radiology* 26(8):1184-1188.
253. Neumann E, Schaefer-Ridder M, Wang Y, & Hofschneider P (1982) Gene transfer into mouse lyoma cells by electroporation in high electric fields. *The EMBO Journal* 1(7):841.
254. Müller-Hartmann H, Riemen G, Rothmann-Cosic K, Thiel C, Altrogge L, Weigel M, *et al.* (2012) Circuit arrangement for injecting nucleic acids and other biologically active molecules into the nucleus of higher eucaryotic cells using electrical current. (Google Patents).
255. Reilly JP, Freeman VT, & Larkin WD (1985) Sensory effects of transient electrical stimulation-evaluation with a neuroelectric model. *Biomedical Engineering, IEEE Transactions on* (12):1001-1011.
256. Arena CB, Sano MB, Rossmeisl JH, Caldwell JL, Garcia PA, Rylander MN, *et al.* (2011) High-frequency irreversible electroporation (h-fire) for non-thermal ablation without muscle contraction. *Biomedical engineering online* 10(1):102.
257. Martin I & Robert C (2015) Irreversible electroporation of stage 3 locally advanced pancreatic cancer: Optimal technique and outcomes. *The Journal of Visualized Surgery* 1(3).
258. Gaynor P & Bodger P (1995) Electrofusion processes: Theoretical evaluation of high electric field effects on cellular transmembrane potentials. *IEE proceedings. Science, measurement and technology* 142(2):176-182.
259. Corovic S, Zupanic A, Kranjc S, Al Sakere B, Leroy-Willig A, Mir LM, *et al.* (2010) The influence of skeletal muscle anisotropy on electroporation: In vivo study and numerical modeling. *Medical & Biological Engineering & Computing* 48(7):637-648.
260. Weaver JC (1993) Electroporation: A general phenomenon for manipulating cells and tissues. *Journal of cellular biochemistry* 51(4):426-435.
261. Kolb JF, Kono S, & Schoenbach KH (2006) Nanosecond pulsed electric field generators for the study of subcellular effects. *Bioelectromagnetics* 27(3):172-187.
262. Kotnik T & Miklavčič D (2006) Theoretical evaluation of voltage inducement on internal membranes of biological cells exposed to electric fields. *Biophysical Journal* 90(2):480-491.
263. Marszalek P, Liu D, & Tsong TY (1990) Schwan equation and transmembrane potential induced by alternating electric field. *Biophysical Journal* 58(4):1053.
264. Postow E & Polk C (1996) *Handbook of biological effects of electromagnetic fields* (Boca Raton: CRC Press).
265. Schwan HP (1957) Electrical properties of tissue and cell suspensions. *Advances in biological and medical physics* 5:147.
266. Nathanson DA, Gini B, Mottahedeh J, Visnyei K, Koga T, Gomez G, *et al.* (2014) Targeted therapy resistance mediated by dynamic regulation of extrachromosomal mutant egfr DNA. *Science* 343(6166):72-76.

267. Stommel JM, Kimmelman AC, Ying H, Nabioullin R, Ponugoti AH, Wiedemeyer R, *et al.* (2007) Coactivation of receptor tyrosine kinases affects the response of tumor cells to targeted therapies. *Science* 318(5848):287-290.
268. Bedard PL, Hansen AR, Ratain MJ, & Siu LL (2013) Tumour heterogeneity in the clinic. *Nature* 501(7467):355-364.
269. Kotnik T, Kramar P, Pucihar G, Miklavcic D, & Tarek M (2012) Cell membrane electroporation- part 1: The phenomenon. *IEEE Electrical Insulation Magazine* 28(5):14-23.
270. Debruin KA & Krassowska W (1999) Modeling electroporation in a single cell. Ii. Effects of ionic concentrations. *Biophysical Journal* 77(3):1225-1233.
271. Sano MB, Arena CB, Dewitt MR, Saur D, & Davalos RV (2014) In-vitro bipolar nano- and microsecond electro-pulse bursts for irreversible electroporation therapies. *Bioelectrochemistry* 100:69-79.
272. Arena CB, Sano MB, Rylander MN, & Davalos RV (2011) Theoretical considerations of tissue electroporation with high-frequency bipolar pulses. *Ieee Transactions on Biomedical Engineering* 58(5):1474-1482.
273. Jin Y, Yang LJ, & White FH (1995) Preliminary assesment of the epithelial nuclear-cytoplasmic ratio and nuclear volume density in human palatal lesions. *Journal of oral pathology & medicine* 24(6):261-265.
274. White FH & Gohari K (1981) Variations in the nuclear-cytoplasmic ration during epithelial differentiation in experimental oral carcinogenesis. *Journal of oral pathology* 10(3):164-172.
275. Seibert K, Shafie SM, Triche TJ, Whang-Peng JJ, O'brien SJ, Toney JH, *et al.* (1983) Clonal variation of mcf-7 breast cancer cells in vitro and in athymic nude mice. *Cancer Research* 43(5):2223-2239.
276. Salmanzadeh A, Romero L, Shafiee H, Gallo-Villanueva RC, Stremler MA, Cramer SD, *et al.* (2012) Isolation of prostate tumor initiating cells (tics) through their dielectrophoretic signature. *Lab on a Chip* 12(1):182-189.
277. Rajan N, Habermehl J, Coté M-F, Doillon CJ, & Mantovani D (2006) Preparation of ready-to-use, storable and reconstituted type i collagen from rat tail tendon for tissue engineering applications. *Nature protocols* 1(6):2753-2758.
278. Haus HA & Melcher JR (1989) *Electromagnetic fields and energy* (Prentice Hall).
279. Asami K, Takahashi Y, & Takashima S (1989) Dielectric-properties of mouse lymphocytes and erythrocytes. *Biochimica Et Biophysica Acta* 1010(1):49-55.
280. Yang J, Huang Y, Wang XJ, Wang XB, Becker FF, & Gascoyne PRC (1999) Dielectric properties of human leukocyte subpopulations determined by electrorotation as a cell separation criterion. *Biophysical Journal* 76(6):3307-3314.
281. Gascoyne PRC, Pethig R, Burt JPH, & Becker FF (1993) Membrane-changes accompanying the induced-differentiation of friend murine erythroleukemia-cells studied by dielectrophoresis. *Biochimica Et Biophysica Acta* 1149(1):119-126.
282. Sano MB, Henslee EA, Schmelz EM, & Davalos RV (2011) Contactless dielectrophoretic spectroscopy: Examination of the dielectric properties of cells found in blood. *Electrophoresis* 32(22):3164-3171.
283. Alberts B, Bray D, Lewis J, Raff M, Roberts K, Watson JD, *et al.* (1995) Molecular biology of the cell (3rd edn). *Trends in Biochemical Sciences* 20(5):210-210.

284. Bier M, Hammer SM, Canaday DJ, & Lee RC (1999) Kinetics of sealing for transient electropores in isolated mammalian skeletal muscle cells. *Bioelectromagnetics* 20(3):194-201.
285. Rossmeisl JH, Garcia PA, Roberston JL, Ellis TL, & Davalos RV (2013) Pathology of non-thermal irreversible electroporation (n-tire)-induced ablation of the canine brain. *Journal of Veterinary Science* 14(4):433-440.
286. Fong ELS, Lamhamedi-Cherradi S-E, Burdett E, Ramamoorthy V, Lazar AJ, Kasper FK, *et al.* (2013) Modeling ewing sarcoma tumors in vitro with 3d scaffolds. *Proceedings of the National Academy of Sciences* 110(16):6500-6505.
287. Rossmeisl JH (2014) New treatment modalities for brain tumors in dogs and cats. *Veterinary Clinics of North America: Small Animal Practice* 44(6):1013-1038.
288. Agarwal A, Zudans I, Weber EA, Olofsson J, Orwar O, & Weber SG (2007) Effect of cell size and shape on single-cell electroporation. *Analytical chemistry* 79(10):3589-3596.
289. Eppich HM, Foxall R, Gaynor K, Dombkowski D, Miura N, Cheng T, *et al.* (2000) Pulsed electric fields for selection of hematopoietic cells and depletion of tumor cell contaminants. *Nature Biotechnology* 18(8):882-887.
290. Zink D, Fischer AH, & Nickerson JA (2004) Nuclear structure in cancer cells. *Nat Rev Cancer* 4(9):677-687.
291. Louis D, Ohgaki H, Wiestler O, Cavenee W, Burger P, Jouvet A, *et al.* (2007) The 2007 who classification of tumours of the central nervous system. *Acta Neuropathologica* 114(2):97-109.
292. Dahl KN, Ribeiro AJS, & Lammerding J (2008) Nuclear shape, mechanics, and mechanotransduction. *Circulation research* 102(11):1307-1318.
293. Neal RE, Millar JL, Kavnoudias H, Royce P, Rosenfeldt F, Pham A, *et al.* (2014) In vivo characterization and numerical simulation of prostate properties for non-thermal irreversible electroporation ablation. *The Prostate* 74(5):458-468.
294. Neal Ii R, Rossmeisl Jr J, D'alfonso V, Robertson J, Garcia P, Elankumaran S, *et al.* (2014) In vitro and numerical support for combinatorial irreversible electroporation and electrochemotherapy glioma treatment. *Annals of biomedical engineering* 42(3):475-487.
295. Carter P & Merchant AM (1997) Engineering antibodies for imaging and therapy. *Current opinion in biotechnology* 8(4):449-454.
296. Schrama D, Reisfeld RA, & Becker JC (2006) Antibody targeted drugs as cancer therapeutics. *Nature Reviews Drug discovery* 5(2):147-159.
297. Hu W & Kavanagh JJ (2003) Anticancer therapy targeting the apoptotic pathway. *The Lancet Oncology* 4(12):721-729.
298. Rommel C, Bodine SC, Clarke BA, Rossman R, Nunez L, Stitt TN, *et al.* (2001) Mediation of igf-1-induced skeletal myotube hypertrophy by pi (3) k/akt/mtor and pi (3) k/akt/gsk3 pathways. *Nature cell biology* 3(11):1009-1013.
299. Pasquale EB (2010) Eph receptors and ephrins in cancer: Bidirectional signalling and beyond. *Nat Rev Cancer* 10(3):165-180.
300. Miao H & Wang B (2012) Epha receptor signaling—complexity and emerging themes. *Seminars in Cell & Developmental Biology* 23(1):16-25.
301. Wykosky J, Gibo DM, Stanton C, & Debinski W (2005) Epha2 as a novel molecular marker and target in glioblastoma multiforme. *Molecular Cancer Research* 3(10):541-551.

302. Flanagan JG & Vanderhaeghen P (1998) The ephrins and eph receptors in neural development. *Annual review of neuroscience* 21(1):309-345.
303. Hafner C, Schmitz G, Meyer S, Bataille F, Hau P, Langmann T, *et al.* (2004) Differential gene expression of eph receptors and ephrins in benign human tissues and cancers. *Clinical chemistry* 50(3):490-499.
304. Yamaguchi Y & Pasquale EB (2004) Eph receptors in the adult brain. *Current opinion in neurobiology* 14(3):288-296.
305. Wykosky J, Gibo DM, Stanton C, & Debinski W (2008) Interleukin-13 receptor α2, epha2, and fos-related antigen 1 as molecular denominators of high-grade astrocytomas and specific targets for combinatorial therapy. *Clinical Cancer Research* 14(1):199-208.
306. Li X, Wang Y, Wang Y, Haining Z, Yang H, Zhou F, *et al.* (2007) Expression of epha2 in human astrocytic tumors: Correlation with pathologic grade, proliferation and apoptosis. *Tumor Biology* 28(3):165-172.
307. Wang L-F, Fokas E, Bieker M, Rose F, Rexin P, Zhu Y, *et al.* (2008) Increased expression of epha2 correlates with adverse outcome in primary and recurrent glioblastoma multiforme patients. *Oncology reports* 19(1):151-156.
308. Hatano M, Eguchi J, Tatsumi T, Kuwashima N, Dusak JE, Kinch MS, *et al.* (2005) Epha2 as a glioma-associated antigen: A novel target for glioma vaccines. *Neoplasia* 7(8):717-722.
309. Liu D-P, Wang Y, Koeffler HP, & Xie D (2007) Ephrin-a1 is a negative regulator in glioma through down-reguation of epha2 and fak. *International Journal of Oncology* 30(4):865-872.
310. Walker-Daniels J, Riese DJ, & Kinch MS (2002) C-cbl-dependent epha2 protein degradation is induced by ligand binding. *Molecular Cancer Research* 1(1):79-87.
311. Wykosky J, Palma E, Gibo D, Ringler S, Turner C, & Debinski W (2008) Soluble monomeric ephrina1 is released from tumor cells and is a functional ligand for the epha2 receptor. *Oncogene* 27(58):7260-7273.
312. Wykosky J, Gibo DM, & Debinski W (2007) A novel, potent, and specific ephrina1-based cytotoxin against epha2 receptor–expressing tumor cells. *Molecular Cancer Therapeutics* 6(12):3208-3218.
313. Ferluga S, Hantgan R, Goldgur Y, Himanen JP, Nikolov DB, & Debinski W (2013) Biological and structural characterization of glycosylation on ephrin-a1, a preferred ligand for epha2 receptor tyrosine kinase. *The Journal of Biological Chemistry* 288(25):18448-18457.
314. Miao H, Burnett E, Kinch M, Simon E, & Wang B (2000) Activation of epha2 kinase suppresses integrin function and causes focal-adhesion-kinase dephosphorylation. *Nature Cell Biology* 2(2):62-69.
315. Van Den Bos W, De Bruin D, Muller B, Varkarakis I, Karagiannis A, Zondervan P, *et al.* (2014) The safety and efficacy of irreversible electroporation for the ablation of prostate cancer: A multicentre prospective human in vivo pilot study protocol. *BMJ open* 4(10):e006382.
316. Ivey JW, Latouche EL, Sano MB, Rossmeisl JH, Davalos RV, & Verbridge SS (2015) Targeted cellular ablation based on the morphology of malignant cells. *Scientific Reports* 5.
317. Foster KR (2000) Thermal and nonthermal mechanisms of interaction of radio-frequency energy with biological systems. *IEEE Transactions on Plasma Science* 28(1):15-23.

318. Huang S-H, Hung L-Y, & Lee G-B (2016) Continuous nucleus extraction by optically-induced cell lysis on a batch-type microfluidic platform. *Lab on a Chip* 16(8):1447-1456.
319. Strovas TJ, Sauter LM, Guo X, & Lidstrom ME (2007) Cell-to-cell heterogeneity in growth rate and gene expression in methylobacterium extorquens am1. *Journal of Bacteriology* 189(19):7127-7133.
320. Parri M, Taddei ML, Bianchini F, Calorini L, & Chiarugi P (2009) Epha2 reexpression prompts invasion of melanoma cells shifting from mesenchymal to amoeboid-like motility style. *Cancer Research* 69(5):2072-2081.
321. Faoro L, Singleton PA, Cervantes GM, Lennon FE, Choong NW, Kanteti R, *et al.* (2010) Epha2 mutation in lung squamous cell carcinoma promotes increased cell survival, cell invasion, focal adhesions, and mammalian target of rapamycin activation. *The Journal of Biological Chemistry* 285(24):18575-18585.
322. Guo H, Miao H, Gerber L, Singh J, Denning MF, Gilliam AC, *et al.* (2006) Disruption of epha2 receptor tyrosine kinase leads to increased susceptibility to carcinogenesis in mouse skin. *Cancer Research* 66(14):7050-7058.
323. Taddei ML, Parri M, Angelucci A, Onnis B, Bianchini F, Giannoni E, *et al.* (2009) Kinase-dependent and-independent roles of epha2 in the regulation of prostate cancer invasion and metastasis. *The American Journal of Pathology* 174(4):1492-1503.
324. Boyd AW, Bartlett PF, & Lackmann M (2014) Therapeutic targeting of eph receptors and their ligands. *Nature Reviews Drug discovery* 13(1):39-62.
325. Zelinski DP, Zantek ND, Stewart JC, Irizarry AR, & Kinch MS (2001) Epha2 overexpression causes tumorigenesis of mammary epithelial cells. *Cancer Research* 61(5):2301-2306.
326. Miyazaki T, Kato H, Fukuchi M, Nakajima M, & Kuwano H (2003) Epha2 overexpression correlates with poor prognosis in esophageal squamous cell carcinoma. *International Journal of Cancer* 103(5):657-663.
327. Thaker PH, Deavers M, Celestino J, Thornton A, Fletcher MS, Landen CN, *et al.* (2004) Epha2 expression is associated with aggressive features in ovarian carcinoma. *Clinical Cancer Research* 10(15):5145-5150.
328. Liu F, Park PJ, Lai W, Maher E, Chakravarti A, Durso L, *et al.* (2006) A genome-wide screen reveals functional gene clusters in the cancer genome and identifies epha2 as a mitogen in glioblastoma. *Cancer Research* 66(22):10815-10823.
329. Liu G, Yuan X, Zeng Z, Tunici P, Ng H, Abdulkadir IR, *et al.* (2006) Analysis of gene expression and chemoresistance of cd133+ cancer stem cells in glioblastoma. *Molecular Cancer* 5(1):67.
330. Binda E, Visioli A, Giani F, Lamorte G, Copetti M, Pitter KL, *et al.* (2012) The epha2 receptor drives self-renewal and tumorigenicity in stem-like tumor-propagating cells from human glioblastomas. *Cancer Cell* 22(6):765-780.
331. Miklavčič D, Beravs K, Šemrov D, Čemažar M, Demšar F, & Serša G (1998) The importance of electric field distribution for effective in vivo electroporation of tissues. *Biophysical Journal* 74(5):2152-2158.
332. Davalos RV, Rubinsky B, & Otten DM (2002) A feasibility study for electrical impedance tomography as a means to monitor tissue electroporation for molecular medicine. *Ieee Transactions on Biomedical Engineering* 49(4):400-403.

333. Bhonsle SP, Arena CB, Sweeney DC, & Davalos RV (2015) Mitigation of impedance changes due to electroporation therapy using bursts of high-frequency bipolar pulses. *Biomedical Engineering Online* 14(3):S3.
334. Beebe SJ, White J, Blackmore PF, Deng Y, Somers K, & Schoenbach KH (2003) Diverse effects of nanosecond pulsed electric fields on cells and tissues. *DNA and Cell Biology* 22(12):785-796.
335. Nuccitelli R, Pliquett U, Chen X, Ford W, Swanson RJ, Beebe SJ, *et al.* (2006) Nanosecond pulsed electric fields cause melanomas to self-destruct. *Biochemical and Biophysical Research Communications* 343(2):351-360.
336. Jordan CT, Guzman ML, & Noble M (2006) Cancer stem cells. *New England Journal of Medicine* 355(12):1253-1261.
337. Fan X, Salford LG, & Widegren B (2007) Glioma stem cells: Evidence and limitation. *Seminars in Cancer Biology*, (Elsevier), pp 214-218.
338. Galli R, Binda E, Orfanelli U, Cipelletti B, Gritti A, De Vitis S, *et al.* (2004) Isolation and characterization of tumorigenic, stem-like neural precursors from human glioblastoma. *Cancer Research* 64(19):7011-7021.
339. Yuan X, Curtin J, Xiong Y, Liu G, Waschsmann-Hogiu S, Farkas DL, *et al.* (2004) Isolation of cancer stem cells from adult glioblastoma multiforme. *Oncogene* 23(58):9392-9400.
340. Dimov I, Tasic-Dimov D, Conic I, & Stefanovic V (2011) Glioblastoma multiforme stem cells. *The Scientific World Journal* 11:930-958.
341. Kang M-K & Kang S-K (2007) Tumorigenesis of chemotherapeutic drug-resistant cancer stem-like cells in brain glioma. *Stem Cells and Development* 16(5):837-848.
342. Chen J, Li Y, Yu T-S, Mckay RM, Burns DK, Kernie SG, *et al.* (2012) A restricted cell population propagates glioblastoma growth after chemotherapy. *Nature* 488(7412):522-526.
343. Kang MK, Hur BI, Ko MH, Kim CH, Cha SH, & Kang SK (2008) Potential identity of multi-potential cancer stem-like subpopulation after radiation of cultured brain glioma. *BMC Neuroscience* 9(1):15.
344. Ji J, Black KL, & John SY (2010) Glioma stem cell research for the development of immunotherapy. *Neurosurgery Clinics of North America* 21(1):159-166.
345. Johannessen T-CA, Bjerkvig R, & Tysnes BB (2008) DNA repair and cancer stem-like cells–potential partners in glioma drug resistance? *Cancer Treatment Reviews* 34(6):558-567.
346. Nakai E, Park K, Yawata T, Chihara T, Kumazawa A, Nakabayashi H, *et al.* (2009) Enhanced mdr1 expression and chemoresistance of cancer stem cells derived from glioblastoma. *Cancer Investigation* 27(9):901-908.
347. Bao S, Wu Q, Mclendon RE, Hao Y, Shi Q, Hjelmeland AB, *et al.* (2006) Glioma stem cells promote radioresistance by preferential activation of the DNA damage response. *Nature* 444(7120):756-760.
348. Wang J, Wakeman TP, Lathia JD, Hjelmeland AB, Wang XF, White RR, *et al.* (2010) Notch promotes radioresistance of glioma stem cells. *Stem Cells* 28(1):17-28.
349. Bhat KP, Balasubramaniyan V, Vaillant B, Ezhilarasan R, Hummelink K, Hollingsworth F, *et al.* (2013) Mesenchymal differentiation mediated by nf-κb promotes radiation resistance in glioblastoma. *Cancer Cell* 24(3):331-346.

350. Kim S-H, Joshi K, Ezhilarasan R, Myers TR, Siu J, Gu C, *et al.* (2015) Ezh2 protects glioma stem cells from radiation-induced cell death in a melk/foxm1-dependent manner. *Stem Cell Reports* 4(2):226-238.
351. Venere M, Hamerlik P, Wu Q, Rasmussen R, Song L, Vasanji A, *et al.* (2014) Therapeutic targeting of constitutive parp activation compromises stem cell phenotype and survival of glioblastoma-initiating cells. *Cell Death & Differentiation* 21(2):258-269.
352. Heddleston JM, Li Z, Mclendon RE, Hjelmeland AB, & Rich JN (2009) The hypoxic microenvironment maintains glioblastoma stem cells and promotes reprogramming towards a cancer stem cell phenotype. *Cell cycle* 8(20):3274-3284.
353. Li Z, Bao S, Wu Q, Wang H, Eyler C, Sathornsumetee S, *et al.* (2009) Hypoxia-inducible factors regulate tumorigenic capacity of glioma stem cells. *Cancer Cell* 15(6):501-513.
354. Hjelmeland AB, Wu Q, Heddleston J, Choudhary G, Macswords J, Lathia J, *et al.* (2011) Acidic stress promotes a glioma stem cell phenotype. *Cell Death & Differentiation* 18(5):829-840.
355. Flavahan WA, Wu Q, Hitomi M, Rahim N, Kim Y, Sloan AE, *et al.* (2013) Brain tumor initiating cells adapt to restricted nutrition through preferential glucose uptake. *Nature Neuroscience* 16(10):1373-1382.
356. Yang B, Wang Y, Yang C, Ouyang W, Zhou F, Zhou Y, *et al.* (2012) The ultrastructural difference between cd133-positive u251 glioma stem cells and normal u251 glioma cells. *Ultrastructural Pathology* 36(6):404-408.
357. Vescovi AL, Galli R, & Reynolds BA (2006) Brain tumour stem cells. *Nature Reviews Cancer* 6(6):425-436.
358. Auffinger B, Tobias A, Han Y, Lee G, Guo D, Dey M, *et al.* (2014) Conversion of differentiated cancer cells into cancer stem-like cells in a glioblastoma model after primary chemotherapy. *Cell Death & Differentiation* 21(7):1119-1131.
359. Zhao Y, Huang Q, Zhang T, Dong J, Wang A, Lan Q, *et al.* (2008) Ultrastructural studies of glioma stem cells/progenitor cells. *Ultrastructural Pathology* 32(6):241-245.
360. Yamamuro S, Okamoto Y, Sano E, Ochiai Y, Ogino A, Ohta T, *et al.* (2015) Characterization of glioma stem-like cells from human glioblastomas. *International Journal of Oncology* 47(1):91-96.
361. Murphy SF, Varghese RT, Lamouille S, Guo S, Pridham KJ, Kanabur P, *et al.* (2016) Connexin 43 inhibition sensitizes chemoresistant glioblastoma cells to temozolomide. *Cancer Research* 76(1):139-149.
362. Kanabur P, Guo S, Rodgers CM, Simonds GR, Kelly DF, Gourdie RG, *et al.* (2016) Patient-derived glioblastoma stem cells respond differentially to targeted therapies. *Oncotarget* 7(52):86406.
363. Wang J, Wang H, Li Z, Wu Q, Lathia JD, Mclendon RE, *et al.* (2008) C-myc is required for maintenance of glioma cancer stem cells. *PLOS ONE* 3(11):e3769.
364. Lubensky IA, Vortmeye AO, Kim S, Lonser RR, Park DM, Ikejiri B, *et al.* (2006) Identification of tumor precursor cells in the brains of primates with radiation-induced de novo glioblastoma multiforme. *Cell Cycle* 5(4):452-456.
365. Thomson KR, Cheung W, Ellis SJ, Federman D, Kavnoudias H, Loader-Oliver D, *et al.* (2011) Investigation of the safety of irreversible electroporation in humans. *Journal of Vascular and Interventional Radiology* 22(5):611-621.
366. Tönsing K, Kakorin S, Neumann E, Liemann S, & Huber R (1997) Annexin v and vesicle membrane electroporation. *European Biophysics Journal* 26(4):307-318.

367. Chu KF & Dupuy DE (2014) Thermal ablation of tumours: Biological mechanisms and advances in therapy. *Nature Reviews Cancer* 14(3):199-208.
368. Scheffer H, Nielsen K, Van Tilborg A, Vieveen J, Bouwman R, Kazemier G, *et al.* (2014) Ablation of colorectal liver metastases by irreversible electroporation: Results of the coldfire-i ablate-and-resect study. *European Radiology* 24(10):2467-2475.
369. Tam AL, Abdelsalam ME, Gagea M, Ensor JE, Moussa M, Ahmed M, *et al.* (2014) Irreversible electroporation of the lumbar vertebrae in a porcine model: Is there clinical-pathologic evidence of neural toxicity? *Radiology* 272(3):709-719.
370. Guo Y, Zhang Y, Klein R, Nijm GM, Sahakian AV, Omary RA, *et al.* (2010) Irreversible electroporation therapy in the liver: Longitudinal efficacy studies in a rat model of hepatocellular carcinoma. *Cancer Research* 70(4):1555-1563.
371. Fink SL & Cookson BT (2005) Apoptosis, pyroptosis, and necrosis: Mechanistic description of dead and dying eukaryotic cells. *Infection and Immunity* 73(4):1907-1916.
372. Dickinson PJ, Lecouteur RA, Higgins RJ, Bringas JR, Roberts B, Larson RF, *et al.* (2008) Canine model of convection-enhanced delivery of liposomes containing cpt-11 monitored with real-time magnetic resonance imaging: Laboratory investigation. *Journal of Neurosurgery* 108(5):989-998.
373. Summers BA, Cummings JF, & De Lahunta A (1995) Tumors of the central nervous system. *Veterinary Neuropathology,* (Mosby-Year Book Publishers, Inc., St. Louis, MO), p 364.
374. Lecouteur RA (2001) Tumors of the nervous system. *Small Animal Clinical Oncology,* eds Withrow SJ & MacEwen EG (WB Saunders Co, Philadelphia, PA), 3rd Ed.